

**COOPERATIVE CONTROL OF COLLECTIVE MOTION  
FOR OCEAN SAMPLING WITH AUTONOMOUS VEHICLES**

**Derek A. Paley**

**A DISSERTATION  
PRESENTED TO THE FACULTY  
OF PRINCETON UNIVERSITY  
IN CANDIDACY FOR THE DEGREE  
OF DOCTOR OF PHILOSOPHY**

**RECOMMENDED FOR ACCEPTANCE  
BY THE DEPARTMENT OF  
MECHANICAL AND AEROSPACE ENGINEERING**

**Advisor: Naomi Ehrich Leonard**

**September 2007**



© Copyright 2007 by Derek A. Paley. All rights reserved.



# Abstract

Cooperative control is an emerging engineering field infused with biology, mathematics, and physics. Cooperative control engineers seek decentralized algorithms to coordinate the motion of robotic vehicles. These algorithms—often inspired by animal and insect grouping behavior—are relevant to applications in national security, geographic surveying, and environmental monitoring. This dissertation studies motion control for autonomous data collection by a network of underwater vehicles. Measurements of ocean circulation enable scientists to study climate processes and ecosystems in the ocean.

We describe a systematic methodology for decentralized feedback stabilization of autonomous vehicle formations. Vehicles are represented by self-propelled particles with coupled-phase oscillator dynamics. The orientation of each particle’s velocity is described by a phase angle that changes in response to the positions and phases of other particles. Particle formations include parallel motion with arbitrary relative spacing and circular motion with symmetric relative spacing. Interaction between particles is modeled by a (state-dependent) graph that may be time-invariant or time-varying and undirected or directed.

We apply a cooperative control methodology to control a fleet of autonomous underwater gliders. Underwater gliders soar through the water on a pair of fixed wings, collecting valuable oceanographic data for weeks at a time. We describe the Glider Coordinated Control System (GCCS), which steers multiple gliders to a set of coordinated trajectories. The GCCS automatically controlled up to six gliders continuously for over three weeks in a 800 km<sup>2</sup> region in California’s Monterey Bay in August 2006. The GCCS enables oceanographers to specify and adapt glider sampling patterns with minimal human intervention.



# Acknowledgements

I gratefully acknowledge the incomparable opportunities provided by my advisor Naomi Leonard. She included me in external collaborations that became instrumental to my dissertation research. I thank Naomi for her encouraging guidance, her painstaking attention to our manuscripts, and her extraordinary kindness to my wife and son. I aspire to achieve her level of academic scholarship—rigorous theoretical analyses, exciting experimental undertakings, and superlative scientific writing—and her commitment to family fulfillment.

I am deeply indebted to Rodolphe Sepulchre of the University of Liège for his collaboration in developing the theoretical framework described in this dissertation. Rodolphe has also been a thoughtful and generous mentor. I thank my readers, Phil Holmes and Clancy Rowley, whose insights, comments, and suggestions greatly improved the end result.

For inspirational discussions about biological collectives I thank Simon Levin, Dan Rubenstein, and Iain Couzin of the Ecology and Evolutionary Biology Department, Danny Grünbaum of the University of Washington, and Stephen Pratt of the University of Arizona.

Membership in the Dynamical Control Systems Lab provided me with collaborators, colleagues, and friends. I thank Fumin Zhang and Francois Lekien for their assistance in the experimental preparation and results. Fumin helped vet the GCCS during two sea trials leading up to the ASAP field experiment. Francois—along with Dmitrijs Gurkins—designed the file format used to specify glider trajectories. The experimental results described here would not have been possible without the previous work of Eddie Fiorelli, Pradeep Bhatta, Josh Graver, and Ralf Bachmayer. I also thank past, present, and visiting lab members for their contributions and comradery, including Spring Berman, Jamie Jeanne, Ben Nabet,

Sujit Nair, Jeff Pinner, Alain Sarlette, Andy Stewart, and Dan Swain.

The pilot and field experiments described in Chapter 9 were part of a multiple-university research initiative. I am especially grateful for the research collaboration with David Fratanoni and John Lund of the Woods Hole Oceanographic Institution and Russ Davis of the Scripps Institution of Oceanography. In addition, I thank Brent Jones and Jeff Sherman of the Scripps Institution of Oceanography; Pat Haley, Pierre Lermusiaux, Wayne Leslie, and Allan Robinson of Harvard University; and Jim Bellingham, Francisco Chavez, Mike Godin, Hans Thomas, and Yanwu Zhang of the Monterey Bay Aquarium Research Institute. I also thank Yi Chao (Jet Propulsion Lab), Sharon Majumdar (University of Miami), Steve Ramp (Naval Postgraduate School), and Igor Shulman (Naval Research Lab).

My department is a happy home that I will truly miss. For their contributions to my professional preparation, I thank faculty members Mike Littman, Luigi Martinelli, and Robert Stengel. Jeremy Kasdin is a valued mentor and collaborator. I also thank the administrative staff Valerie Carroll, Maureen Hickey, Jenny Kokini, Sharon Matarese, Kelly-Lynn O’Neal, and Jody Whitehead. A special thanks goes to Jess O’Leary, for both her organizational prowess and her friendship. Fellow graduate students—Grunde Jomaas, Egemen Kolemen, and Juan Melli—have provided welcome counsel. I would be remiss if I did not thank my teammates on the MAE softball team for many entertaining afternoons.

My family has provided the foundation of my support. I thank my parents Heath and Karen for the work ethic they instilled in me. I often think of an aphorism generated by memories of family hiking trips: *it takes many small steps to climb a mountain*. I thank my grandparents Warren and Claire for their genuine interest, which endured my long-winded explanations. I thank Peter and Emily Weinstein for their avuncular and materteral concern, and, of course, my in-laws—Dennis and Caryn—for treating me like their own son. To my brothers and sisters (in-law)—Sean, Alicia, Erica, and Brian—your affection and support have been very important to me.

I dedicate this dissertation to my wife Robyn—whose love, patience, and understanding buoy me in any sea state—and to Ethan, my biggest accomplishment.

My research has been supported by a National Defense Science and Engineering Graduate Fellowship, a National Science Foundation Graduate Research Fellowship, and the Pew Training Program in Biocomplexity (Pew Charitable Trust grant 2000-002558). I am thankful for the following generous awards from the Princeton University Graduate School: a Gordon Y. S. Wu Graduate Fellowship, a Harold W. Dodds Honorific Fellowship, and a grant from the Dean's Fund for Scholarly Travel.

This dissertation carries the designation 3172T in the records of the Department of Mechanical and Aerospace Engineering, Princeton University.



To Robyn and Ethan



# Contents

<b>Abstract</b>	<b>iii</b>
<b>Acknowledgements</b>	<b>v</b>
<b>Contents</b>	<b>xi</b>
<b>List of Figures</b>	<b>xv</b>
<b>List of Tables</b>	<b>xix</b>
<b>1 Introduction</b>	<b>1</b>
1.1 Statement of Problem . . . . .	3
1.2 Survey of Related Work . . . . .	5
1.2.1 Control of Collective Motion . . . . .	5
1.2.2 Sampling with Autonomous Vehicles . . . . .	11
1.3 Contributions of Dissertation . . . . .	13
1.4 Dissertation Outline and Conventions . . . . .	15
<b>2 Ocean Sampling with Gliders</b>	<b>19</b>
2.1 Autonomous Underwater Gliders . . . . .	22
2.2 Mapping Performance Metric . . . . .	28
2.2.1 Example of Mapping Error in Space . . . . .	32
2.2.2 Example of Mapping Error in Space and Time . . . . .	34

2.3	Adaptive Sampling Strategy and Challenges . . . . .	37
2.3.1	Analysis of a Field Experiment . . . . .	39
2.3.2	Example of an Open-Loop Survey with Flow . . . . .	42
2.3.3	Feedback Control at the Level of the Glider Fleet . . . . .	45
<b>3</b>	<b>Motion and Interaction Models</b>	<b>49</b>
3.1	Particles with Phase Oscillator Dynamics . . . . .	49
3.2	Shape Control and Relative Equilibria . . . . .	57
3.3	Interaction Networks and Graph Theory . . . . .	62
<b>4</b>	<b>Phase Synchronization and Balancing</b>	<b>69</b>
4.1	All-to-all Interaction . . . . .	69
4.2	Time-invariant and Undirected Interaction . . . . .	74
4.3	General Interaction . . . . .	80
<b>5</b>	<b>Circular Formations</b>	<b>91</b>
5.1	All-to-all Interaction . . . . .	92
5.2	Time-invariant and Undirected Interaction . . . . .	97
5.3	General Interaction . . . . .	99
<b>6</b>	<b>Symmetric Circular Formations</b>	<b>109</b>
6.1	All-to-all Interaction . . . . .	110
6.2	Time-invariant and Undirected Interaction . . . . .	120
6.3	General Interaction . . . . .	128
<b>7</b>	<b>Applied Control Design</b>	<b>133</b>
7.1	Continuous Symmetry Breaking Using a Virtual Particle . . . . .	133
7.1.1	Time-invariant and Undirected Interaction . . . . .	135
7.1.2	General Interaction . . . . .	141
7.2	Discrete Symmetry Breaking Using Network Design . . . . .	144
7.3	Symmetric Formations on Convex Loops . . . . .	150

<b>8</b>	<b>Glider Control Synthesis</b>	<b>161</b>
8.1	Specifying Glider Trajectories . . . . .	162
8.2	Modeling Glider Motion . . . . .	167
8.2.1	Simple Glider Model . . . . .	167
8.2.2	Detailed Glider Model . . . . .	169
8.3	The Glider Coordinated Control System: Architecture and Operation . . .	175
8.3.1	Glider Planner . . . . .	175
8.3.2	Glider Simulator . . . . .	179
8.3.3	Remote Input/Output . . . . .	180
<b>9</b>	<b>GCCS Experimental Results</b>	<b>181</b>
9.1	Adaptive Sampling and Prediction Research Initiative . . . . .	182
9.1.1	Upwelling in Monterey Bay . . . . .	183
9.1.2	ASAP Glider Experimental Methods . . . . .	185
9.2	Summary of an ASAP Virtual Pilot Experiment . . . . .	187
9.3	ASAP 2006 Field Experiment . . . . .	194
9.3.1	Evaluation of Coordination Performance . . . . .	200
9.3.2	Evaluation of Mapping Performance . . . . .	211
<b>10</b>	<b>Conclusion</b>	<b>217</b>
10.1	Summary of Contributions . . . . .	217
10.1.1	Control of Collective Motion . . . . .	218
10.1.2	Sampling with Autonomous Vehicles . . . . .	220
10.2	Ongoing and Proposed Work . . . . .	222
10.2.1	Increasing Autonomy of Underwater Gliders . . . . .	222
10.2.2	Interaction Networks in Biological Collectives . . . . .	226
<b>A</b>	<b>Supplemental Theoretical Results</b>	<b>229</b>
<b>B</b>	<b>Curvature and Parameterization of a Superellipse</b>	<b>233</b>

<b>C Geodetic Utilities</b>	<b>235</b>
<b>D Supplemental Experimental Materials</b>	<b>237</b>
<b>References</b>	<b>241</b>
<b>Index</b>	<b>275</b>

# List of Figures

1.1	Flock of European starlings . . . . .	2
2.1	Parameter space of lawn-mowing analogy for ocean sampling . . . . .	20
2.2	Slocum gliders prepared for deployment on the deck of R/V Shana Rae in August 2003 . . . . .	23
2.3	The stages of a glider dive . . . . .	24
2.4	Selected oceanographic processes in the space-time sampling regime of gliders and propellor-driven AUVs . . . . .	27
2.5	Exponential and normal covariance functions $C(R, t, R', t')$ for $t = t'$ . . . .	30
2.6	Mapping error example . . . . .	33
2.7	Sensor swath and sampling constraints . . . . .	35
2.8	Mapping a one-dimensional domain with periodic boundary conditions . . .	36
2.9	Constructing a time sequence of cross-shelf ocean dynamics from glider measurements . . . . .	39
2.10	AOSN-II glider profile positions . . . . .	40
2.11	AOSN-II Spray glider mapping error . . . . .	41
2.12	AOSN-II Spray glider mapping performance $\mathcal{J}(t)$ and average number of profiles used per day to compute $\mathcal{J}(t)$ . . . . .	42
2.13	Simple model of two gliders on a circular track in a uniform flow field . . .	43
2.14	Numerical results for the simple model of Figure 2.13: two gliders on a circular track in a flow field . . . . .	44

2.15	Illustrations of coordinated glider movement . . . . .	46
3.1	Planar particle dynamics . . . . .	50
3.2	Phase synchronization and balancing for $N = 2$ . . . . .	53
3.3	Symmetric phase patterns . . . . .	56
3.4	Shape variables . . . . .	60
3.5	Interaction network . . . . .	63
3.6	Circulant graphs . . . . .	66
3.7	Results by level of interaction . . . . .	68
4.1	All-to-all phase control . . . . .	73
4.2	All-to-all phase control during circular motion . . . . .	75
4.3	Dynamic phase control . . . . .	90
5.1	All-to-all composite phase and formation control . . . . .	95
5.2	Dynamic circular formation control . . . . .	103
6.1	All-to-all symmetric circular formation control . . . . .	118
6.2	Symmetric phase patterns with all-to-all interaction . . . . .	119
6.3	Symmetric phase patterns with ring interaction . . . . .	124
6.4	Dynamic symmetric circular formation control . . . . .	132
7.1	Augmented interaction network . . . . .	134
7.2	Augmented Laplacian phase control . . . . .	137
7.3	Augmented Laplacian circular formation control . . . . .	140
7.4	Multi-level symmetric configuration and supporting interaction network . . . . .	145
7.5	Multi-level Laplacian symmetric circular formation control . . . . .	149
7.6	Particle orbiting closed loop $C$ . . . . .	151
7.7	Curvature as feedback . . . . .	153
7.8	Laplacian loop formation control . . . . .	155

8.1	The Glider Coordinated Control System . . . . .	162
8.2	Illustration of a GCT near Point Año Nuevo, California . . . . .	164
8.3	A GCT glider tree corresponding to levels 1 and 2 of the multi-level interaction network example shown in Figure 7.4(c) . . . . .	167
8.4	Coordinates for the glider model . . . . .	170
8.5	Waypoint geometry and completion conditions . . . . .	172
8.6	Glider planner block diagram . . . . .	175
8.7	Output of a GCCS planning cycle . . . . .	176
9.1	AOSN-II and ASAP mapping domains and ocean circulation . . . . .	183
9.2	Default ASAP glider sampling plans . . . . .	185
9.3	Snapshots of model-ocean flow conditions during ASAP VPE . . . . .	188
9.4	Spray GCT and snapshots of glider trajectories during an ASAP VPE . . . . .	190
9.5	Slocum GCT and snapshots of glider trajectories during an ASAP VPE . . . . .	191
9.6	Slocum GCT and snapshots of glider trajectories after adaptation of sampling plan during ASAP VPE . . . . .	192
9.7	Slocum glider normalized mapping error during ASAP VPE . . . . .	193
9.8	Slocum mapping performance $\mathcal{J}(t)$ during ASAP VPE . . . . .	194
9.9	Times of glider profiles collected during ASAP 2006 FE . . . . .	196
9.10	Locations of glider profiles collected during ASAP 2006 FE . . . . .	197
9.11	Two snapshots of the ocean circulation during the ASAP FE . . . . .	198
9.12	ASAP FE flow velocity and GCCS prediction accuracy . . . . .	199
9.13	Timeline of GCTs used by the GCCS to control Slocum gliders during ASAP 2006 FE . . . . .	201
9.14	Metrics of coordination performance . . . . .	202
9.15	Slocum glider trajectories and depth-averaged flow measurements during ASAP 2006 FE GCT #6 . . . . .	204
9.16	Slocum glider speed and depth-averaged flow velocity during GCT #6 . . . . .	205
9.17	Coordination performance of Slocum gliders during GCT #6 . . . . .	206

9.18 Slocum glider trajectories and depth-averaged flow measurements during ASAP 2006 FE GCT #9 . . . . .	207
9.19 Slocum glider speed and depth-averaged flow velocity during GCT #9 . . .	208
9.20 Coordination performance of Slocum gliders during GCT #9 . . . . .	209
9.21 Slocum glider trajectories and depth-averaged flow measurements during ASAP 2006 FE GCT #11 . . . . .	210
9.22 Slocum glider speed and depth-averaged flow velocity during GCT #11 . .	211
9.23 Coordination performance of Slocum gliders during GCT #11 . . . . .	212
9.24 Glider mapping performance during ASAP 2006 FE . . . . .	213
10.1 Increasing autonomy of underwater gliders . . . . .	223
10.2 Illustration of dynamic interaction network for three organisms . . . . .	227
A.1 Geometric representation of sets in the proof of Lemma A.2 . . . . .	230
D.1 GCTs used during ASAP 2006 field experiment from 23:15 GMT August 2 to 21:09 GMT August 11 . . . . .	239
D.2 GCTs used during ASAP 2006 field experiment from 21:09 GMT August 11 to 11:10 GMT August 21 . . . . .	240

# List of Tables

2.1	Adaptive sampling strategy . . . . .	47
8.1	Specification of a GCT operating domain . . . . .	165
8.2	Specification of a GCT track list . . . . .	165
8.3	Specification of a GCT structured glider list . . . . .	166
8.4	Particle integrator algorithm . . . . .	178
C.1	WGS84 geoid parameters . . . . .	236
D.1	GCCS parameters used during ASAP August 2006 FE . . . . .	238



# Chapter 1

## Introduction

Coordinated motion of an animal group is a remarkable phenomenon to observe. Flocks of birds wheel and turn in unison, often forming large congregations before roosting at dusk (see Figure 1.1). Fish schools turn and glide spontaneously, so that the impetus for changing direction appears to travel through the school instantly. And from the deliberate movement of ants within a colony a complex society emerges, notwithstanding the minimal sizes and capabilities of its members.

Collective behavior of animal aggregations is often emulated by engineers in the design of collaborating teams of mobile robots. Such robots, called autonomous or unmanned vehicles, have recently made forays off of the printed pages of academic journals and out of research laboratories into the challenging arenas of the air, sea, and space. The promise of collaborative operation with minimal human intervention has been fulfilled in support of missions pertaining to national defense, homeland security, and environmental monitoring. Nonetheless, many exciting challenges remain.

A growing number of engineers and biologists interested in studying collective motion have coalesced into an active, interdisciplinary research community. From this fertile mix of disciplines has emerged the topic of *cooperative control*, which addresses the integration of quantitative and empirical methods for the purpose of designing and modeling collective motion algorithms. Advances in this topic have been enabled by tools from mathematics

## 2 Introduction



Figure 1.1: Flock of European starlings. These social birds form communal night roosts that can contain millions of individuals [1]. Photo credit: H. Paley.

and motivated and validated by experiments.

In this dissertation, we present a mathematical framework to generate coordinated motion in a group of autonomous vehicles. We also describe the implementation and at-sea demonstration of the framework to automatically control a fleet of autonomous underwater vehicles. The framework uses simple models of individual motion and interaction to automatically steer vehicles into coordinated, moving patterns. We describe a class of patterns relevant to applications in environmental monitoring. When vehicle motion is coordinated by our automatic control system, the fleet seeks to collect measurements containing the most information about the ocean; this data enables scientists to make new discoveries that may improve our understanding of climate processes and ecosystems in the ocean.

## 1.1 Statement of Problem

A common trait among groups that exhibit collective motion is the capability to act without centralized control. By centralized control, we mean the actions of a single, omnipotent entity that organizes the behavior of the group. For example, the coordinated action of the tentacles of an octopus is likely generated by a central nervous system. Likewise, the scripted maneuvers of battalions within a military regimen may be orchestrated by a military commander. In both examples, the individual units—tentacles and battalions, respectively—certainly have some capacity for autonomous movement and interaction with one another and their environment, but without centralized control, organized behavior of multiple units may not reliably occur.

Coordination under *decentralized* control, which emerges so effortlessly in biological collectives, represents a major challenge for groups of autonomous vehicles. Decentralized control (also called distributed control) is a process by which each agent in a group executes a simple algorithm such that all of the agents converge to a common activity. Knowledge of a desired group activity may be available to a few agents or to none at all. Convergence to a common activity occurs literally or figuratively through the process of *consensus*. A school of fish in tight formation is an example of consensus about the direction of motion; formation flight of migrating geese is another example.

One challenge to achieving consensus in artificial agents is limited inter-vehicle sensing and communication. Instruments for sensing and communication are not yet as refined as their biological counterparts. Sensing and communication modalities that use mechanical or electromagnetic wave transmission may not have sufficient bandwidth for a large group, and may operate under restrictions on range and transmission medium. For example, interaction between autonomous underwater vehicles using electromagnetic waves in the visible or radio frequency ranges is restricted by the short attenuation length of such waves in water. Underwater communication using acoustic waves is possible over long distances, but competing and scattering sources can limit bandwidth.

As a result of limited sensing and communication, interaction between vehicles may

## 4 Introduction

be local in space and intermittent in time. In the absence of any single, absolute frame of reference, inter-vehicle interaction may consist only of relative measurements. That is, in order to direct its own motion, a robot may have available to it only the distance and direction to each one of its neighbors; a robot may not know its own absolute position or the absolute position of its neighbors. The direction of motion of a robot presents an additional challenge for mathematical modeling since the space of all possible directions (angles) is nonlinear and so not a vector space.

Interaction limitations are often compounded by vehicle kinematic constraints that limit maneuverability. For example, rolling land vehicles are subject to the constraint that they cannot move “sideways”, a limitation familiar to anyone who has parallel-parked an automobile. A similar limitation exists for aerial and underwater vehicles. Aerial and underwater vehicles may face the additional challenge of being dynamically underactuated; strong gusts of wind or strong ocean currents impede or even preclude motion in certain directions.

For autonomous vehicles tasked to collect sensor data in a variable environment, it is a challenge—even with centralized control—to automate vehicle trajectory planning. The design of trajectories for optimal data collection is aided by use of metrics that quantitatively distinguish between coordinated and uncoordinated motion. The desire to execute, evaluate, and adapt these trajectories without human intervention motivates the development of a control system that uses feedback: a principle at the heart of automatic control.

The three main challenges addressed in this dissertation are as follows:

1. *Develop a methodology to provide decentralized cooperative algorithms that operate with limited interaction and account for vehicle kinematic constraints.*
2. *Automate the motion planning for a collaborative group of autonomous underwater vehicles monitoring a highly-variable region of ocean.*
3. *Demonstrate at sea the automated control of an underwater vehicle fleet in support of an oceanographic experiment.*

## 1.2 Survey of Related Work

Due to the breadth and abundance of literature on topics related to this dissertation, we provide here an overview that is necessarily incomplete. We describe previous work pertaining to collective motion, from both biological and engineering perspectives. Then we summarize research related to ocean sampling, paying special attention to autonomous underwater vehicles. References to these and other supporting materials also appear throughout the dissertation.

### 1.2.1 Control of Collective Motion

#### Ecological Inspirations

Despite their ubiquity, biological collectives are difficult to define and model. In research related to fish schools, Partridge asserts that common definitions of schooling are inadequate to describe the wide variety of grouping behavior observed in fish [204, 205]; see also [11, 12, 203]. Since schools are highly variable in size and constituency, Partridge suggests that any definition of a fish school should include the amount of time each individual spends in the school and a description of the organization of the school, such as the ratio of distances to first and second nearest neighbors. Nonetheless, the fact that collective motions occur in such a diverse set of organisms implies there may exist common underlying principles that can be placed in a single framework [76]. Deneubourg and Goss contend that the ubiquity of collective motion and decision-making implies that complex social patterns may originate from simple individual behaviors [68]. However, these authors note that—under the influence of a variable environment—the same individual behavior may lead to different group motion. Apparently, *why* animals aggregate is better understood than *how* they do it. Selfishness (for example, reduced risk of predation) is a classic explanation [111]. For a catalogue of benefits of group formation see, for example, [135, pp. 6-40].

Dynamic patterns of large animal groups have been modeled by ecologists using continuum methods. By transforming a binomial distribution into a diffusion equation with linear

## 6 Introduction

temporal variance, Hallam and Levin demonstrate how a random walk model of individual movement can generate a propagating wave at the front of a group [152]. Theoretical analysis of these traveling wave fronts in wildebeest herds are validated by comparing solutions of a partial differential equation with aerial photos [105]. The results from such comparisons are better for short ranges, which implies that local interactions may be modeled more accurately than group-level patterns. The dynamics of group formation are modeled by Gueron and Levin in terms of fusion and fission processes: the parameters in this model can be set to produce either small groups or a bimodal distribution of group size [106]. These authors also consider alternatives to continuum modeling, such as individual-based modeling, where integration of many individuals is replaced by studying interaction between neighboring individuals [107]. They show that the eccentricity (elongation of shape) of an animal formation depends on individual velocities, heterogeneity, and neighborhood structure. More recently, a statistical-mechanics characterization of the types of collective motion produced by pairwise interaction forces has been presented in [74].

Continuum models of animal aggregations have been studied mathematically using partial differential equations, whereas ordinary differential or difference equations describing the motions of individual fish have been studied by biologists using numerical simulations. An early numerical-simulation study of fish schools by Aoki asserts that the behavior of individual fish leading to collective motion necessarily includes attraction to neighbors and turning to match neighbor velocities [12]. The behavior components of attraction and orientation, along with repulsion from neighbors on a collision course, were subsequently utilized by Huth for the purposes of studying cohesion in fish schools [120]. For a more recent explanation of schooling behaviors, see, for example, [55], where Couzin reveals via numerical simulation the co-existence of parallel and circular group motions for a single set parameters. For a review of recent research on schooling fish, see [53].

Mathematical transformations between continuum- and individual-based models of animal aggregations engender a taxonomy of grouping behavior. In a pioneering work, Okubo shows how individual behavior modeled using Newtonian dynamics resembles a diffusion

process [188]. Grünbaum studies the transformation from stochastic individual-based (Lagrangian) models to continuum (Eulerian) models [102]. A comprehensive catalogue of individual models of aggregation is presented in [86], including the following: directional response to environmental cues (*taxis*), non-directional response to environmental cues (*kinesis*), movement toward/away from neighbors, preference for neighbors' velocities, and non-directional social behavior, such as reduced movement in areas of high population density. Individuals can also be advected by environmental forces. A dynamic environment can promote or prevent group formation depending on advection strength and turbulence. In fact, the interplay between individuals and the environment may be as significant in modeling group formation as the interplay between individual and population dynamics [151].

Proposed functional advantages of group formation—gradient-climbing [103], decision-making [54], and migration [289, 288]—can be validated through field observations and manipulative experiments on grouping organisms. Such experiments also shed insight on grouping mechanisms. Early observations of migratory birds suggests that night calls facilitate flocking by providing other birds with directional cues and motivation to take-off [112]. Quantitative measurements of waves of turning in fish schools have revealed that the speed of information travel exceeds by an order of magnitude faster than the speed of an individual fish [214, pp. 77-99]. Parrish, Grünbaum, and Viscido have shown using system identification methods that schooling fish data can be classified as either tight-milling (preference for lateral nearest neighbor position) or diffuse-milling (preference for head/tail nearest neighbor position) [104]. These authors quantify fish trajectory data using metrics based on polarity, speed, and nearest-neighbor distance [281]. Sufficient organism density triggers the onset of collective motion in desert locusts [41].

## Analysis and Design

A seminal paper by Vicsek *et al.* catalyzed a burst of interest in collective behavior in the physics community [280]. In this paper, the authors propose a simple, linear model for collective motion in which individuals move in the average direction of their neighbors.

Simulations of this model that exhibit long-range ordered motion were validated mathematically using continuum models by Toner and Yu [268]. A key requirement of the model is mobility: if the agents do not move, then long-range alignment is not possible. A comprehensive description of this continuum theory is available in [269]. For other references in this vein, see, for example, [245, 100, 231, 99].

Interest in the Vicsek model bloomed in the controls community when Jadbabaie *et al.* applied nearest-neighbor rules to the coordination of groups of autonomous agents [122]. Using tools from matrix analysis, the authors describe the coordination of direction of motion using a switched linear system, and prove convergence to a common direction of motion under certain restrictions on the switching times (see [92] for corrections and [154] for extensions). As noted in [274], related results were previously available in the literature on distributed and decentralized computing [273, 275]. In fact, early studies of the problem of decentralized agreement or consensus appear in the statistics and probability literature: DeGroot provided a condition for convergence of expert opinions [67]; his analysis was extended and formalized by Chatterjee and Seneta [46].

Controls research on the topic of consensus has flourished recently. Consensus of agent positions is studied in the contexts of rendezvous [154], flocking [266], and swarming [270]. We devote special attention here to research on groups with limited and time-varying interaction between individuals. Fax and Murray utilized algebraic graph theory to describe the network of interactions between individuals, and related the spectrum of a matrix representation of the interaction network to rate of convergence in vehicle formations [79, 80]; see also [140]. Building on the connection to graph theory, Olfati-Saber and Murray identified the utility of a class of graphs—known as balanced graphs (see Section 3.3)—in solving consensus problems with fixed or switching interaction networks [192]. The authors also describe trade-offs between performance, robustness, and communication cost. Convergence to consensus among interacting groups can be modeled by operations on graphs and predicted by the spectra of the graph matrices [16].

The strongest results on the consensus problem provide necessary conditions on the

minimum level of interaction required to achieve consensus. Two such results are utilized in this dissertation (see Section 4.3) to support cooperative control algorithms with dynamic interaction networks: (i) Moreau’s discrete-time analysis [175], extended to continuous-time in [174], and (ii) Ren and Beard’s corresponding analysis on discrete- and continuous-time consensus algorithms [219]. Moreau’s result, which uses a set-valued Lyapunov stability approach to prove contraction of a convex hull of individual states, is extended to prove contraction of non-convex sets in [10]. Contraction analysis is also applied to the consensus problem with time-delayed communication in [270]. In the event that interaction between individuals is probabilistic, Hatano and Mesbahi predict whether or not consensus will occur based on time-averaged properties of the network [113]. For recent synopses of the consensus literature, see, for example, [220, 191].

In most cases, the consensus literature models the agreement problem using linear dynamics. However, agreement among mobile robots about a common direction of motion is a decidedly nonlinear problem. The direction of motion of a robot can be represented by a point on the unit circle  $S^1$ , which is the space of angles. Each direction is called a *phase*. In a group of  $N$  mobile robots, the collection of all phases evolves on the  $N$ -torus  $\mathbb{T}^N$ , which is equal to  $S^1 \times \cdots \times S^1$  ( $N$  times). Modeling on the torus leads to global results such as Theorem 4.2, while modeling on the real line can provide only local results since the configuration space is not Euclidean. An important leap from linear consensus to consensus on the  $N$ -torus was made in Scardovi *et al.* [233], summarized here in Theorem 4.10.

Consensus on the  $N$ -torus, called *synchronization*, has a long and elegant history in the literature on a set of periodic phenomena known as *coupled-phase oscillators*. This literature can be traced back to mathematical models of interacting periodic processes developed in biology by Winfree [292] and in chemistry by Kuramoto [138]. Coupled-phase oscillator models seek to provide better understanding of the behavior of interacting populations of oscillatory units. They have been applied and extended to study superconductors [285], animal gaits [50], hopping and juggling robots [133], ant colonies [31], and neurons [39].

In many applications, variations of the *Kuramoto model* [139] are studied (see [259, 5] for

a review). The Kuramoto model describes the evolution in time of a group of coupled-phase oscillators with global interaction. The strength and form of this interaction determines the group behavior. In populations of weakly interacting oscillators, Ashwin, Swift and others study the existence of phase clusters [15, 189, 38]; see also [134, 271, 94, 156, 18, 257, 119]. When the interaction gain crosses a specific threshold, some populations tend to synchronize [6]. Populations with repulsive or negative coupling have been studied [272], as have populations with time-delayed interaction [296, 202]. Golubitsky *et al.* have shown that network architecture can enforce synchronized oscillator behavior, independent of the form of coupling [95]. Lyapunov-stability analyses of oscillator networks appear in [278, 206, 125].

The link between coupled-phase oscillators and collective motion is fundamental to the mathematical model of individual movement employed in this dissertation. This dynamic motion model was adopted from Justh and Krishnaprasad, who developed steering controls for groups of autonomous air vehicles moving at constant speed [126, 127]. These authors emphasize a geometric approach summarized in Section 3.2. The constant-speed constraint—also applicable to many types of underwater vehicles—distinguishes the Justh and Krishnaprasad motion model from an unconstrained motion model. When a vehicle moves at constant speed, its only control authority is to steer its direction of motion. Such a model is sometimes called a self-propelled or unicycle model. When a vehicle’s motion is unconstrained, it is capable of moving (and accelerating) in any direction (see, for example, [145] and [190], for work on coordinated control of unconstrained vehicles). Other work on steering control of unicycle models includes [301, 176, 253, 232]. The latter two citations study an early unicycle model called a *Dubins’ vehicle*, which is subject to an additional constraint on the minimum turning radius [75].

In this dissertation, we represent each vehicle using a dynamic model of a particle subject to Newtonian physics. When a particle obeys Newton’s second law, it accelerates in response to an applied force—usually the control input. Note, steering control is an applied force normal to the direction of motion. A particle model in which the velocity is determined directly by the control input are called kinematic; see, for example, [270]. Note, a particle

has no orientation. To represent the orientation of a vehicle, one could use a rigid-body model. Synchronization of rigid-body orientation is considered in [180], for a chain-like interaction network, and in [230], for a more general class of limited interaction. Stability of satellite rings in the scalar, gravitational potential of a large body is studied in [136]. Control of particles using artificial scalar potentials is studied in [221, 145, 185] and artificial vector potentials in [283].

### 1.2.2 Sampling with Autonomous Vehicles

An emerging topic of study within the cooperative control community is motion coordination for information gathering. Sometimes motivated by social foraging behavior in animal groups [9], control engineers have studied boundary tracking [262, 24, 301, 117], coverage control [47, 52], gradient descent [17, 186], target tracking [164], and sensor networks [251, 45, 187]. Grocholsky incorporates Kalman filtering theory into a so-called information filter (see, for example, [160]) that can be used to steer vehicles so as to maximize their information collection [101]. Cortés formulates a distributed implementation of a classical estimation algorithm from geostatistics to steer vehicles to extrema in a scalar field [51].

Steering underwater vehicles to gather data in the ocean has been envisioned on a global scale. In a visionary article, Stommel describes the World Ocean Observing System (WOOS)—to be installed during the period 1995–2025—that parallels the network of upper-air observation stations installed by meteorologists during the period 1945–1975 [258]. Stommel’s vision for WOOS consists of approximately 550 autonomous underwater vehicles (AUVs) called gliders (see, for example, [65] and Section 2.1) that are distributed around the world. Gliders and propeller-driven AUVs [21, 7, 297] are two modern platforms for autonomous oceanographic data collection. Stommel’s vision has not yet materialized with gliders or AUVs, but it has been effectively realized with drifting sensor platforms that collect measurements while moving vertically in the water column [2]. Drifters are an effective oceanographic monitoring device that periodically surface transmit data to scientists on shore via satellites [61, 62].

A major distinction between a drifting sensor platform and a self-propelled one is the latter's ability to maneuver in response to data collected so as to improve the value of future measurements. Metrics to evaluate and design data-collection trajectories for individual vehicles were defined in [290, 291] and used to analyze survey performance in [22]. Underwater vehicles can be steered to identify important features in the ocean [23], classify an ocean circulation process [303], or to simultaneously map its environment and then use that map to navigate [81, 143]. Steering gliders in the presence of strong ocean currents is a difficult challenge considered by Davis *et al.* using a ray tracing approach—assuming the flow field is known [66]; see also [121]. The integration of multiple sensing platforms, both manned and unmanned, for the purpose of environmental assessment has been dubbed an *autonomous ocean sampling network* (AOSN) [59, 58]. Such networks seek to perform ocean mapping surveys with at very high resolution [217]. Ocean sampling strategies can be designed to improve ocean model predictive skill; see, for example, [246, 247], for optimization of a sampling strategy to measure and model bioluminescence.

Control of multiple underwater vehicles plays an important role in enabling sustained ocean observation [236, 207]. Since the inception of the AOSN concept, there have been several demonstrations of (remote) control systems for multiple underwater vehicles. The Glider Mission Control Center, which is an agent-based software system designed for manual and automated control of underwater gliders, has been demonstrated in multi-vehicle operations in the New York Bight and west coast Florida shelf [56]. Also, the Fleet Logistical Interface and Control Software, developed to coordinate multi-vehicle missions such as formation control of micro-AUVs, was tested in Newport River on the coast of North Carolina [237]. The software application Autonomous Systems Monitoring and Control has controlled a solar-powered underwater vehicle in Lake George, New York [178]. Semi-autonomous coordination of gliders with manual assistance has been demonstrated [65, 83].

Data sets from multi-vehicle ocean surveys are incorporated into ocean forecasting systems through a process called data *assimilation*. There exists a broad literature on the assimilation of a set of irregularly spaced measurements into stochastic models of physical and

biological processes in the air and sea. An early pioneer in this field of research—Gandin—developed computerized algorithms using classical linear estimation theory to form so-called *objective* maps of weather patterns [91] (as opposed to *subjective* maps generated by a human). Gandin’s approach, called objective analysis (OA), was applied to oceanographic experimental data by Bretherton *et al.* [36, 37, 63] and is described in Section 2.2. For examples of OA techniques applied to measurement data in the mid-ocean, see [166, 118], and in a coastal region, see [157]. More recent assimilation techniques supplement statistical models of the underlying oceanographic process with dynamic models, including Error Subspace Statistical Estimation [150, 147], Ensemble Transform Kalman Filtering [27, 159], multiscale optimization [167], and Monte Carlo techniques [8]. Two articles of a tutorial nature on this topic are [223] and [149].

### 1.3 Contributions of Dissertation

This dissertation makes contributions to the general theory on stabilization of collective motion and in the application to adaptive ocean sampling. Some materials from this dissertation have been previously published or accepted for publication, including [239, 243, 241, 201, 197, 146]. Conference papers in which early versions of these results appeared include [196, 238, 198, 123, 240, 242, 199]. Some results—including the analysis of the field experiment described in Chapter 9—have not yet appeared elsewhere.

We study cooperative control of a planar model of self-propelled particles with coupled phase-oscillator dynamics. We describe a systematic methodology that yields decentralized feedback controls to provably stabilize *relative equilibria* of the particle model. Relative equilibria correspond to either parallel motion of all particles with fixed relative spacing or circular motion of all particles with fixed relative phases. Using the methodology, we can also isolate circular motion of particles in symmetric patterns. We design artificial potentials to serve as control-Lyapunov functions and gradient, or gradient-like, feedback laws to ensure that these potentials monotonically decrease along solutions of the closed-loop system.

The potential-based design of feedback control laws applies to groups with all-to-all

interaction and to groups with limited interaction [243, 243]. For groups with undirected and time-invariant interaction, we utilize the gradient of a quadratic potential induced from a matrix representation of the particle interaction network. In groups with directed and/or time-varying interaction, we achieve gradient-like control by augmenting the gradient algorithm with a decentralized filter to estimate averaged quantities.

We develop symmetry-breaking controls to stabilize patterns suitable for a mobile sensor network. Stabilization to either parallel motion in a fixed direction or circular motion about a fixed point is provided by introducing a virtual particle as a reference. We also show how limitations in the interaction network can be introduced to advantage. By using nests of multiple, limited graphs, we can steer particles to symmetric configurations on multiple loops. The entire framework is portable to formations on convex loops that are not necessarily circular [197].

The implementation our cooperative control framework on a fleet of underwater gliders is called the Glider Coordinated Control System (GCCS) [201]. The GCCS automatically steers a fleet of gliders to a set of coordinated trajectories. The GCCS uses both a simple planar model for planning future trajectories and a detailed three-dimensional model to predict vehicle motion underwater. We describe a vehicle simulator used the development and evaluation of fleet-level feedback controllers. The simulator also provides an invaluable tool for investigating how to tackle challenges like strong ocean currents and intermittent communication—challenges not yet fully addressed by theoretical methods.

The oceanographic utility of the GCCS has been demonstrated at sea. During a field experiment in Monterey Bay, California in August 2006, the GCCS automatically steered up to six gliders continuously to a series of coordinated trajectories for nearly twenty-four days. The desired set of vehicle trajectories were modified by a human operator at a few discrete times during the experiment, in response to changes in the ocean circulation. The human adaptations were implemented by an interrupt followed by a restart of the automatic routine. Otherwise, the twenty-four day operation was performed without a human in the loop. The gliders were controlled in Monterey Bay by a computer at Princeton University.

## 1.4 Dissertation Outline and Conventions

Chapter 2 contains an ocean-sampling primer that motivates the theoretical development in the subsequent chapters. In Chapter 3, we introduce the mathematical description of our cooperative control framework. Chapter 4 presents a control design methodology to stabilize parallel formations. Chapter 5 extends this methodology to circular formations. In Chapter 6, we study the stabilization of symmetric phase patterns and symmetric circular formations. In the bridge between the theoretical and applied chapters, Chapter 7, we augment the cooperative control framework for applications in environmental monitoring. In Chapter 8, we describe the GCCS—the infrastructure created to control underwater gliders for ocean sampling. In Chapter 9, we describe experimental results from the at-sea demonstration of the GCCS. The concluding Chapter 10 discusses ongoing and proposed work on both theoretical and applied topics.

In Chapter 2, we seek to provide the reader with intuition about the exciting and challenging problem of ocean sampling with autonomous vehicles. In Section 2.1, we introduce an operational overview of autonomous underwater gliders, and their capacity to serve as mobile ocean sensor platforms. A metric for evaluating ocean sensing—based on classical linear estimation theory—is presented in Section 2.2, along with several illustrative examples. In Section 2.3, we formulate a coherent sampling strategy. This strategy is motivated by performance analysis of a 2003 glider field experiment and a numerical example involving a simplified model of two gliders.

Simple models of vehicle motion and interaction are the subject of Chapter 3, which provides an introduction to the theoretical analysis contained in Chapters 4–7. In Section 3.1, we introduce the mathematical notation to describe a planar system of particles moving at constant speed and identify a special set of solution trajectories to be feedback-stabilized. Section 3.2 summarizes a geometric formulation of the closed-loop system with a control law that depends on the position and direction of motion of each particle relative to other particles (and not relative to an absolute frame of reference). In Section 3.3, we introduce terminology from graph theory to describe the network formed from particle interaction.

Levels of particle interaction are used to structure the contents of Chapters 4–6. Chapters 4–6 contain results on stabilization of relative equilibria of the particle model using state feedback. Our approach to relative-equilibrium stabilization depends on the level of the interaction. In the first section of each of the three Chapters 4, 5, and 6, we consider the case of all-to-all interaction, when each particle has access (either by communication or sensing) to the relative state information of every other particle. Algorithms developed for this level of interaction—called *all-to-all* interaction—serve as a roadmap for algorithms developed subsequently for particles with limited interaction. In the second section of each of the three chapters, we introduce and analyze algorithms for time-invariant and undirected interaction. Here the interaction network is fixed and interactions are mutual: that is, if particle 1 has access to the relative state information of particle 2, then particle 2 has access to the relative state information of particle 1. In the third and final section of each of the three chapters, we examine the case of general interaction under very mild assumptions.

Chapter 4 describes stabilization of particles to formations with a common direction of motion (and arbitrary spacing) or to formations in which the average position is fixed. In Chapter 5, we consider the problem of stabilizing circular motion of all particles around the same fixed point. In this chapter, we also show that combining the circular formation algorithm with control of the particles' direction of motion stabilizes circular formations in which particles have a common direction of motion (they are all co-located) or have a fixed average position. In Chapter 6, we present an algorithm that stabilizes circular formations in which the particles are arranged in a symmetric pattern.

We bridge the theoretical results for stabilization of collective motion to applications using mobile sensor networks in Chapter 7. In Section 7.1, by introducing a virtual particle with dynamics unaffected by any other particle, we show how to break the continuous symmetries of translation and rotation of the particle collective. A virtual particle can provide a reference direction for a parallel formation or a reference center for a circular formation. The discrete symmetry associated to permutation of the particle labels can be broken as well. In Section 7.2, we describe how interaction networks that break permutation

symmetries can be used to steer particles in symmetric patterns that span multiple circular formations. Lastly, in Section 7.3, we describe a procedure to stabilize formations on convex loops. This procedure links particle motion to a system coupled-phase oscillators: the position of each particle on a loop is described by a phase angle.

Chapter 8 synthesizes of our theoretical tools to the coordination control of a fleet of underwater gliders. We describe the Glider Coordinated Control System (GCCS), a modular software application that automatically performs fleet-level feedback control a group of gliders to a set of coordinated trajectories. In Section 8.1, we define the specification of a set of glider coordinated trajectories (GCT) that serves as input to the GCCS. In order to steer the gliders to a GCT, the GCCS uses both a simple, planar model of glider motion—described in Section 8.2.1—and a detailed, three-dimensional model—described in Section 8.2.2. Section 8.3 describes the architecture and operation of the three main GCCS modules: the glider planner, which steers the gliders, the glider simulator, which is used to test control algorithms during virtual deployments, and the remote input/output module, which interacts with the gliders indirectly via the internet and satellite communication.

Chapter 9 describes experimental results from an at-sea demonstration of the GCCS. This demonstration was conducted in support of a Department of Defense-sponsored research initiative described in Section 9.1. The initiative seeks to develop optimal strategies for the management of sensor platforms to support environmental assessment and forecasting. Section 9.2 gives an overview of a virtual pilot experiment conducted using the GCCS simulator. Section 9.3 evaluates the performance of the GCCS during the field experiment.

We conclude in Chapter 10. Section 10.1 summarizes the dissertation contributions. In Section 10.2, we describe ongoing and proposed work, which has two major components. The first component is to develop new capabilities to expand glider autonomy for both local and global operations in support of applications relevant to national defense and environmental monitoring. The second component is in the application of cooperative control techniques to the modeling and analysis of collective motion in natural systems.

Supporting material is provided in four appendices: Appendix A provides supplemen-

tary theoretical results for Chapters 4–6; Appendix B provides supporting calculations for Section 7.3 on stabilization of trajectories to convex loops; Appendix C, a supplement to Chapters 2 and 8, contains geodetic utilities; and Appendix D augments the glider field experiment results in Section 9.3.

We apply the following conventions to present the theoretical results in Chapters 3–7. We use *theorem* to label a primary result. There is usually no more than one theorem per section. A *lemma* is a short theorem used to prove subsequent results. A *corollary* contains a result that follows from one or more theorems. We also use *corollary* to label a theorem whose proof is nearly identical to another theorem. A *proposition* is a theorem for which the proof is not included. We accompany each proposition with references to supporting theorems/proofs.

To help find definitions and usage of key terminology, we append to the end of the dissertation a terminology index.

## Chapter 2

# Ocean Sampling with Gliders

There are many—sometimes competing—objectives in ocean sampling, including gradient-climbing [186], feature tracking [84], boundary monitoring [262], and perimeter surveillance [130]. The sampling objective considered here is *mapping* [146]. We seek to *minimize the uncertainty in the estimate of a dynamic signal for a long time over a large domain by adapting the trajectories of a limited number of mobile sensor platforms*. The dynamic signal of interest can be any scalar field—temperature, salinity, fluorescence—that varies over space and time. The estimate of this signal is a time-varying map generated by assimilation of measurement data [177, 129].

When using autonomous sensor platforms to collect measurements, the number of platforms and the mobility required to achieve the mapping objective depends on the spatial and temporal variability of the field. We illustrate this principle below using a simple analogy. In Section 2.1, we describe a class of autonomous sensor platforms known as underwater gliders. In Section 2.2, we define a metric to evaluate mapping performance and, in Section 2.3, we formulate an adaptive sampling strategy and summarize selected challenges to the implementation of the strategy with underwater gliders.

Consider the following analogy. Mapping a scalar field in a region of the ocean, called the *mapping domain*, with one or more (autonomous) sensor platforms is like mowing a lawn with one or more lawn mowers. A lawn, like a mapping domain, can be parametrized

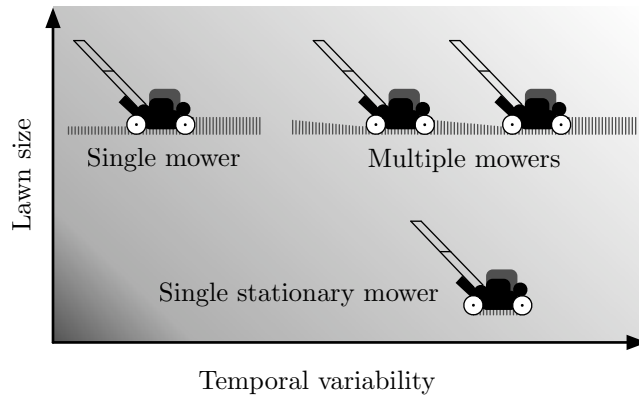


Figure 2.1: Parameter space of lawn-mowing analogy for ocean sampling. The temporal variability of a lawn is a measure of the rate at which the grass grows. Very small lawns and lawns with low temporal variability can be adequately mowed by one mower, whereas a large, highly-variable lawn requires multiple, coordinated mowers (or one very fast mower).

by its size and its *temporal variability*. The temporal variability of a lawn is a measure of the rate at which the grass grows, whereas the temporal variability of a mapping domain describes the magnitude of fluctuations in the field that occur over time. Simply put, the greater the temporal variability, the more frequent the need arises to revisit a patch of lawn or a portion of the mapping domain. The temporal variability of a normal lawn is quite low, since a single patch of lawn requires only a single visit from a mower during the time it takes to mow the lawn. We are interested in mapping a domain with high temporal variability. We gain insight into this challenge by considering a highly variable lawn in which each patch requires a return visit from the mower during the time it takes to mow a normal lawn of the same size.

Lawn size and temporal variability span a two-dimensional parameter space illustrated in Figure 2.1. Each point in the parameter space represents a lawn of a particular size and temporal variability. By considering points first near the boundary of the parameter space, and then in its interior, we gain intuition about how size and temporal variability of a lawn affect the required number and mobility of mowers. We then translate this intuition from the lawn-mowing scenario to the mapping scenario.

The vertical strip of parameter space just inside the vertical axis of the plot in Figure 2.1

corresponds to normal lawns. These lawns can be adequately mowed by a single mower, even if the lawn is quite big. The maximum size of a lawn that can be adequately mowed by a single mower scales like the inverse of the temporal variability. For example, if each patch of an extremely large lawn needs to be mowed once a week and, after a week of continuously mowing, the mower has not visited each patch at least once, then that lawn needs multiple mowers. Any lawn that is smaller than this extremely-large lawn can be mowed by a single mower (although it may be advantageous to use multiple mowers to save time).

The portion of parameter space consisting of very small lawns lies along the horizontal axis of the plot in Figure 2.1. To mow a lawn that is the same size as—or smaller than—the mower, the mower itself does not need to be mobile. A non-mobile mower is called *stationary*. If the lawn is very small but bigger than the mower, then multiple, stationary mowers would be adequate for any level of temporal variability.

Now consider large lawns with high temporal variability. When mowing such a lawn, each patch may need to be visited more than once during the time it takes to mow a normal lawn of the same size. Consequently, a single mower is inadequate, unless the mower is very fast and can continue mowing— even at high speeds—for a long time. On the other hand, a large, highly-variable lawn can be adequately mowed by several mowers, provided that they are coordinated in some way. For example, one coordination scheme is to “divide and conquer”. That is, divide the large lawn into smaller, equally-sized lawns to be mowed by a single mower. Multiple mowers acting independently may not perform significantly better than a single mower. For example, one mower might unnecessarily revisit a patch recently mowed by another mower.

For the purpose of mapping a large and highly-variable ocean domain, the lawn-mower analogy motivates the coordinated use of multiple, mobile sensor platforms. The domain size drives the need for mobility of sensor platforms, since the number of sensor platforms required to map a large domain is reduced when the sensor platforms are mobile. The temporal variability of the domain drives the need for multiplicity of sensor platforms, since a single vehicle would have to move very fast to cover the domain. Although fast-moving

underwater vehicles do exist, they may not have sufficient endurance to sustain a high speed for the duration of interest. When using multiple, mobile sensor platforms, each vehicle does not have to be particularly fast, but they should be coordinated. Coordination of sensor platforms helps avoid inefficiencies in collective sensing such as redundant sampling of a single point in space or time.

Another benefit of coordination of sensor platforms that is not addressed by the lawn-mower analogy is *synergy* between sensor platforms. Synergy between sensor platforms yields mapping performance that scales super-linearly with respect to the number of sensor platforms. It can arise, for example, when the temporal variability within a mapping domain is not homogeneous. Inhomogeneities in the mapping domain lead to inhomogeneities in the desired distribution of sensor platforms. That is, one seeks to take more samples in the highly-variable patches and fewer samples in the less-variable patches [142]. In an inhomogeneous mapping domain, the divide-and-conquer approach should be modified so that the domains after division are small if the local variability is high and the domains are large if the local variability is low. The discovery of inhomogeneities in the mapping domain and subsequent adaptation of the sampling pattern can lead to synergy between sensor platforms.

## 2.1 Autonomous Underwater Gliders

A class of autonomous underwater vehicle (AUV) particularly well-suited for long-duration oceanographic sampling is the underwater glider. An underwater glider soars through the ocean on a pair of fixed wings using an efficient, buoyancy-driven propulsion system [65, 229]. A type of underwater glider called the *Slocum* glider is shown in Figure 2.2. The Slocum glider is manufactured by the Webb Research Corporation in Falmouth, Massachusetts [286]. One group that operates the Slocum glider for a variety of oceanographic objectives—including mapping—is the Autonomous Systems Laboratory of the Woods Hole Oceanographic Institution (WHOI) in Woods Hole, Massachusetts. Another underwater glider, the *Spray* glider, was created by the Scripps Institution of Oceanography (SIO) in La Jolla,

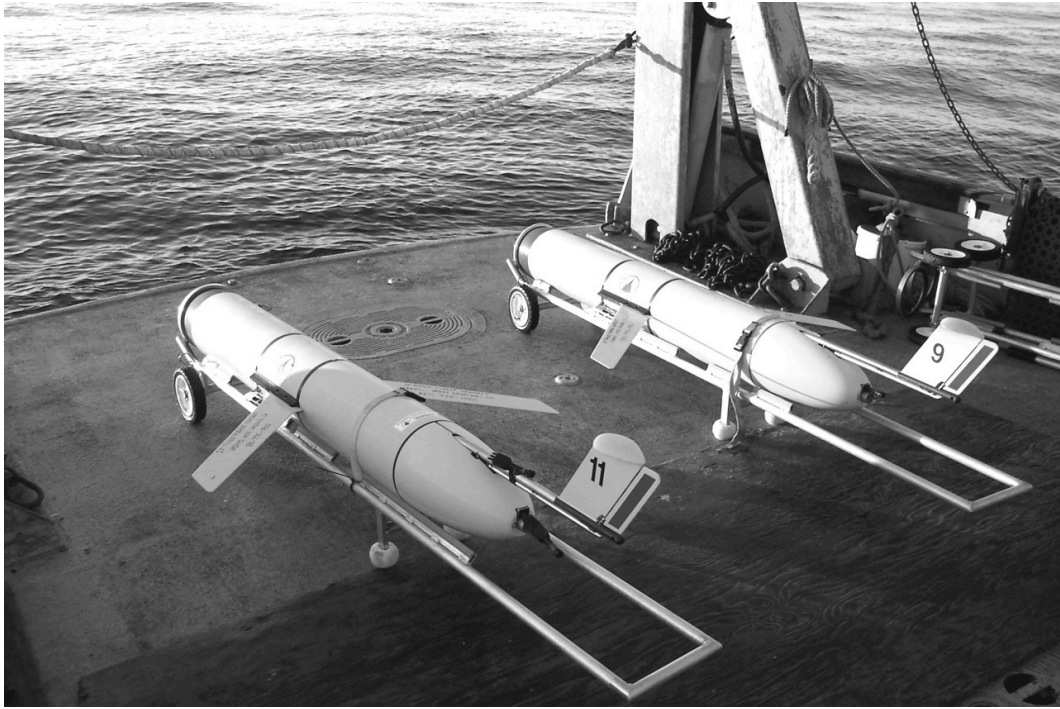


Figure 2.2: Slocum gliders prepared for deployment on the deck of R/V Shana Rae in August 2003. When a Slocum is on the surface, the vehicle tail, which houses antennas for satellite communication, is elevated by an internal air bladder to obtain better reception. Photograph (taken by the author) previously appeared in [146].

California and is manufactured by the Bluefin Robotics Corporation in Cambridge, Massachusetts [244]. A third model of glider, the *Seaglider*, is the result of a collaborative effort of the Applied Physics Laboratory (APL) at the University of Washington and the University of Washington School of Oceanography [77].

Although the design and capabilities of each glider model may differ, all of the glider models use a propulsion system called a buoyancy engine, which changes the vehicle's buoyancy to produce vertical velocity [65]. A glider's vertical velocity is converted to horizontal velocity by the force of lift generated by the flow of water over its wings. A glider follows a "roller-coaster" motion through the water, as shown in Figure 2.3, by cyclically changing its buoyancy and glide angle. A glider controls its glide angle, which is the sum of its pitch angle and angle of attack, by moving an internal mass until it reaches a desired pitch. When ascending and descending, the lift force on a glider balances its buoyancy and hydrodynamic

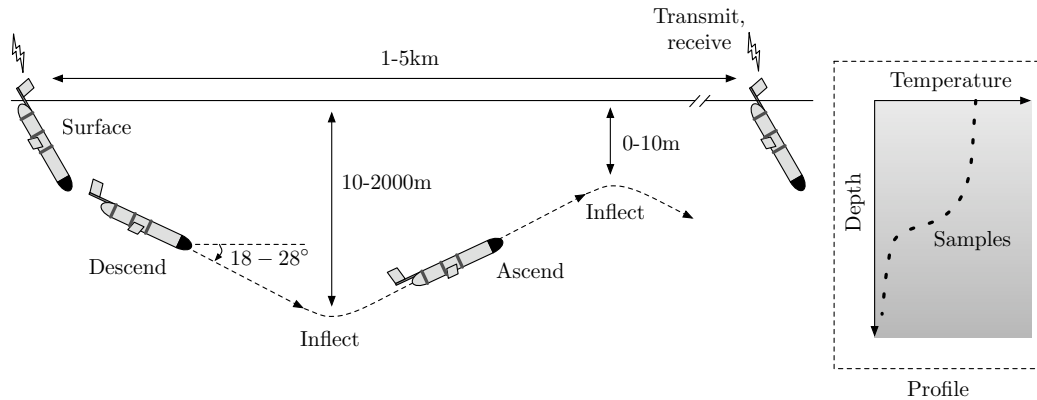


Figure 2.3: The stages of a glider dive. A glider descends by becoming nose-heavy and ascends by becoming nose-light. A single dive might consist of multiple *inflections*, which are transitions between descending and ascending. When on the surface, a glider can communicate with a shore station. During each descent and ascent, a glider intermittently samples the surrounding sea water. The set of all measurements of a scalar field (such as temperature) collected during a descent or ascent is called a *profile* (see box on right).

drag so that the vehicle travels at nearly constant speed relative to the water. On a single dive, a glider can ascend or descend multiple times between its minimum dive depth and maximum dive depth. The transition from ascending to descending or from descending to ascending is called an *inflection*.

Gliders steer to a desired heading in the horizontal plane by moving an internal mass to bank and turn or by actuating an external rudder. How a glider chooses its desired heading depends on glider-specific control algorithms. One such algorithm, described in Section 8.2.2, chooses the desired heading so that the glider homes in on destination point called a *waypoint*, specified by its latitude and longitude coordinates. Gliders can be supplied by an operator with a list of waypoints, in which case a glider steers to reach each waypoint in order. In the presence of a strong current, a glider might instead choose its desired heading using a “river-crossing” algorithm [64], in which the glider seeks to head in a direction perpendicular to the current.

Steering to avoid a strong current can improve a glider’s speed over ground, which is the glider speed through the water plus the speed of the water current. A glider typically travels through the water at a lower speed than a propeller-driven AUV. The through-water

speed of a glider is on the order of 0.3 m/s to 0.5 m/s, whereas a propeller-driven AUV is typically configured to travel at 1.5 m/s to 3 m/s, and some are capable of achieving even higher speeds. A newer glider model, the *XRAY* glider under development by the Marine Physical Laboratory at SIO, seeks to address this limitation by using a “flying-wing” design that improves gliding efficiency [124].

An advantage of traveling at low speeds relative to the water is a significant reduction in hydrodynamic drag, which scales like the square of speed [141, p. 180]. Reduced drag translates into reduced energy consumption and enables longer deployments. Glider designers seek to further extend deployments by limiting the energy consumption of the scientific and control electronics carried onboard, called the *hotel load*. A glider typically carries only small, low-power instruments that intermittently sample the ocean water, unlike a propeller-driven AUV, which can carry a high-power sonar that continuously collects detailed images of the ocean bottom. Low drag and small hotel load enable a glider to be deployed for several weeks to several months, whereas a propeller-driven AUV deployment rarely exceeds a day or two.

Energy and size constraints prevent gliders from carrying accurate navigation sensors commonly carried by propeller-driven AUVs. For example, a glider does not carry a Doppler Velocity Log (DVL), which is a device that uses acoustic waves to measure vehicle velocity over ground. A glider navigates underwater by integrating an estimate of its velocity over ground to find its (horizontal) position. To estimate its velocity over ground, a glider must estimate the water velocity over ground as well as its own through-water velocity (see Section 8.2.2). Inaccuracies in the velocity estimate accumulate into position errors on the order of 10% to 20% of distance travelled.

To reset errors in its position estimate and to communicate with a shore station, a glider periodically comes to the surface. A glider is equipped with both satellite and radio frequency communication systems. It is also possible to equip a glider with acoustic modems to communicate over short distances underwater [224], although this configuration is not yet common. A glider uses the Global Position System (GPS) to find its actual position. By

comparing its actual position to its estimated position, a glider can estimate the magnitude and direction of the depth-averaged ocean current encountered during the previous dive. Before diving again, a glider may receive an updated waypoint list from a computer or operator on shore. A glider can also be configured to transmit scientific data.

The scientific measurements collected by a glider depends on its sensor suite. A glider can sample physical properties of sea water including temperature, salinity, dissolved oxygen, and density, and bio-optical properties like optical backscatter and chlorophyll fluorescence. Bio-optical properties indirectly measure the concentration of microscopic plants (phytoplankton) and animals (zooplankton). Spray glider can also measure variations in water speed and/or direction over short distances using a device called an Acoustic Doppler Current Profiler (ADCP).

The set of all measurements of a single scalar field collected during a glider descent or ascent is called a *profile*.<sup>1</sup> These measurements are typically plotted versus depth, as illustrated on the right-hand side of Figure 2.3. Note a glider moves both vertically and horizontally when producing a single profile. Nonetheless, to represent the profile position, we use the GPS position of the glider at either the start or the end of the dive. The profile time is the time of the GPS position fix.

Because of its deployment duration, a glider is capable of collecting profiles over horizontal scales ranging from meters to hundreds of kilometers and temporal scales from seconds to months. In Figure 2.4, we illustrate for both a glider and a propellor-driven AUV the space-time *sampling regime*, which is the portion of the space-time plane that a sensor platform can effectively sample. The spatial limit of a sensor platform's sampling regime is determined by the sensor platform's speed, whereas the temporal limit is determined by the duration of a single deployment. Note in Figure 2.4 that the greater speed of an AUV, as compared to the speed of a glider, increases the spatial extent of the sampling regime, but this does not yield access to additional oceanographic processes. The greater endurance of a glider, however, increases the temporal extent of its sampling regime, which yields access

---

<sup>1</sup>A glider automates the process of collecting profile data. Profile data can also be collected by an instrument cast over the side of a research vessel.

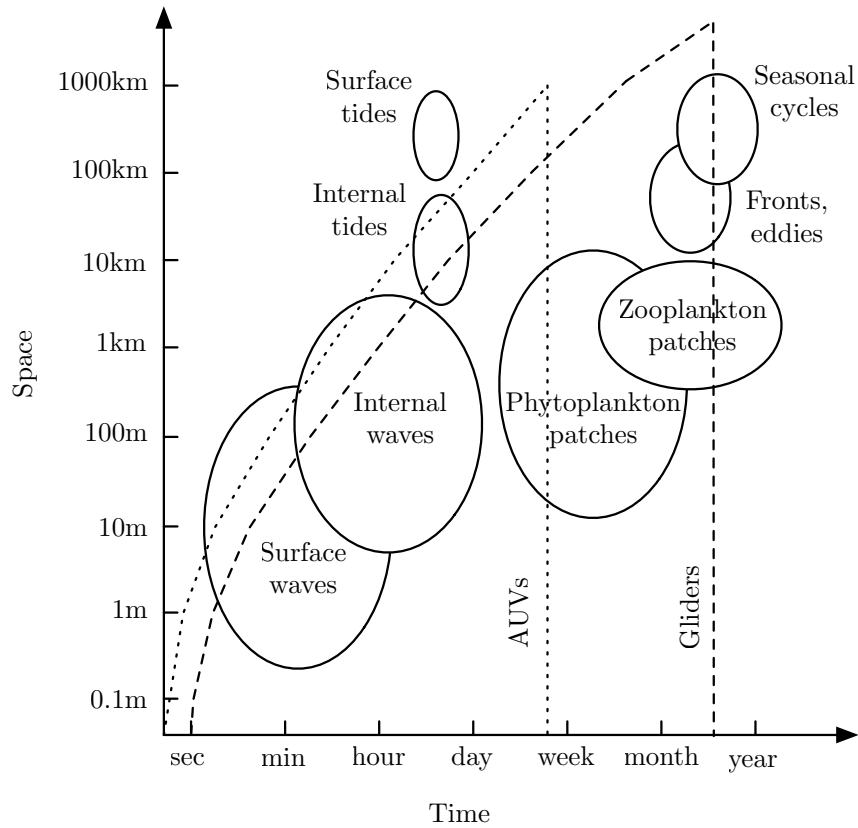


Figure 2.4: Selected oceanographic processes in the space-time sampling regime of gliders and propellor-driven AUVs. The sampling regime of a sensor platform is the portion of the space-time plane that it can effectively sample. Note, the vertical axis is on a logarithmic scale and the horizontal axis is quasi-logarithmic. Compared to a propellor-driven AUV, a glider has greater endurance, which yields access to additional oceanographic processes like plankton patches, fronts, eddies, and seasonal cycles. Figure based on [72, 115, 290].

to additional, important oceanographic processes like zooplankton patches, fronts, eddies, and seasonal cycles. For example, one type of seasonal cycle effectively sampled by gliders is the annual upwelling of cold, nutrient-rich water in regions such as coastal California [218] (see Section 9.1).

A glider is faced with the predicament of trying to measure properties of the fluid in which the glider is itself advected, often in an undesirable direction. A glider is especially vulnerable at the ocean surface, where it drifts passively. Attempts by a glider to communicate or navigate on the surface can be thwarted by waves breaking over its antenna, since electromagnetic waves at radio frequencies attenuate over very short distances in sea

water. Coastal surface tides and constructive interference between internal waves can generate currents at speeds greater than that of a glider [88].<sup>2</sup> An important figure of merit for a glider is its *effective speed*, which is the speed over ground between sequential profile positions. A glider’s effective speed is reduced by long surface intervals and can be reduced or increased by ocean currents.

## 2.2 Mapping Performance Metric

Quantitatively evaluating a set of glider profiles, or optimizing a glider mapping trajectory, requires a quantitative performance metric. For example, one might consider as performance metric the density of profile positions, which is inversely proportional to the sampling area. For a simple divide-and-conquer strategy with equally-sized subdivisions and a fixed deployment duration, this metric scales linearly with the number of sensor platforms.<sup>3</sup> However, profile-position density may be inadequate as a performance metric if the desired profile distribution is not uniform, that is, if the profile-position density varies in space and time.

Assuming that the profiles are to be assimilated into a time-varying estimate of a scalar field, another performance metric is based on the *objective analysis* (OA) estimation error [91, 36]. Computing the OA estimation error, called the *mapping error*, requires an *a priori* description of the covariance of fluctuations around the mean of the scalar field, parametrized by the field’s spatial and temporal *decorrelation lengths*. OA provides the residual uncertainty in an estimate of the field—the mapping error—which can be used to compute mapping performance. If an *a priori* description of the mean of the field is available, OA also provides an estimate or map of the field itself.

Consider an OA framework for sampling a scalar field  $T$  with respect to two (horizontal)

---

<sup>2</sup>Surface, or *barotropic*, tides are depth-independent oscillations of sea water generated by the pressure gradients that arise from variations in sea height due to astronomical influences [88]. An *internal wave* is a depth-dependent oscillation generated by the opposing pressure gradients that arise from variations in the depth of the *thermocline*, a layer of sea water that has a rapid decrease of temperature with depth. Internal tides are a type of internal wave. Variations in the depth of the thermocline are driven by the barotropic tide sloshing against the topography of the bottom and of the coastline.

<sup>3</sup>To see this, let  $A_0$  be area of the mapping domain and  $A_0/N$  be the area of each subdivision, where  $N$  is the number of sensor platforms. The increase in sampling density generated by adding one sensor platform is  $(N + 1)/A_0 - N/A_0 = 1/A_0$ .

space dimensions and time. The scalar field  $T$  at a point  $R$  and time  $t$  can be viewed as a random variable  $T(R, t)$  (for example, temperature at a fixed depth as a function of horizontal position and time). Let  $E[\cdot]$  denote an operator that produces the expected value of a random variable. The mean  $\bar{T}$  is defined by  $\bar{T}(R, t) \triangleq E[T(R, t)]$  and the covariance  $C$  of fluctuations about the mean is

$$C(R, t, R', t') \triangleq E[(T(R, t) - \bar{T}(R, t))(T(R', t') - \bar{T}(R', t'))]. \quad (2.1)$$

For a stationary, homogeneous, and isotropic field, the variance  $\sigma_0 \triangleq C(R, t, R, t)$  of  $T(R, t)$  around its mean  $\bar{T}(R, t)$  is independent of  $R$  and  $t$ . The covariance  $C(R, t, R', t')$  of such a field is often approximated by a function parametrized by the spatial  $\sigma$  and temporal  $\tau$  decorrelation lengths. For example, a common model of the covariance of an oceanographic process is the exponential function [64]

$$C(R, t, R', t') = \sigma_0 e^{-\frac{\Gamma(R, R')}{\sigma} - \frac{|t-t'|}{\tau}}, \quad (2.2)$$

where  $\Gamma(R, R') \geq 0$  is a measure of the distance between  $R$  and  $R'$  (see Appendix C). Note that  $C(R, t, R', t')/\sigma_0$ , which we call the *normalized* covariance function, evaluates to  $1/e$  when  $\Gamma(R, R') = \sigma$  and  $t = t'$ , or when  $R = R'$  and  $|t - t'| = \tau$ . The exponential covariance function is illustrated in Figure 2.5, along with a *normal* or Gaussian covariance function, variations of which are frequently used to describe oceanographic processes [115, 147].

Let  $\tilde{T}(R_k, t_k)$ ,  $k = 1, \dots, P$ , denote a set of  $P$  discrete measurements collected by one or more gliders at the points  $R_k$  and times  $t_k$ . Assuming that the measurements are noisy and that the noise is uniform and uncorrelated, then the  $P \times P$  *measurement covariance matrix*  $\tilde{C}$  has entries  $[\tilde{C}]_{kj} \triangleq \tilde{\sigma}_0 \delta_{kj} + C(R_k, t_k, R_j, t_j)$  for all pairs  $k$  and  $j$ , where  $\tilde{\sigma}_0$  is the *measurement-noise variance* and  $\delta_{kj} \in \{0, 1\}$  is the Dirac delta function. Suppose that we linearly combine all of the measurements  $\tilde{T}(R_k, t_k)$  to form an estimate  $\hat{T}(R, t)$  of the scalar field at a point  $R$  and time  $t$ . The covariance  $\hat{C}(R, t, R', t')$  of the error in the estimate is given by

$$\hat{C}(R, t, R', t') \triangleq E[(T(R, t) - \hat{T}(R, t))(T(R', t') - \hat{T}(R', t'))]. \quad (2.3)$$

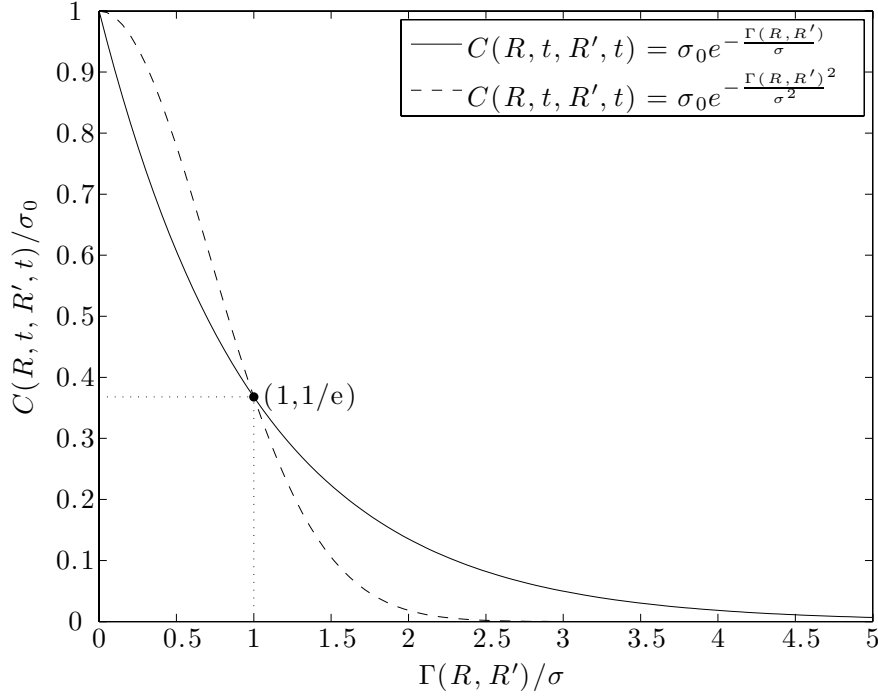


Figure 2.5: Exponential and normal covariance functions  $C(R, t, R', t')$  for  $t = t'$ . Note, the vertical axis is normalized by the variance  $\sigma_0$  and the horizontal axis is normalized by the spatial decorrelation scale  $\sigma$ . By setting  $t = t'$ , only the variation of  $C(R, t, R', t')$  with distance  $\Gamma(R, R')$  is evaluated. Exponentially-correlated points are less correlated at short lengths and more correlated at large lengths than normally-correlated points. When  $\Gamma(R, R') = \sigma$ , both covariance functions evaluate to  $1/e$ .

According to the Gauss-Markov theorem, the covariance (2.3) of the error in a linear minimum mean-square estimate  $\hat{T}(R, t)$  is [153, p. 138]

$$\hat{C}(R, t, R', t') = C(R, t, R', t') - \sum_{k=1}^P \sum_{j=1}^P C(R, t, R_k, t_k) [\tilde{C}^{-1}]_{kj} C(R_j, t_j, R', t'), \quad (2.4)$$

where  $[\tilde{C}^{-1}]_{kj}$  denotes the entry in the  $k$ th row and  $j$ th column of the inverse  $\tilde{C}^{-1}$  of the measurement covariance matrix  $\tilde{C}$ . The OA map, also provided by the Gauss-Markov theorem, is the estimate

$$\hat{T}(R, t) = \bar{T}(R, t) + \sum_{k=1}^P \sum_{j=1}^P (\tilde{T}(R_k, t_k) - \bar{T}(R_k, t_k)) [\tilde{C}^{-1}]_{kj} C(R_j, t_j, R, t). \quad (2.5)$$

This leads to the following definition.

**Definition 2.1. Mapping error** *The mapping error at point  $R$  and time  $t$  is the error variance  $\hat{C}(R, t, R, t)$ , defined in (2.4), of the corresponding point in the OA map. The normalized mapping error  $\hat{C}(R, t, R, t)/\sigma_0$ , where  $\sigma_0$  is the variance of a stationary, homogeneous, and isotropic process, is a number in the interval  $[0, 1]$ .*

Typically, the mapping error and OA map are evaluated over a regularly-spaced grid of points and times, although the OA computation at each grid point  $R$  and time  $t$  is independent of the OA computation at all of the other grid points. OA can be viewed as an optimal method of interpolating an irregularly-spaced set of measurements. To compute the mapping error one needs to know the profile positions and times, estimate the measurement noise variance  $\tilde{\sigma}_0$ , and choose a functional form of the covariance function  $C(R, t, R', t')$  parametrized by the decorrelation lengths  $\sigma$  and  $\tau$ . The mapping error does not depend on the measurement values  $\tilde{T}(R_k, t_k)$ .

Next we define a mapping performance metric based on the mapping error, after [146].

**Definition 2.2. Mapping performance** *The mapping performance  $\mathcal{I}(t)$  in mapping domain  $\mathcal{B}$  is the area integral over  $\mathcal{B}$  of the mapping error at time  $t$ , normalized by the process variance  $\sigma_0$  and represented in log-space by*

$$\mathcal{I}(t) \triangleq -\log \left( \frac{1}{\sigma_0 |\mathcal{B}|} \int_{\mathcal{B}} \hat{C}(R, t, R, t) dR \right), \quad (2.6)$$

where  $|\mathcal{B}|$  is the area of  $\mathcal{B}$ . The mapping performance  $\mathcal{I}(t)$  on the boundary  $\delta\mathcal{B}$  of  $\mathcal{B}$  is the line integral over  $\delta\mathcal{B}$  of the mapping error at time  $t$ , normalized by the process variance  $\sigma_0$  and represented in log-space by

$$\mathcal{I}(t) \triangleq -\log \left( \frac{1}{\sigma_0 |\delta\mathcal{B}|} \int_{\delta\mathcal{B}} \hat{C}(R, t, R, t) dR \right), \quad (2.7)$$

where  $|\delta\mathcal{B}|$  is the perimeter of  $\mathcal{B}$ .

The metric (2.6) can be viewed as the amount of information at time  $t$  contained in the measurements  $\tilde{T}(R_k, t_k)$ , for all  $k = 1, \dots, P$  [101, pp. 34-35]. Mapping performance on the boundary of a domain is a measure of the effectiveness with which measurements

can be used to compute the flux of quantities like heat and mass into or out of the domain [64].<sup>4</sup> In order to compute mapping performance at time  $t$ , one theoretically uses all of the measurements collected before and after time  $t$ . However, for an exponential covariance function, measurements outside the interval  $(t - 4\tau, t + 4\tau)$  have less than a 2% correlation with measurements at time  $t$  and, consequently, no appreciable effect on  $\mathcal{J}(t)$ . In order to decrease the time to compute  $\mathcal{J}(t)$  without a significant reduction in accuracy, measurements outside this interval may be ignored.

Oceanographic processes typically contain energy at multiple scales. The decorrelation lengths  $\sigma$  and  $\tau$ , which can be estimated from local or remote (satellite) measurements of the mapping domain, correspond to the average decorrelation length in space and time of all signals across the energy spectrum. Estimates exist for ocean process decorrelation lengths on a global scale [256] and in the eastern Mediterranean Sea [148], the northwest Atlantic Ocean [279], the northeastern Atlantic Ocean [168], the tropical Pacific Ocean [171], and the California Current System [212, 69, 229, 213].

An alternative to the mapping objective is collecting measurements to best estimate the decorrelation scales. One approach to this problem is called *co-array design* [64]. Results for the co-array design of static sensors [19, 109, 78] suggest that co-array design for mobile sensors may yield different trajectories than array design for optimal mapping performance. Estimation of decorrelation lengths requires the collection of samples over a range of separation distances and times, whereas minimization of mapping error occurs when measurements are separated by the characteristic decorrelation lengths, as we see next.

### 2.2.1 Example of Mapping Error in Space

To illustrate the computation of mapping error and its implications for measurement placement, we present a simple, one-dimensional example where  $R \in \mathbb{R}$  (the real line). In this example, we consider two, simultaneous measurements at positions  $R_1 = -d\sigma/2 < 0$  and  $R_2 = d\sigma/2 > 0$ , where the separation parameter  $d \triangleq (R_2 - R_1)/\sigma > 0$  determines the spatial

---

<sup>4</sup>Flux measurements can be used to compute a heat or mass budget [228].

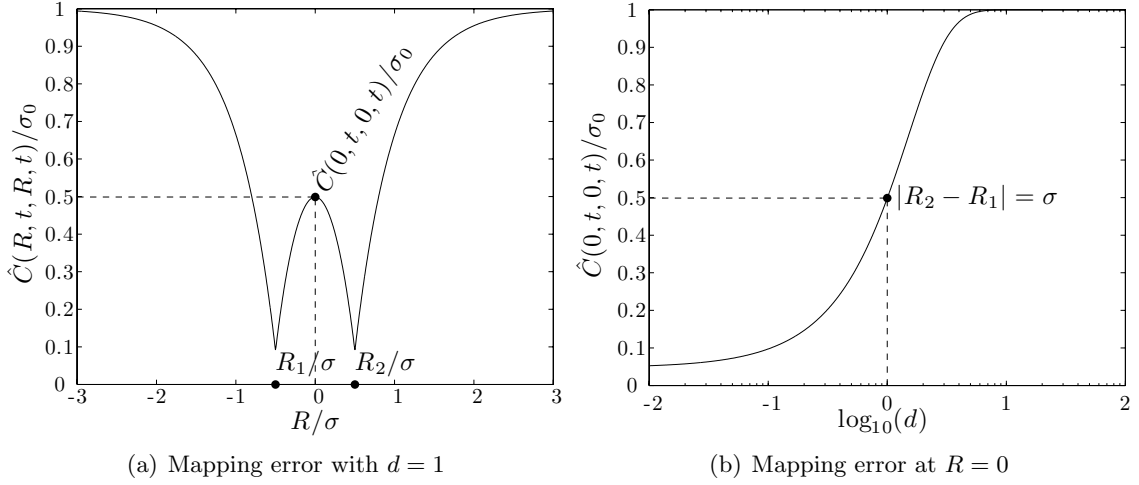


Figure 2.6: Mapping error example. (a) The normalized mapping error  $\hat{C}(R, t, R, t)/\sigma_0$  in the vicinity of two measurements located at  $\pm\sigma/2$ ; (b) the normalized mapping error at the origin  $R = 0$  versus parameter  $d$ , which determines the separation of the two measurements. There is negligible reduction in mapping error when measurements separated by 10% of  $\sigma$  are moved closer. Measurements separated by more than  $3\sigma$  generate a coverage gap with high mapping error.

separation of the measurements. We investigate the impact of varying  $d$  on the mapping error evaluated at the origin  $R = 0$ .

Using the exponential covariance function (2.2), the measurement covariance matrix is

$$\tilde{C} = \begin{bmatrix} \tilde{\sigma}_0 + \sigma_0 & \sigma_0 e^{-d} \\ \sigma_0 e^{-d} & \tilde{\sigma}_0 + \sigma_0 \end{bmatrix}.$$

According to (2.4), the normalized mapping error is

$$\frac{\hat{C}(R, t, R, t)}{\sigma_0} = 1 - \sigma_0 \sum_{k=1}^2 \sum_{j=1}^2 e^{-\frac{|R-R_k|}{\sigma} - \frac{|R-R_j|}{\sigma}} [\tilde{C}^{-1}]_{kj}, \quad (2.8)$$

where

$$\tilde{C}^{-1} = \frac{1}{(\tilde{\sigma}_0 + \sigma_0)^2 - \sigma_0^2 e^{-2d}} \begin{bmatrix} \tilde{\sigma}_0 + \sigma_0 & -\sigma_0 e^{-d} \\ -\sigma_0 e^{-d} & \tilde{\sigma}_0 + \sigma_0 \end{bmatrix}.$$

In Figure 2.6(a), we plot the normalized mapping error (2.8) with  $d = 1$  and measurement noise  $\tilde{\sigma}_0$  equal to 10% of  $\sigma_0$ . The normalized mapping error reaches its minimum value at the measurement positions  $R = R_1$  and  $R = R_2$ . Its minimum value of 0.1 is determined by the measurement noise. The normalized mapping error approaches its maximum

value of 1.0 when  $R < 3\sigma$  or  $R > 3\sigma$ . Among all of the points between  $R_1$  and  $R_2$ , the normalized mapping error is maximum at  $R = 0$ .

The value  $\hat{C}(0, t, 0, t)/\sigma_0$  of the normalized mapping error at the origin, given by

$$\frac{\hat{C}(0, t, 0, t)}{\sigma_0} = 1 - \frac{2e^{-d} \left( \frac{\tilde{\sigma}_0}{\sigma_0} + 1 - e^{-d} \right)}{\left( \frac{\tilde{\sigma}_0}{\sigma_0} + 1 \right)^2 - e^{-2d}},$$

is plotted as a function of  $d$  in Figure 2.6(b). If  $d < 0.1$ , then the measurements are nearly co-located and the mapping error at the origin is on the order of the measurement noise. If the measurements move closer to one another, there is negligible reduction in mapping error at the origin. On the other hand, if  $d > 3$  ( $\log_{10} d > 0.5$ ), then the normalized mapping error at the origin is nearly one, which is its maximum value. For  $0.1 < d < 3$ , the mapping error varies smoothly between approximately 10% and 100% of  $\sigma_0$ , with largest slope in the vicinity of  $d = 1$ , or  $|R_2 - R_1| = \sigma$ .

From this example, we produce the following heuristic: the greatest reduction in mapping error obtained from a limited set of simultaneous measurements occurs when the measurements are spatially separated by a distance approximately equal to the spatial decorrelation length  $\sigma$ . Measurements much closer together than  $\sigma$  do not yield significant reduction in mapping error, whereas measurements much further apart than  $\sigma$  leave portions of the domain under-sampled. For sequential measurements collected at the same point, a similar heuristic holds: the greatest reduction in mapping error occurs when the measurements are temporally separated by a time interval approximately equal to the temporal decorrelation length  $\tau$ . A more complicated situation is, of course, when measurements are neither co-located nor simultaneous. We examine this situation next.

### 2.2.2 Example of Mapping Error in Space and Time

We now consider the reduction of mapping error in space and time along a sensor path, using as an example a mobile sensor platform with constant heading and constant speed  $s_0$ . Assume that the time period between sequential measurements is small compared with the overall time spent collecting measurements. In this example, we treat the sensor as

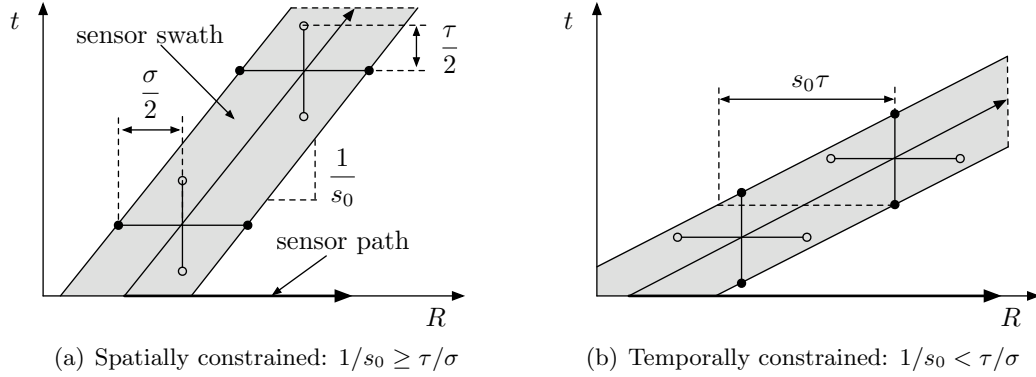


Figure 2.7: Sensor swath and sampling constraints. The area of reduced mapping error due to a single sensor platform moving along the positive  $R$  axis at a constant speed  $s_0$  can be represented by a sensor swath (gray patch) in the  $(t, R)$ -plane whose width is determined either by  $\sigma$  (a, spatially constrained) or by  $s_0\tau$  (b, temporally constrained).

collecting measurements continuously. Using the insight gained from the previous section, we represent the reduction in mapping error in the  $(t, R)$ -plane by a sensor *swath*, which contains a set of points along the sensor path as illustrated in Figure 2.7. A point  $(t, R)$  is contained in the sensor swath if the distance between  $R$  and the position of the sensor position at time  $t$  is less than  $\sigma/2$ , or the time span between  $t$  and when the sensor passes over  $R$  is less than  $\tau/2$ . As shown in Figure 2.7(a), the slope of the sensor swath in the  $(t, R)$ -plane is  $1/s_0$ .

The sensor swath representation of the reduction of mapping error along a sensor path allows us to characterize a sensor platform as either *spatially constrained* or *temporally constrained*. For a given  $\sigma$  and  $\tau$ , the type of constraint is determined by the non-dimensionalized speed, given by [146]

$$\mathfrak{s}_0 \triangleq \frac{s_0\tau}{\sigma}. \quad (2.9)$$

A sensor platform is spatially constrained if  $\mathfrak{s}_0 \leq 1$ . In this case, the slope  $1/s_0$  of the sensor swath satisfies  $1/s_0 \geq \tau/\sigma$ , which means the swath width  $\sigma$  is independent of  $\tau$ . A stationary sensor platform is always spatially-constrained. A sensor platform is temporally constrained if  $\mathfrak{s}_0 > 1$ , that is,  $1/s_0 < \tau/\sigma$ . In this case, the swath width  $s_0\tau$  is independent of  $\sigma$ . A mobile sensor platform may be spatially- or temporally-constrained depending on

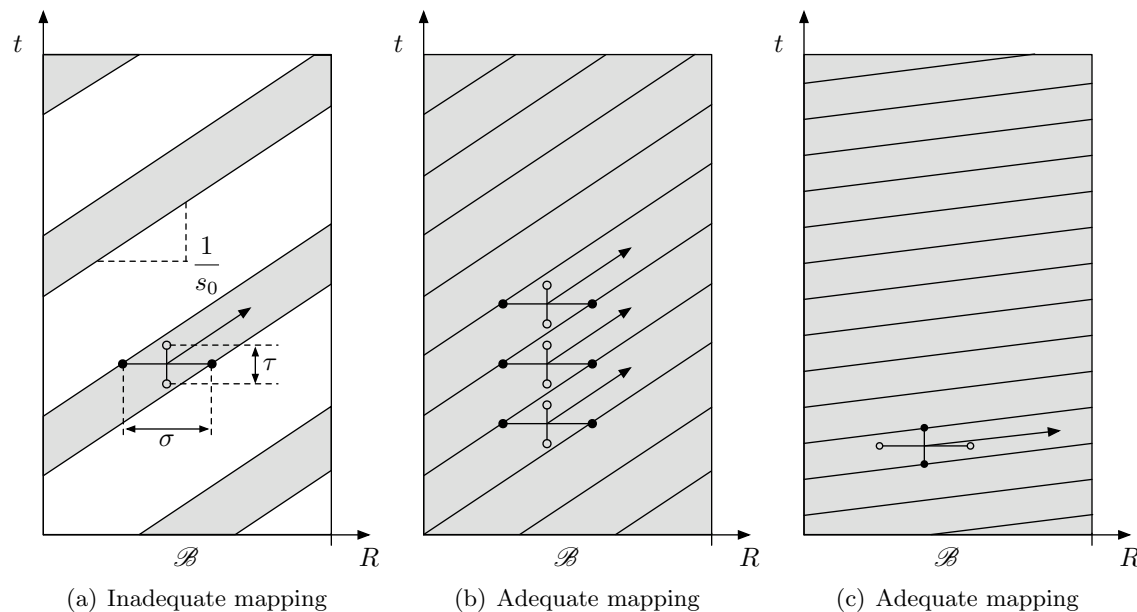


Figure 2.8: Mapping a one-dimensional domain with periodic boundary conditions. Portions of the  $(t, R)$ -plane that are gray are contained in a sensor swath. (a) A single, spatially-constrained sensor inadequately maps the domain if the sensor swath  $\sigma$  is less than the width  $|\mathcal{B}|$  of the domain; (b) three spatially-constrained sensors adequately map the domain; (c) a single temporally-constrained sensor platform moving at the minimum speed required to adequately map the same domain.

its speed and the decorrelation lengths. The swath width of a spatially-constrained sensor platform depends only on the spatial decorrelation scale, whereas the swath width of a temporally-constrained sensor platform depends on the temporal decorrelation scale and the platform speed. Note, the swath width as defined here is measured along the sensor platform trajectory.

We now use swath width to determine the number of sensor platforms required to adequately sample a finite, one-dimensional domain  $\mathcal{B}$  with periodic boundary conditions. That is, we identify the edges of  $\mathcal{B}$  so that a sensor platform exiting to the right will re-enter from the left as shown in Figure 2.8(a). In this setting, if the swath width is less than the width  $|\mathcal{B}|$  of the domain, then a single sensor cannot adequately map the domain. We consider a domain to be adequately mapped from  $t = 0$  to  $t = T_0$  if every point in the  $(t, R)$ -plane where  $0 \leq t \leq T_0$  and  $R \in \mathcal{B}$  is contained in a sensor swath. For

a set of spatially-constrained sensor platforms with identical speed, the minimum number of sensor platforms needed to map the domain is  $\lceil |\mathcal{B}|/\sigma \rceil$ , where  $\lceil x \rceil$  is the smallest integer greater than or equal to  $x$ . If the sensor platforms are temporally constrained, then the number needed to map the domain is  $\lceil |\mathcal{B}|/(s_0\tau) \rceil$ . We show in Figure 2.8(b) a set of three spatially-constrained sensor platforms that collectively map domain  $\mathcal{B}$ . In Figure 2.8(c), a single, temporally-constrained sensor platform is adequate to map the same domain if it moves fast enough: traveling at the minimum speed, the sensor swath fills the  $(R, t)$ -plane with no gaps or overlap.

This subsection and the previous one illustrate how glider spacing and speed can significantly impact mapping performance. In particular, we observe that gliders should not bunch together, or else their profiles may become redundant. In addition, gliders should be configured to travel as fast as possible and not backtrack. This implies that a glider should seek to travel in the direction of the prevailing ocean currents and not attempt to fight against currents as that may decrease its effective speed over ground. In order to adequately map a closed path represented by a one-dimensional domain with periodic boundary conditions, multiple gliders traveling at the same speed should be evenly spaced around the path. We utilize in the next section data analysis of real glider trajectories to further develop this intuition and to formulate a concise statement of sampling strategy.

## 2.3 Adaptive Sampling Strategy and Challenges

We describe here an *adaptive sampling* (AS) strategy for mapping one or more scalar fields with a fleet of underwater gliders. The strategy, intended to minimize mapping error subject to constraints on glider trajectories, was developed in collaboration with D. Fratantoni of WHOI and R. Davis of SIO. The strategy can also be used to reduce errors in ocean-model forecasts; see, for example, [222]. In developing the strategy we were motivated by the 2003 Autonomous Ocean Sampling Network (AOSN-II) field experiment [217]. Analysis of the AOSN-II glider sampling strategy via mapping performance is summarized below. This analysis, the glider kinematic constraints, and the intuition provided by the simple

heuristics in the previous two sections, lead naturally to an AS strategy in which gliders are automatically coordinated to travel around closed curves that are adapted according to evolving knowledge of dynamic processes within the mapping domain.

A central component of our AS strategy is the automatic control of a fleet of gliders to a set of coordinated trajectories. The automatic control system described in Chapter 8 enables a glider fleet to operate effectively with only minimal intervention, while conventional approaches require manual trajectory planning. The specification of a set of glider coordinated trajectories—described in detail in Chapter 8—contains a description of the path followed by each glider as well as the position of each glider on its path relative to the other gliders.

In order to design glider paths in a coastal mapping domain, we adopt a method consistent with previous glider deployments. We assume that each glider travels around an elongated, closed path called a *track* (short for racetrack). The long sides of a track should be nearly straight and oriented so that the glider crosses over the *shelf break* [64], which is the end of the continental shelf characterized by a sharp increase in the slope of the ocean bottom. Each time a glider travels around a track it samples a cross-section of the dynamic ocean processes that propagate parallel to the shelf break. By constructing a time sequence of cross-section plots, oceanographers can reconstruct, identify, and monitor ocean processes even before assimilating the glider profile data into a sophisticated ocean model (see Figure 2.9). Each cross-section plot is a snapshot of an ocean process generated by interpolating glider measurements, for example, using OA. A snapshot is typically plotted as a function of depth on the vertical axis—the direction of increasing depth is down—versus time/distance on the horizontal axis—the direction of increasing time/distance is to the right. For slow platforms like gliders, the time-evolution of an ocean process during a single snapshot can make it difficult to identify the process [302, pp. 39-41].

Accurately mapping a dynamic ocean process using a track-based design method requires coordination of gliders on the tracks. When there are multiple tracks, they should be designed so that any two gliders assigned to different tracks maintain a minimum separation

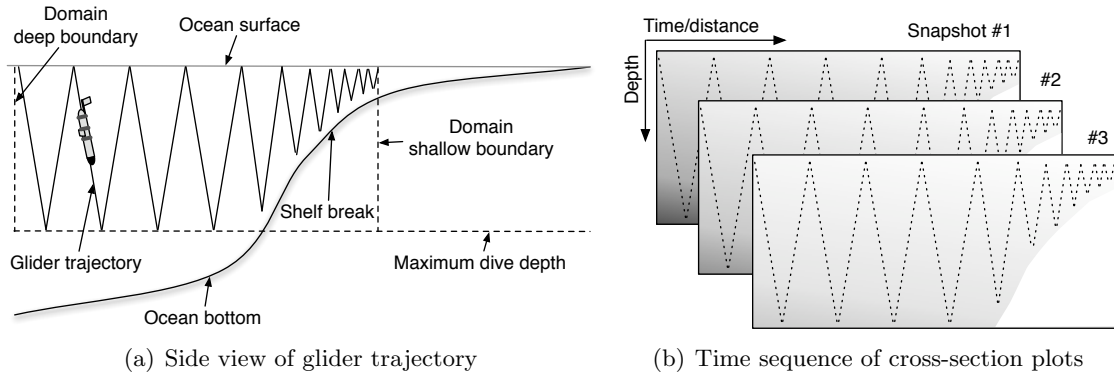


Figure 2.9: Constructing a time sequence of cross-shelf ocean dynamics from glider measurements. When a glider travels around a closed path whose long sides (when viewed from above) are nearly straight and orthogonal to lines of constant bathymetry, it can repeatedly sample the coastal processes in a vertical plane across the shelf break. (a) A glider travels from left to right collecting measurements over the shelf break (note, the horizontal length scale is not proportional to the vertical length scale); (b) each time the glider travels over the shelf break it generates a new snapshot of the ocean dynamics. By constructing a time-sequence of snapshots, oceanographers can analyze changes in the ocean dynamics even without assimilating the glider data into a sophisticated ocean model.

from one another. Even so, gliders may bunch together and collect redundant measurements if they deviate off course. Glider bunching can also occur on a single track, particularly in the presence of strong ocean currents. We use mapping error to assess the impact of gliders traveling off course during the AOSN-II experiment in the next section and, in Section 2.3.2, we illustrate current-driven bunching on a single track using a simple example. These analyses motivate a coherent sampling strategy, described in Section 2.3.3.

### 2.3.1 Analysis of a Field Experiment

As part of the AOSN-II experiment, more than a dozen gliders were simultaneously deployed in the vicinity of Monterey Bay, California during the annual upwelling event in August 2003. The gliders were deployed in two groups to capture signals at multiple scales within two overlapping domains. The first group, a set of five Spray gliders, patrolled a large mapping domain spanning 123 km by 143 km as shown in Figure 2.10(a). Deployed and recovered inside the bay, the Spray gliders traveled back and forth on five linear tracks evident in Figure 2.10(a) from the glider profile positions, which are depicted by black dots.

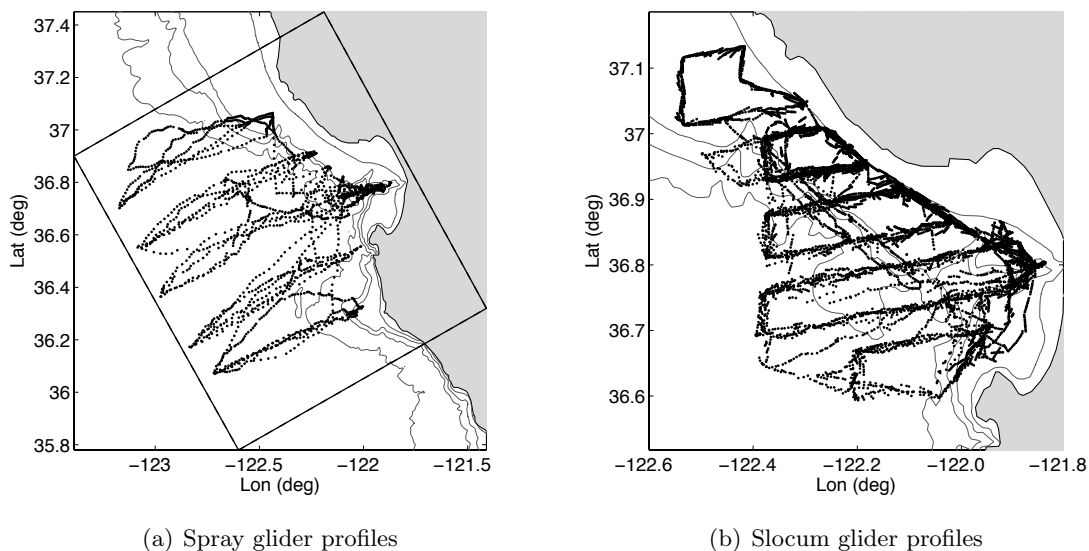


Figure 2.10: AOSN-II glider profile positions. Each black dot represents the position of a glider profile collected in Monterey Bay, California during August 2003. Contour lines representing bottom depths of 50, 150, 400, and 1000 m are shown. (a) Five Spray gliders, deployed and recovered in the bay, were assigned to five cross-shelf linear tracks spanning a 123 km by 143 km domain; (b) concurrently, ten Slocum gliders were assigned to orbit five trapezoidal tracks across the mouth of the bay.

The second group, consisting of ten Slocum gliders, was deployed on five trapezoidal tracks inside a second, smaller domain across the mouth of the bay. The Slocum glider tracks are evident from the profile positions illustrated in Figure 2.10(b).

We evaluate the mapping performance of the Spray gliders using OA, after [146]. We use spatial and temporal decorrelation lengths estimated from the glider data to be 22 km and 2.2 days, respectively [229]. We set the measurement noise  $\tilde{\sigma}_0$  equal to 10% of  $\sigma_0$ . A snapshot of the mapping error at midnight GMT on August 14 is shown in Figure 2.11(a). At this point in the experiment, the mapping performance  $\mathcal{J}(t)$  in the large mapping domain is equal to 0.16. A second snapshot of the mapping error from midnight GMT on August 21 is shown in Figure 2.11(b). At this point, the mapping performance has dipped to 0.13, because two gliders have deviated off course. The off-course gliders bunched together with gliders on neighboring tracks.

The Spray gliders' mapping performance during AOSN-II, plotted versus time in Fig-

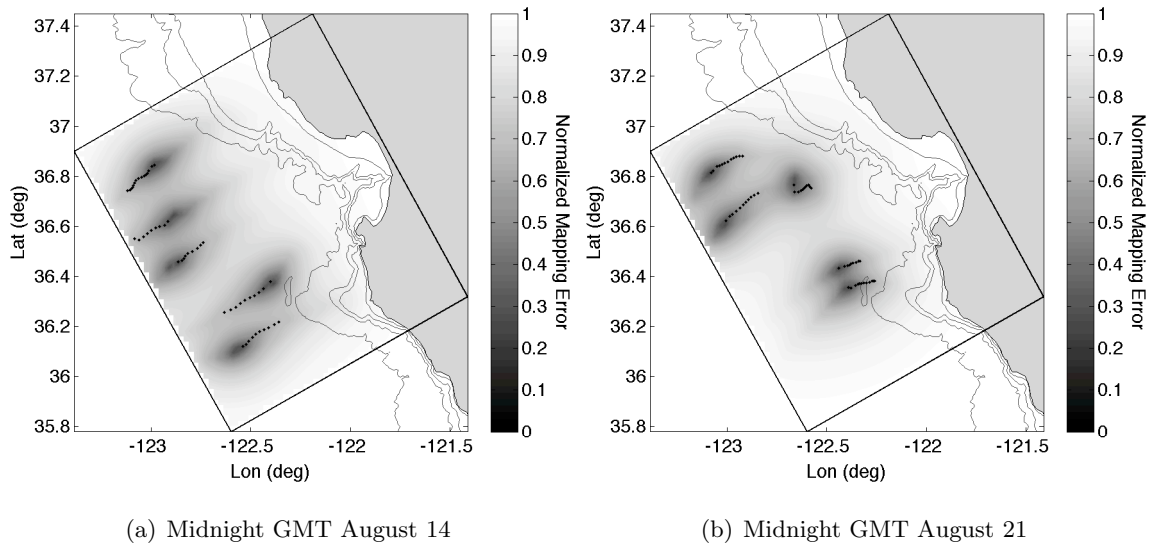


Figure 2.11: AOSN-II Spray glider mapping error. The black dots represent the positions of profiles collected by the five Spray gliders during the previous 24 hours. The gray scale represents the value of the normalized mapping error, which is smallest (dark gray) at the current position of each glider. (a) When all five gliders are on-course, the mapping performance is 0.16; (b) when two gliders deviate off course, the mapping performance dips by nearly 20% to 0.13.

Figure 2.12, illustrates that mapping performance is related to the number of glider profiles, unless the profiles are poorly distributed in space or time. Figure 2.12 shows variations in mapping performance not caused by changes in the number of profiles. These variations are due to changes in the profile-position distribution in space and time. In a distribution of profiles leading to a downward fluctuation of mapping performance some profiles may be spaced too close together and others may be spaced too far apart. The large dip in the mapping performance that occurred around August 22 was a result of the course deviations of two gliders. The smaller dips in performance that occurred with a period of about one week might have been due to the distribution of all the gliders within the mapping domain, since one week was approximately the time it took for a glider to travel the length of its track. Mapping performance suffered when all of the gliders were either near shore or off-shore. To avoid this reduction in performance, one could stagger the back-and-forth motion of gliders across the domain.

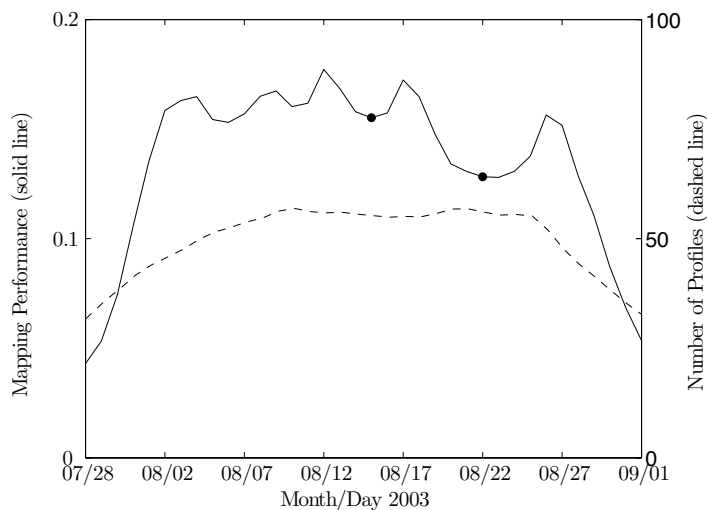


Figure 2.12: AOSN-II Spray glider mapping performance  $\mathcal{I}(t)$  and average number of profiles used per day to compute  $\mathcal{I}(t)$ . The mapping performance of the Spray gliders from July 28, 2003 to September 1, 2003 is related to the number of profiles used to compute the mapping error, except when the profiles are poorly distributed in space and time. The black dots correspond to the snapshots of the mapping error illustrated in Figures 2.11(a) and 2.11(b).

The AOSN-II results demonstrate how glider mapping performance depends on glider spacing. Glider spacing is determined in part by track placement and partly by the ability of each glider to stay on its track. It also depends on the position of each glider on its track relative to the position of other gliders on the same or even different tracks. A central component of the AS strategy is to coordinate the glider movements around their assigned tracks in order to maintain proper spacing. A major challenge to this type of motion coordination is the presence of ocean currents. The impact an ocean current can have on along-track glider spacing is illustrated in the following simple example, which motivates the use of feedback control to maintain proper spacing.

### 2.3.2 Example of an Open-Loop Survey with Flow

Consider two gliders traveling counterclockwise around a circular track in a uniform flow field as shown in Figure 2.13(a). We study the impact of the flow speed on the distance between the gliders, which are initially on opposite sides of the circle. Bunching together

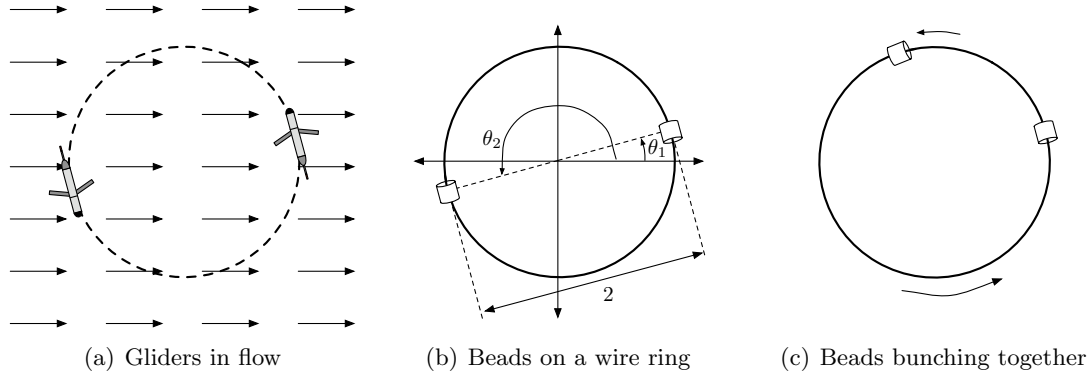


Figure 2.13: Simple model of two gliders on a circular track in a uniform flow field. (a) Two gliders, initially on opposite sides of the track, seek to travel counterclockwise; (b) the gliders are represented by a beads on a wire ring of unit radius (dimensionless); (c) the beads bunch together along the top of the ring, where they travel slowly.

on a closed track leads to reduction in mapping performance since the portion of the track between the gliders is over-sampled and the opposite side is under-sampled.

Assume that the gliders do not adjust their course to regulate their spacing. Also assume that, in the presence of light or moderate flow, each glider’s trajectory precisely traces the track. This allows us to represent the gliders by a pair of beads on a frictionless wire ring as shown in Figure 2.13(b). The latter assumption is reasonable, because a glider’s onboard control system is typically configured to steer the glider to compensate for the component of the flow orthogonal to its desired direction of motion. (On the other hand, modeling the gliders as beads fails to account for the reduction in speed necessary to fight the flow to keep the glider on the track.)

We normalize the dimensions of the problem so that the wire ring has unit radius. We place the ring’s center at the origin of the complex plane. In the absence of flow, the beads move at a constant speed around the ring. The bead positions can be represented by the unit vectors  $e^{i\theta_1}$  and  $e^{i\theta_2}$ , where  $\theta_1$  and  $\theta_2$  are measured relative to the positive real axis as shown in Figure 2.13(b). The motion of bead  $k \in \{1, 2\}$  around the ring is described by the constant rate  $\omega_0$  of the angle  $\theta_k$ , that is,  $\dot{\theta}_k = \omega_0$ , for  $k = 1, 2$ . Since the beads are initially on opposite sides of the track,  $\theta_1(t) = \theta_2(t) + \pi$  for all time  $t$  in the absence of flow.

In the presence of a uniform flow field parallel to the positive real axis, a bead slows

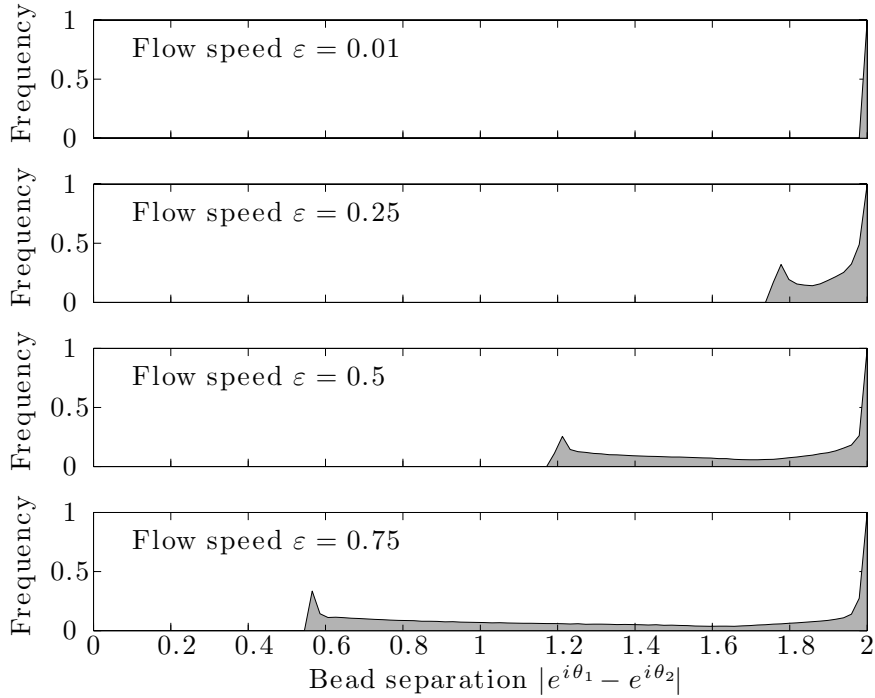


Figure 2.14: Numerical results for the simple model of Figure 2.13: two gliders on a circular track in a flow field. Each row represents a histogram of the distance  $|e^{i\theta_2} - e^{i\theta_1}|$  between the beads for flow strength equal to  $\varepsilon$  times the bead speed. Although the beads are initially on opposite sides of the track (so their initial distance apart is 2), as flow strength increases, the beads are increasingly likely to bunch together.

down at the top of the ring where it is traveling against the flow and speeds up at the bottom of the ring where it is traveling with the flow, as shown in Figure 2.13(c). The bead kinematics in the presence of flow of strength  $\omega_0\varepsilon$ , where  $0 \leq \varepsilon < 1$ , can be modeled by

$$\dot{\theta}_k = \omega_0(1 - \varepsilon \sin \theta_k), \quad k = 1, 2, \quad (2.10)$$

since  $\dot{\theta}_k < \omega_0$  when  $\theta_k = \pi/2$  (the top of the ring) and  $\dot{\theta}_k > \omega_0$  when  $\theta_k = 3\pi/2$  (the bottom of the ring). We have  $\dot{\theta}_k = \omega_0$  when  $\theta_k = 0$  or  $\theta_k = \pi$ .

We numerically study the dependence of glider separation on the flow speed parameter  $\varepsilon$  by integrating the two differential equations in (2.10) for several values of  $\varepsilon$ . We consider  $\varepsilon = 0.01, 0.25, 0.5$ , and  $0.75$ . Figure 2.14 shows a histogram of the distance  $|e^{i\theta_2} - e^{i\theta_1}|$  between the beads after many revolutions around the ring. Since the beads are initially on opposite sides of the unit circle, their initial separation is 2. For a flow strength of only

1% of bead speed, shown in the top row of Figure 2.14, the beads remain at this spacing. However, as flow strength increases, we observe that the beads are increasingly likely to bunch together, which is indicated by a separation distance less than 2. For example, when  $\varepsilon = 0.5$ , the frequency distribution of particle spacing extends as low as 1.2. For  $\varepsilon = 0.75$ , the frequency distribution extends lower than 0.6.

This example illustrates how the presence of even moderate flow degrades glider along-track spacing. Glider deployments are called *open-loop* if each glider does not adjust its course to regulate the distance to other gliders. For example, the AOSN-II field experiment described in the previous section was primarily an open-loop deployment.<sup>5</sup> Glider deployments are called *closed-loop* if each glider adjusts its course to regulate glider spacing using feedback control at the level of the fleet. The ASAP field experiment described in Chapter 9 was a closed-loop deployment. Note, a glider under fleet-level feedback control necessarily diverts some onboard control authority away from the task of following a track and applies it to the task of regulating glider spacing. Consequently, fleet-level feedback control improves mapping performance at the cost of a reduction in track-following performance.

### 2.3.3 Feedback Control at the Level of the Glider Fleet

Feedback control at the level of the fleet can be used to stabilize coordinated glider motion. Two illustrations of coordinated glider movement are shown in Figure 2.15(a) and 2.15(c) (again assuming near continuous sampling rate for each individual). In the first illustration, two gliders travel on opposite sides around a single track. Each point on the track is sampled at a regular interval equal to half of a glider's period of revolution around the track. The configuration shown in Figure 2.15(b), where the gliders are not on opposite sides of the track, may not achieve as high mapping performance as in Figure 2.15(a) because the gliders are bunched together. In the second illustration, two gliders travel in unison around two, identical tracks: that is, if one track were placed on top of the other track, then the gliders would be co-located as they move around their tracks. The configuration shown

<sup>5</sup>Closed-loop control of several gliders was demonstrated during portions of the deployment [83].

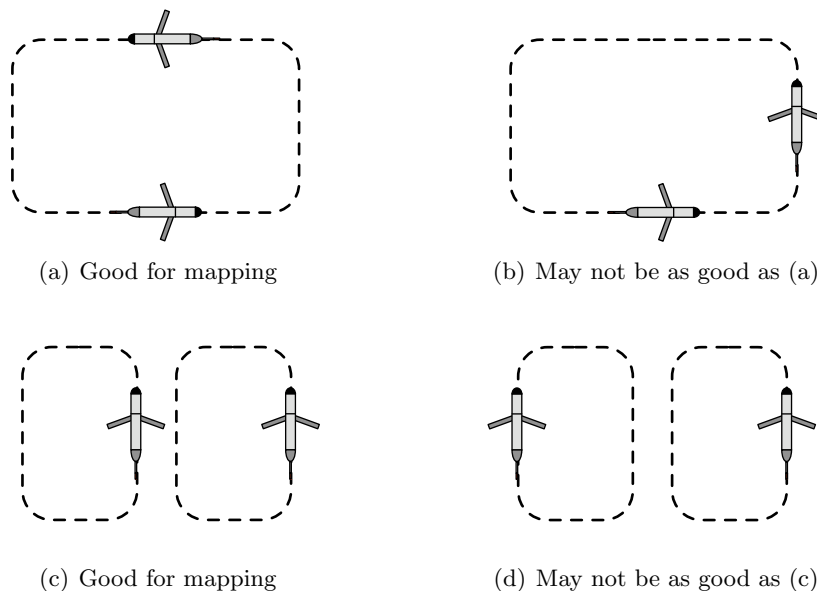


Figure 2.15: Illustrations of coordinated glider movement. (a) Two gliders travel on opposite sides around a single track so that each point on the track is sampled at a regular interval; (b) an undesirable configuration of two gliders bunched together on a single track; (c) two gliders traveling in unison around two identical tracks; (d) a configuration with two gliders traveling in opposite directions around two identical tracks may be better suited for estimating the spatial decorrelation length than for maximizing mapping performance.

in Figure 2.15(d), where the two gliders travel in opposite directions so that the distance between them oscillates over time, may not yield as high mapping performance. On the other hand, this configuration, in which the pair of gliders collect simultaneous measurements over a range of spatial separations, may be effective for estimating spatial decorrelation length.

The cartoons in Figure 2.15 illustrate the concept and guidelines for coordinated glider movement, but implementation of these guidelines depends on the specific flow conditions. The presence of strong flow can drive a pair of gliders from the configuration shown in Figure 2.15(a) to the one shown in Figure 2.15(b), unless the gliders are able to adjust their course to regulate their spacing. For some flow conditions, the two counter-revolving gliders in Figure 2.15(d) might yield the higher mapping performance than the two gliders in Figure 2.15(c). For example, consider a flow condition in which the flow circulates clockwise in the left track and counterclockwise in the right track. This configuration would boost glider effective speed, which could improve mapping performance.

AS1. (Every second) <i>Use feedback control onboard each glider to steer it along a path connecting an ordered list of waypoints.</i>
AS2. (Hourly) <i>Use feedback control at the level of the fleet to generate and update waypoint lists in order to produce coordinated trajectories.</i>
AS3. (Daily-weekly) <i>Design and adapt the glider coordinated trajectories to maximize mapping performance.</i>

Table 2.1: Adaptive sampling strategy. The strategy involves three nested feedback loops labeled *AS1*, *AS2*, and *AS3*, whose periodicity ranges from seconds to weeks. The first two loops are automated: *AS1* is automated onboard each glider and *AS2* is automated on shore. *AS3* requires operator intervention.

Table 2.1 summarizes our strategy for glider mapping. The strategy consists of three nested feedback loops labeled *AS1*, *AS2*, and *AS3*. These three loops are listed in order of the magnitude of the period of time between successive iterations of the loop, which ranges from every second (*AS1*) to daily or even weekly (*AS3*). *AS1* represents a capability developed by glider manufacturers and is described in Section 2.1. *AS2*—one of the main contributions of this thesis—represents the implementation of decentralized control algorithms (described in Chapter 7) by an automatic control system (described in Chapter 8). A practical implementation of *AS3*, yet to be fully automated, is described in Chapter 9.

Many challenges faced in the implementation of *AS2* in Table 2.1 arise from limitations of underwater gliders [83, 146]. A glider’s relatively low speed renders it highly vulnerable to ocean currents and, when it is on the surface and drifting passively, it is completely at the mercy of currents, tides, and wind. In order to mitigate drifting and other hazards faced by gliders during surface intervals, one seeks to limit time on the surface by reducing the frequency and duration of out-of-water communication. Limiting the frequency of out-of-water communication—by configuring a glider to surface for communication less frequently—presents a challenge to achieving *AS2*, because it increases the interval between updates to the glider waypoint list. From the standpoint of a digital control system, increasing the sample period degrades control performance [87, p. 646-705]. Choosing the interval between waypoint list updates requires trading-off degradation in the fleet-level feedback control performance, which leads to degradation of overall mapping performance,

with improvements in glider effective horizontal speed, which improves individual mapping performance.

Limiting the duration of communication on the surface also presents a challenge to achieving AS2, since it may preclude “closing the loop” when the glider is on the surface. That is, after uploading data from the previous dive, a glider may not wait on the surface for a waypoint list to be generated by a fleet-level feedback controller. In this scenario, updated waypoint lists must be computed and made available for each glider before it surfaces. Since waypoint lists can be as much as one dive old, this scenario introduces time delay into the fleet-level feedback control, leading to degradation in control performance [87, p. 331-334].

Another challenge to implementation of AS2 is the fact that gliders come to the surface to communicate asynchronously. That is, there is no guarantee at any given time that more than one glider will be on the surface. Therefore, although the time-averaged communication network of a glider fleet may be represented by a “hub and spoke” model, it is rare for more than one “spoke” in the communication network to be instantaneously active. Consequently, information communicated to a glider about any other glider is necessarily old [146].

In Chapters 3–7 we develop a design methodology for fleet-level feedback control that stabilizes collective motion suitable for oceanographic sampling. Another design for fleet-level feedback of underwater gliders is described in Fiorelli *et al.* [83]. Strategies for controller design with infrequent and asynchronous sensing have been studied in [300]. However, since this and other challenges have yet to be fully addressed from a theoretical standpoint, their consideration is deferred to Chapters 8 and 9.

## Chapter 3

# Motion and Interaction Models

In this chapter we describe the mathematical models that underly our design of cooperative control laws to stabilize collective motion. We study a dynamic model of self-propelled particles with possibly limited interaction. Section 3.1 presents the particle model. Section 3.2 describes symmetries and steady motions of the particle model. Section 3.3 uses graph theory to present our notation for describing particle interaction.

### 3.1 Particles with Phase Oscillator Dynamics

Consider a collective with  $N$  individuals. We model each individual in the collective as a Newtonian point mass (particle) constrained to a two-dimensional Euclidean plane  $\mathbb{R}^2$ . We identify  $\mathbb{R}^2$  with the complex plane  $\mathbb{C}$  to facilitate our analysis. Let  $\mathcal{I} = (O, 1, i)$  denote an inertial reference frame with origin  $O$  and orthonormal basis vectors  $1$  and  $i \triangleq \sqrt{-1}$ . We label each particle with an index from the set of integers  $\mathcal{N} \triangleq \{1, \dots, N\}$ .

We derive the particle kinematics using the coordinates shown in Figure 3.1. The position of the  $k$ th particle with respect to the origin of the inertial frame is  $r_k \in \mathbb{C}$ , where  $k \in \mathcal{N}$ . The velocity of the  $k$ th particle is the time-derivative with respect to the inertial frame of the position, that is,  $\dot{r}_k \triangleq \frac{d}{dt}r_k$ . We express the velocity in complex polar coordinates as  $\dot{r}_k = s_k e^{i\theta_k}$ , where  $s_k > 0$  is the speed of particle  $k$  and  $\theta_k$  is the direction of motion of particle  $k$ . We call  $\theta_k \in \mathbb{T}$  the phase of particle  $k$ , where  $\mathbb{T} \triangleq S^1$  is the circle or

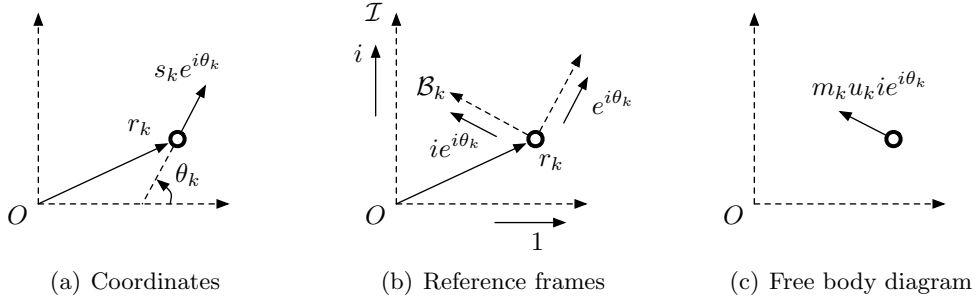


Figure 3.1: Planar particle dynamics. Each individual is modeled as a self-propelled particle with position  $r_k$ , speed  $s_k$ , phase  $\theta_k$ , and mass  $m_k$ . Particle  $k$  is steered by control  $u_k$ .

one-torus. We will represent  $\mathbb{T}$  also by the interval  $[0, 2\pi)$ , where 0 and  $2\pi$  are identified.

The acceleration of the  $k$ th particle is

$$\ddot{r}_k \triangleq \frac{d}{dt} \dot{r}_k = \dot{s}_k e^{i\theta_k} + s_k \dot{\theta}_k i e^{i\theta_k}. \quad (3.1)$$

We use Newton's second law to describe the particle dynamics. Let  $\mathcal{B}_k = (r_k, e^{i\theta_k}, i e^{i\theta_k})$  denote a path coordinate reference frame fixed to particle  $k$  with origin  $r_k$  and orthonormal basis vectors  $e^{i\theta_k}$  and  $i e^{i\theta_k}$ . Let  $m_k > 0$  denote the mass of particle  $k$ . We assume that the only force acting on each particle is  $m_k u_k i e^{i\theta_k}$ , where  $u_k \in \mathbb{R}$  is the steering control. Since the steering force acts on particle  $k$  in the direction of the unit vector  $i e^{i\theta_k}$  and there is no force in the direction of motion  $e^{i\theta_k}$ , the steering force is conservative and does no work. Using (3.1) and Newton's second law, we have

$$m_k u_k i e^{i\theta_k} = m_k (\dot{s}_k e^{i\theta_k} + s_k \dot{\theta}_k i e^{i\theta_k}) \quad (3.2)$$

Projecting (3.2) onto the unit vectors of the path frame  $\mathcal{B}_k$ —equivalent to equating real and imaginary parts—yields two scalar equations:

$$\dot{s}_k = 0 \quad (3.3)$$

$$s_k \dot{\theta}_k = u_k. \quad (3.4)$$

From (3.3), we observe that the speed of the  $k$ th particle remains fixed at its initial value  $s_k(0)$ . Equation (3.4) yields the equation of motion for the phase  $\theta_k$ ; the equation is

nonsingular for  $s_k(0) > 0$ . In fact, we assume that  $s_k(0) = 1$  for all  $k \in \mathcal{N}$ . This leads to the following definition.

**Definition 3.1. Particle model** *Let  $N$  denote the number of particles. Let  $r_k \in \mathbb{C}$ ,  $\theta_k \in \mathbb{T}$ , and  $u_k \in \mathbb{R}$  denote the position, phase (direction of motion), and steering control for particle  $k \in \mathcal{N}$ , respectively. The particle model is*

$$\begin{aligned}\dot{r}_k &= e^{i\theta_k} \\ \dot{\theta}_k &= u_k.\end{aligned}\tag{3.5}$$

The particle model (3.5) assumes all of the particles travel in a plane at unit speed. Under these assumptions, solutions of the particle model conserve total kinetic energy but not total linear momentum. The kinetic energy of particle  $k$  is  $(1/2)m_k|\dot{r}_k|^2$ . To compute its time-derivative, we use the inner product  $\langle z_1, z_2 \rangle \triangleq \operatorname{Re}\{z_1^* z_2\} = \operatorname{Re}\{z_2^* z_1\}$ , where  $z_1, z_2 \in \mathbb{C}$  and  $*$  denotes complex conjugate.<sup>1</sup> The time-derivative of the kinetic energy of particle  $k$  along solutions of (3.5) is

$$\frac{d}{dt} \left( \frac{1}{2} m_k |\dot{r}_k|^2 \right) = m_k \langle \dot{r}_k, \ddot{r}_k \rangle = m_k \langle e^{i\theta_k}, u_k i e^{i\theta_k} \rangle = m_k u_k \operatorname{Re}\{i\} = 0,$$

which implies that the total kinetic energy is constant. On the other hand, the linear momentum of particle  $k$  is  $m_k \dot{r}_k$ . The time-derivative of the linear momentum of particle  $k$  along solutions of (3.5) is

$$\frac{d}{dt} \left( m_k e^{i\theta_k} \right) = m_k u_k i e^{i\theta_k},$$

which implies that the time-derivative of the total linear momentum is

$$\frac{d}{dt} \left( \sum_{j=1}^N m_j e^{i\theta_j} \right) = \sum_{j=1}^N m_j u_j i e^{i\theta_j}.$$

In general, the total linear momentum is time-varying. If  $u_k = 0$  for all  $k$  or  $m_k u_k = m_j u_j$  for all pairs  $j$  and  $k$  and  $\sum_{j=1}^N e^{i\theta_j} = 0$ , then the total linear momentum is constant. The sum  $\sum_{j=1}^N e^{i\theta_j} = 0$  plays an important role in our control of total linear momentum.

<sup>1</sup>This inner product is equivalent to the standard inner product on  $\mathbb{R}^2$ . To see this consider  $\langle z_1, z_2 \rangle$  for some  $z_k = x_k + iy_k$ ,  $k = 1, 2$ , which equals  $\operatorname{Re}\{(x_1 - iy_1)(x_2 + iy_2)\} = x_1 x_2 + y_1 y_2$ .

We use state feedback to define the steering control  $u_k$ . Let  $\mathbf{r} \triangleq (r_1, \dots, r_N)^T \in \mathbb{C}^N$  and  $\boldsymbol{\theta} \triangleq (\theta_1, \dots, \theta_N)^T \in \mathbb{T}^N$ . If each steering control  $u_k$  is a function of some or all of the positions  $\mathbf{r}$  and phases  $\boldsymbol{\theta}$ , then we refer to  $u_k$  as a *closed-loop* control and (3.5) as the closed-loop particle model. Otherwise, if  $u_k$  is not a function of  $\mathbf{r}$  or  $\boldsymbol{\theta}$ , then we refer to  $u_k$  as an *open-loop* control and (3.5) as the open-loop particle model. If the steering control  $\mathbf{u} \triangleq (u_1, \dots, u_N)^T \in \mathbb{R}^N$  is a function of  $\boldsymbol{\theta}$  only, then we can study the phase dynamics independent of the position dynamics. This leads to the following definition.

**Definition 3.2. Phase model** *Let  $N$  denote the number of particles. Let  $\theta_k \in \mathbb{T}$  and  $u_k \in \mathbb{R}$  denote the phase (direction of motion) and steering control for particle  $k \in \mathcal{N}$ , respectively. The phase model is*

$$\dot{\theta}_k = u_k, \quad (3.6)$$

where  $u_k$  is a function of  $\boldsymbol{\theta}$  only.

The phase model (3.6) is equivalent to a system of coupled phase oscillators. Every solution of the oscillator system induces a trajectory in the particle model. The interplay between the phase model and the particle model (3.5) is fundamental to our control design methodology. To illustrate this interplay, we introduce and relate their collective properties.

Let  $p(\mathbf{z}) \triangleq (1/N) \sum_{j=1}^N z_j$  denote the centroid of  $\mathbf{z} \triangleq (z_1, \dots, z_N)^T \in \mathbb{C}^N$ . In the particle model, the centroid of the particle positions is  $p_r \triangleq p(\mathbf{r}) = (1/N) \sum_{j=1}^N r_j$ . If all of the particles have unit mass, then the position centroid is the center of mass of the collective. In the phase model, we refer to the unit vector  $e^{i\theta_k}$  as the phasor of particle  $k$ . Let  $e^{i\boldsymbol{\theta}} = (e^{i\theta_1}, \dots, e^{i\theta_N})^T \in \mathbb{C}^N$ . The centroid of the particle phasors is called the *phase order parameter* [139, p. 71] and is denoted by

$$p_\theta \triangleq p(e^{i\boldsymbol{\theta}}) = \frac{1}{N} \sum_{j=1}^N e^{i\theta_j}. \quad (3.7)$$

If all of the particles have unit mass, then the phase order parameter is the average linear momentum. In fact, the phase order parameter is equal to the time-derivative of the position

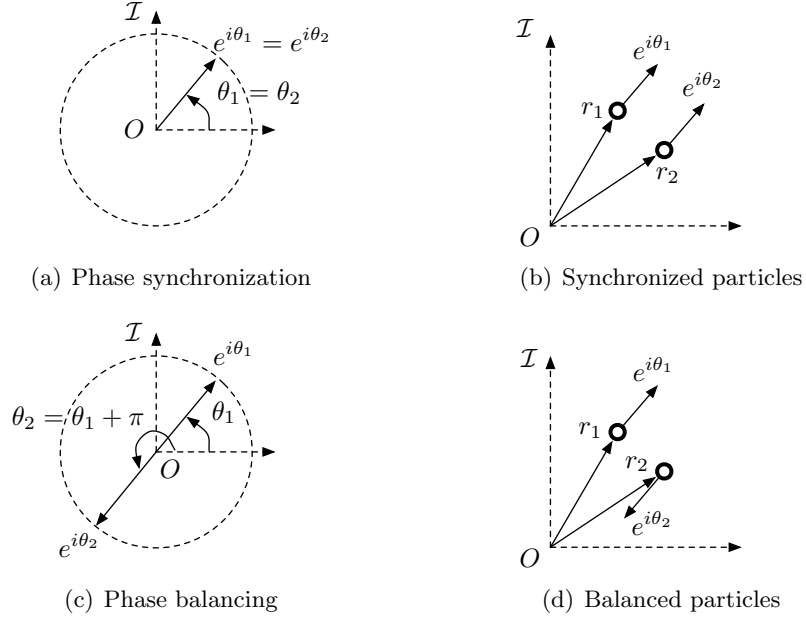


Figure 3.2: Phase synchronization and balancing for  $N = 2$ . (a,b) Two particles with synchronized phases move in parallel; (c,d) two particles with balanced phases move in opposite directions.

centroid along solutions of (3.5), that is,

$$\dot{p}_r = \frac{1}{N} \sum_{j=1}^N \dot{r}_j = p(e^{i\theta}) = p_\theta.$$

This implies that the motion of the position centroid depends on the value of the phase order parameter. The magnitude  $|p_\theta|$  of the phase order parameter satisfies  $0 \leq |p_\theta| \leq 1$ . We use the phase order parameter in the following two definitions, illustrated in Figure 3.2.

**Definition 3.3. Phase synchronization and balancing** *The phase arrangement  $\theta$  is synchronized if the modulus of the phase order parameter (3.7) equals one, that is,  $|p_\theta| = 1$ . The phase arrangement  $\theta$  is balanced if the phase order parameter (3.7) equals zero, that is,  $p_\theta = 0$ .*

If the phases are synchronized, then all of the particles travel in the same direction. The set of synchronized states, which we call the synchronized set, is an isolated point modulo the action of the symmetry group  $S^1$ . The synchronized set defines a manifold of dimension

one. If the phases are balanced, then the particles travel in such a way as to keep the position centroid fixed. The set of balanced states, which we call the balanced set, includes all of the phase arrangements  $\boldsymbol{\theta} \in \mathbb{T}^N$  for which  $p_\theta = 0$ .

The codimension of the manifold defined by the balanced set equals the rank of the equation  $p_\theta = 0$  [32, pp. 68-69]. The equation  $p_\theta = 0$  is equivalent to

$$\cos \theta_1 + \cos \theta_2 + \cdots + \cos \theta_N = 0 \quad (3.8)$$

$$\sin \theta_1 + \sin \theta_2 + \cdots + \sin \theta_N = 0. \quad (3.9)$$

The rank of (3.8)–(3.9) is the rank of the  $2 \times N$  Jacobian matrix

$$\mathbf{D}p_\theta \triangleq \begin{bmatrix} -\sin \theta_1 & -\sin \theta_2 & \cdots & -\sin \theta_N \\ \cos \theta_1 & \cos \theta_2 & \cdots & \cos \theta_N \end{bmatrix}. \quad (3.10)$$

The matrix  $\mathbf{D}p_\theta$  loses rank if there exists an  $\alpha \in \mathbb{R}$  such that

$$\alpha \cos \theta_k - \sin \theta_k = 0, \quad \forall k \in \mathcal{N}. \quad (3.11)$$

Using the identity  $\sin^2 \theta_k + \cos^2 \theta_k = 1$ , (3.11) becomes

$$\cos \theta_k = \frac{\pm 1}{\sqrt{\alpha^2 + 1}} \quad \text{and} \quad \sin \theta_k = \frac{\pm \alpha}{\sqrt{\alpha^2 + 1}}, \quad \forall k \in \mathcal{N}. \quad (3.12)$$

Let  $N_1$  be the number of phases for which  $\cos \theta_k = 1/\sqrt{\alpha^2 + 1}$  and  $N_2$  be the number of phases for which  $\cos \theta_k = -1/\sqrt{\alpha^2 + 1}$ . There exists a balanced phase arrangement that satisfies (3.12) for any  $\alpha$  if and only if  $N$  is even. This is because in order for (3.12) to hold in the balanced set, it must be true that

$$N_1 + N_2 = N \quad (3.13)$$

and

$$\sum_{j=1}^N \cos \theta_j = \frac{1}{\sqrt{\alpha^2 + 1}} (N_1 - N_2) = 0. \quad (3.14)$$

Equations (3.13) and (3.14) hold only if  $N_1 = N_2$ , which implies  $N$  must be even.

For  $N$  odd, the equation  $p_\theta = 0$  has full rank everywhere and the balanced set defines a manifold of codimension two. For  $N$  even, the balanced set is not a manifold of codimension

two. The equation  $p_\theta = 0$  loses rank at points where (3.12) holds. For example,  $p_\theta = 0$  loses rank when there is a cluster of  $N/2$  phases at 0 and another cluster of  $N/2$  phases at  $\pi$  ( $\alpha = 0$ ). The equation  $p_\theta = 0$  also loses rank for phase arrangements with four clusters—each with  $N/4$  phases—and mirror symmetry about both axes.

In Chapter 4, we derive a steering control  $\mathbf{u}$  that stabilizes synchronized and balanced phase arrangements and the corresponding collective particle motion. In Chapter 6, we use phase synchronization and balancing to stabilize symmetric phase patterns, defined next.

**Definition 3.4. Symmetric phase pattern** *Let  $M$  be a divisor of  $N$ . An  $(M, N)$ -pattern  $\boldsymbol{\theta}$ , called a symmetric phase pattern, is a phase arrangement of  $N$  phases consisting of  $M$  clusters with  $N/M$  synchronized phases in each cluster. If  $M = 1$ , then the phases are synchronized and all of the phases are contained in one cluster; if  $M > 1$ , then the clusters are uniformly spaced around the unit circle.*

For any  $N$ , there exist at least two symmetric phase patterns: the  $(1, N)$ -pattern, which is the synchronized pattern, and the  $(N, N)$ -pattern, which is the so-called *splay pattern* [110], characterized by  $N$  phases uniformly spaced around the circle.<sup>2</sup> For example, for  $N = 12$ , there are six symmetric phase patterns corresponding to the six divisors of  $N$ ; these patterns are illustrated in Figure 3.3. An early classification of symmetric phase patterns appears in [15], and is extended in [38].

Every symmetric phase pattern shown in Figure 3.3 other than the synchronized pattern is balanced. For each balanced phase pattern, consider what happens to the pattern if we multiply all of the phases by the number of phase clusters. (Note, multiplying phase  $\theta_k$  by  $M$  rotates  $\theta_k$  by  $(M - 1)\theta_k$  radians.) For example, starting with the  $(2, 12)$ -pattern, if we multiple all of the phases by  $M = 2$ , then the resulting pattern is synchronized. In fact, multiplying any  $(M, N)$ -pattern by  $M$  yields the synchronized pattern. Less obvious is the fact that if  $\boldsymbol{\theta}$  is an  $(M, N)$ -pattern, then each phase arrangement  $m\boldsymbol{\theta}$ , where  $m = 1, \dots, M - 1$ , is balanced. We summarize the synchronization and balancing properties of

<sup>2</sup>Also called “antiphase” states [110, 287] and “ponies on a merry-go-round” [13], splay patterns in coupled oscillator systems have been studied in [298, 249, 260, 183].

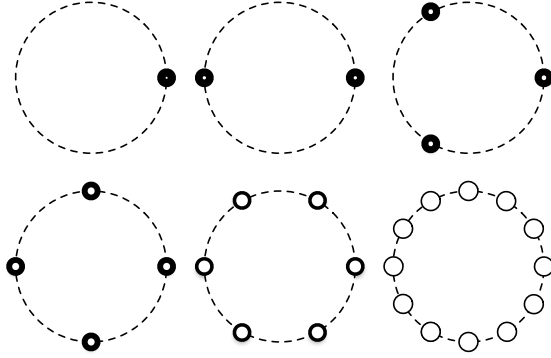


Figure 3.3: Symmetric phase patterns. The six symmetric phase patterns for  $N = 12$  correspond to the six divisors of  $N$ , which are  $M = 1, 2, 3, 4, 6,$  and  $12$ . Each pattern contains one to twelve phase clusters depicted here on a unit circle (dashed line). The number  $N/M$  of phases in each cluster is depicted by the width of the cluster annulus.

symmetric phase patterns in the following lemma; the lemma is proven in Chapter 6, where we provide feedback controls to stabilize symmetric phase patterns.

**Lemma 3.5. Symmetric phase pattern** *Let  $M$  be a divisor of  $N$ . An arrangement  $\theta$  of  $N$  phases is an  $(M, N)$ -pattern if and only if, for all  $m \in \{1, \dots, M - 1\}$ , the phase arrangement  $m\theta$  is balanced and the phase arrangement  $M\theta$  is synchronized.*

As a precursor to the design of closed-loop controls to stabilize synchronized, balanced, and symmetric phase patterns, we describe two open-loop steering controls and the resulting particle motion. In the case  $u_k = 0$ , the phase  $\theta_k$  remains fixed at its initial value  $\theta_k(0)$  and particle  $k$  travels in a straight line. In the case  $u_k = \omega_0 \neq 0$ , where  $\omega_0$  is constant, the phase  $\theta_k$  evolves linearly with time according to  $\theta_k(t) = \omega_0 t + \theta_k(0)$ . In this case, to find the trajectory of particle  $k$ , we integrate the particle velocity  $\dot{r}_k = e^{i(\omega_0 t + \theta_k(0))}$  using separation of variables:

$$r_k(t) = r_k(0) + i\omega_0^{-1}e^{i\theta_k(0)} - i\omega_0^{-1}e^{i(\omega_0 t + \theta_k(0))}$$

We observe that

$$c_k(t) \triangleq r_k(t) + i\omega_0^{-1}e^{i\theta_k(t)} \quad (3.15)$$

is constant along solutions of the particle model with  $u_k = \omega_0$ . The particle trajectory is  $r_k(t) = c_k(0) - i\omega_0^{-1}e^{i(\omega_0 t + \theta_k(0))}$ , which implies particle  $k$  orbits a circle of radius  $|\omega_0|^{-1}$

centered at  $c_k(0)$ . The direction of rotation of particle  $k$  around the circle depends on the sign of  $\omega_0$ . If  $\omega_0 > 0$ , then the particle travels counterclockwise; if  $\omega_0 < 0$ , then it travels clockwise.

The simple examples of straight line and circular motion are building blocks for two types of collective motion: straight line motion of all particles in the same direction and circular motion of all particles around the same circle in the same direction.

**Definition 3.6. Parallel and circular formations** *Let  $\mathbf{1} \triangleq (1, \dots, 1)^N \in \mathbb{R}^N$  and  $\theta_0 \in \mathbb{T}$ . A parallel formation of the particle model is a set of trajectories for which  $\boldsymbol{\theta} = \theta_0 \mathbf{1}$ , that is, all of the phases are constant and synchronized. The relative positions of particles in a parallel formation are arbitrary. Let  $c_k$  be given by (3.15),  $\mathbf{c} \triangleq (c_1, \dots, c_N)^T \in \mathbb{C}^N$ ,  $c_0 \in \mathbb{C}$ ,  $\omega_0 \in \mathbb{R}$ , and  $\omega_0 \neq 0$ . A circular formation of the particle model is set of trajectories for which  $\dot{\boldsymbol{\theta}} = \omega_0 \mathbf{1}$  and  $\mathbf{c} = c_0 \mathbf{1}$ , that is, all of the particles travel around a circle of radius  $|\omega_0|^{-1}$ , the direction of rotation is determined by the sign of  $\omega_0$ , and all of the circle centers  $c_k$  are equal. The relative phases of particles in a circular formation are arbitrary.*

For particles in a circular formation, the (relative) phase arrangement is arbitrary. To describe circular formations with specific phase arrangements, we use the corresponding phase pattern terminology. That is, synchronized, balanced, and symmetric circular formations are circular formations in which the phase arrangement is a synchronized, balanced, and symmetric, respectively.

## 3.2 Shape Control and Relative Equilibria

Relative equilibria correspond to steady motions of an uncontrolled system that are fixed points in a reduced configuration space [161, p. 263], [42, pp. 21, 57]; see also [29]. Parallel and circular formations are relative equilibria of the particle model (3.5), that is, they are fixed points in the reduced configuration space called *shape space*. We describe below the shape space of the particle model and its equilibria using a Lie group formulation, after [127]. A control law that depends only on coordinates of shape space is called a *shape control*.

In the particle model, the state of each particle is  $(r_k, \theta_k)$ , which implies that solutions of the particle model evolve on the configuration space  $(\mathbb{C} \times \mathbb{T}) \times \dots \times (\mathbb{C} \times \mathbb{T})$  ( $N$  times). This configuration space is topologically equivalent to  $N$  copies of the special Euclidean group in the plane  $SE(2)$ , which we denote  $SE(2)^N$ . Let  $z_1, z_2 \in \mathbb{C}$  and  $\theta_1, \theta_2 \in \mathbb{T}$ . In complex notation, the special Euclidean group  $SE(2)$  acts on  $\mathbb{C}$  according to  $(z_1, \theta_1) \cdot z_2 = e^{i\theta_1} z_2 + z_1$ . The group operation is  $(z_1, \theta_1) \cdot (z_2, \theta_2) = (e^{i\theta_1} z_2 + z_1, \theta_1 + \theta_2)$ , which is suitably represented by matrix multiplication. A complex matrix representation is

$$\begin{bmatrix} e^{i\theta_1} & z_1 \\ 0 & 1 \end{bmatrix} \begin{bmatrix} e^{i\theta_2} & z_2 \\ 0 & 1 \end{bmatrix} = \begin{bmatrix} e^{i(\theta_1+\theta_2)} & e^{i\theta_1} z_2 + z_1 \\ 0 & 1 \end{bmatrix}.$$

If the closed-loop particle model is invariant under the action of  $SE(2)$  on the configuration space  $SE(2)^N$ , then solutions evolve on the reduced shape space  $SE(2)^N/SE(2)$ . The space  $SE(2)^N/SE(2)$  is called shape space since it describes the position and phase of the particles relative to one another as opposed to the absolute particle positions and phases (relative to the inertial frame  $\mathcal{I}$ ).  $SE(2)$ -invariance of the closed-loop particle model means that solutions do not depend on the origin or orientation of the inertial frame  $\mathcal{I}$ . In order for the closed-loop particle model to be  $SE(2)$ -invariant, then the steering control  $\mathbf{u}$  must be  $SE(2)$ -invariant, which means that the control does not depend on the origin or orientation of  $\mathcal{I}$ ;  $SE(2)$ -invariant controls are called shape controls.

To illustrate  $SE(2)$ -invariance and to formalize the requirement for  $\mathbf{u}$  to be a shape control, let  $r_0 \in \mathbb{C}$ , let  $\theta_0 \in \mathbb{T}$ , and consider the smooth  $SE(2)$  map  $\Phi : (r_k, \theta_k) \mapsto (\bar{r}_k, \bar{\theta}_k) \triangleq (e^{i\theta_0} r_k + r_0, \theta_k + \theta_0)$ . The output  $(\bar{r}_k, \bar{\theta}_k)$  relative to the frame  $\mathcal{I} = (0, 1, i)$  is equal to the input  $(r_k, \theta_k)$  relative to the frame  $(O - r_0, e^{-i\theta_0}, ie^{-i\theta_0})$ , which is frame  $\mathcal{I}$  rotated by  $-\theta_0$  and translated by  $-r_0$ . Inverting  $\Phi(r_k, \theta_k)$  yields  $r_k = (\bar{r}_k - r_0)e^{-i\theta_0}$  and  $\theta_k = \bar{\theta}_k - \theta_0$ . The time-derivatives of  $r_k$  and  $\theta_k$  in the transformed coordinates are

$$\begin{aligned} \dot{r}_k &= \dot{\bar{r}}_k e^{-i\theta_0} \\ \dot{\theta}_k &= \dot{\bar{\theta}}_k. \end{aligned} \tag{3.16}$$

Using the closed-loop particle model (3.5) with  $\mathbf{u} = \mathbf{u}(\mathbf{r}, \boldsymbol{\theta})$ ,  $r_k$  replaced by  $(\bar{r}_k - r_0)e^{-i\theta_0}$ ,

and  $\theta_k$  replaced by  $\bar{\theta}_k - \theta_0$ , we find

$$\begin{aligned}\dot{r}_k &= e^{i(\bar{\theta}_k - \theta_0)} \\ \dot{\theta}_k &= u_k((\bar{\mathbf{r}} - r_0 \mathbf{1})e^{-i\theta_0}, \bar{\boldsymbol{\theta}} - \theta_0 \mathbf{1}).\end{aligned}\tag{3.17}$$

Using (3.16) and (3.17), we obtain  $\dot{r}_k = e^{i\bar{\theta}_k}$  and  $\dot{\theta}_k = u_k((\bar{\mathbf{r}} - r_0 \mathbf{1})e^{-i\theta_0}, \bar{\boldsymbol{\theta}} - \theta_0 \mathbf{1})$ . The closed-loop particle model is  $SE(2)$ -invariant if  $u_k((\bar{\mathbf{r}} - r_0 \mathbf{1})e^{-i\theta_0}, \bar{\boldsymbol{\theta}} - \theta_0 \mathbf{1}) = u_k(\bar{\mathbf{r}}, \bar{\boldsymbol{\theta}})$  for all  $k \in \mathcal{N}$ . This leads to the following definition.

**Definition 3.7. Shape control** *Let  $r_0 \in \mathbb{C}$  and  $\theta_0 \in \mathbb{T}$ . The steering control  $\mathbf{u} = \mathbf{u}(\mathbf{r}, \boldsymbol{\theta})$  is a shape control of the particle model (3.5) if*

$$u_k((\mathbf{r} - r_0 \mathbf{1})e^{-i\theta_0}, \boldsymbol{\theta} - \theta_0 \mathbf{1}) = u_k(\mathbf{r}, \boldsymbol{\theta}), \quad \forall k \in \mathcal{N}.\tag{3.18}$$

*The steering control  $\mathbf{u} = \mathbf{u}(\boldsymbol{\theta})$  is a shape control of the phase model (3.6) if*

$$u_k(\boldsymbol{\theta} - \theta_0 \mathbf{1}) = u_k(\boldsymbol{\theta}), \quad \forall k \in \mathcal{N}.\tag{3.19}$$

In order to satisfy condition (3.18) or (3.19), the control  $\mathbf{u}$  must depend only on the so-called shape variables. We derive the shape variables for  $N = 2$  using a Lie group formulation of the particle model (3.5), after [127]. Let  $g_1, g_2 \in SE(2)$  be given by

$$g_1 = \begin{bmatrix} e^{i\theta_1} & r_1 \\ 0 & 1 \end{bmatrix}, \quad g_2 = \begin{bmatrix} e^{i\theta_2} & r_2 \\ 0 & 1 \end{bmatrix}.\tag{3.20}$$

Since  $N = 2$ , the shape space is  $SE(2)^2/SE(2)$ . Let  $g \in SE(2)^2/SE(2)$  be given by  $g \triangleq g_1^{-1}g_2$ . The entries of  $g$  and its inverse  $g^{-1}$  are shape variables. Let  $\theta_{k,j} \triangleq \theta_k - \theta_j$  denote phase  $\theta_k$  relative to phase  $\theta_j$  and let  $r_{k,j} = r_k - r_j$  denote position  $r_k$  relative to position  $r_j$ . We have

$$g = \begin{bmatrix} e^{-i\theta_1} & -e^{-i\theta_1}r_1 \\ 0 & 1 \end{bmatrix} \begin{bmatrix} e^{i\theta_2} & r_2 \\ 0 & 1 \end{bmatrix} = \begin{bmatrix} e^{i\theta_{2,1}} & r_{2,1}e^{-i\theta_1} \\ 0 & 1 \end{bmatrix}\tag{3.21}$$

and

$$g^{-1} = \begin{bmatrix} e^{i\theta_{1,2}} & r_{1,2}e^{-i\theta_2} \\ 0 & 1 \end{bmatrix}.\tag{3.22}$$

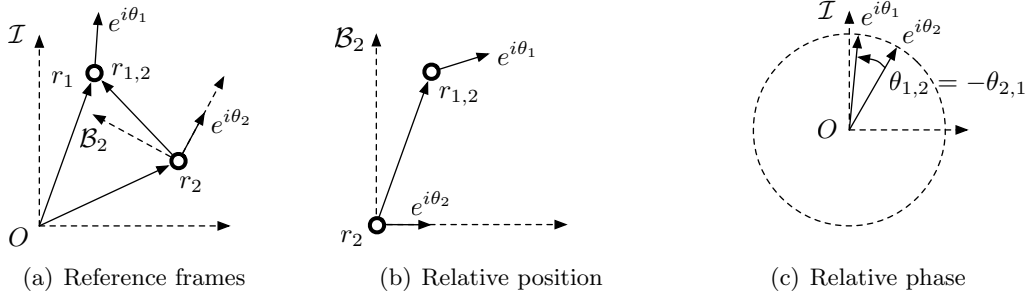


Figure 3.4: Shape variables. The shape variables are shown for control  $u_2$  with  $N = 2$ .

Using (3.21) and (3.22), we observe that the quantity  $e^{i\theta_{1,2}} = (e^{i\theta_{2,1}})^{-1}$  is a shape variable, which implies that the relative phase  $\theta_{1,2} = -\theta_{2,1}$  is a shape variable. The quantities  $r_{2,1}e^{-i\theta_1}$  and  $r_{1,2}e^{-i\theta_2}$  are also shape variables. We interpret the quantity  $r_{1,2}e^{-i\theta_k}$  as the relative position  $r_{1,2}$  with respect to the path frame  $\mathcal{B}_k$ ,  $k = 1, 2$ . The steering controls  $u_1 = u_1(r_{1,2}e^{-i\theta_1}, \theta_{1,2})$  and  $u_2 = u_2(r_{1,2}e^{-i\theta_2}, \theta_{1,2})$  satisfy the shape control condition (3.18) since

$$u_k((r_{1,0}e^{-i\theta_0} - r_{2,0}e^{-i\theta_0})e^{-i\theta_{k,0}}, \theta_{1,0} - \theta_{2,0}) = u_k(r_{1,2}e^{-i\theta_k}, \theta_{1,2}).$$

The shape variables for control  $u_2$  are shown in Figure 3.4.

The discussion for  $N = 2$  help to identify shape variables for  $N \geq 2$ , given in the following lemma.

**Lemma 3.8. Shape variables** *For all  $j, k \in \mathcal{N}$ ,  $j \neq k$ , the relative phases  $\theta_{j,k}$  and the relative positions  $r_{j,k}$  with respect to the path frame  $\mathcal{B}_k$  are shape variables of the closed-loop particle model (3.5). The relative phases  $\theta_{j,k}$  are shape variables of the closed-loop phase model (3.6).*

*Proof.* Steering controls of the form

$$u_k = (r_{1,k}e^{-i\theta_k}, \dots, r_{N,k}e^{-i\theta_k}, \theta_{1,k}, \dots, \theta_{N,k}), \quad k \in \mathcal{N},$$

are shape controls of the particle model because they satisfy condition (3.18).  $\square$

Note that we don't need all  $\theta_{j,k}$ ,  $j \neq k$ , to span the phase shape space  $\mathbb{T}^N/\mathbb{T}$ , since only  $N - 1$  of the relative phases are linearly independent. Similarly, we need only  $N - 1$

relative phases and  $N - 1$  relative positions to span the shape space  $SE(2)^N/SE(2)$ , which is topologically equivalent to  $SE(2)^{N-1}$ .

If the particle model is  $SE(2)$ -invariant, then the shape variables evolve on the shape space. Fixed points of the shape dynamics are called relative equilibria of the particle model. We find the relative equilibria for  $N = 2$  using a Lie group formulation, after [127]. The time-derivatives of  $g_1$  and  $g_2$  from (3.20) along solutions of (3.5) are

$$\dot{g}_1 = \begin{bmatrix} u_1 i e^{i\theta_1} & e^{i\theta_1} \\ 0 & 0 \end{bmatrix}, \quad \dot{g}_2 = \begin{bmatrix} u_2 i e^{i\theta_2} & e^{i\theta_2} \\ 0 & 0 \end{bmatrix}.$$

Let  $\mathbf{a}, \mathbf{b} \in \mathfrak{se}(2)$ , where  $\mathfrak{se}(2)$  is the Lie algebra of  $SE(2)$ , be given by

$$\mathbf{a} \triangleq \begin{bmatrix} 0 & 1 \\ 0 & 0 \end{bmatrix}, \quad \mathbf{b} \triangleq \begin{bmatrix} i & 0 \\ 0 & 0 \end{bmatrix}. \quad (3.23)$$

In the Lie formulation, the particle model (3.5) with  $N = 2$  becomes

$$\begin{aligned} \dot{g}_1 &= g_1(\mathbf{a} + \mathbf{b}u_1) \\ \dot{g}_2 &= g_2(\mathbf{a} + \mathbf{b}u_2). \end{aligned} \quad (3.24)$$

Note that the Lie bracket of  $\mathbf{a}$  and  $\mathbf{b}$  is  $[\mathbf{a}, \mathbf{b}] \triangleq \mathbf{a} \cdot \mathbf{b} - \mathbf{b} \cdot \mathbf{a} = \begin{bmatrix} 0 & -i \\ 0 & 0 \end{bmatrix}$ , which implies that the basis  $(\mathbf{a}, \mathbf{b}, [\mathbf{a}, \mathbf{b}])$  spans  $\mathfrak{se}(2)$ . Therefore, even though the particle model is not *small-time local controllability* (see, for example [263, Theorem 2.4]), it is *locally strongly accessible* (see, for example [184, Theorem 3.21]). That is, even though a particle cannot stop or move directly sideways, it can be steered to reach any nearby point in a short amount of time.

Let  $u_k$  be a shape control of the particle model, that is,  $u_k$  depends only on the shape variables  $\theta_{1,2}$  and  $r_{1,2}e^{-i\theta_k}$ . The time-derivative of  $g = g_1^{-1}g_2$  along the solutions of (3.24) yields the shape dynamics

$$\begin{aligned} \dot{g} &= -g_1^{-1}\dot{g}_1g_1^{-1} + g_1^{-1}\dot{g}_2 \\ &= -(\mathbf{a} + \mathbf{b}u_1)g + g(\mathbf{a} + \mathbf{b}u_2). \end{aligned}$$

Fixed points of the shape dynamics satisfy  $\dot{g} = 0$ , which evaluates to

$$\begin{bmatrix} u_2 i e^{i\theta_{2,1}} & e^{i\theta_{2,1}} \\ 0 & 0 \end{bmatrix} = \begin{bmatrix} u_1 i e^{i\theta_{2,1}} & 1 + u_1 i r_{2,1} e^{-i\theta_1} \\ 0 & 0 \end{bmatrix}. \quad (3.25)$$

Equation (3.25) holds for  $u_1 = u_2$  and  $e^{i\theta_{2,1}} = 1 + u_1 i r_{2,1} e^{-i\theta_1}$ . If  $u_1 \neq 0$ , the latter condition is equivalent to  $r_{2,1} + u_1^{-1} i (e^{i\theta_2} - e^{i\theta_1}) = 0$ . Two relative equilibria that satisfy these conditions are (i)  $u_1 = u_2 = 0$  and  $\theta_{1,2} = 0$ ; and (ii)  $u_1 = u_2 = \omega_0 \neq 0$  and  $c_{1,2} \triangleq c_1 - c_2 = 0$ , where the center  $c_k$  is defined in (3.15). These two relative equilibria correspond to a parallel formation and a circular formation, respectively. More generally, the following proposition holds [127, Proposition 4].

**Proposition 3.9. Relative equilibria of the particle model** *Let  $j, k \in \mathcal{N}$ . On the collision-free configuration space  $\{SE(2)^N \mid r_{j,k} \neq 0 \ \forall j \neq k\}$ , relative equilibria of the closed-loop particle model (3.5) with shape control  $\mathbf{u}$  satisfy  $u_1 = u_2 = \dots = u_N$  and either: (a)  $u_1 = u_2 = \dots = u_N = 0$ , in which case relative equilibria are parallel formations; or (b)  $u_1 = u_2 = \dots = u_N \neq 0$ , in which case relative equilibria are circular formations.*

### 3.3 Interaction Networks and Graph Theory

In the previous section we describe the steering control restrictions that enable the closed-loop particle and phase models to evolve on a reduced shape space. In this section, we describe the steering control restrictions that enable the closed-loop particle and phase models to accurately reflect (limited) interaction between particles. Particle interaction induces (or is limited by) a particle interaction network that we describe by a *time-varying* and *directed graph*. For general graph theory references, see, for example [26, 49, 73].

**Definition 3.10. Interaction network** *Let  $j, k \in \mathcal{N}$ . An interaction network is described by the graph  $G(t) \triangleq (\mathcal{N}, E(t))$ , where  $E(t) \subset \mathcal{N} \times \mathcal{N}$  is a set of ordered pairs  $(j, k)$ ,  $j \neq k$ . Each node  $k$  in the graph is identified with a particle or phase. Each edge  $(j, k)$  in the graph represents the directed flow from the tail  $j$  to the head  $k$  of information used to compute the steering control  $u_k$  at time  $t$ .*

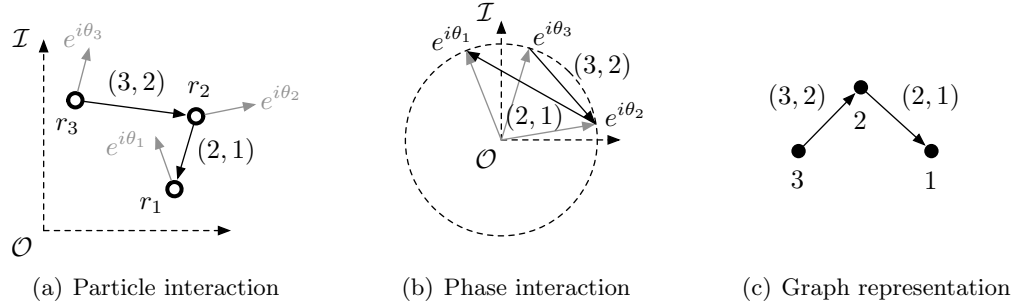


Figure 3.5: Interaction network. An interaction network is shown at time  $t$  for  $N = 3$  with graph  $G(t) = (\{1, 2, 3\}, \{(2, 1), (3, 2)\})$ , which contains a directed edge from node 2 to node 1 and another from node 3 to node 2.

We illustrate the graph representation of the interaction network in the complex plane. In the particle model, the ordered pair  $(j, k)$  corresponds to the relative position  $r_{k,j}$ . In the phase model, the ordered pair  $(j, k)$  corresponds to the relative phasor  $e^{i\theta_k} - e^{i\theta_j}$ . See Figure 3.5 for an illustration of an interaction network for  $N = 3$  with graph  $G(t) = (\{1, 2, 3\}, \{(2, 1), (3, 2)\})$ . This notation means that, between the three nodes  $k = 1, 2, 3$  there is one directed edge from node 2 to node 1 and another from node 3 to node 2.

If  $(j, k) \in E(t)$ , then node  $j$  is a *neighbor* of node  $k$  at time  $t$ . The set  $\mathcal{N}_k(t) \triangleq \{j \mid (j, k) \in E(t)\}$  contains the neighbors of node  $k$  at time  $t$ . The number of neighbors of node  $k$  at  $t$  is the cardinality  $|\mathcal{N}_k(t)|$ . Graph  $G(t)$  is *undirected* if, for all  $t$ ,  $j$  is a neighbor of  $k$  if and only if  $k$  is a neighbor of  $j$ . Graph  $G(t)$  is *time-invariant* if  $E(t_1) = E(t_2)$  for all  $t_1$  and  $t_2$  and we write  $G(t) = G$  and  $E(t) = E$ , *etc.* A *complete* graph is an undirected and time-invariant graph in which every pair of nodes is connected, that is,  $(j, k) \in E$  for all  $j, k \in \mathcal{N}$ .

We define the connectivity of an interaction network as follows. A *path* is an ordered sequence of distinct edges in which the head of every edge in the sequence is the tail of the next edge, except for the head of the last edge in the sequence, which is arbitrary. For example, let  $(j, k), (k, l), (l, m) \in E(t)$ , then  $\{(j, k), (k, l), (l, m)\}$  is a path in  $E(t)$  from node  $j$  to node  $m$  through nodes  $k$  and  $l$ . If there is a path from one node (the *root*) to every other node in a graph, then the graph is *rooted*. This leads to the following definition.

**Definition 3.11. Graph connectivity** Consider a graph  $G(t) = (\mathcal{N}, E(t))$ . Assume that  $E(t)$  is piecewise constant over finite lengths of time. Graph  $G(t)$  is strongly connected if and only if there is a path in  $E(t)$  between every pair of distinct nodes for all  $t$ . Graph  $G(t)$  is uniformly connected if and only if there is a bounded time  $T > 0$  such that the graph  $\bar{G}(t) \triangleq (\mathcal{N}, \bigcup_{\tau \in [t, t+T]} E(\tau))$  is rooted for all  $t$ . Graph  $G(t)$  is uniformly connected to a single node if and only if it is uniformly connected and there exists a  $k \in \mathcal{N}$  such that node  $k$  is the root of  $\bar{G}(t)$  for all  $t$ .

Note, a graph is *weakly* connected if and only if there is an edge sequence that does not necessarily obey the edge directions between every pair of distinct nodes. Weak and strong connectivity are identical for undirected graphs. A strongly connected, undirected graph is called *connected*. Note, if graph  $G$  is time-invariant and strongly connected, then  $G$  is uniformly connected to a single node.

We have the following matrix representation of the interaction network.

**Definition 3.12. Graph Laplacian** Let  $\mathcal{N}_k$  denote the neighbors of  $k$  in graph  $G(t) = (\mathcal{N}, E(t))$ . The Laplacian matrix  $L(t) \triangleq [l_{kj}(t)] \in \mathbb{R}^{N \times N}$  of  $G(t)$  has components

$$l_{kj}(t) = \begin{cases} -1, & j \in \mathcal{N}_k(t), \\ |\mathcal{N}_k(t)|, & j = k, \\ 0, & \text{otherwise.} \end{cases} \quad (3.26)$$

For example, consider the special case of *all-to-all* interaction, which means that the interaction network is described by a complete graph. In this case, the Laplacian matrix is  $L = NP$ , where

$$P \triangleq \text{diag}\{\mathbf{1}\} - \frac{1}{N} \mathbf{1}\mathbf{1}^T = \frac{1}{N} \begin{bmatrix} N-1 & -1 & \cdots & -1 \\ -1 & N-1 & \cdots & -1 \\ \vdots & & \ddots & \\ -1 & \cdots & -1 & N-1 \end{bmatrix} \quad (3.27)$$

is a symmetric *projection matrix* [170, pp. 386-388]. That is,  $P = P^T$  and  $P^2 = P$ . The matrix  $P$  has only two distinct eigenvalues: zero, which has multiplicity one, and one, which has multiplicity  $N - 1$ . The eigenvector associated to the eigenvalue zero is  $\mathbf{1}$ . We have

$P\mathbf{1} = \mathbf{1}^T P = \mathbf{0}$  for  $\mathbf{0} = (0, \dots, 0)^T \in \mathbb{R}^N$ , which means  $P$  projects from  $\mathbb{C}^N$  to the subspace complementary to the space spanned by  $\mathbf{1}$ .

By inspection of (3.26), we observe that  $L(t)$  is symmetric if and only if  $G(t)$  is undirected. Also, by inspection, the Laplacian has zero row sums, which implies that the vector  $\mathbf{1}$  is in the kernel of  $L(t)$ , that is,  $L(t)\mathbf{1} = \mathbf{0}$  for all  $t$ . We have  $\sum_{j=1, j \neq k}^N |l_{kj}(t)| = l_{kk}(t) \geq 0$ , which implies by the Gershgorin circle theorem [116, Theorem 6.1.1] that all of the eigenvalues of  $L(t)$  other than zero have positive real part. Consequently, if  $G(t)$  is undirected, then  $L(t)$  is positive semidefinite. If  $G(t)$  is strongly connected, then the zero eigenvalue of  $L(t)$  is simple [192, Theorem 1]. For additional spectral properties of the Laplacian, see, for example, [173]. If  $L(t)$  has zero column sums then the number of edges in  $E(t)$  with head  $k$  equals the number of edges with tail  $k$  and we call  $G(t)$  *balanced*. Balanced graph Laplacians satisfy  $L(t) + L^T(t) \geq 0$  [174, Proposition 1]. Every undirected graph is balanced.

If  $G(t) = (\mathcal{N}, E(t))$  is undirected, then the Laplacian  $L(t)$  factors into the product of a non-square matrix  $B(t)$  and its transpose, that is  $L(t) = B(t)B(t)^T = L(t)^T$  [93, p. 279]. The matrix  $B(t)$  is called the *incidence matrix* of  $G(t)$ . The incidence matrix has  $N$  rows and  $|E(t)|$  columns, where  $|E(t)|$  is the edge set cardinality. Each column of  $B(t)$  corresponds to an edge  $(j, k) \in E(t)$  in the following way: entry  $j$  is  $-1$ , entry  $k$  is  $+1$ , and all of the other entries are zero. Note that the vector  $B(t)^T \mathbf{r}$  contains all of the relative positions  $r_{k,j}$  such that  $(j, k) \in E(t)$ .

A relevant generalization of the complete graph is the *circulant graph*. Graph  $G$  is circulant if and only if  $L$  is a circulant matrix, that is,  $L$  is defined completely by its first row. If  $L$  is circulant then every row other than the first is equal to the last entry of the previous row followed by the first  $N - 1$  entries of the previous row. Let  $L_k$  denote the  $k$ th row of a graph Laplacian at time  $t$ . An example of a circulant graph is the time-invariant and undirected graph with  $L_1 = (1, 0, -1, 0)$  shown in Figure 3.6(a). The complete graph is a circulant graph with  $L_1 = (N - 1, -1, \dots, -1)$  (see Figure 3.6(b)). A *cycle* is a path in which the head of the last edge is equal to the tail of the first edge. The *cyclic graph*, which

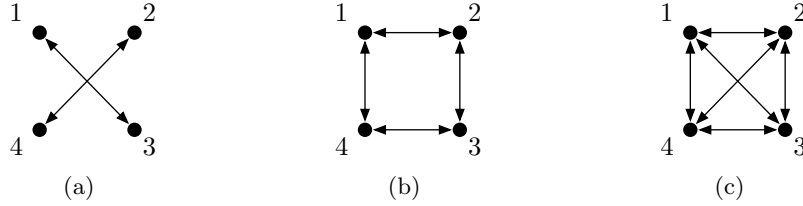


Figure 3.6: Circulant graphs. Three undirected circulant graphs for  $N = 4$ . The graph in (b) is a cycle; the graph in (c) is complete. Only (b) and (c) are connected.

contains one cycle through all of its nodes, is a circulant graph with  $L_1 = (2, -1, 0, \dots, 0, 1)$  (see Figure 3.6(c)). We refer to an interaction network described by a cyclic graph as a *ring*. Note cyclic graphs are balanced because each node has exactly one incoming edge and one outgoing edge. Cyclic pursuit is type of rendezvous problem in which agents have a directed ring interaction network [155, 163, 250]. Circulant graphs have been studied in the context of oscillator synchrony [209, 226], formation control [162, 225], and network reliability [30].

Circulant graphs play an important role in stabilization of symmetric phase patterns with time-invariant and undirected interaction, described in Chapter 6. This is because circulant graph Laplacians are circulant matrices, which have the following spectral property: every circulant matrix is diagonalized by the discrete Fourier transform matrix [60, Theorem 3.2.2], [98, p. 187]. We formalize this statement in the following proposition [241, Lemma 1].

**Proposition 3.13. Eigenvectors of circulant graph Laplacians** *Let  $L$  be the Laplacian of an undirected circulant graph  $G = (\mathcal{N}, E)$ . Set  $\phi_k = \frac{2\pi}{N}(k - 1)$  for  $k \in \mathcal{N}$ . The vectors*

$$\mathbf{f}^{(l)} \triangleq e^{i\phi(l-1)}, \quad l \in \mathcal{N}, \quad (3.28)$$

*define a basis of  $N$  orthogonal eigenvectors of  $L$ . The unitary matrix  $F$  whose columns are the  $N$  normalized eigenvectors  $\frac{1}{\sqrt{N}}\mathbf{f}^{(l)}$  diagonalizes  $L$ , that is,  $L = F\Lambda F^*$ , where  $\Lambda = \text{diag}\{\lambda_1, \dots, \lambda_N\} \geq 0$  is the (real) diagonal matrix of eigenvalues of  $L$ .*

A meaningful class of time-varying and directed interaction networks is generated by local interaction between neighboring particles. This leads to the following definition.

**Definition 3.14. Proximity-based interaction networks** *A network in which particle interaction occurs only between particles in proximity to one another is called a proximity-based interaction network.*

We give several examples of proximity-based interaction and the network each generates. One type of proximity-based interaction occurs between two particles  $j$  and  $k$  if particle  $j$  is in the  $k$ th particle's *perceptual zone*, which is a set points in  $\mathbb{C}$  (not necessarily containing  $r_k$ ). For example, if the perceptual zone of the  $k$ th particle at time  $t$  is a circle of radius  $\rho_k(t) > 0$  centered at  $\mathbf{r}_k(t)$ , then particle  $j$  is a neighbor of  $k$  at time  $t$  if and only if the relative position  $\mathbf{r}_{k,j}(t)$  satisfies  $\|\mathbf{r}_{k,j}(t)\| \leq \rho_k(t)$ . We refer to interaction networks with this type of interaction as *zonal* interaction networks. Another type of proximity-based interaction occurs between each particle  $k$  and up to  $|\mathcal{N}_k|^{\max}$  of its nearest neighbors. We refer to interaction networks with this type of interaction as *nearest-neighbor* interaction networks. The intersection of zonal and nearest-neighbor interaction generates a third type of proximity-based interaction network in which interaction occurs between each particle  $k$  and up to  $|\mathcal{N}_k|^{\max}$  nearest neighbors contained in the perceptual zone of particle  $k$ . Interactions weighted by distance between individuals is studied in, for example, [57].

The interaction network and the corresponding graph  $G(t)$  impact the design of steering control of the particle and phase models. In fact, we classify the steering control algorithms according to three types of interaction networks: (i) all-to-all interaction, (ii) undirected and time-invariant interaction, and (iii) general interaction. We refer to the corresponding steering algorithms as all-to-all, Laplacian, and dynamic, respectively. In Chapters 4–6, we describe feedback control algorithms that stabilize synchronized, balanced, and symmetric phase patterns. We also describe algorithms that stabilize arbitrary, synchronized, balanced, and symmetric circular formations. A Venn diagram of these algorithms and the requirements imposed on the interaction network appears in Figure 3.7. For each algorithm, the approach we take for all-to-all interaction provides a roadmap for the approach to limited interaction.

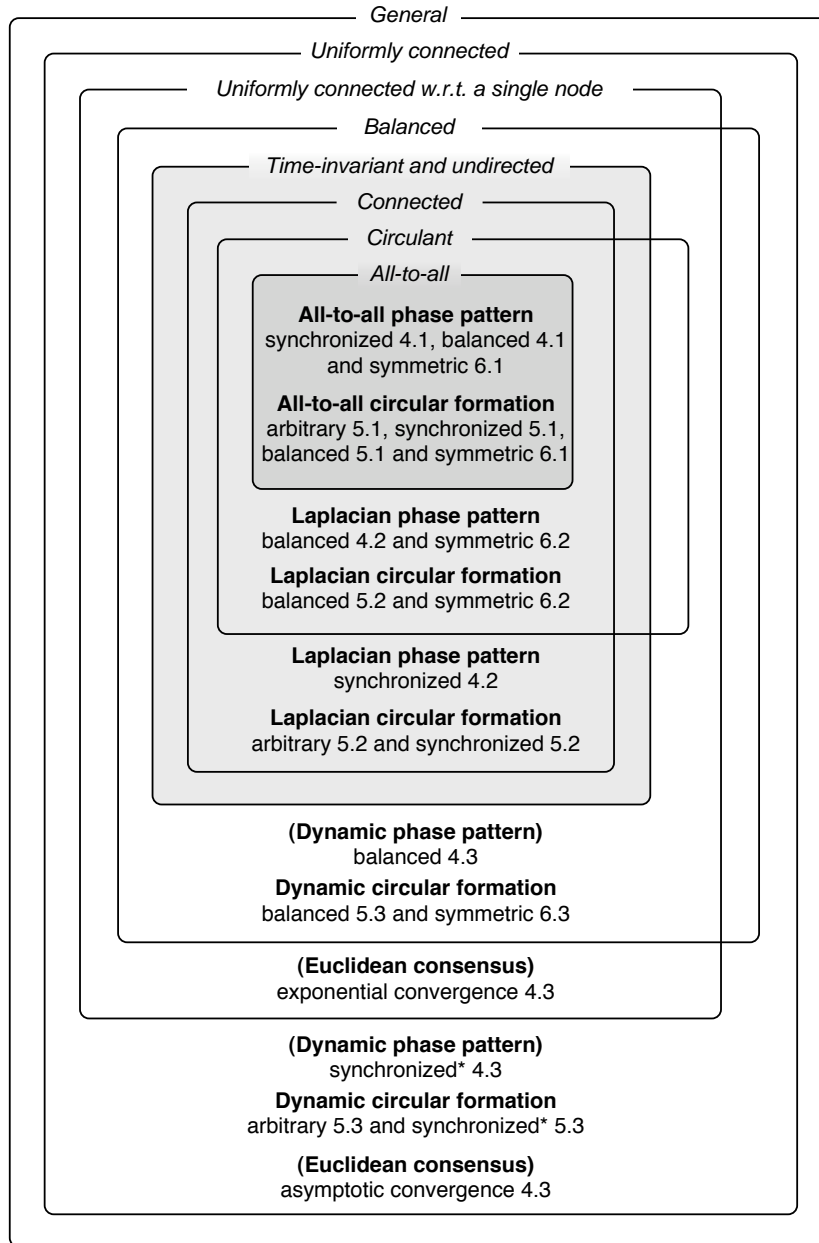


Figure 3.7: Results by level of interaction. A Venn diagram of the feedback control algorithms described in Chapters 4, 5, and 6 (algorithms are labeled with chapter and section numbers). The algorithm position indicates the requirements imposed on the interaction network. Each of the next three chapters describes all-to-all control algorithms for all-to-all interaction (gray set), Laplacian control algorithms for time-invariant and undirected interaction (light gray set), and dynamic control algorithms for general interaction (white set). The design of algorithms contained in parenthesis (·) did not involve the author; these algorithms are important to the design of the dynamic circular formation algorithms and are summarized here. The dynamic control algorithms marked with an asterisk \* converge with probability one; convergence is guaranteed if the interaction network is balanced.

## Chapter 4

# Phase Synchronization and Balancing

We now consider the design of steering controls that stabilize synchronized and balanced phase arrangements. Recall that the phase model (3.6) describes the first-order dynamics  $\dot{\theta}_k = u_k(\boldsymbol{\theta})$  of  $N$  phases on the  $N$ -torus  $\mathbb{T}^N$ . We describe shape controls  $u_k(\theta_{1,k}, \dots, \theta_{N,k})$  that preserve the rotation symmetry of the closed-loop phase model and adhere to the limitations of the interaction network. We start in Section 4.1 by considering the phase model with all-to-all interaction, that is, the interaction network is described by a time-invariant and complete graph  $G$ . In Section 4.2, we extend the control design to time-invariant and undirected interaction networks that are not all-to-all; in this case, the Laplacian  $L$  of  $G$  plays a significant role. In Section 4.3, we describe a control algorithm for time-varying and directed interactions that recovers the all-to-all results.

### 4.1 All-to-all Interaction

Let  $G = (\mathcal{N}, E)$  be the complete graph that describes an all-to-all interaction network. The set of neighbors of node  $k$  of graph  $G$  is  $\mathcal{N}_k = \{j \mid j \in \mathcal{N}, j \neq k\}$ . Consequently, we seek a shape control of the form  $u_k = u_k(\theta_{1,k}, \dots, \theta_{N,k})$ . That is, the control of phase  $\theta_k$  may

depend on the relative phase of every other phase  $j \neq k$ . This suggests a control design that depends on average quantities.

Consider the *all-to-all phase potential*

$$U(\boldsymbol{\theta}) \triangleq \frac{N}{2} |p_\theta|^2 = \frac{1}{2N} \left| \sum_{j=1}^N e^{i\theta_j} \right|^2, \quad (4.1)$$

which reaches its minimum when  $p_\theta = 0$  (balancing) and its maximum  $N/2$  when  $|p_\theta| = 1$  (synchronization). Let  $\theta_0 \in \mathbb{T}$ . The potential  $U(\boldsymbol{\theta})$  is invariant to rigid rotation of all of the phases since  $U(\boldsymbol{\theta} + \theta_0 \mathbf{1}) = (N/2) |p_\theta e^{i\theta_0}|^2 = U(\boldsymbol{\theta})$ . Let  $\nabla U \triangleq (\frac{\partial U}{\partial \theta_1}, \dots, \frac{\partial U}{\partial \theta_N})^T$  denote the gradient of  $U(\boldsymbol{\theta})$ . The  $k$ th component of  $\nabla U$  is

$$\begin{aligned} \frac{\partial U}{\partial \theta_k} &= \frac{N}{2} (\langle \frac{\partial p_\theta}{\partial \theta_k}, p_\theta \rangle + \langle p_\theta, \frac{\partial p_\theta}{\partial \theta_k} \rangle) = \langle i e^{i\theta_k}, p_\theta \rangle \\ &= \frac{1}{N} \sum_{j=1}^N \operatorname{Re}\{-i e^{i\theta_j, k}\} = \frac{1}{N} \sum_{j=1}^N \sin \theta_{j, k}. \end{aligned} \quad (4.2)$$

Critical points of  $U(\boldsymbol{\theta})$  satisfy  $\nabla U = 0$ . For example, the global extrema of phase synchronization and phase balancing are critical points. We characterize critical points that are not synchronized or balanced as follows [243, Theorem 1].

**Lemma 4.1. Critical points of the all-to-all phase potential** *Critical points of the all-to-all phase potential  $U(\boldsymbol{\theta})$  defined in (4.1), where  $0 < |p_\theta| < 1$ , are isolated in the phase shape space  $\mathbb{T}^N/\mathbb{T}$  and are saddle points of  $U(\boldsymbol{\theta})$ .*

*Proof.* Let  $\bar{\boldsymbol{\theta}} \in \mathbb{T}^N$  be a critical point of  $U(\boldsymbol{\theta})$  with  $0 < |\bar{p}_\theta| < 1$ , where  $\bar{p}_\theta \triangleq p(e^{i\bar{\boldsymbol{\theta}}})$ . We have  $\frac{\partial U}{\partial \theta_k} = \langle i e^{i\bar{\theta}_k}, \bar{p}_\theta \rangle = 0$  for all  $k \in \mathcal{N}$ , which implies  $\bar{p}_\theta = \pm |\bar{p}_\theta| e^{i\bar{\theta}_k}$ . We observe that the phases  $\bar{\theta}_k$  necessarily lie in one of two clusters that are on opposite sides of the unit circle; all of the phases within each cluster are identical. The clusters have an unequal number of phases since  $\bar{\boldsymbol{\theta}}$  is not balanced and each cluster has at least one phase since  $\bar{\boldsymbol{\theta}}$  is not synchronized. If  $\bar{\theta}_k$  is in the bigger cluster then  $\langle e^{i\bar{\theta}_k}, \bar{p}_\theta \rangle > 0$  and if  $\bar{\theta}_k$  is in the smaller cluster then  $\langle e^{i\bar{\theta}_k}, \bar{p}_\theta \rangle < 0$ . The modulus  $|\bar{p}_\theta|$  satisfies  $|\bar{p}_\theta| \geq 1/N$ , where  $|\bar{p}_\theta| = 1/N$  if and only if  $N$  is odd and the number of phases in each cluster differs by one.

First we prove that  $\bar{\boldsymbol{\theta}}$  is isolated in the phase shape space. Let  $\boldsymbol{\varphi} \triangleq (\varphi_1, \dots, \varphi_{N-1})^T \in \mathbb{T}^N/\mathbb{T}$  denote coordinates in shape space, where  $\varphi_j \triangleq \theta_{k+1, k} = \theta_{k+1} - \theta_k$ . Let  $\bar{\boldsymbol{\varphi}} \in \mathbb{T}^N/\mathbb{T}$

be the point that corresponds to  $\bar{\theta}$ . We observe  $\bar{\varphi}_j \in \{0, \pi\}$  for all  $j \in \{1, \dots, N-1\}$ , that is,  $\bar{\varphi}_k = 0$  or  $\bar{\varphi}_k = \pi$ . Let  $\Phi \triangleq \{\varphi \mid |\varphi_j - \bar{\varphi}_j| < \epsilon, j = 1, \dots, N-1\}$  define an open neighborhood about  $\bar{\varphi}$ . If  $\epsilon < \pi$ , then the neighborhood  $\Phi$  contains only one critical point, which is  $\bar{\varphi}$ . This completes the first part of the proof.

Let  $\delta\theta \triangleq (\delta\theta_1, \dots, \delta\theta_N)^T \in \mathbb{R}^N$  be a small variation of the vector  $\theta$ . The Taylor series expansion of  $U(\theta)$  about the critical point  $\bar{\theta}$  is

$$U(\bar{\theta} + \delta\theta) = U(\bar{\theta}) + \underbrace{(\nabla U(\bar{\theta}))^T}_0 \delta\theta + \delta\theta^T H(\bar{\theta}) \delta\theta + O(\|\delta\theta\|^3), \quad (4.3)$$

where  $H(\bar{\theta}) = [h_{kj}(\bar{\theta})]$  is the Hessian of  $U(\theta)$  evaluated at  $\bar{\theta}$ . We find the components  $h_{kj}(\theta)$  of the Hessian  $H(\theta)$  by evaluating the second derivatives  $\frac{\partial^2 U}{\partial\theta_k \partial\theta_j}$  for all pairs  $j$  and  $k$ , which yields

$$h_{kj}(\theta) \triangleq \begin{cases} \frac{1}{N} \langle e^{i\theta_k}, e^{i\theta_j} \rangle, & j \neq k, \\ \frac{1}{N} - \langle e^{i\theta_k}, p_\theta \rangle, & j = k. \end{cases} \quad (4.4)$$

We prove that  $\bar{\theta}$  is a saddle point by showing that  $\delta U(\bar{\theta}) \triangleq U(\bar{\theta} + \delta\theta) - U(\bar{\theta})$  can be positive or negative. Consider the variation  $\delta\theta = (\delta\theta_1, \delta\theta_2, 0, \dots, 0)^T$ , which implies

$$\delta U(\bar{\theta}) = h_{11}(\bar{\theta}) \delta\theta_1^2 + (h_{12}(\bar{\theta}) + h_{21}(\bar{\theta})) \delta\theta_1 \delta\theta_2 + h_{22}(\bar{\theta}) \delta\theta_2^2. \quad (4.5)$$

First, consider the case  $|\bar{p}_\theta| > 1/N$ . In this case, set  $\delta\theta_2 = 0$ , which implies  $\delta U(\bar{\theta}) = h_{11}(\bar{\theta}) \delta\theta_1^2 = 1/N - \langle e^{i\theta_1}, \bar{p}_\theta \rangle$ . In this case, if  $\bar{\theta}_1$  is in the big cluster, then  $\delta U(\bar{\theta}) < 0$ ; otherwise, if  $\bar{\theta}_1$  is in the small cluster, then  $\delta U(\bar{\theta}) > 0$ . Next, consider the case  $|\bar{p}_\theta| = 1/N$ . In this case, assume, without loss of generality, that both  $\bar{\theta}_1$  and  $\bar{\theta}_2$  are in the big cluster, which implies  $h_{11}(\bar{\theta}) = h_{22}(\bar{\theta}) = 0$ ,  $h_{12}(\bar{\theta}) = h_{21}(\bar{\theta}) = 1/N$ , and  $\delta U(\bar{\theta}) = (2/N) \delta\theta_1 \delta\theta_2$ . In this case, if  $\delta\theta_1$  and  $\delta\theta_2$  have opposite signs, then  $\delta U(\bar{\theta}) < 0$ ; if  $\delta\theta_1$  and  $\delta\theta_2$  have the same sign, then  $\delta U(\bar{\theta}) > 0$ . This completes the proof.  $\square$

The time-derivative of  $U(\theta)$  along solutions of the phase model (3.6) is

$$\dot{U} = \sum_{j=1}^N \frac{\partial U}{\partial\theta_j} u_j = \sum_{j=1}^N \langle i e^{i\theta_j}, p_\theta \rangle u_j$$

Choosing the gradient control

$$u_k = -K \langle i e^{i\theta_k}, p_\theta \rangle, \quad (4.6)$$

yields

$$\dot{U} = -K \sum_{j=1}^N \langle i e^{i\theta_j}, p_\theta \rangle^2.$$

This leads to the following theorem, extracted from [243, Theorem 1]. This result is related to [40, Propositions 4.3.4], on gradient control of the phase model, and [40, Propositions 4.3.5], on gradient control using sinusoids.

**Theorem 4.2. All-to-all phase synchronization and balancing** *For the shape control (4.6), all of the solutions of the closed-loop phase model (3.6) converge to the critical set of the all-to-all phase potential (4.1). If  $K < 0$ , then all of the synchronized phase arrangements are asymptotically stable and all of the remaining equilibria are unstable. If  $K > 0$ , then the balanced equilibria for which  $p_\theta = 0$  are asymptotically stable and all of the remaining equilibria are unstable.*

*Proof.* The closed-loop phase model (3.6) with the shape control (4.6) evolves on the compact shape space  $\mathbb{T}^N/\mathbb{T}$  under the gradient dynamics

$$\dot{\boldsymbol{\theta}} = -K \nabla U. \quad (4.7)$$

The potential  $KU(\boldsymbol{\theta}) : \mathbb{T}^N/\mathbb{T} \rightarrow \mathbb{R}$  is a continuously differentiable function with  $\frac{d}{dt}(KU) \leq 0$  along solutions of (4.7). Let  $\Omega$  denote the set of all points in the shape space where  $\frac{d}{dt}(KU) = 0$ . Points in  $\Omega$  satisfy

$$\langle i e^{i\theta_k}, p_\theta \rangle = 0. \quad (4.8)$$

The set  $\Omega$  is invariant since the condition (4.8) implies  $\dot{\theta}_{k,j} = u_k - u_j = 0$  for all pairs  $j$  and  $k$ . By the invariance principle [131, Theorem 4.4], every solution of (4.7) approaches  $\Omega$  as  $t \rightarrow \infty$ . Comparing (4.2) and (4.8), we conclude that  $\Omega$  is the set of critical points of  $U(\boldsymbol{\theta})$ , which completes the first part of the proof.

Critical points where  $p_\theta = 0$  are global minima of  $U(\boldsymbol{\theta})$ , which implies the balanced set is asymptotically stable if  $K > 0$  and unstable if  $K < 0$ . Similarly, critical points where  $|p_\theta| = 1$  are global maxima of  $U(\boldsymbol{\theta})$ , which implies the synchronized set is asymptotically stable if  $K < 0$  and unstable if  $K > 0$ . By Lemma 4.1, all other critical points of  $U(\boldsymbol{\theta})$  are

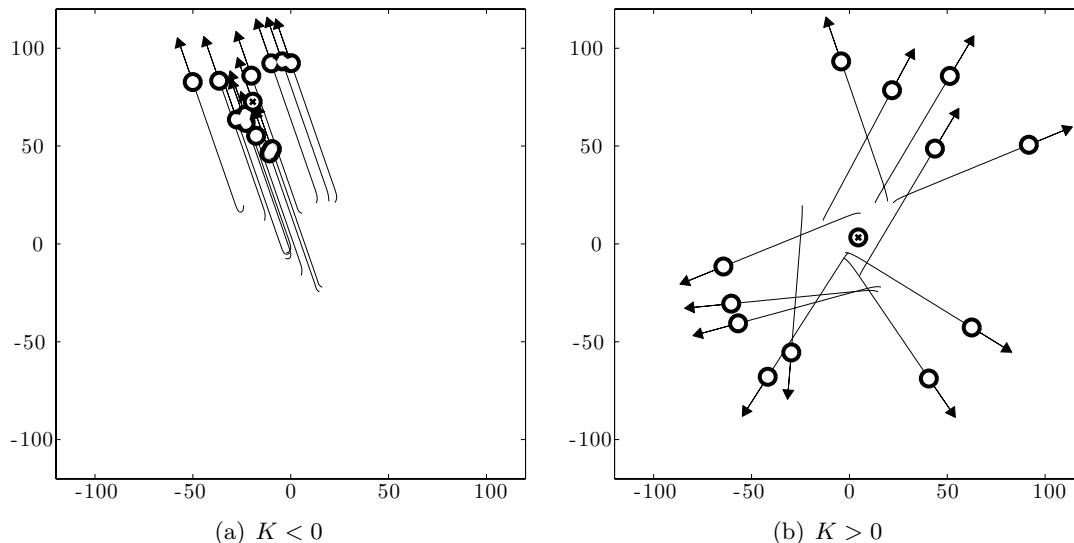


Figure 4.1: All-to-all phase control. Simulations of the closed-loop particle model with the all-to-all phase control (4.6) for  $N = 12$ . We denote the position centroid  $p_r$  by a circle marked with an x; the velocity  $\dot{p}_r$  equals the order parameter  $p_\theta$ . (a) Phase synchronization generates a parallel formation; (b) phase balancing fixes the position centroid. Only (a) is a relative equilibrium of the particle model.

isolated in the shape space and are saddle points of  $U(\boldsymbol{\theta})$ , which implies they are unstable for any  $K \neq 0$ .  $\square$

Theorem 4.2 enables control of the magnitude  $|p_\theta|$  of the order parameter. In the particle model, control of  $|p_\theta|$  corresponds to control of the speed  $|\dot{p}_r|$  of the particle position centroid. By Theorem 4.2, almost all solutions of the closed-loop particle model (3.5) under the phase control (4.6) with  $K > 0$  converge to the balanced set where the velocity of the position centroid is zero. If  $K < 0$ , then almost all solutions converge to a parallel formation, which is a relative equilibrium of the particle model. The direction of motion of the parallel formation depends on the initial conditions since (4.6) is a shape control and is invariant to rigid rotation of all of the phases. We illustrate these results with the simulations shown in Figures 4.1(a) and 4.1(b).

The control (4.6) is rotationally invariant because it is proportional to the gradient of the rotationally invariant phase potential  $U(\boldsymbol{\theta})$ . The rotational invariance of  $U(\boldsymbol{\theta})$  has another implication that is described in the following corollary. Let  $\omega_0 \in \mathbb{R}$  and consider the shape

control

$$u_k = \omega_0 - K \langle i e^{i\theta_k}, p_\theta \rangle = \omega_0 - \frac{K}{N} \sum_{j=1}^N \sin \theta_{j,k}. \quad (4.9)$$

**Corollary 4.3. All-to-all phase synchronization and balancing** *The results of Theorem 4.2 still apply if control (4.6) is replaced by (4.9).*

*Proof.* The time-derivative of  $U(\boldsymbol{\theta})$  along solutions of the closed-loop particle model with the control (4.9) is

$$\dot{U} = \sum_{j=1}^N \left( \omega_0 \langle i e^{i\theta_j}, p_\theta \rangle - K \langle i e^{i\theta_j}, p_\theta \rangle^2 \right) = \omega_0 N \underbrace{\langle i p_\theta, p_\theta \rangle}_0 - K \sum_{j=1}^N \langle i e^{i\theta_j}, p_\theta \rangle^2.$$

The remainder of the proof is identical to the proof of Theorem 4.2 since the constant  $\omega_0$  vanishes in the reduced shape space.  $\square$

Recall that the open-loop control  $\mathbf{u} = \omega_0 \mathbf{1}$ , where  $\omega_0 \neq 0$ , drives each particle around a circle of radius  $|\omega_0|^{-1}$  in a direction determined by the sign of  $\omega_0$ . The control (4.9) drives each particle around a (different) circle with a collective phase arrangement that is a critical point of  $U(\boldsymbol{\theta})$ . If  $K < 0$ , then only the set of synchronized solutions is asymptotically stable and every other equilibrium is unstable. If  $K > 0$ , then only the set of balanced solutions where  $\dot{p}_r = p_\theta = 0$  is asymptotically stable and every other equilibrium is unstable. We illustrate these results with the simulations shown in Figures 4.2(a) and 4.2(b).

The control (4.9) is a simplified version of the Kuramoto model [138] of a system phase oscillators that are sinusoidally coupled. If one interprets the constant term  $\omega_0$  as the natural frequency of each oscillator  $\theta_k$ , then all of the oscillators are identical; in the Kuramoto model, the oscillators have different natural frequencies. Another property of the Kuramoto model is all-to-all interaction. In the next section we consider a version of the Kuramoto model with identical oscillators and limited interaction.

## 4.2 Time-invariant and Undirected Interaction

The all-to-all phase control (4.6) requires an all-to-all interaction network, because one must use the relative phases  $\theta_{j,k}$  for all pairs  $j$  and  $k$  in order to compute  $u_k$ . In this

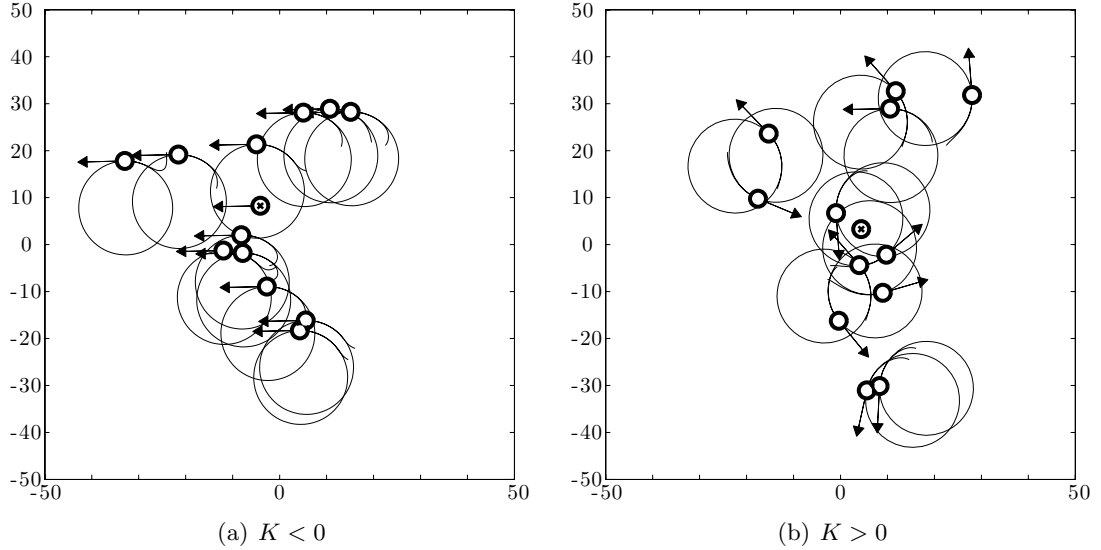


Figure 4.2: All-to-all phase control during circular motion. Simulations of the closed-loop particle model with the all-to-all phase control (4.9) for  $N = 12$  and  $\omega_0 = 0.1$ . We denote the position centroid  $p_r$  by a circle marked with an  $\times$ ; the velocity  $\dot{p}_r$  equals the order parameter  $p_\theta$ . (a) Phase synchronization in circular orbits; (b) phase balancing fixes the position centroid. Neither (a) nor (b) are relative equilibria of the particle model.

section, we consider a generalization of the all-to-all phase control methodology that enables phase synchronization and balancing with time-invariant and undirected interaction that is limited. We start by generalizing the all-to-all phase potential (4.1) using a *Laplacian quadratic form* defined as follows [169].

**Definition 4.4. Laplacian quadratic form** *Let  $L$  be the Laplacian matrix of graph  $G = (\mathcal{N}, E)$ . Let  $\mathbf{x}, \mathbf{y}, \mathbf{z} \in \mathbb{C}^N$ . The Laplacian quadratic form associated to  $L$  is*

$$Q_L(\mathbf{z}) \triangleq \langle \mathbf{z}, L\mathbf{z} \rangle, \quad (4.10)$$

where  $\langle \mathbf{x}, \mathbf{y} \rangle \triangleq \sum_{k=1}^N \langle x_k, y_k \rangle = \sum_{k=1}^N \operatorname{Re}\{x_k^* y_k\}$ .

The first part of the following lemma is based on [192, Theorem 6].

**Lemma 4.5. Properties of the Laplacian quadratic form** *If  $G$  is strongly connected and balanced, then the Laplacian quadratic form  $Q_L(\mathbf{z})$  defined in (4.10) is positive semidefinite and is zero if and only if  $\mathbf{z} = z_0 \mathbf{1}$ ,  $z_0 \in \mathbb{C}$ . Furthermore,  $Q_L(\mathbf{z})$  is invariant to the action of  $SE(2)$  on the argument  $\mathbf{z}$ .*

*Proof.* Let  $z_0 \in \mathbb{C}$  and  $\theta_0 \in \mathbb{T}$ . If  $G$  is strongly connected and balanced, then  $L\mathbf{1} = \mathbf{1}^T L = 0$ ,  $L + L^T \geq 0$ , and  $\mathbf{1}$  spans the kernel of  $L$ . To prove the first part of Proposition 4.5, we observe that

$$Q_L(\mathbf{z}) = \frac{1}{2} \underbrace{\langle \mathbf{z}, (L + L^T)\mathbf{z} \rangle}_{\geq 0} + \frac{1}{2} \underbrace{\langle \mathbf{z}, (L - L^T)\mathbf{z} \rangle}_0.$$

Let  $\mathbf{z} \mapsto e^{i\theta_0}\mathbf{z} + z_0\mathbf{1}$  denote the action of  $(z_0, \theta_0) \in SE(2)$  on  $\mathbf{z} \in \mathbb{C}^N$ . To prove the second part of the proposition, we observe that

$$\begin{aligned} Q_L(e^{i\theta_0}\mathbf{z} + z_0\mathbf{1}) &= \langle e^{i\theta_0}\mathbf{z} + z_0\mathbf{1}, L(e^{i\theta_0}\mathbf{z} + z_0\mathbf{1}) \rangle = \langle e^{i\theta_0}\mathbf{z} + z_0\mathbf{1}, e^{i\theta_0}L\mathbf{z} \rangle \\ &= \underbrace{\langle e^{i\theta_0}\mathbf{z}, e^{i\theta_0}L\mathbf{z} \rangle}_{Q_L(\mathbf{z})} + \underbrace{\langle z_0L^T\mathbf{1}, e^{i\theta_0}\mathbf{z} \rangle}_0. \end{aligned}$$

This completes the proof.  $\square$

If  $G = (\mathcal{N}, E)$  is undirected and connected, then  $L = BB^T$ . Suppose we identify node  $k$  of  $G$  with component  $z_k$  of the vector  $\mathbf{z} \in \mathbb{C}^N$  for all  $k \in \mathcal{N}$ . In this case,

$$Q_L(\mathbf{z}) = \langle B^T\mathbf{z}, B^T\mathbf{z} \rangle = \sum_{(j,k) \in E} |z_j - z_k|^2. \quad (4.11)$$

Consequently, we interpret the Laplacian quadratic form of an undirected and connected graph as the sum of the squared length of the graph edges.

The Laplacian quadratic form leads naturally to a generalization of the all-to-all phase potential (4.1) for limited, time-invariant interaction. Note the all-to-all phase potential can be written

$$U(\boldsymbol{\theta}) = \frac{N}{2} \langle p_\theta, p_\theta \rangle = \frac{1}{2N} \langle \mathbf{1}^T e^{i\boldsymbol{\theta}}, \mathbf{1}^T e^{i\boldsymbol{\theta}} \rangle = \frac{1}{2} \langle e^{i\boldsymbol{\theta}}, \frac{1}{N} \mathbf{1}\mathbf{1}^T e^{i\boldsymbol{\theta}} \rangle. \quad (4.12)$$

Compare this expression to the *Laplacian phase potential* [240]

$$W_L(\boldsymbol{\theta}) \triangleq \frac{1}{2} Q_L(e^{i\boldsymbol{\theta}}) = \frac{1}{2} \langle e^{i\boldsymbol{\theta}}, L e^{i\boldsymbol{\theta}} \rangle. \quad (4.13)$$

We see that the term  $(\mathbf{1}\mathbf{1}^T)/N = \text{diag}\{\mathbf{1}\} - P$  in (4.12) has been replaced by  $L$  in (4.13), where  $P$  is the projection matrix defined in (3.27) and  $L$  is the graph Laplacian.

The Laplacian phase potential  $W_L(\boldsymbol{\theta})$  preserves many of the same properties as  $U(\boldsymbol{\theta})$ , and permits us to define a gradient control law that respects limitations in particle interaction. If  $G$  is either undirected or directed, then the Laplacian phase potential (4.13) is positive semidefinite, since

$$W_L(\boldsymbol{\theta}) = \sum_{k=1}^N \langle e^{i\theta_k}, |\mathcal{N}_k| e^{i\theta_k} - \sum_{j \in \mathcal{N}_k} e^{i\theta_j} \rangle = \sum_{k=1}^N \underbrace{\left( |\mathcal{N}_k| - \sum_{j \in \mathcal{N}_k} \langle e^{i\theta_k}, e^{i\theta_j} \rangle \right)}_{\geq 0}.$$

If  $\boldsymbol{\theta}$  is synchronized, that is, if  $e^{i\boldsymbol{\theta}} = e^{i\theta_0} \mathbf{1}$  for any  $\theta_0 \in \mathbb{T}$ , then  $W_L(\boldsymbol{\theta}) = 0$ . If  $G$  is strongly connected, then  $W_L(\boldsymbol{\theta}) = 0$  if and only if  $\boldsymbol{\theta}$  is synchronized. If  $G$  is strongly connected and balanced, then the Laplacian phase potential is invariant to rotation by  $\theta_0$  of all of the phases by Lemma 4.5.

If  $G$  is undirected, then  $k \in \mathcal{N}_j$  if and only if  $j \in \mathcal{N}_k$  and the  $k$ th component of the gradient of  $W_L(\boldsymbol{\theta})$ ,  $k \in \mathcal{N}$ , is

$$\begin{aligned} \frac{\partial W_L}{\partial \theta_k} &= \frac{1}{2} \sum_{j=1}^N \frac{\partial}{\partial \theta_k} \langle e^{i\theta_j}, L_j e^{i\boldsymbol{\theta}} \rangle = \frac{1}{2} \left( \langle i e^{i\theta_k}, L_k e^{i\boldsymbol{\theta}} \rangle + \sum_{j=1}^N \langle e^{i\theta_j}, \frac{\partial}{\partial \theta_k} (L_j e^{i\boldsymbol{\theta}}) \rangle \right) \\ &= \frac{1}{2} \left( \langle i e^{i\theta_k}, L_k e^{i\boldsymbol{\theta}} \rangle - \underbrace{\sum_{j \in \mathcal{N}_k} \langle e^{i\theta_j}, i e^{i\theta_k} \rangle}_{-\langle i e^{i\theta_k}, L_k e^{i\boldsymbol{\theta}} \rangle} \right) = \langle i e^{i\theta_k}, L_k e^{i\boldsymbol{\theta}} \rangle = \sum_{j \in \mathcal{N}_k} \sin \theta_{k,j}. \end{aligned} \quad (4.14)$$

If  $G$  is undirected and connected, we see by (4.11) that  $W_L(\boldsymbol{\theta})$  is maximum in the set of phase arrangements that maximizes the total length of all of the graph edges. By comparing (4.14) with (4.2), we observe that if  $G$  is complete, then the critical points of  $W_L(\boldsymbol{\theta})$  are identical to the critical points of the all-to-all phase potential  $U(\boldsymbol{\theta})$ . The Laplacian of a complete graph is  $NP$ , where  $P$  is the projection matrix defined in (3.27). We have

$$W_{NP}(\boldsymbol{\theta}) = \frac{N}{2} \sum_{j=1}^N \langle e^{i\theta_j}, P_j e^{i\boldsymbol{\theta}} \rangle = \frac{N}{2} \sum_{j=1}^N \langle e^{i\theta_j}, e^{i\theta_j} - p_{\boldsymbol{\theta}} \rangle = \frac{N}{2} (N - N|p_{\boldsymbol{\theta}}|^2) = N \left( \frac{N}{2} - U(\boldsymbol{\theta}) \right).$$

Thus, if  $G$  is complete, then the minimum of  $U(\boldsymbol{\theta})$  (balancing) corresponds to the maximum of  $W_L(\boldsymbol{\theta})$ . If  $G$  is undirected and connected, we have the following partial characterization of the critical points of  $W_L(\boldsymbol{\theta})$ .

**Lemma 4.6. Critical points of the Laplacian phase potential** *Let  $L$  be the Laplacian of an undirected and connected graph  $G = (\mathcal{N}, E)$ . Consider the Laplacian phase potential*

$W_L(\boldsymbol{\theta})$  defined in (4.13). If  $e^{i\boldsymbol{\theta}}$  is an eigenvector of  $L$ , then  $\boldsymbol{\theta}$  is a critical point of  $W_L(\boldsymbol{\theta})$  and  $\boldsymbol{\theta}$  is either synchronized or balanced. The potential  $W_L(\boldsymbol{\theta})$  reaches its global minimum if and only if  $\boldsymbol{\theta}$  is synchronized. If  $G$  is circulant, then  $W_L(\boldsymbol{\theta})$  reaches its global maximum in a balanced phase arrangement.

*Proof.* Let  $e^{i\bar{\boldsymbol{\theta}}}$  be an eigenvector of  $L$  with eigenvalue  $\lambda \in \mathbb{R}$ . Then  $Le^{i\bar{\boldsymbol{\theta}}} = \lambda e^{i\bar{\boldsymbol{\theta}}}$  and

$$\left. \frac{\partial W_L}{\partial \theta_k} \right|_{\boldsymbol{\theta}=\bar{\boldsymbol{\theta}}} = \langle ie^{i\bar{\theta}_k}, L_k e^{i\bar{\boldsymbol{\theta}}} \rangle = \lambda \langle ie^{i\bar{\theta}_k}, e^{i\bar{\theta}_k} \rangle = 0,$$

which implies that  $\bar{\boldsymbol{\theta}}$  is a critical point of  $W_L(\boldsymbol{\theta})$ . Since graph  $G$  is undirected, then the Laplacian  $L$  is Hermitian and the eigenvectors of  $L$  associated with distinct eigenvalues are mutually orthogonal. Since  $G$  is also connected, then  $\mathbf{1}$  spans the kernel of  $L$ . Therefore, the eigenvector associated to  $\lambda = 0$  is  $e^{i\bar{\boldsymbol{\theta}}} = e^{i\theta_0} \mathbf{1}$  for any  $\theta_0 \in \mathbb{T}$ , which implies  $\bar{\boldsymbol{\theta}}$  is synchronized. All of the remaining eigenvectors satisfy  $\mathbf{1}^T e^{i\bar{\boldsymbol{\theta}}} = 0$ , which implies that  $\bar{\boldsymbol{\theta}}$  is balanced.

By Proposition 3.13, a sufficient condition for  $L$  to have eigenvectors of the form  $e^{i\boldsymbol{\theta}}$  is that  $G$  be a circulant graph. If  $G$  is circulant, then, using the notation of Proposition 3.13, we have  $L = F\Lambda F^*$ , where  $F$  is unitary and  $\Lambda$  is the diagonal matrix whose entries are all of the eigenvalues of  $L$ . Let  $\lambda_{\max} \triangleq \max_{k \in \mathcal{N}} \lambda_k > 0$  be the maximum eigenvalue of  $L$ . We find

$$W_L(\bar{\boldsymbol{\theta}}) = \frac{1}{2} \langle F^* e^{i\bar{\boldsymbol{\theta}}}, \Lambda F^* e^{i\bar{\boldsymbol{\theta}}} \rangle \leq \frac{1}{2} \lambda_{\max} \|F^* e^{i\bar{\boldsymbol{\theta}}}\| = \frac{\sqrt{N}}{2} \lambda_{\max}.$$

The upper bound  $(\sqrt{N}/2)\lambda_{\max}$  is attained if  $e^{i\bar{\boldsymbol{\theta}}}$  is the eigenvector of  $L$  associated to the maximum eigenvalue. Since  $e^{i\bar{\boldsymbol{\theta}}}$  is orthogonal to  $\mathbf{1}$ , the phase arrangement  $\bar{\boldsymbol{\theta}}$  that maximizes  $W_L(\boldsymbol{\theta})$  must be balanced.  $\square$

If  $G$  is undirected, taking the time-derivative of  $W_L(\boldsymbol{\theta})$  along solutions of the phase model (3.6) yields

$$\dot{W}_L = \sum_{j=1}^N \frac{\partial W_L}{\partial \theta_j} u_j = \sum_{j=1}^N \langle ie^{i\theta_j}, L_j e^{i\boldsymbol{\theta}} \rangle u_j.$$

Choosing the gradient control

$$u_k = K \langle ie^{i\theta_k}, L_k e^{i\boldsymbol{\theta}} \rangle \quad (4.15)$$

yields

$$\dot{W}_L = K \sum_{j=1}^N \langle ie^{i\theta_j}, L_j e^{i\theta} \rangle^2,$$

which leads to the following result [241, Theorem 2].

**Theorem 4.7. Laplacian phase synchronization and balancing** *Let  $L$  be the Laplacian of an undirected and connected graph  $G = (\mathcal{N}, E)$ . For the shape control (4.15), all of the solutions of the closed-loop phase model (3.6) converge to the critical set of the Laplacian phase potential  $W_L(\boldsymbol{\theta})$  defined in (4.13). If  $K < 0$ , then all of the synchronized phase arrangements are asymptotically stable. If  $K > 0$ , then all of the synchronized phase arrangements are unstable. If  $K > 0$  and  $G$  is circulant, then all of the phase arrangements where  $W_L(\boldsymbol{\theta})$  reaches its global maximum are balanced and asymptotically stable.*

*Proof.* As in the proof of Theorem 4.2, we prove Theorem 4.7 using the invariance principle [131, Theorem 4.4]. The closed-loop phase model (3.6) evolves on the compact shape space  $\mathbb{T}^N/\mathbb{T}$  under the gradient dynamics  $\dot{\boldsymbol{\theta}} = K\nabla W_L$ . The potential  $-KW_L(\boldsymbol{\theta}) : \mathbb{T}^N/\mathbb{T} \mapsto \mathbb{R}$  is a continuously differentiable function with  $\frac{d}{dt}(-KW_L) \leq 0$  along solutions of (3.6). Let  $\Omega$  denote the set of all points in the shape space where  $\frac{d}{dt}(-KW_L) = 0$ . Points in  $\Omega$  satisfy

$$\langle ie^{i\theta_k}, L_k e^{i\theta} \rangle = 0. \quad (4.16)$$

The set  $\Omega$  is invariant since the condition (4.16) implies  $\dot{\theta}_{k,j} = 0$  for all pairs  $j$  and  $k$ . By the invariance principle [131, Theorem 4.4], every solution of the closed-loop dynamics approaches  $\Omega$  as  $t \rightarrow \infty$ . Comparing (4.14) and (4.16), we conclude that  $\Omega$  is the set of critical points of  $W_L(\boldsymbol{\theta})$ , which completes the first part of the proof.

Critical points where  $\theta_{k,j} = 0$  for all pairs  $j$  and  $k$ , are global minima of  $W_L(\boldsymbol{\theta})$ , which implies the synchronized set is asymptotically stable if  $K < 0$  and unstable if  $K > 0$ . By Lemma 4.6, if  $G$  is circulant, then the global maximum of  $W_L(\boldsymbol{\theta})$  is balanced; this set is asymptotically stable if  $K > 0$ .  $\square$

Rotational invariance of the phase potential  $W_L(\boldsymbol{\theta})$  leads to the following result, analo-

gous to Corollary 4.3. Let  $\omega_0 \in \mathbb{R}$  and consider the shape control

$$u_k = \omega_0 + K \langle i e^{i\theta_k}, L_k e^{i\theta} \rangle = \omega_0 - K \sum_{j \in \mathcal{N}_k} \sin \theta_{j,k} \quad (4.17)$$

**Corollary 4.8. Laplacian phase synchronization and balancing** *The results of Theorem 4.7 still apply if the control (4.15) is replaced by (4.17).*

*Proof.* The time-derivative of  $W_L(\boldsymbol{\theta})$  along solutions of the closed-loop particle model with the control (4.17) is

$$\begin{aligned} \dot{W}_L &= \sum_{j=1}^N (\omega_0 \langle i e^{i\theta_j}, L_j e^{i\theta} \rangle + K \langle i e^{i\theta_j}, L_j e^{i\theta} \rangle^2) \\ &= \omega_0 N \langle i e^{i\theta}, L e^{i\theta} \rangle + K \sum_{j=1}^N \langle i e^{i\theta_j}, L_j e^{i\theta} \rangle^2 \\ &= \omega_0 N \underbrace{\langle i B^T e^{i\theta}, B^T e^{i\theta} \rangle}_0 + K \sum_{j=1}^N \langle i e^{i\theta_j}, L_j e^{i\theta} \rangle^2. \end{aligned}$$

The remainder of the proof is identical to the proof of Theorem 4.7 since the constant  $\omega_0$  vanishes in the reduced shape space.  $\square$

### 4.3 General Interaction

In this section, we describe an approach to phase synchronization and balancing with time-varying and/or directed interaction networks. Such networks preclude the use of the gradient algorithms from the previous section, since that algorithm requires undirected interaction. Nonetheless, the gradient algorithm with all-to-all interaction motivates the approach below, which achieves the same result under very mild assumptions on the interaction network connectivity. The results in this section were developed by Scardovi *et al.* [234, 233].

Recall that the all-to-all phase control (4.6) depends on the average quantity  $p_\theta$ . That is, control of phase  $\theta_k$  is proportional to

$$\langle i e^{i\theta_k}, p_\theta \rangle = \langle i e^{i\theta_k}, \frac{1}{N} \sum_{j=1, j \neq k}^N e^{i\theta_j} \rangle.$$

The Laplacian control (4.15) is proportional to

$$-\langle i e^{i\theta_k}, L_k e^{i\theta} \rangle = |\mathcal{N}_k| \langle i e^{i\theta_k}, \frac{1}{|\mathcal{N}_k|} \sum_{j \in \mathcal{N}_k} e^{i\theta_j} \rangle.$$

In both algorithms, the control  $u_k$  depends on the instantaneous centroid of the neighboring phases. In the general setting, which has possibly time-varying and directed interaction, we use an algorithm for control  $u_k$  that replaces the instantaneous centroid  $p_\theta$  of all of the phases with another quantity. In the phase balancing algorithm below, it is accurate to interpret this quantity as a dynamic estimate of  $p_\theta$ . On the other hand, in the phase synchronization algorithm below, the dynamics of the quantity that replaces  $p_\theta$  are decoupled from the phase dynamics. This quantity is the output of a decentralized *consensus algorithm*.

We consider the dynamic phase balancing algorithm first. The estimation of  $p_\theta$  is decentralized, which means that each control uses a different estimate. Let  $z_k \in \mathbb{C}$  denote the estimate of  $p_\theta$  used in control  $k \in \mathcal{N}$ . To introduce this approach, consider the all-to-all phase control (4.6) with  $p_\theta$  replaced by  $z_k$ , that is,

$$u_k = -K \langle i e^{i\theta_k}, z_k \rangle, \quad (4.18)$$

with the trivial estimator dynamics

$$\dot{z}_k = \dot{p}_\theta. \quad (4.19)$$

Integrating (4.19) yields  $z_k(t) - z_k(0) = p_\theta(t) - p_\theta(0)$ . Thus, if  $z_k(0) = p_\theta(0)$  then  $z_k(t) = p_\theta(t)$ . In this case, the control (4.18) is identical to the all-to-all phase control (4.6) since  $u_k = -K \langle i e^{i\theta_k}, p_\theta \rangle$ .

Now suppose  $z_k(0) \neq p_\theta(0)$ , which implies  $z_k(t) \neq p_\theta(t)$  in (4.18). We can force each  $z_k$  to asymptotically converge to  $p_\theta$  by modifying its dynamics as follows. Let

$$\dot{z}_k = \dot{p}_\theta + \sum_{j=1}^N (z_j - z_k), \quad z_k(0) = e^{i\theta_k(0)}, \quad (4.20)$$

which is equivalent to

$$\dot{\mathbf{z}} = \dot{p}_\theta \mathbf{1} - NP\mathbf{z}, \quad \mathbf{z}(0) = e^{i\boldsymbol{\theta}(0)}.$$

Note that  $P$  is the symmetric projection matrix defined in (3.27) and  $NP$  is the Laplacian of the complete graph with  $N$  nodes, which means the estimator dynamics (4.20) require knowledge of  $z_k$  for all  $k \in \mathcal{N}$ . The function  $V(\mathbf{z}) = (1/2)\|P\mathbf{z}\|^2$  is positive definite with

respect to the set where  $\mathbf{z} = \bar{z}\mathbf{1}$  for any  $\bar{z} \in \mathbb{C}$ . The time-derivative of  $V(\mathbf{z})$  along solutions of the closed-loop phase model (3.6) with control (4.18) and estimator (4.20) is

$$\dot{V} = \langle P\mathbf{z}, P\dot{\mathbf{z}} \rangle = \langle P\mathbf{z}, P(\dot{p}_\theta\mathbf{1} - NP\mathbf{z}) \rangle = -N\langle P\mathbf{z}, P\mathbf{z} \rangle + \underbrace{\langle \mathbf{z}, \dot{p}_\theta P\mathbf{1} \rangle}_0 = -2NV(\mathbf{z}(t)).$$

This means that  $V(\mathbf{z}(t)) = V(\mathbf{z}(0))e^{-2Nt}$ , which implies  $V(\mathbf{z}(t))$  decays exponentially to zero. Consequently, we observe that  $z_k \rightarrow \bar{z}$  for some  $\bar{z} \in \mathbb{C}$  as  $t \rightarrow \infty$  for all  $k \in \mathcal{N}$ .

Next, we show that  $\bar{z} = p_\theta$ . Multiplying the  $\mathbf{z}$  dynamics in (4.20) from the left by  $\mathbf{1}^T$  yields

$$\mathbf{1}^T \dot{\mathbf{z}} = N\dot{p}_\theta - \underbrace{N\mathbf{1}^T P\mathbf{z}}_0 = N\dot{p}_\theta.$$

This means  $\frac{d}{dt} \left( (1/N) \sum_{j=1}^N z_j \right) = \dot{p}_\theta$ , which, when integrated, yields

$$\frac{1}{N} \sum_{j=1}^N z_j(t) - \underbrace{\frac{1}{N} \sum_{j=1}^N z_j(0)}_{p_\theta(0)} = p_\theta(t) - p_\theta(0).$$

In the limit  $t \rightarrow \infty$ , we have  $(1/N) \sum_{j=1}^N z_k(t) = \bar{z} = p_\theta$ . This means that the control (4.18) asymptotically converges as desired to

$$u_k = -K \langle ie^{i\theta_k}, \bar{z} \rangle = -K \langle ie^{i\theta_k}, p_\theta \rangle.$$

The estimator (4.20) achieves the desired result, but we must modify it for use with limited, time-varying interaction. Note that in order to compute  $\dot{z}_k$  we use the term  $\dot{p}_\theta = (1/N) \sum_{j=1}^N ie^{i\theta_j} u_j$ . This means that control (4.18) of phase  $\theta_k$  with estimator (4.20) requires knowledge of  $u_j$  for all  $j \in \mathcal{N}$  and knowledge of the relative variables  $z_{k,j} \triangleq z_k - z_j$  for all  $j \in \mathcal{N}$ . In the particle model, we assume that the instantaneous value of the control  $u_j$  for all  $j \in \mathcal{N}$  are not transmitted over the interaction network. However, let us assume that the consensus variables  $z_j$  are transmitted over the interaction network to each node  $k \in \mathcal{N}$  from its neighboring nodes  $j \in \mathcal{N}_k(t)$ . That is, we assume that, to compute (4.20) for node  $k$ , we have available the values  $u_k$  and  $z_{k,j}$  for all  $j \in \mathcal{N}_k(t)$ . This suggests that we modify (4.20) as follows:

$$\dot{z}_k = \frac{d}{dt} e^{i\theta_k} + \sum_{j \in \mathcal{N}_k(t)}^N (z_j - z_k), \quad z_k(0) = e^{i\theta_k(0)}, \quad (4.21)$$

which is equivalent to

$$\dot{\mathbf{z}} = i\text{diag}\{\mathbf{u}\}e^{i\boldsymbol{\theta}} - L(t)\mathbf{z}, \quad \mathbf{z}(0) = e^{i\boldsymbol{\theta}(0)}.$$

Under mild assumptions on the Laplacian  $L(t)$ , we prove in Theorem 4.10 that the control (4.18) with  $K > 0$  and estimator (4.21) stabilizes the set of balanced phases. Note that, if  $\mathcal{N}_k(t) = \emptyset$  for all  $t \geq 0$ , then integrating (4.21) gives  $z_k(t) = e^{i\theta_k(t)}$ . In this case, the control (4.18) is  $u_k = -K\langle ie^{i\theta_k}, e^{i\theta_k} \rangle = 0$ . We interpret the estimator algorithm (4.21) as a consensus algorithm and the limit  $\bar{z}$  as a consensus value.

We also use a consensus algorithm for phase synchronization. Eliminating the term  $\frac{d}{dt}e^{i\theta_k}$  from (4.21) decouples the phase dynamics from the  $z_k$  dynamics, that is,

$$\dot{\mathbf{z}} = -L(t)\mathbf{z}, \quad \mathbf{z}(0) = e^{i\boldsymbol{\theta}(0)}, \quad (4.22)$$

is independent of  $\mathbf{u}$ . In this case, the  $\mathbf{z}$  are not estimates of  $p_\theta(t)$ ,  $t > 0$ , but they still can reach consensus to some  $\bar{z} \in \mathbb{C}$  as described below. This means that the closed-loop phase model (3.6) asymptotically converges to

$$\dot{\theta}_k = -K\langle ie^{i\theta_k}, \bar{z} \rangle = -K|\bar{z}| \sin(\arg\{\bar{z}\} - \theta_k). \quad (4.23)$$

We prove in Theorem 4.10 that the limiting dynamics (4.23) with  $K < 0$  stabilizes the set of critical points with  $\boldsymbol{\theta} = \arg\{\bar{z}\}\mathbf{1}$ . The proof of Theorem 4.10 requires the following result, which is based on [219, Theorem 3.12] and [174, Theorem 1].

**Proposition 4.9. Euclidean consensus algorithm** *Let  $L(t)$  be the Laplacian matrix of a graph  $G(t) = (\mathcal{N}, E(t))$ . Consider the linear time-varying system*

$$\dot{\mathbf{x}} = -L(t)\mathbf{x}, \quad \mathbf{x} \in \mathbb{R}^N, \quad (4.24)$$

*which is a consensus algorithm. Let  $\mathbf{x} = \bar{x}\mathbf{1}$  denote a consensus state, where  $\bar{x} \in \mathbb{R}$ .*

*If  $G(t)$  is uniformly connected, then the consensus algorithm (4.24) asymptotically converges to a consensus state.*

*If  $G(t)$  is uniformly connected to a single node, then the consensus algorithm (4.24) uniformly exponentially converges to a consensus state.*

If  $G(t)$  is balanced for all time and the consensus algorithm (4.24) converges to a consensus state, then the asymptotic consensus value  $\bar{x}$  is the centroid of the initial conditions, that is,  $\bar{x} = \frac{1}{N} \sum_{j=1}^N x_j(0)$ .

We summarize the proof of Proposition 4.9. The consensus algorithm (4.24) has the solution  $\mathbf{x}(t) = \Phi(t, 0)\mathbf{x}(0)$ , where  $\Phi(t, 0) = e^{\int_0^t L(\tau)d\tau}$  is the transition matrix. The proof of the first part of Proposition 4.9 uses the fact that  $\lim_{t \rightarrow \infty} \Phi(t, 0) = \mathbf{1}\mathbf{y}^T$  for some  $\mathbf{y} \in \mathbb{R}^N$ , which implies that  $x_k \rightarrow \bar{x} = \mathbf{y}^T \mathbf{x}(0)$  for all  $k \in \mathcal{N}$  [219, Theorem 3.12]. The proof of the second part of Proposition 4.9 uses the Lyapunov function

$$V(\mathbf{x}) \triangleq \max\{x_1, \dots, x_N\} - \min\{x_1, \dots, x_N\},$$

which is positive definite with respect to the set of consensus states [174, Theorem 1]. Under the dynamics  $\dot{x}_k = -L_k(t)\mathbf{x} = \sum_{j \in \mathcal{N}_k(t)} (x_j - x_k)$  each  $x_k$  moves only in the direction of its neighbors. Consequently, it can be shown that  $V(\mathbf{x})$  is non-increasing. The proof of the third part of Proposition 4.9 starts with the assumption that  $G(t)$  is balanced, which implies  $\mathbf{1}^T \dot{\mathbf{x}} = \mathbf{1}^T L(t)\mathbf{x} = 0$ . This means  $\sum_{j=1}^N x_j$  is a constant of motion of the system (4.24) and  $\sum_{j=1}^N x_j = N\bar{x}$ .

Proposition 4.9 shows that the decoupled dynamics (4.22) converge to an arbitrary consensus  $\bar{z}$ . This is because (4.22) is equivalent to the two independent subsystems  $\frac{d}{dt} \text{Re}\{\mathbf{z}\} = -L(t)\text{Re}\{\mathbf{z}\}$  and  $\frac{d}{dt} \text{Im}\{\mathbf{z}\} = -L(t)\text{Im}\{\mathbf{z}\}$ , each of which is an instance of the Euclidean consensus algorithm (4.24).

The main result of this section is a dynamic phase synchronization and balancing algorithm for general interaction. In order to use shape coordinates, we introduce the variable  $w_k \triangleq z_k e^{-i\theta_k}$ . Also let  $H(x)$ , where  $x \in \mathbb{R}$ , denote the Heaviside step function

$$H(x) \triangleq \begin{cases} 0 & x < 0 \\ \frac{1}{2} & x = 0 \\ 1 & x > 0. \end{cases} \quad (4.25)$$

The dynamic phase synchronization and balancing algorithm is the control (4.18). For phase balancing, we use  $K > 0$  and the consensus dynamics (4.21). For phase synchronization, we

use  $K < 0$  and the consensus dynamics (4.22). We have, equivalently in shape coordinates,

$$\begin{aligned} u_k &= -K\langle w_k, i \rangle, \quad K \neq 0 \\ \dot{w}_k &= u_k i (\mathbf{H}(K) - w_k) - \sum_{j=1}^N l_{kj}(t) w_j e^{i\theta_{j,k}}, \quad w_k(0) = 1. \end{aligned} \quad (4.26)$$

The term  $\sum_{j=1}^N l_{kj}(t) w_j e^{i\theta_{j,k}} = \sum_{j \in \mathcal{N}_k(t)} (w_k - w_j e^{i\theta_{j,k}})$  is in shape coordinates, but it requires the transmission to node  $k$  of the variable  $w_j$  from node  $j$  for all  $j \in \mathcal{N}_k(t)$  and all  $t$ . Furthermore, to compute (4.26) we must have available at each node  $k$  the variable  $w_k$ . We have the following result [233, Theorems 3 and 4], which was summarized in [241, Theorems 3 and 4].

**Theorem 4.10. Dynamic phase synchronization and balancing** *Let  $L(t)$  be the Laplacian matrix of a graph  $G(t) = (\mathcal{N}, E(t))$ . Consider the closed-loop phase model (3.6) with the shape control (4.26).*

*Let  $K < 0$  and assume  $G(t)$  is uniformly connected. All of the solutions of (3.6) converge to the critical set of the autonomous system (4.23), where  $\bar{z} \in \mathbb{C}$  is the consensus limit. If  $|\bar{z}| > 0$ , then all of the synchronized phase arrangements where  $\boldsymbol{\theta} = \arg \bar{z} \mathbf{1}$  are asymptotically stable and all of the remaining equilibria are unstable. If  $G(t)$  is balanced and the initial phase arrangement  $\boldsymbol{\theta}(0)$  is not balanced, then the consensus limit satisfies  $\bar{z} = p_{\boldsymbol{\theta}}(0) \neq 0$ .*

*Let  $K > 0$  and assume  $G(t)$  is uniformly connected to a single node and balanced for all time. All of the balanced phase arrangements are asymptotically stable equilibria of (3.6) and all of the remaining equilibria are unstable. The consensus limit is  $\bar{z} = \lim_{t \rightarrow \infty} p_{\boldsymbol{\theta}}(t) = 0$ .*

*Proof.* Let  $K < 0$ , which means  $\mathbf{H}(K) = 0$ , and assume  $G(t)$  is uniformly connected. The time-derivative of  $z_k \triangleq w_k e^{i\theta_k}$  along solutions of the closed-loop phase model (3.6) with control (4.26) is

$$\dot{z}_k = \dot{w}_k e^{i\theta_k} + u_k i w_k e^{i\theta_k} = - \sum_{j=1}^N l_{kj}(t) w_j e^{i\theta_j} = -L_k(t) \mathbf{z}.$$

Consequently,  $\mathbf{z}$  obeys the consensus dynamics (4.24), which means it exponentially converges to the asymptotic consensus value  $\bar{z} \mathbf{1}$  by Proposition 4.9. The limit set of the closed-loop phase model is the critical set of the limiting (autonomous) system (4.23) [172,

Theorem 1.8]. If  $|\bar{z}| = 0$ , then there are no isolated critical points of (4.23). If  $|\bar{z}| > 0$ , the critical points of (4.23) satisfy  $\theta_k = \arg\{\bar{z}\} \bmod \pi$  for all  $k \in \mathcal{N}$ . Linearization of (4.23) at these critical points shows that synchronization of all of the phases to  $\arg\{\bar{z}\}$  is exponentially stable and the set of phase arrangements where at least one phase (but not all) equals  $\arg\{\bar{z}\} + \pi$  is unstable. If  $G(t)$  is balanced, then  $\bar{z} = (1/N) \sum_{j=1}^N w_j(0)e^{i\theta_j(0)} = p_\theta(0)$  is a constant of motion. If, in addition to  $G(t)$  being balanced,  $\theta(0)$  is not balanced, then  $|\bar{z}| > 0$  and the critical points of (4.23) are isolated.

Let  $K > 0$ , which means that  $H(K) = 1$ , and assume  $G(t)$  is uniformly connected to a single node and balanced for all time. The time-derivative of  $z_k \triangleq w_k e^{i\theta_k}$  along solutions of the closed-loop phase model (3.6) with control (4.26) is

$$\dot{z}_k = - \sum_{j=1}^N l_{kj}(t) w_j e^{i\theta_j} + u_k i e^{i\theta_k} = -L_k(t) \mathbf{z} + \frac{d}{dt} e^{i\theta_k}. \quad (4.27)$$

This implies that  $\mathbf{z}$  obeys the consensus dynamics (4.24) with an additive perturbation. We now show that the perturbation is vanishing. Under a vanishing perturbation, the set of consensus states  $\mathbf{z} = \bar{z} \mathbf{1}$  is an exponentially stable set of the perturbed system (4.27) [131, Lemma 9.1].

Consider the positive definite and proper quadratic form  $V(\mathbf{z}) \triangleq \frac{1}{2} \|\mathbf{z}\|^2$ .<sup>1</sup> The time-derivative of  $V(\mathbf{z})$  is

$$\begin{aligned} \dot{V} &= \langle \mathbf{z}, \dot{\mathbf{z}} \rangle = \langle \mathbf{z}, -L(t)\mathbf{z} + \text{diag}\{\mathbf{u}\} i e^{i\theta} \rangle \\ &= -\langle \mathbf{z}, L(t)\mathbf{z} \rangle + \sum_{j=1}^N \langle z_j, i e^{i\theta_j} \rangle u_j = -Q_{L(t)}(\mathbf{z}) - \frac{1}{K} \|\mathbf{u}\|^2 \leq 0, \end{aligned}$$

which implies  $V(\mathbf{z})$  is nonincreasing along the solutions. This means that  $\|\mathbf{z}(t)\|^2 \leq 2V(\mathbf{z}(0))$  is bounded. Using Lemma A.1 with  $\phi_1(t) \triangleq Q_{L(t)}(\mathbf{z}(t))$  and  $\phi_2(t) \triangleq (1/K) \|\mathbf{u}\|^2$  (see Appendix A), we observe that  $\|\mathbf{u}(t)\|^2 : [0, \infty) \rightarrow \mathbb{R}$  is bounded. The time-derivative

$$\dot{\phi}_2 = \frac{1}{K} \frac{d}{dt} \|\mathbf{u}(t)\|^2 = \frac{2}{K} \sum_{j=1}^N |u_j|^2 \dot{u}_j$$

is bounded if  $\dot{u}_k$  is bounded for all  $k \in \mathcal{N}$ . We have

$$\dot{u}_k = -K \langle \dot{z}_k, i e^{i\theta_k} \rangle + K \langle z_k, e^{i\theta_k} \rangle u_k = -K \langle i e^{i\theta_k} u_k - L_k \mathbf{z}, i e^{i\theta_k} \rangle + K \langle z_k, e^{i\theta_k} \rangle u_k,$$

<sup>1</sup>In this context, *proper* means  $\lim_{\|\mathbf{z}\| \rightarrow \infty} V(\mathbf{z}) = \infty$ .

which is bounded because both  $z_k$  and  $u_k$  are bounded for all  $k \in \mathcal{N}$ . Consequently, a second application of Lemma A.1 proves that  $\|\mathbf{u}(t)\|^2 \rightarrow 0$  as  $t \rightarrow \infty$ . This means  $u_k(t) \rightarrow 0$  as  $t \rightarrow \infty$  for all  $k \in \mathcal{N}$  and the perturbation  $\text{diag}\{\mathbf{u}\}ie^{i\boldsymbol{\theta}}$  of the dynamics (4.27) vanishes.

Now that we have shown that  $z_k \rightarrow \bar{z}$  as  $t \rightarrow \infty$ , we find the consensus limit  $\bar{z}$ . Since  $G(t)$  is balanced, then  $\mathbf{1}^T L(t) = 0$ . Consequently, multiplying from the left by  $\mathbf{1}^T$  the  $\dot{z}_k$  dynamics (4.27) yields

$$\mathbf{1}^T \dot{\mathbf{z}} = \sum_{j=1}^N \frac{d}{dt} e^{i\theta_j},$$

which means

$$\frac{d}{dt}(\mathbf{1}^T \mathbf{z}) = \frac{d}{dt}(Np_\theta). \quad (4.28)$$

Integrating (4.28) yields  $\mathbf{1}^T \mathbf{z}(t) - \mathbf{1}^T \mathbf{z}(0) = Np_\theta(t) - Np_\theta(0)$ . We have

$$\mathbf{1}^T \mathbf{z}(0) = \sum_{j=1}^N w_j(0) e^{i\theta_j(0)} = Np_\theta(0),$$

which implies  $\mathbf{1}^T \mathbf{z}(t) = Np_\theta(t)$ . In the limit  $t \rightarrow \infty$ , we have  $\mathbf{1}^T \bar{\mathbf{z}} = N\bar{z} = Np_\theta(t)$ , that is,  $\bar{z} = p_\theta(t)$ .

Thus, we have shown that the dynamics of the closed-loop phase model asymptotically converge to

$$\dot{\theta}_k = -K \langle ie^{i\theta_k}, \bar{\mathbf{z}} \rangle = -K \langle ie^{i\theta_k}, p_\theta \rangle = -K \frac{\partial U}{\partial \theta_k}, \quad (4.29)$$

where  $U(\boldsymbol{\theta})$  is the all-to-all phase potential defined in (4.1). In addition, we have shown that  $\dot{\theta}_k \rightarrow 0$  as  $t \rightarrow \infty$ , since  $\dot{\theta}_k = u_k$  and  $\lim_{t \rightarrow \infty} u_k(t) = 0$ . This implies that  $\boldsymbol{\theta}(t)$  asymptotically converges to the set of critical points where  $\frac{\partial U}{\partial \theta_k} = 0$ , which is the set of critical points of  $U(\boldsymbol{\theta})$ . The stability of critical points of (4.29) with  $K > 0$  follows from Theorem 4.2, which completes the proof.  $\square$

Theorem 4.10 requires  $G(t)$  to be balanced in order for the dynamic algorithm (4.26) to isolate either the set of synchronized phases or the set of balanced phases. If  $G(t)$  is balanced, then  $z_k$  is an estimator in the following sense: if  $K < 0$ , then  $z_k$  estimates the initial state  $p_\theta(0)$ ; if  $K > 0$ , then  $z_k$  estimates the limiting state  $p_\theta(t)$ . We illustrate this result in Figure 4.3 for a time-invariant, directed ring interaction network, which is

strongly connected. In Figure 4.3(c), the asymptotic value of the order parameter is equal to the normalized initial value of the order parameter, that is,  $\lim_{t \rightarrow \infty} p_\theta(t) = \bar{z}/|\bar{z}| = p_\theta(0)/|p_\theta(0)|$ .

The balancing requirement on  $G(t)$  for phase synchronization need not be strictly enforced. This is because the dynamic algorithm (4.26) with  $K < 0$  fails to isolate the set of synchronized phases only if  $G(t)$  is not balanced for all time and the asymptotic consensus value  $\bar{z} = 0$ . Since the Euclidean consensus dynamics (4.24) are invariant to translation in the complex plane, they converge with probability one to  $\bar{z} \neq 0$  [233, Theorem 3]. This implies that the dynamic phase synchronization algorithm applies to non-balanced interaction networks. If  $G(t)$  is not balanced, then the order parameter  $p_\theta$  asymptotically converges to an arbitrary (normalized) limit  $\bar{z}/|\bar{z}|$ .

Next we address the addition to the control (4.18) of a constant  $\omega_0 \in \mathbb{R}$ . In this case, the dynamic phase synchronization and balancing algorithm (4.26) becomes

$$\begin{aligned} u_k &= \omega_0 - K \langle w_k, i \rangle, \quad K \neq 0 \\ \dot{w}_k &= (u_k - \omega_0) i (\mathbf{H}(K) - w_k) - \sum_{j=1}^N l_{kj}(t) w_j e^{i\theta_{j,k}}, \quad w_k(0) = 1. \end{aligned} \quad (4.30)$$

We have the following corollary to Theorem 4.10.

**Corollary 4.11. Dynamic phase synchronization and balancing** *The results of Theorem 4.10 still apply when control (4.26) is replaced by (4.30).*

*Proof.* This proof follows the proof of Theorem 4.10 using the definition  $z_k \triangleq w_k e^{i(\theta_k - \omega_0 t)}$ . Note, if  $\omega_0 = 0$ , then this definition is  $z_k \triangleq w_k e^{i\theta_k}$ , which is the previous definition for  $z_k$ . The time-derivative of  $z_k$  along solutions of the closed-loop phase model (3.6) with control (4.30) is

$$\begin{aligned} \dot{z}_k &= \dot{w}_k e^{i(\theta_k - \omega_0 t)} + (u_k - \omega_0) i w_k e^{i(\theta_k - \omega_0 t)} = (u_k - \omega_0) i \mathbf{H}(K) e^{i(\theta_k - \omega_0 t)} - \\ &\quad \sum_{j=1}^N l_{kj}(t) w_j e^{i(\theta_j - \omega_0 t)} = \mathbf{H}(K) \frac{d}{dt} e^{i(\theta_k - \omega_0 t)} - L_k(t) \mathbf{z}. \end{aligned}$$

If  $K < 0$ , then  $\mathbf{H}(K) = 0$  and  $\mathbf{z}$  obeys the consensus dynamics (4.24). Let  $\bar{z}$  denote the consensus value, that is,  $z_k \rightarrow \bar{z}$ ,  $k \in \mathcal{N}$ , as  $t \rightarrow \infty$ . The limiting dynamics are

$$\dot{\theta}_k - \omega_0 = -K \langle i e^{i(\theta_k - \omega_0 t)}, \bar{z} \rangle = -K |\bar{z}| \sin(\arg\{\bar{z}\} - (\theta_k - \omega_0 t)), \quad K < 0. \quad (4.31)$$

We express (4.31) in a frame rotating at  $\omega_0$  using the change of coordinates  $\phi_k \triangleq \theta_k - \omega_0 t$ . In the rotating frame, the dynamics are

$$\dot{\phi}_k = -K \langle i e^{i\phi_k}, \bar{z} \rangle = -K |\bar{z}| \sin(\arg\{\bar{z}\} - \phi_k), \quad K < 0,$$

which is equivalent to (4.23) with  $\theta_k$  replaced by  $\phi_k$ . Consequently, the remaining proof of the synchronization results of Theorem 4.10 hold with  $\theta_k$  replaced by  $\phi_k$ .

If  $K > 0$  and  $G(t)$  is balanced, then  $H(K) = 1$  and  $\mathbf{z}$  obeys the consensus dynamics (4.24) with an additive perturbation proportional to  $\mathbf{u} - \omega_0 \mathbf{1}$ . In order to show that the perturbation vanishes, consider  $V(\mathbf{z}) \triangleq 1/2 \|\mathbf{z}\|^2$ . The time-derivative of  $V(\mathbf{z})$  is

$$\begin{aligned} \dot{V} &= \langle \mathbf{z}, \dot{\mathbf{z}} \rangle = \langle \mathbf{z}, -L(t)\mathbf{z} + \text{diag}\{\mathbf{u} - \omega_0 \mathbf{1}\} i e^{i(\boldsymbol{\theta} - \omega_0 t \mathbf{1})} \rangle \\ &= -\langle \mathbf{z}, L(t)\mathbf{z} \rangle + \sum_{j=1}^N \langle z_j, i e^{i(\theta_j - \omega_0 t)} \rangle (u_j - \omega_0) = -Q_{L(t)}(\mathbf{z}) - \frac{1}{K} \|\mathbf{u} - \omega_0 \mathbf{1}\|^2 \leq 0. \end{aligned}$$

Using Lemma A.1 with  $\phi_1(t) \triangleq Q_{L(t)}(\mathbf{z}(t))$  and  $\phi_2(t) \triangleq \frac{1}{K} \|\mathbf{u}(t) - \omega_0 \mathbf{1}\|^2$ , one can show that  $u_k(t) \rightarrow \omega_0$  as  $t \rightarrow \infty$  for all  $k \in \mathcal{N}$ , which means that the perturbation vanishes. Consequently, the remaining proof of the balancing results of Theorem 4.10 hold with  $\theta_k$  replaced by  $\phi_k$ .  $\square$

The estimator component (4.21) of the dynamic phase balancing algorithm, which first appeared in [234], is an example *dynamic consensus filter*. One can view  $e^{i\theta_k}$  as the filter input and  $z_k$  as the filter output. The output of a dynamic consensus filter tracks the average of a set of time-varying inputs [255], in this case,  $p_\theta$ . Lynch *et al.* have studied dynamic consensus filters for cooperative control and sensing [89, 295, 158]. A “low-pass” variation of the dynamic consensus filter is described in [193]. Proportional and proportional-integral versions are described in [90].

The convergence rate of a dynamic consensus filter depends on the magnitude of the second smallest eigenvalue of the Laplacian matrix [192]. Algorithms to improve the convergence rate by weighting the entries of the Laplacian matrix have been studied in [293, 132, 44, 195, 294]. This topic is related to the optimal mixing rate in a Markov process [34, 261].

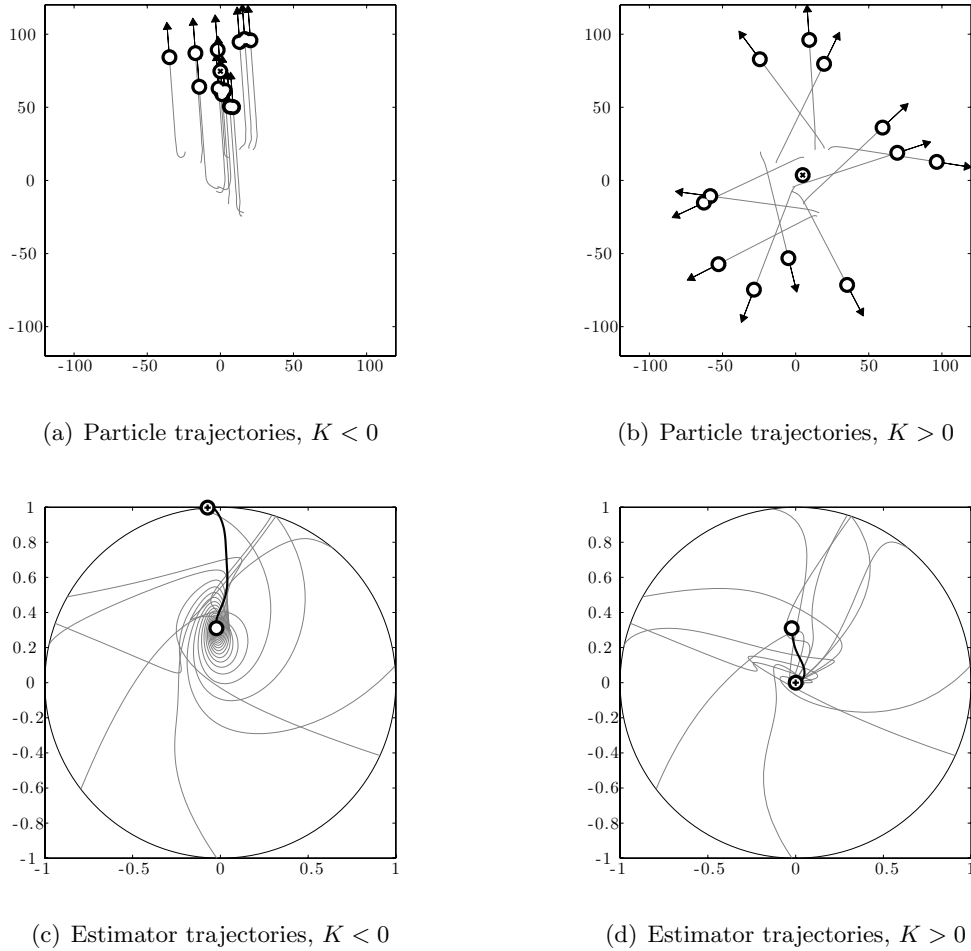


Figure 4.3: Dynamic phase control. Simulations of the closed-loop particle model with the dynamic phase control (4.26) for  $N = 12$ . The interaction network is a time-invariant, directed ring. (a, b) We denote the position centroid  $p_r$  by a circle marked with an  $\times$ ; the velocity  $\dot{p}_r$  equals the order parameter  $p_\theta$ . (c, d) We denote the initial phase order parameter  $p_\theta(0)$  by a circle and the limiting phase order parameter  $\lim_{t \rightarrow \infty} p_\theta(t)$  by a circle marked with  $+$ . (a) Phase synchronization generates a parallel formation. (b) Phase balancing fixes the position centroid. (c) Every estimator  $z_k = w_k e^{i\theta_k}$ ,  $w_k(0) = 1$ , starts on the unit circle and converges to  $\bar{z} = p_\theta(0)$ . In addition, each phase converges to  $\bar{z}$ , which means that the phases synchronize and  $p_\theta(t)$  converges to  $\bar{z}/|\bar{z}| = p_\theta(0)/|p_\theta(0)|$ . (d) Every estimator converges to  $\bar{z} = \lim_{t \rightarrow \infty} p_\theta(t) = 0$ , which implies that the phases balance.

## Chapter 5

# Circular Formations

In the previous chapter, we describe synchronization and balancing algorithms for the phase model (3.6) with three levels of interaction. Phase synchronization generates a parallel formation in the particle model. Parallel formations are relative equilibria of the particle model because they are invariant to rigid rotation and rigid translation of all particles. Another class of relative equilibria of the particle model is the set of circular formations, in which all particles travel around the same circle in the same direction. In this chapter, we describe control algorithms that stabilize circular formations in the particle model with three levels of interaction. Using results from the previous chapter, we also describe algorithms that isolate subsets of circular formations in which the particle phases are either synchronized or balanced. We call these relative equilibria synchronized circular formations and balanced circular formations, respectively.

Recall that to drive a particle in a circle, we need simply to use an open-loop control equal to a nonzero constant  $\omega_0 \neq 0$ . The center  $c_k$  of the circle, which is defined in (3.15), has the dynamics

$$\dot{c}_k = e^{i\theta_k} - \omega_0^{-1} e^{i\theta_k} u_k = \omega_0^{-1} (\omega_0 - u_k) e^{i\theta_k}. \quad (5.1)$$

If  $u_k = \omega_0$ , then particle  $k$  travels around a circle with radius  $|\omega_0|^{-1}$  and direction of rotation determined by the sign of  $\omega_0$ . In this case,  $\dot{c}_k = 0$  and  $c_k$  is a constant of motion. Let  $u_k = \omega_0 + u'_k$ , where  $u'_k = u'_k(\mathbf{r}, \boldsymbol{\theta})$ . This means that each particle orbits a circle and

the center dynamics of each circle are  $\dot{c}_k = -\omega_0^{-1}u'_k e^{i\theta_k}$ . We seek to find the  $u'_k$  that drives the centers to a consensus value  $\bar{c} \in \mathbb{C}$ .

## 5.1 All-to-all Interaction

As with the all-to-all phase control algorithm, we develop the all-to-all circular formation control algorithm by designing a potential that has a minimum at the desired configuration. In this case, the desired configuration is  $\dot{\boldsymbol{\theta}} = \omega_0 \mathbf{1}$  and  $\mathbf{c} = \bar{c} \mathbf{1}$ . The *all-to-all circular formation potential*

$$S(\mathbf{r}, \boldsymbol{\theta}) \triangleq \frac{1}{2} \|P\mathbf{c}\|^2, \quad (5.2)$$

where the projection matrix  $P$  is defined in (3.27), is zero if and only if  $\mathbf{c} = \bar{c} \mathbf{1}$  and positive otherwise. Using (5.1), the time-derivative of  $S(\mathbf{r}, \boldsymbol{\theta})$  along solutions of the closed-loop particle model is

$$\dot{S} = \langle \dot{\mathbf{c}}, P\mathbf{c} \rangle = \omega_0^{-1} \sum_{j=1}^N (\omega_0 - u_j) \langle e^{i\theta_j}, P_j \mathbf{c} \rangle.$$

Choosing the circular formation control

$$u_k = \omega_0(1 + K_0 \langle e^{i\theta_k}, P_k \mathbf{c} \rangle), \quad K_0 > 0, \quad (5.3)$$

yields

$$\dot{S} = -K_0 \sum_{j=1}^N \langle e^{i\theta_j}, P_j \mathbf{c} \rangle^2 \leq 0. \quad (5.4)$$

The control (5.3) is a shape control since the terms

$$\langle e^{i\theta_k}, P_k \mathbf{c} \rangle = \sum_{j=1}^N \langle e^{i\theta_k}, r_{k,j} + \omega_0^{-1} i e^{i\theta_j} \rangle$$

depend only on the shape variables  $e^{-i\theta_k} r_{k,j}$  and  $\theta_{k,j}$  for all pairs  $j$  and  $k$ . Lyapunov analysis produces the following result [243, Theorem 2].

**Theorem 5.1. All-to-all circular formation control** *For the shape control (5.3), all of the solutions of the closed-loop particle model (3.5) converge to the set of circular formations with radius  $|\omega_0|^{-1}$  and direction of rotation determined by the sign of  $\omega_0 \neq 0$ .*

*Proof.* Since the control (5.3) is a shape control, then the closed-loop particle model evolves on the reduced shape space with coordinates  $e^{-i\theta_k}r_{k,j}$  and  $\theta_{k,j}$  for all pairs  $j$  and  $k$ . The potential  $S(\mathbf{r}, \boldsymbol{\theta})$  is positive definite and proper in the reduced shape space, since

$$S(\mathbf{r}, \boldsymbol{\theta}) = \frac{1}{2} \sum_{k=1}^N |P_k \mathbf{c}|^2 = \frac{1}{2} \sum_{k=1}^N \sum_{j=1}^N |c_{k,j}|^2$$

and

$$|c_{k,j}| = |r_{k,j} + \omega_0^{-1}i(e^{i\theta_k} - e^{i\theta_j})| = |e^{-i\theta_k}r_{k,j} + \omega_0^{-1}i(1 - e^{i\theta_{j,k}})|,$$

which is a function of shape variables.

Note  $\dot{S}(\mathbf{r}, \boldsymbol{\theta}) \leq 0$  by (5.4). Let the set  $\Omega$  contain all of the points in the reduced shape space where  $\dot{S} = 0$ , that is,

$$\langle e^{i\theta_k}, P_k \mathbf{c} \rangle = 0. \quad (5.5)$$

In  $\Omega$ ,  $\dot{\boldsymbol{\theta}} = \omega_0 \mathbf{1}$  and  $\mathbf{c}$  is constant, which implies that (5.5) can hold only if  $P\mathbf{c} = 0$ . Since zero is a simple eigenvalue of  $P$  and the corresponding eigenvector is  $\mathbf{1}$ , then the condition  $P\mathbf{c} = 0$  is equivalent to  $\mathbf{c} = \bar{c}\mathbf{1}$  for some  $\bar{c} \in \mathbb{C}$ . Let  $\Lambda$  denote the set of all of the points in  $\Omega$  where  $\dot{\boldsymbol{\theta}} = \omega_0 \mathbf{1}$  and  $\mathbf{c} = \bar{c}\mathbf{1}$ . For all pairs  $j$  and  $k$  in  $\Lambda$ , we have  $\frac{d}{dt}(\theta_{k,j}) = 0$ ,  $\frac{d}{dt}(c_{k,j}) = 0$ , and

$$0 = \frac{d}{dt}(c_{k,j}) = \frac{d}{dt} \left( e^{i\theta_k} (e^{-i\theta_k} r_{k,j} + \omega_0^{-1}i(1 - e^{i\theta_{j,k}})) \right) = \omega_0 i \underbrace{c_{k,j}}_0 + e^{i\theta_k} \frac{d}{dt} \left( e^{-i\theta_k} r_{k,j} \right),$$

which implies  $\frac{d}{dt}(e^{-i\theta_k} r_{k,j}) = 0$ . This means that  $\Lambda$  is the largest invariant set in  $\Omega$ . By the invariance principle [131, Theorem 4.4 and Corollary 4.2], every solution of the closed-loop particle model approaches  $\Lambda$  as  $t \rightarrow \infty$ . Since  $\Lambda$  is the set of circular formations, this completes the proof.  $\square$

The all-to-all circular formation control (5.3) stabilizes the set of circular formations. Within this set, the position centroid  $p_r$  is confined to the area within the circular formation. In fact, the position centroid orbits the formation center  $\bar{c}$  at a constant speed less than or equal to one and a constant distance less than or equal to the radius  $|\omega_0|^{-1}$  of the formation.

To see this, consider the quantity  $\tilde{p}_r \triangleq p_r - \bar{c}$ , which is a (complex) vector from the formation center to the position centroid. Note  $\dot{\tilde{p}}_r = \dot{p}_r = p_\theta$ . Since  $\mathbf{c} = \bar{c}\mathbf{1}$ , we have

$$\tilde{p}_r = \frac{1}{N} \sum_{j=1}^N (r_j - c_j) = -i\omega_0^{-1} \frac{1}{N} \sum_{j=1}^N e^{i\theta_j} = -i\omega_0^{-1} p_\theta = -i\omega_0^{-1} \dot{\tilde{p}}_r, \quad (5.6)$$

which implies  $|\tilde{p}_r| \leq \omega_0^{-1}$  and  $\dot{\tilde{p}}_r = i\omega_0 \tilde{p}_r$ . Let  $\tilde{p}_r = |\tilde{p}_r| e^{i \arg\{\tilde{p}_r\}}$ . We have

$$\dot{\tilde{p}}_r = e^{i \arg\{\tilde{p}_r\}} \frac{d}{dt} |\tilde{p}_r| + i |\tilde{p}_r| e^{i \arg\{\tilde{p}_r\}} \frac{d}{dt} (\arg\{\tilde{p}_r\}) = i\omega_0 |\tilde{p}_r| e^{i \arg\{\tilde{p}_r\}}.$$

That is,  $\frac{d}{dt} |\tilde{p}_r| = 0$  and  $\frac{d}{dt} \arg\{\tilde{p}_r\} = \omega_0$ .

Equation (5.6) suggests a means to control the position centroid of a circular formation. If  $p_\theta = 0$ , that is, if the phases are balanced, then  $\tilde{p}_r = p_r - \bar{c} = 0$  and the position centroid coincides with the formation center. If  $|p_\theta| = 1$ , that is, if the phases are synchronized, then  $|\tilde{p}_r| = |\omega_0|^{-1}$ , which implies that the position centroid orbits the same circle as all of the particles (this is possible only if all of the particles are co-located). We refer to these two types of configurations as: (i) balanced circular formations and (ii) synchronized circular formations, respectively.

Next we provide an algorithm to isolate either the set of balanced circular formations or the set of synchronized circular formations using a linear combination of the circular formation control (5.3) with the phase synchronization and balancing control (4.6). Intuitively, such a composite control should simultaneously stabilize the set of circular formations and the set of synchronized or balanced phase arrangements. This intuition is formalized below.

Consider the composite potential

$$V(\mathbf{r}, \boldsymbol{\theta}) \triangleq \omega_0^2 K_0 S(\mathbf{r}, \boldsymbol{\theta}) + K U(\boldsymbol{\theta}), \quad K_0 > 0, K \in \mathbb{R}. \quad (5.7)$$

The time derivative of  $V(\mathbf{r}, \boldsymbol{\theta})$  along solutions of the closed-loop particle model (3.5) is

$$\begin{aligned} \dot{V} &= \omega_0 K_0 \sum_{j=1}^N (\omega_0 - u_j) \langle e^{i\theta_j}, P_j \mathbf{c} \rangle + K \sum_{j=1}^N \langle i e^{i\theta_j}, p_\theta \rangle u_j \\ &= \sum_{j=1}^N (\omega_0 K_0 \langle e^{i\theta_j}, P_j \mathbf{c} \rangle - K \langle i e^{i\theta_j}, p_\theta \rangle) (\omega_0 - u_j), \end{aligned}$$

where we used the fact that  $\sum_{j=1}^N \langle i e^{i\theta_j}, p_\theta \rangle = N \langle i p_\theta, p_\theta \rangle = 0$ . Choosing a shape control that is a composite of (5.3) and (4.6), that is,

$$u_k = \omega_0 (1 + K_0 \langle e^{i\theta_k}, P_k \mathbf{c} \rangle) - K \langle i e^{i\theta_k}, p_\theta \rangle, \quad K_0 > 0, \quad (5.8)$$

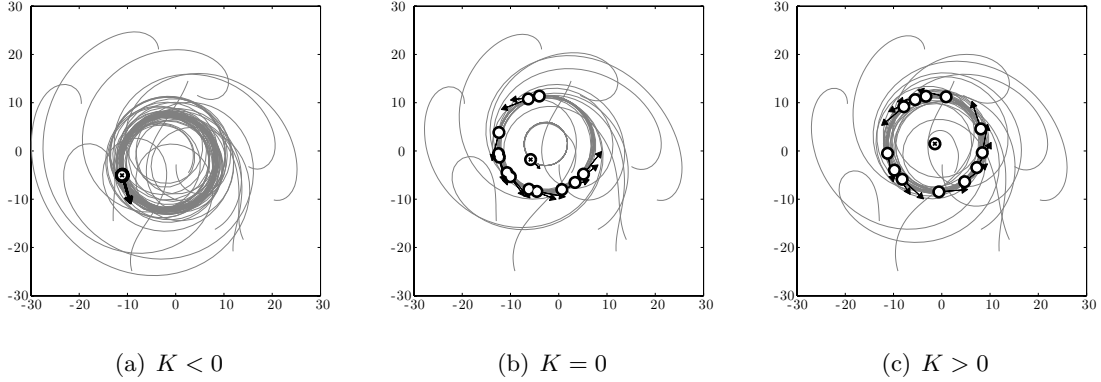


Figure 5.1: All-to-all composite phase and formation control. Simulations of the closed-loop particle model with the all-to-all, composite circular formation control (5.8) for  $N = 12$ ,  $\omega_0 = K_0 = 0.1$ , and  $K \in \{-0.1, 0, 0.1\}$ . We denote the position centroid  $p_r$  by a circle marked with an x; the velocity  $\dot{p}_r$  equals the order parameter  $p_\theta$ . (a) Synchronized circular formation; (b) arbitrary circular formation; (c) balanced circular formation.

yields

$$\dot{V} = - \sum_{j=1}^N \left( \omega_0 K_0 \langle e^{i\theta_j}, P_j \mathbf{c} \rangle - K \langle i e^{i\theta_j}, p_\theta \rangle \right)^2 \leq 0. \quad (5.9)$$

This leads to the following corollary to Theorem 5.1 [243, Theorem 3], which is illustrated in Figure 5.1.

**Corollary 5.2. All-to-all synchronized and balanced circular formation control**

*The results of Theorem 5.1 apply when control (5.3) is replaced by (5.8). If  $K \neq 0$ , then all of the circular formations in the limiting set have a phase arrangement in the critical set of the all-to-all phase potential (4.1). If  $K < 0$ , then all of the synchronized circular formations are asymptotically stable and all of the remaining circular formations are unstable. If  $K > 0$ , then all of the balanced circular formations are asymptotically stable and all of the remaining circular formations are unstable.*

*Proof.* This proof follows the proof of Theorem 5.1. Since the control (5.8) is a shape control, then the closed-loop particle model evolves on the reduced shape space. Furthermore, the potential  $V(\mathbf{r}, \boldsymbol{\theta})$  is positive definite and proper in the reduced shape space and  $\dot{V}(\mathbf{r}, \boldsymbol{\theta}) \leq 0$  by (5.9). Let  $\Omega$  be the set of all of the points in the reduced shape space where  $\dot{V} = 0$ . In

this set,

$$\omega_0 K_0 \langle e^{i\theta_k}, P_k \mathbf{c} \rangle - K \langle ie^{i\theta_k}, p_\theta \rangle = 0, \quad (5.10)$$

which implies  $\dot{\boldsymbol{\theta}} = \omega_0 \mathbf{1}$  and  $\mathbf{c}$  is constant. Let  $\Lambda$  denote the largest invariant set in  $\Omega$ .

Taking the time-derivative of (5.10) in  $\Omega$  yields

$$\langle ie^{i\theta_k}, P_k \mathbf{c} \rangle \omega_0^2 + \langle e^{i\theta_k}, \underbrace{\sum_{j=1}^N \dot{c}_{k,j}}_0 \rangle \omega_0 + \underbrace{\langle e^{i\theta_k}, p_\theta \rangle \omega_0 - \langle ie^{i\theta_k}, ip_\theta \rangle \omega_0}_0 = 0,$$

where we used  $\dot{p}_\theta = \omega_0 ip_\theta$ . Consequently, for all points in  $\Lambda$ , we have

$$\langle ie^{i\theta_k}, P_k \mathbf{c} \rangle = 0. \quad (5.11)$$

Equation (5.11) holds only if  $P\mathbf{c} = 0$ , which implies  $\mathbf{c} = \bar{c}\mathbf{1}$  for some  $\bar{c} \in \mathbb{C}$ . Since  $\mathbf{c} = \bar{c}\mathbf{1}$  in  $\Lambda$ , then using (5.10) with  $K \neq 0$ , we observe that points in  $\Lambda$  also satisfy

$$\langle ie^{i\theta_k}, p_\theta \rangle = \frac{\partial U}{\partial \theta_k} = 0, \quad (5.12)$$

where the all-to-all phase potential  $U(\boldsymbol{\theta})$  is defined in (4.1). Equation (5.12) holds only if  $\boldsymbol{\theta}$  is a critical point of  $U(\boldsymbol{\theta})$ . By the invariance principle [131, Theorem 4.4 and Corollary 4.2], every solution of the closed-loop particle model approaches  $\Lambda$  as  $t \rightarrow \infty$ . Using Lemma A.2 with  $V_1(\mathbf{x})$  replaced by  $\omega_0^2 K_0 S(\mathbf{r}, \boldsymbol{\theta})$  and  $V_2(\mathbf{x})$  replaced by  $KU(\boldsymbol{\theta})$ , we obtain the stability of critical points of  $U(\boldsymbol{\theta})$  in  $\Lambda$  from Theorem 4.2.  $\square$

The set of circular formations defines a manifold of dimension  $N$ , since the particle model has  $3N$  states and the equation  $\mathbf{c} = \bar{c}\mathbf{1}$  has rank  $2N$ .<sup>1</sup> The set of synchronized circular formations is a manifold of dimension 1, since the equation  $|p_\theta| = 1$  imposes  $N - 1$  linearly-independent constraints. The dimension of the manifold defined by the set of balanced circular formations depends on the parity of  $N$  (see discussion after Definition 3.3). For  $N$  odd, the equation  $p_\theta = 0$  has rank two and the set of balanced circular formations defines a manifold of dimension  $N - 2$ . For  $N$  even, the equation  $p_\theta = 0$  is not full rank and the set of balanced circular formations is an  $(N - 1)$ -parameter family.

<sup>1</sup>When a submanifold is defined by an equation, the codimension of the submanifold is the rank of the Jacobian matrix of the equation [32, pp. 68-69].

## 5.2 Time-invariant and Undirected Interaction

We now derive the circular formation control for limited interaction that is time-invariant and undirected. The development mirrors the all-to-all analysis in Section 5.1 with the all-to-all potentials replaced by Laplacian quadratic forms. We combine the Laplacian circular formation control with the Laplacian phase control to isolate circular formations where the phase arrangement is a critical point of the phase potential.

Let  $L$  be the Laplacian of a time-invariant and undirected graph  $G = (\mathcal{N}, E)$ . The *Laplacian circular formation potential* is

$$S_L(\mathbf{r}, \boldsymbol{\theta}) \triangleq \frac{1}{2} Q_L(\mathbf{c}) = \frac{1}{2} \langle \mathbf{c}, L\mathbf{c} \rangle. \quad (5.13)$$

By the properties of the Laplacian quadratic form, the potential (5.13) is zero if  $\mathbf{c} = \bar{c}\mathbf{1}$ . Note that the all-to-all circular formation potential  $S(\mathbf{r}, \boldsymbol{\theta})$  defined in (5.2) is equivalent to  $\frac{1}{N} S_{NP}(\mathbf{r}, \boldsymbol{\theta})$ , since  $NP$  is the Laplacian matrix of a complete graph. The time-derivative of  $S_L(\mathbf{r}, \boldsymbol{\theta})$  along solutions of the closed-loop particle model (3.5) is

$$\dot{S}_L = \frac{1}{2} \langle \dot{\mathbf{c}}, \underbrace{(L + L^T)}_{2L} \mathbf{c} \rangle = \omega_0^{-1} \sum_{j=1}^N (\omega_0 - u_j) \langle e^{i\theta_j}, L_j \mathbf{c} \rangle.$$

Choosing the Laplacian circular formation control

$$u_k = \omega_0(1 + K_0 \langle e^{i\theta_k}, L_k \mathbf{c} \rangle), \quad K_0 > 0, \quad (5.14)$$

results in

$$\dot{S}_L = -K_0 \sum_{j=1}^N \langle e^{i\theta_j}, L_j \mathbf{c} \rangle^2 \leq 0.$$

The control (5.14) is a shape control since the terms

$$\langle e^{i\theta_k}, L_k \mathbf{c} \rangle = \sum_{j \in \mathcal{N}_k} \langle e^{i\theta_k}, r_{k,j} + \omega_0^{-1} i e^{i\theta_j} \rangle$$

depend only on the shape variables  $e^{-i\theta_k} r_{k,j}$  and  $\theta_{k,j}$  for all pairs  $j$  and  $k$ .

Following Section 5.1, we consider a linear combination of the Laplacian circular formation potential  $S_L(\mathbf{r}, \boldsymbol{\theta})$  and the Laplacian phase potential  $W_L(\boldsymbol{\theta})$  defined in (4.13). The

composite potential is

$$V_L(\mathbf{r}, \boldsymbol{\theta}) = \omega_0^2 K_0 S_L(\mathbf{r}, \boldsymbol{\theta}) - K W_L(\boldsymbol{\theta}), \quad K_0 > 0, K \in \mathbb{R}. \quad (5.15)$$

The time-derivative of  $V_L(\mathbf{r}, \boldsymbol{\theta})$  along solutions of the closed-loop particle model (3.5) is

$$\begin{aligned} \dot{V}_L &= \omega_0 \sum_{j=1}^N (\omega_0 - u_j) \langle e^{i\theta_j}, L_j \mathbf{c} \rangle - K \sum_{j=1}^N \langle i e^{i\theta_j}, L_j e^{i\theta} \rangle u_j \\ &= \sum_{j=1}^N (\omega_0 K_0 \langle e^{i\theta_j}, L_j \mathbf{c} \rangle + K \langle i e^{i\theta_j}, L_j e^{i\theta} \rangle) (\omega_0 - u_j), \end{aligned}$$

where we used the fact that  $\sum_{j=1}^N \langle i e^{i\theta_j}, L_j e^{i\theta} \rangle = \langle i e^{i\theta}, L e^{i\theta} \rangle = \langle i B^T e^{i\theta}, B^T e^{i\theta} \rangle = 0$ .

Choosing a shape control that is a composite of (5.14) and (4.15), that is,

$$u_k = \omega_0 (1 + K_0 \langle e^{i\theta_k}, L_k \mathbf{c} \rangle) + K \langle i e^{i\theta_k}, L_k e^{i\theta} \rangle, \quad K_0 > 0, \quad (5.16)$$

yields

$$\dot{V}_L = - \sum_{j=1}^N \left( \omega_0 K_0 \langle e^{i\theta_j}, L_j \mathbf{c} \rangle + K \langle i e^{i\theta_j}, L_j e^{i\theta} \rangle \right)^2 \leq 0. \quad (5.17)$$

This leads to the following result [241, Theorem 5].

**Theorem 5.3. Laplacian circular formation control** *Let  $L$  be the Laplacian of an undirected and connected graph  $G$ . All solutions of the closed-loop particle model (3.5) with the shape control (5.16) converge to the set of circular formations with radius  $|\omega_0|^{-1}$  and direction of rotation determined by the sign of  $\omega_0$ . If  $K \neq 0$ , then the limiting phase arrangement is in the set of critical points of the Laplacian phase potential  $W_L(\boldsymbol{\theta})$  defined in (4.13). If  $K < 0$ , then all of the synchronized circular formations are asymptotically stable, whereas, if  $K > 0$ , then all of the synchronized circular formations are unstable. If  $K > 0$  and  $G$  is circulant, then all of the balanced circular formations with phase arrangements that maximize  $W_L(\boldsymbol{\theta})$  are asymptotically stable.*

*Proof.* The first part of the proof follows the proofs of Theorem 5.1 and Corollary 5.2. Since the control (5.8) is a shape control, then the closed-loop particle model evolves on the reduced shape space. Furthermore, the potential  $V_L(\mathbf{r}, \boldsymbol{\theta})$  is positive definite and proper in the reduced shape space and  $\dot{V}_L(\mathbf{r}, \boldsymbol{\theta}) \leq 0$  by (5.17). Let  $\Omega$  be the set of all of the points in the reduced shape space where  $\dot{V}_L = 0$ . In this set,

$$\omega_0 K_0 \langle e^{i\theta_k}, L_k \mathbf{c} \rangle + K \langle i e^{i\theta_k}, L_k e^{i\theta} \rangle = 0, \quad (5.18)$$

which implies  $\dot{\boldsymbol{\theta}} = \omega_0 \mathbf{1}$  and  $\mathbf{c}$  is constant. Let  $\Lambda$  denote the largest invariant set in  $\Omega$ . Taking the time-derivative of (5.18) in  $\Omega$  yields

$$\langle ie^{i\theta_k}, L_k \mathbf{c} \rangle \omega_0^2 + \langle e^{i\theta_k}, \underbrace{\sum_{j \in \mathcal{N}_k} \dot{c}_{k,j}}_0 \rangle \omega_0 + \underbrace{\langle -e^{i\theta_k}, L_k e^{i\boldsymbol{\theta}} \rangle \omega_0 + \langle ie^{i\theta_k}, iL_k e^{i\boldsymbol{\theta}} \rangle \omega_0}_0 = 0,$$

where we used  $\frac{d}{dt}(L_k e^{i\boldsymbol{\theta}}) = \omega_0 i L_k e^{i\boldsymbol{\theta}}$ . Thus, points in  $\Lambda$  satisfy

$$\langle ie^{i\theta_k}, L_k \mathbf{c} \rangle = 0. \quad (5.19)$$

Equation (5.19) holds only if  $L\mathbf{c} = 0$ , which implies  $\mathbf{c} = \bar{c}\mathbf{1}$  for some  $\bar{c} \in \mathbb{C}$ . Since  $\mathbf{c} = \bar{c}\mathbf{1}$  in  $\Lambda$ , then using (5.18) with  $K \neq 0$ , we observe that points in  $\Lambda$  also satisfy

$$\langle ie^{i\theta_k}, L_k e^{i\boldsymbol{\theta}} \rangle = \frac{\partial W_L}{\partial \theta_k} = 0. \quad (5.20)$$

Equation (5.20) holds only if  $\boldsymbol{\theta}$  is a critical point of  $W_L(\boldsymbol{\theta})$ . By the invariance principle [131, Theorem 4.4 and Corollary 4.2], every solution of the closed-loop particle model approaches  $\Lambda$  as  $t \rightarrow \infty$ . Using Lemma A.2 with  $V_1(\mathbf{x})$  replaced by  $\omega_0^2 K_0 S_L(\mathbf{r}, \boldsymbol{\theta})$  and  $V_2(\mathbf{x})$  replaced by  $-KW_L(\boldsymbol{\theta})$ , we obtain the stability of critical points of  $W_L(\boldsymbol{\theta})$  in  $\Lambda$  from Theorem 4.7.  $\square$

### 5.3 General Interaction

In this section, we design a dynamic algorithm to stabilize the set of circular formations with possibly time-varying and/or directed interaction. Let  $L(t)$  denote the graph Laplacian of an interaction network  $G(t)$  that is uniformly connected. The development of the dynamic circular formation control follows the design of the dynamic phase control. In the design of the dynamic phase control, we started by revisiting the all-to-all phase control. Here, we start by revisiting the all-to-all circular formation control (5.3).

We rewrite the all-to-all circular formation control in such a way as to expose its dependence on two average quantities: the phase order parameter  $p_\theta$  and the position centroid  $p_r$ . The all-to-all circular formation control is

$$\begin{aligned} u_k &= \omega_0 \left( 1 + K_0 \langle e^{i\theta_k}, r_k + \omega_0^{-1} i e^{i\theta_k} - \frac{1}{N} \sum_{j=1}^N (r_j + \omega_0^{-1} i e^{i\theta_j}) \rangle \right) \\ &= \omega_0 (1 + K_0 \langle e^{i\theta_k}, r_k - p_r \rangle) + K_0 \langle i e^{i\theta_k}, p_\theta \rangle, \quad K_0 > 0. \end{aligned} \quad (5.21)$$

Let  $u'_k = \omega_0 K_0 \langle e^{i\theta_k}, r_k - p_r \rangle$ , so that  $u_k = \omega_0 + u'_k + K_0 \langle i e^{i\theta_k}, p_\theta \rangle$ . For the moment, consider the control  $u_k$  with  $u'_k = 0$ . In this case,  $u_k$  is equivalent to (4.9) with  $K = -K_0 < 0$ . This means that the all-to-all circular formation control includes a term that is identical to the all-to-all phase synchronization control. For the purposes of designing the dynamic circular formation control, this suggests to incorporate the dynamic phase synchronization algorithm. That is, in place of the average quantity  $p_\theta$ , we use the consensus variable  $z_k$ , where (see Theorem 4.10)

$$\dot{z} = -L(t)z. \quad (5.22)$$

We also seek to replace the position centroid  $p_r$  in (5.21) with a consensus variable  $y_k \in \mathbb{C}$ . Consider the estimator dynamics

$$\dot{y}_k = \dot{p}_r + \sum_{j \in \mathcal{N}_k(t)} (y_j - y_k) = p_\theta - L_k(t)y. \quad (5.23)$$

If  $y_k(0) = p_r(0)$ , then the solution to (5.23) is  $y_k(t) = p_r(t)$ . If  $y_k(0) \neq p_r(0)$ , then it seems reasonable that the estimator dynamics (5.23) converge to  $\bar{y} \in \mathbb{C}$  and that  $\bar{y} = \lim_{t \rightarrow \infty} p_r(t)$ . However, the value of  $p_\theta$  may not be available at each node. One might consider using a dynamic phase balancing algorithm in order to estimate  $p_\theta$ , but this would require interaction network to be balanced. To avoid this requirement, we consider an alternative algorithm.

Suppose, instead of (5.23), we let  $y_k$  obey the consensus dynamics

$$\dot{y} = -L(t)y. \quad (5.24)$$

Using (5.24), each  $y_k$  converges to  $\bar{y}$  by Proposition 4.9. But (5.24) is not an estimator of  $p_r$  since it is uncoupled from the particle dynamics. Nonetheless, we use (5.24) and (5.22) to create the dynamic circular formation algorithm, which is the all-to-all circular formation control (5.21) with  $p_r$  replaced by  $y_k$  and  $p_\theta$  replaced by  $z_k$ . We write the dynamic circular formation algorithm in shape coordinates using  $y_k \triangleq v_k e^{i\theta_k} + r_k$  and  $z_k \triangleq w_k e^{i\theta_k}$ :

$$\begin{aligned} u_k &= \omega_0(1 - K_0 \langle v_k, 1 \rangle) + K_0 \langle w_k, i \rangle, \quad K_0 > 0 \\ \dot{w}_k &= -u_k i w_k - \sum_{j=1}^N l_{kj}(t) w_j e^{i\theta_{j,k}}, \quad w_k(0) = 1 \\ \dot{v}_k &= -1 - u_k i v_k - \sum_{j=1}^N l_{kj}(t) (v_j e^{i\theta_{j,k}} - r_j e^{-i\theta_k}), \quad v_k(0) = 0. \end{aligned} \quad (5.25)$$

Note that the terms  $\sum_{j=1}^N l_{kj}(t)w_j e^{i\theta_{j,k}} = \sum_{j \in \mathcal{N}_k(t)} (w_k - w_j e^{i\theta_{j,k}})$  and  $\sum_{j=1}^N l_{kj}(t)(v_j e^{i\theta_{j,k}} - r_j e^{-i\theta_k}) = \sum_{j \in \mathcal{N}_k(t)} (v_k - v_j e^{i\theta_{j,k}} - r_{k,j} e^{-i\theta_k})$  are indeed in shape coordinates. However, computing (5.25) requires the transmission to node  $k$  of the consensus variables  $w_j$  and  $v_j$  from each node  $j \in \mathcal{N}_k(t)$  for all  $t$ . We have the following result [241, Theorem 6]).

**Theorem 5.4. Dynamic circular formation control** *Let  $L(t)$  be the Laplacian matrix of a graph  $G(t)$  that is uniformly connected. The shape control (5.25) enforces asymptotic convergence of  $z_k \triangleq w_k e^{i\theta_k}$  to  $\bar{z} \in \mathbb{C}$  and  $y_k \triangleq v_k e^{i\theta_k} + r_k$  to  $\bar{y} \in \mathbb{C}$ . In addition, all of the solutions of the closed-loop particle model (3.5) converge to the set of circular formations with radius  $|\omega_0|^{-1}$ , direction of rotation determined by the sign of  $\omega_0 \neq 0$ , and center  $\bar{c} \triangleq \bar{y} + \omega_0^{-1} i \bar{z}$ . If  $G(t)$  is balanced, then  $\bar{z} = p_\theta(0)$ ,  $\bar{y} = p_r(0)$ , and  $\bar{c} = p_c(0)$ , where  $p_c \triangleq p(\mathbf{c}) = p_r + \omega_0^{-1} i p_\theta$  is the centroid of all the circle centers.*

*Proof.* The time-derivatives of  $z_k$  and  $y_k$  along solutions of the closed-loop particle model (3.5) with shape control (5.25) are

$$\dot{z}_k = \dot{w}_k e^{i\theta_k} + u_k w_k i e^{i\theta_k} = - \sum_{j=1}^N l_{kj}(t) w_j e^{i\theta_j} = -L_k(t) \mathbf{z}$$

and

$$\dot{y}_k = \dot{v}_k e^{i\theta_k} + u_k v_k i e^{i\theta_k} + e^{i\theta_k} = - \sum_{j=1}^N l_{kj}(t) (v_j e^{i\theta_j} - r_j) = -L_k(t) \mathbf{y},$$

which means that  $\mathbf{z}$  and  $\mathbf{y}$  obey the consensus dynamics (5.22) and (5.24). By Proposition 4.9, the set of consensus states  $\mathbf{z} = \bar{z} \mathbf{1}$  and  $\mathbf{y} = \bar{y} \mathbf{1}$  is asymptotically stable. If  $G(t)$  is balanced, then  $\bar{z} = (1/N) \sum_{j=1}^N w_k(0) e^{i\theta_k(0)} = p_\theta(0)$  and  $\bar{y} = (1/N) \sum_{j=1}^N (v_k(0) e^{i\theta_k(0)} + r_k(0)) = p_r(0)$ . In the limit  $t \rightarrow \infty$ , the control (5.25) converges to

$$\begin{aligned} u_k &= \omega_0 (1 + K_0 \langle e^{i\theta_k}, r_k - \bar{y} \rangle) + K_0 \langle i e^{i\theta_k}, \bar{z} \rangle \\ &= \omega_0 (1 + K_0 \langle e^{i\theta_k}, r_k - \underbrace{(\bar{y} + \omega_0^{-1} i \bar{z})}_{\bar{c}} \rangle) \end{aligned} \quad (5.26)$$

The limit set of the closed-loop particle model in the reduced shape space is the set of relative equilibria of the closed-loop particle model with the limiting control (5.26) [172,

Theorem 1.8]. The closed-loop particle model with the control (5.26) is a collection of  $N$  decoupled, autonomous subsystems:

$$\begin{aligned}\dot{r}_k &= e^{i\theta_k} \\ \dot{\theta}_k &= \omega_0(1 + K_0\langle e^{i\theta_k}, r_k - \bar{c} \rangle).\end{aligned}\tag{5.27}$$

Along the solutions of (5.27), the quadratic form

$$\bar{S}(\mathbf{r}, \boldsymbol{\theta}) \triangleq \frac{1}{2} \|\mathbf{c} - \bar{c}\mathbf{1}\|^2$$

has the time-derivative

$$\begin{aligned}\dot{\bar{S}} &= \sum_{j=1}^N \langle \dot{c}_j, c_j - \bar{c} \rangle = \omega_0^{-1} \langle e^{i\theta_j}, r_j + \omega_0^{-1} i e^{i\theta_j} - \bar{c} \rangle (\omega_0 - u_j) \\ &= -K_0 \sum_{j=1}^N \langle e^{i\theta_j}, r_j - \bar{c} \rangle^2 \leq 0.\end{aligned}$$

Let  $\Omega$  be the set of all of the points for which  $\dot{\bar{S}} = 0$ . In this set,

$$\langle e^{i\theta_k}, r_k - \bar{c} \rangle = \langle e^{i\theta_k}, c_k - \bar{c} \rangle = 0,\tag{5.28}$$

which implies  $\dot{\boldsymbol{\theta}} = \omega_0 \mathbf{1}$  and  $\mathbf{c}$  is constant. Equation (5.28) holds only if  $\mathbf{c} = \bar{c}\mathbf{1}$ . Let  $\Lambda$  denote the set of circular formations with radius  $|\omega_0|^{-1}$ , direction of rotation determined by the sign of  $\omega_0$ , and center  $\bar{c}$ . Note  $\Lambda$  is the largest invariant set in  $\Omega$ . By the invariance principle [131, Theorem 4.4 and Corollary 4.2], every solution of (5.27) approaches  $\Lambda$  as  $t \rightarrow \infty$ .

If the interaction network is uniformly connected and balanced, then by Theorem 5.4, we have  $\bar{z} \rightarrow p_\theta(0)$ ,  $\bar{y} \rightarrow p_r(0)$ , and  $c_k \rightarrow \bar{c} = \bar{y} + \omega_0^{-1} i \bar{z} = p_c(0)$ . Furthermore, we have

$$\bar{c} = \lim_{t \rightarrow \infty} \frac{1}{N} \sum_{j=1}^N (r_k(t) + \omega_0^{-1} i e^{i\theta_k(t)}) = \lim_{t \rightarrow \infty} p_c(t),$$

which implies  $p_c(t) \rightarrow p_c(0)$  as  $t \rightarrow \infty$ . □

We illustrate in Figure 5.2 a numerical simulation of the closed-loop particle model (3.5) with the dynamic circular formation control (5.25) and a time-varying interaction network  $G(t)$ . In the simulation, proximity-based interaction occurs between two particles  $j$  and  $k$  if the relative position  $\mathbf{r}_{k,j}$  satisfies  $\|\mathbf{r}_{k,j}\| \leq \rho_0$ . The perceptual zone radius  $\rho_0 > 0$

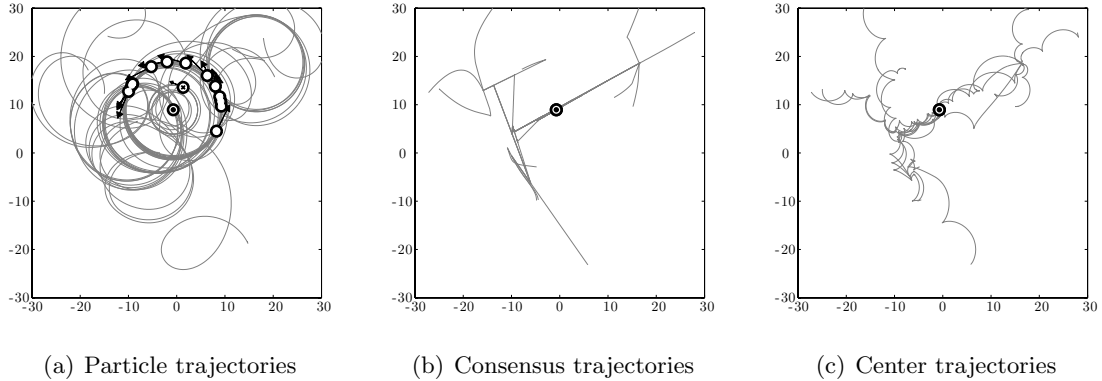


Figure 5.2: Dynamic circular formation control. Simulations of the closed-loop particle model (3.5) with the dynamic circular formation control (5.25) for  $N = 12$ ,  $K_0 = 0.1$ , and  $\omega_0 = 0.1$ . The interaction network is proximity-based and zonal; there is interaction only between neighboring particles separated by less than  $|\omega_0|^{-1}$ . We denote the position centroid  $p_r$  by a circle marked with  $\times$ ; the velocity of  $p_r$  equals the order parameter  $p_\theta$ . We denote the final center centroid  $p_c(t)$ ,  $t \rightarrow \infty$ , by a circle marked with  $\bullet$ . (a) Trajectories of the particles converge to a circular formation centered at  $p_c(0)$ . In (b), trajectories of the consensus quantity  $y_k + \omega_0^{-1}iz_k$  converge to  $p_c(0)$ . In (c), trajectories of the centers  $c_k$  converge to  $p_c(0)$ .

is the same for all particles, which means that  $G(t)$  is an example of a zonal interaction network that is balanced. This type of interaction network is not guaranteed to be uniformly connected with respect to a single node. For example, if  $\rho_0$  is infinitesimally small, then the particles may not interact at all. In the simulation shown in Figure 5.2, we used  $N = 12$  and  $\rho_0 = |\omega_0|^{-1} = 10$ . The particle initial positions were selected at random from a uniform distribution, such that  $-25 \leq \text{Re}\{r_k(0)\} < 25$  and  $-25 \leq \text{Im}\{r_k(0)\} < 25$ ,  $k \in \mathcal{N}$ .

The simulation interaction network is not initially connected since the initial graph Laplacian  $L(0)$  has three zero eigenvalues (the multiplicity of zero as an eigenvalue of  $L(t)$  is the number of connected components of  $G(t)$  [93, Lemma 13.1.1]). Furthermore, after becoming connected, the interaction network does not necessarily stay connected since the multiplicity of zero as an eigenvalue of  $L(t)$  increases from one to two on several occasions. Nonetheless, we infer that the interaction network is most likely uniformly connected since the simulated particle trajectories converge to a circular formation, shown in Figure 5.2(a),

with a connected interaction network.<sup>2</sup> Since the circular formation is a relative equilibrium of the particle model, the interaction network will remain connected in the limit  $t \rightarrow \infty$ . Therefore, a value of  $T$  that satisfies the definition of uniform connectivity in Definition 3.11 is  $T = t^*$ , where  $t^*$  is the end time of the simulation.

Figure 5.2 also confirms several expectations for the simulated solutions. First, Figure 5.2(b) shows that the consensus quantity  $y_k + \omega_0^{-1}iz_k$  converges to the center consensus  $\bar{c} = p_c(0)$ , which is the initial center centroid. Note that the trajectories of the consensus quantity are piecewise-smooth; the discontinuities occur in the  $k$ th trajectory whenever the neighbor set  $\mathcal{N}_k(t)$  changes. Second, Figure 5.2(c) shows that each center  $c_k$  converges to the initial center centroid  $p_c(0)$ . The trajectories of all of the  $c_k$  appear to be cycloidal; the discontinuities are presumably due to changing neighbor sets. Thirdly, Figure 5.2 shows that the limiting center centroid  $\lim_{t \rightarrow \infty} p_c(t) = p_c(0)$ , although  $p_c(t)$  is not conserved ( $p_c(0)$  may not be visible if it is hidden behind  $p_c(t)$ ).

In addition, Figure 5.2 illustrates an unexpected and possibly revealing phenomenon, which is, the consensus trajectories in Figure 5.2(b) tend to coalesce in a tree-like pattern. That is, individual trajectories (leaves) merge with neighboring trajectories to form branches; the branches merge with neighboring branches to form the trunk; and the trunk leads to the root (the final formation center  $p_c(t) = p_c(0)$ ). This phenomenon is also apparent in Figure 5.2(a)), which shows that the particle trajectories collectively trace several intermediate circular formations before finally converging on a single common formation. The incremental path from local to global consensus illustrated in Figure 5.2 is perhaps a fundamental tendency of consensus algorithms with time-varying interaction. This observation is perhaps related to recent results on time-scale separations due to weak and strong coupling in networks [28].

To complete this section, we provide a corollary to Theorem 5.4 analogous to Corollary 5.2. In Corollary 5.5 below, we provide an algorithm by which to isolate either the set

---

<sup>2</sup>We cannot conclude from convergence to an arbitrary circular formation that the network is uniformly connected, because by Proposition 4.9, uniform connectedness is sufficient condition for consensus, not a necessary one. In fact, there may be a weaker sufficient condition.

of synchronized circular formations or the set of balanced circular formations with time-varying and/or directed interaction. The design of this algorithm is intuitive in that it follows the design of the corresponding algorithm described in Corollary 5.2. Namely, we combine the dynamic circular formation control (5.25) with the dynamic phase synchronization and balancing control (4.26) defined in Section 4.3. Recall  $H(K)$  denotes the Heaviside function defined in (4.25). The composite control is

$$\begin{aligned}
u_k &= \omega_0(1 - K_0\langle v_k, \mathbf{1} \rangle) + K_0\langle w_k, i \rangle - K\langle w_k^{(1)}, i \rangle, \quad K_0 > 0, \\
\dot{w}_k &= -u_k i w_k - \sum_{j=1}^N l_{kj}(t) w_j e^{i\theta_{j,k}}, \quad w_k(0) = 1 \\
\dot{v}_k &= -1 - u_k i v_k - \sum_{j=1}^N l_{kj}(t) (v_j e^{i\theta_{j,k}} - r_j e^{-i\theta_k}), \quad v_k(0) = 0 \\
\dot{w}_k^{(1)} &= (u_k - \omega_0) i (H(K) - w_k^{(1)}) - \sum_{j=1}^N l_{kj}(t) w_j^{(1)} e^{i\theta_{j,k}}, \quad w_k^{(1)}(0) = 1.
\end{aligned} \tag{5.29}$$

(The choice of the superscript  $(1)$  notation to distinguish the term  $w_k^{(1)}$  from  $w_k$  is motivated by Section 6.3.) The following result is a consequence of Theorems 5.4 and 4.10.

**Corollary 5.5. Dynamic synchronized and balanced circular formation control.**

*The results of Theorem 5.4 apply when control (5.25) is replaced by (5.29). Furthermore, the control (5.29) enforces asymptotic convergence of  $z_k^{(1)} \triangleq w_k^{(1)} e^{i(\theta_k - \omega_0 t)}$  to  $\bar{z}^{(1)} \in \mathbb{C}$ .*

*Let  $K < 0$  and assume  $|\bar{z}^{(1)}| > 0$ . The synchronized circular formations where  $\boldsymbol{\theta} - \omega_0 t \mathbf{1} = \arg \bar{z}^{(1)} \mathbf{1}$  are asymptotically stable and all of the remaining circular formations are unstable. If  $G(t)$  is balanced and the initial phase arrangement  $\boldsymbol{\theta}(0)$  is not balanced, then  $\bar{z}^{(1)} = p_\theta(0) \neq 0$ .*

*Let  $K > 0$  and assume  $G(t)$  is balanced and uniformly connected to a single node. All of the balanced circular formations are asymptotically stable and all of the remaining circular formations are unstable. In addition,  $\bar{z}^{(1)} = \lim_{t \rightarrow \infty} p_\theta(t) = 0$ .*

*Proof.* As in the proof of Theorem 5.4, the consensus variables  $\mathbf{z}$  and  $\mathbf{y}$  obey the consensus dynamics (4.24). This means that  $\lim_{t \rightarrow \infty} z_k(t) = \bar{z}$  and  $\lim_{t \rightarrow \infty} y_k(t) = \bar{y}$ . Let  $\bar{c} \triangleq \bar{y} + \omega_0^{-1} i \bar{z}$ . The time-derivative of  $z_k^{(1)}$  along solutions of the closed-loop particle model with control (5.29) is

$$\dot{z}_k^{(1)} = H(K)(u_k - \omega_0) i e^{i(\theta_k - \omega_0 t)} - L_k(t) \mathbf{z}^{(1)} = H(K) \frac{d}{dt} e^{i(\theta_k - \omega_0 t)} - L_k \mathbf{z}^{(1)}.$$

We consider the case  $K < 0$  first. In this case,  $H(K) = 0$  and the consensus variable  $\mathbf{z}^{(1)}$  obeys the consensus dynamics (4.24), which means that  $\lim_{t \rightarrow \infty} z_k^{(1)}(t) = \bar{z}^{(1)}$ . In the limit  $t \rightarrow \infty$ , the closed-loop particle model with the control (5.29) converges to

$$\begin{aligned} \dot{r}_k &= e^{i\theta_k} \\ \dot{\theta}_k &= \omega_0(1 + K_0 \langle e^{i\theta_k}, r_k - \bar{c} \rangle) - K \langle i e^{i(\theta_k - \omega_0 t)}, \bar{z}^{(1)} \rangle. \end{aligned} \quad (5.30)$$

The limit set of the closed-loop particle model is the critical set of the limiting (autonomous) system (5.30) [172, Theorem 1.8]. Along the solutions of (5.30), the quadratic form

$$\bar{V}(\mathbf{r}, \boldsymbol{\theta}) \triangleq \omega_0^2 \frac{K_0}{2} \|\mathbf{c} - \bar{c}\mathbf{1}\|^2 - \frac{K}{2} \|e^{i(\boldsymbol{\theta} - \omega_0 \mathbf{1})} - \bar{z}^{(1)}\mathbf{1}\|^2$$

has the time-derivative

$$\begin{aligned} \dot{\bar{V}} &= \sum_{j=1}^N (\omega_0 K_0 \langle e^{i\theta_j}, r_j + \omega_0^{-1} i e^{i\theta_j} - \bar{c} \rangle - K \langle i e^{i(\theta_j - \omega_0 t)}, e^{i(\theta_j - \omega_0 t)} - \bar{z}^{(1)} \rangle) (\omega_0 - u_j) \\ &= \sum_{j=1}^N (\omega_0 K_0 \langle e^{i\theta_j}, r_j - \bar{c} \rangle - K \langle i e^{i(\theta_j - \omega_0 t)}, \bar{z}^{(1)} \rangle)^2 \leq 0. \end{aligned}$$

Let  $\Omega$  be the set of all of the points for which  $\dot{\bar{V}} = 0$ . In this set,

$$\omega_0 K_0 \underbrace{\langle e^{i\theta_j}, r_j - \bar{c} \rangle}_{\langle e^{i\theta_j}, c_j - \bar{c} \rangle} - K \langle i e^{i(\theta_k - \omega_0 t)}, \bar{z}^{(1)} \rangle = 0, \quad (5.31)$$

which implies  $\dot{\boldsymbol{\theta}} = \omega_0 \mathbf{1}$  and  $\mathbf{c}$  is constant. Let  $\Lambda$  denote the largest invariant set in  $\Omega$ . Taking the time-derivative of (5.31) in  $\Omega$  yields

$$\langle i e^{i\theta_k}, c_k - \bar{c} \rangle \omega_0 + \underbrace{\langle e^{i\theta_k}, \dot{c}_k \rangle}_0 - \langle e^{i(\theta_k - \omega_0 t)}, \bar{z} \rangle \underbrace{(\dot{\theta}_k - \omega_0)}_0 = 0.$$

Thus, points in  $\Lambda$  satisfy  $\langle i e^{i\theta_k}, c_k - \bar{c} \rangle = 0$ , which holds only if  $\mathbf{c} = \bar{c}\mathbf{1}$  (that is, every point in  $\Lambda$  is a circular formation centered at  $\bar{c}$ ). Using (5.31) with  $K \neq 0$ , this implies that points in  $\Lambda$  also satisfy

$$\langle i e^{i(\theta_k - \omega_0 t)}, \bar{z}^{(1)} \rangle = |\bar{z}^{(1)}| \sin(\arg\{\bar{z}^{(1)}\} - (\theta_k - \omega_0 t)) = 0. \quad (5.32)$$

Equation (5.32) holds only if  $|\bar{z}^{(1)}| = 0$  or both  $|\bar{z}^{(1)}| > 0$  and  $\phi_k \triangleq \theta_k - \omega_0 t = \arg\{\bar{z}^{(1)}\} \bmod \pi$ . If  $|\bar{z}^{(1)}| = 0$ , then  $\boldsymbol{\theta} = \boldsymbol{\phi} + \omega_0 \mathbf{1}$  is arbitrary. If  $|\bar{z}^{(1)}| > 0$ , then synchronization of all phases  $\phi_k$  to  $\arg\{\bar{z}^{(1)}\}$  is exponentially stable and the set of phase arrangements  $\boldsymbol{\phi}$

where at least one phase equals  $\arg\{\bar{z}^{(1)}\} + \pi$  is unstable. If  $G(t)$  is balanced, then  $\bar{z}^{(1)} = \frac{1}{N} \sum_{j=1}^N w_k^{(1)}(0) e^{i\theta_k(0)} = p_\theta(0)$  is conserved. If, in addition to  $G(t)$  being balanced,  $\boldsymbol{\theta}(0)$  is not balanced, then  $\bar{z}^{(1)} > 0$ . By the invariance principle [131, Theorem 4.4 and Corollary 4.2], every solution of the limiting dynamics (5.30) approaches  $\Lambda$  as  $t \rightarrow \infty$ . This completes the proof for  $K < 0$ .

Let  $K > 0$ , which means that  $H(K) = 1$ , and assume  $G(t)$  is balanced and uniformly connected to a single node. In this case, the control (5.29) converges to

$$\begin{aligned} \bar{u}_k &\triangleq \omega_0(1 + K_0 \langle e^{i\theta_k}, c_k - \bar{c} \rangle) - K \langle i e^{i(\theta_k - \omega_0 t)}, z_k^{(1)} \rangle \\ \dot{z}_k^{(1)} &= (\bar{u}_k - \omega_0) i e^{i(\theta_k - \omega_0 t)} - L_k(t) \mathbf{z}^{(1)}. \end{aligned} \quad (5.33)$$

Let  $\mathbf{z}^{(1)} \triangleq (z_1^{(1)}, \dots, z_N^{(1)})^T \in \mathbb{C}^N$ . Note  $\mathbf{z}^{(1)}$  obeys the consensus dynamics (4.24) with an additive perturbation. To prove that the perturbation vanishes, consider the quadratic form

$$V(\mathbf{r}, \boldsymbol{\theta}, \mathbf{z}^{(1)}) = \omega_0^2 \frac{K_0}{2} \|\mathbf{c} - \bar{c}\mathbf{1}\|^2 + \frac{K}{2} \|\mathbf{z}^{(1)}\|^2.$$

Along solutions of the closed-loop particle model with control (5.33),  $V(\mathbf{r}, \boldsymbol{\theta}, \mathbf{z}^{(1)})$  has the time-derivative

$$\begin{aligned} \dot{V} &= \sum_{j=1}^N \left( \omega_0 K_0 \langle e^{i\theta_j}, c_j - \bar{c} \rangle - K \langle i e^{i(\theta_j - \omega_0 t)}, z_j^{(1)} \rangle \right) (\omega_0 - \bar{u}_j) - K \langle z_j^{(1)}, L_j(t) \mathbf{z}^{(1)} \rangle \\ &= -\|\bar{\mathbf{u}} - \omega_0 \mathbf{1}\|^2 - Q_{L(t)}(\mathbf{z}^{(1)}) \leq 0. \end{aligned}$$

This means that  $\|\mathbf{c} - \bar{c}\mathbf{1}\|^2$  and  $\|\mathbf{z}^{(1)}\|^2$  are bounded on the interval  $t \in [0, \infty)$ . By two successive applications of Lemma A.1 with  $\phi_1(t) \triangleq Q_{L(t)}(\mathbf{z}^{(1)}(t))$  and  $\phi_2(t) \triangleq \|\bar{\mathbf{u}} - \omega_0 \mathbf{1}\|^2$ , one can show that (i)  $\|\bar{\mathbf{u}}(t) - \omega_0 \mathbf{1}\| : [0, \infty) \rightarrow \mathbb{R}$  is bounded and (ii)  $\bar{u}_k(t) \rightarrow \omega_0$  as  $t \rightarrow \infty$ . Since  $|\bar{u}_k - \omega_0|$  is the magnitude of the perturbation of the consensus dynamics  $\dot{z}_k^{(1)}$ , this implies that the perturbation in (5.33) vanishes.

The computation of the consensus limit  $\bar{z}^{(1)}$  also follows the proof of Theorem 4.10. Since  $G(t)$  is balanced, then  $\mathbf{1}^T L(t) = 0$ . Consequently, left-multiplying  $\dot{\mathbf{z}}^{(1)}$  defined in (5.33) by  $\mathbf{1}^T$  yields

$$\mathbf{1}^T \dot{\mathbf{z}}^{(1)} = \sum_{j=1}^N \frac{d}{dt} e^{i(\theta_j - \omega_0 t)} = \frac{d}{dt} (N p_\theta e^{-i\omega_0 t}),$$

which integrates to  $\mathbf{1}^T \mathbf{z}^{(1)}(t) = N p_\theta(t) e^{-i\omega_0 t}$ . In the limit  $t \rightarrow \infty$ , we have  $\mathbf{1}^T \mathbf{z}^{(1)} = N \bar{z}^{(1)} = N p_\theta(t) e^{-i\omega_0 t}$ , that is,  $\bar{z}^{(1)} e^{i\omega_0 t} = p_\theta(t)$ .

The closed-loop particle model with the control (5.33) asymptotically converges to the time-invariant dynamics

$$\begin{aligned}\dot{r}_k &= e^{i\theta_k} \\ \dot{\theta}_k &= \omega_0(1 + K_0\langle e^{i\theta_k}, r_k - \bar{c} \rangle) - K\langle ie^{i\theta_k}, p_\theta \rangle.\end{aligned}\tag{5.34}$$

Since  $\dot{\theta}_k = \bar{u}_k$  asymptotically converges to  $\omega_0$ , the solutions of (5.34) asymptotically converge to the set  $\Lambda$  of relative equilibria with

$$\omega_0 K_0 \underbrace{\langle e^{i\theta_k}, r_k - \bar{c} \rangle}_{\langle e^{i\theta_k}, c_k - \bar{c} \rangle} - K\langle ie^{i\theta_k}, p_\theta \rangle = 0.\tag{5.35}$$

In  $\Lambda$ ,  $\dot{\boldsymbol{\theta}} = \omega_0 \mathbf{1}$  and  $\mathbf{c}$  is constant. Taking the time-derivative of (5.35) in  $\Lambda$  yields

$$\omega_0^2 K_0 \langle ie^{i\theta_k}, c_k - \bar{c} \rangle + \underbrace{\langle e^{i\theta_k}, \dot{c}_k \rangle}_0 + \underbrace{K\langle e^{i\theta_k}, p_\theta \rangle \omega_0 - K\langle ie^{i\theta_k}, ip_\theta \rangle \omega_0}_0 = 0,$$

where we used  $\dot{p}_\theta = \omega_0 ip_\theta$ . Thus, points in  $\Lambda$  satisfy  $\langle ie^{i\theta_k}, c_k - \bar{c} \rangle = 0$ , which holds only if  $\mathbf{c} = \bar{c}\mathbf{1}$ , and  $\langle ie^{i\theta_k}, p_\theta \rangle = \frac{\partial U}{\partial \theta_k} = 0$ , where  $U(\boldsymbol{\theta})$  is the all-to-all phase potential defined in (4.1). That is, every point in  $\Lambda$  is a circular formation with a phase arrangement in the critical set of  $U(\boldsymbol{\theta})$ . Using Lemma A.2 with  $V_1(\mathbf{x})$  replaced by  $\omega_0^2(K_0/2)\|\mathbf{c} - \bar{c}\mathbf{1}\|^2$  and  $V_2(\mathbf{x})$  replaced by  $U(\boldsymbol{\theta})$ , we obtain the stability of critical points of  $U(\boldsymbol{\theta})$  in  $\Lambda$  from Theorem 4.2.  $\square$

## Chapter 6

# Symmetric Circular Formations

In the previous chapter we describe control algorithms to stabilize circular formations in the particle model. We combine the circular formation algorithms with the phase synchronization and balancing algorithms from Chapter 4 in order to stabilize synchronized and balanced circular formations. That is, a composite phase and formation algorithm stabilizes the set of circular formations where the phase arrangement is a critical point of the all-to-all phase potential.

In this chapter we seek to identify an algorithm to stabilize the set of symmetric circular formations, which are circular formations where the phase arrangement is an  $(M, N)$ -pattern (see Definition 3.4 and Figure 3.3). Circular formations with symmetric phase arrangements also have symmetric particle arrangements, that is, the particles are arranged around the circular formation in the same pattern as the phases are arranged around the unit circle. To see this, let  $\bar{c}$  denote the center of a circular formation and assume  $\boldsymbol{\theta}$  is a symmetric phase pattern. The vector  $r_k - \bar{c}$  represents the position of particle  $k$  relative to the center of the formation. We have

$$\mathbf{r} - \bar{c}\mathbf{1} = \omega_0^{-1} i e^{i\boldsymbol{\theta}} \neq 0.$$

This implies  $\arg\{\mathbf{r} - \bar{c}\mathbf{1}\} = \boldsymbol{\theta} + \frac{\pi}{2}\mathbf{1}$  is also a symmetric phase pattern.

To find a symmetric circular formation algorithm with all-to-all interaction, we first describe a general composite phase and formation algorithm that stabilizes the set of circular

formations where the phase arrangement is a critical point of a rotationally symmetric phase potential. Then we describe the design of phase potentials that are minimized on the set of  $(M, N)$ -patterns. The desired algorithm is an immediate consequence of these two results. The all-to-all algorithm in Section 6.1 provides a roadmap for the design of symmetric circular formation algorithms with limited interaction in Sections 6.2 and 6.3.

## 6.1 All-to-all Interaction

Motivated by the composite phase and formation algorithm in Section 5.1, we first describe a methodology that stabilizes the set of circular formations where the phase arrangement is in the critical set of a phase potential. The only requirements on the phase potential are rotational symmetry and nondegeneracy of the desired critical points in the phase shape space. That is, the phase potential must be invariant to rigid rotation of all of the phases and the critical points of interest must be isolated in the reduced space of relative phases.

Let  $U^*(\boldsymbol{\theta})$  be a rotationally symmetric phase potential. Rotational symmetry implies that  $U^*(\boldsymbol{\theta})$  is invariant to the change of coordinates  $\boldsymbol{\theta} \mapsto \boldsymbol{\theta} + \theta_0 \mathbf{1}$ , where  $\theta_0 \in \mathbb{T}$ . Expanding  $U^*(\boldsymbol{\theta} + \theta_0 \mathbf{1})$  about the point  $\boldsymbol{\theta}$  yields

$$U^*(\boldsymbol{\theta} + \theta_0 \mathbf{1}) = U(\boldsymbol{\theta}) + \theta_0 \mathbf{1}^T \nabla U^*(\boldsymbol{\theta}) + \theta_0^2 \mathbf{1}^T H^*(\boldsymbol{\theta}) \mathbf{1} + \dots, \quad (6.1)$$

where  $\nabla U^* \triangleq \left( \frac{\partial U^*}{\partial \theta_1}, \dots, \frac{\partial U^*}{\partial \theta_N} \right)^T$  and  $H^*$  are the gradient and Hessian of  $U^*(\boldsymbol{\theta})$ , respectively. If  $U^*(\boldsymbol{\theta} + \theta_0 \mathbf{1}) = U(\boldsymbol{\theta})$ , then (6.1) requires that every term on the right-hand side of (6.1), other than  $U(\boldsymbol{\theta})$ , is identically equal to zero (to see this, take  $\theta_0$  arbitrarily small). This implies that the vector  $\mathbf{1}$  is orthogonal to the gradient  $\nabla U^*$  and  $\mathbf{1}$  is in the kernel of the Hessian  $H^*$ . Let  $\boldsymbol{\theta}$  be a critical point of  $U^*(\boldsymbol{\theta})$ . Note that  $\mathbf{1}$  spans the kernel of  $H^*$  evaluated at  $\boldsymbol{\theta}$  if and only if  $\boldsymbol{\theta}$  is isolated in shape space.

Consider the composite potential

$$V^*(\mathbf{r}, \boldsymbol{\theta}) \triangleq \omega_0^2 K_0 S(\mathbf{r}, \boldsymbol{\theta}) + U^*(\boldsymbol{\theta}), \quad K_0 > 0, \quad (6.2)$$

where the circular formation potential  $S(\mathbf{r}, \boldsymbol{\theta})$  is defined in (5.2). The time derivative of

$V^*(\mathbf{r}, \boldsymbol{\theta})$  along solutions of the closed-loop particle model (3.5) is

$$\begin{aligned}\dot{V}^* &= \omega_0 K_0 \sum_{j=1}^N (\omega_0 - u_j) \langle e^{i\theta_j}, P_j \mathbf{c} \rangle + \sum_{j=1}^N \frac{\partial U^*}{\partial \theta_j} u_j \\ &= \sum_{j=1}^N \left( \omega_0 K_0 \langle e^{i\theta_j}, P_j \mathbf{c} \rangle - \frac{\partial U^*}{\partial \theta_j} \right) (\omega_0 - u_j),\end{aligned}$$

where we used the fact that  $\sum_{j=1}^N \frac{\partial U^*}{\partial \theta_j} = \mathbf{1}^T \nabla U^* = 0$ . Choosing the composite shape control

$$u_k = \omega_0 (1 + K_0 \langle e^{i\theta_k}, P_k \mathbf{c} \rangle) - \frac{\partial U^*}{\partial \theta_k}, \quad K_0 > 0, \quad (6.3)$$

yields

$$\dot{V}^* = - \sum_{j=1}^N \left( \omega_0 K_0 \langle e^{i\theta_j}, P_j \mathbf{c} \rangle - \frac{\partial U^*}{\partial \theta_k} \right)^2 \leq 0. \quad (6.4)$$

This leads to the following result [243, Theorem 3].

**Lemma 6.1. All-to-all composite phase and circular formation control** *Let  $U^*(\boldsymbol{\theta})$  be a smooth and rotationally symmetric phase potential. For the shape control (6.3), all of the solutions of the closed-loop particle model (3.5) converge to the set of circular formations with radius  $|\omega_0|^{-1}$  and direction of rotation determined by the sign of  $\omega_0 \neq 0$ . Each circular formation in the limiting set has a phase arrangement in the critical set of the phase potential  $U^*(\boldsymbol{\theta})$ . Every isolated local minimum of  $U^*(\boldsymbol{\theta})$  defines an asymptotically stable set of circular formations; every circular formation for which  $U^*(\boldsymbol{\theta})$  does not attain a minimum and  $\boldsymbol{\theta}$  is isolated in shape space is unstable.*

*Proof.* This proof follows the proof of Corollary 5.2 with  $V(\mathbf{r}, \boldsymbol{\theta})$  replaced by  $V^*(\mathbf{r}, \boldsymbol{\theta})$  and  $\langle ie^{i\theta_k}, p_\theta \rangle = \frac{\partial U}{\partial \theta_k}$  replaced by  $\frac{\partial U^*}{\partial \theta_k}$ . Since the control (6.3) is a shape control, then the closed-loop particle model evolves on the reduced shape space. Furthermore, the potential  $V^*(\mathbf{r}, \boldsymbol{\theta})$  is positive definite and proper in the reduced shape space and  $\dot{V}^*(\mathbf{r}, \boldsymbol{\theta}) \leq 0$  by (6.4). Let  $\Omega$  be the set of all of the points in the reduced shape space where  $\dot{V}^* = 0$ . In this set,

$$\omega_0 K_0 \langle e^{i\theta_k}, P_k \mathbf{c} \rangle + \frac{\partial U^*}{\partial \theta_k} = 0, \quad (6.5)$$

which implies  $\dot{\boldsymbol{\theta}} = \omega_0 \mathbf{1}$  and  $\mathbf{c}$  is constant. Let  $\Lambda$  denote the largest invariant set in  $\Omega$ .

Taking the time-derivative of (6.5) in  $\Omega$  yields

$$K_0 \langle ie^{i\theta_k}, P_k \mathbf{c} \rangle \omega_0^2 + \langle e^{i\theta_k}, \underbrace{\sum_{j=1}^N \dot{c}_{k,j}}_0 \rangle \omega_0 + \frac{d}{dt} \left( \frac{\partial U^*}{\partial \theta_k} \right) \Big|_{\Omega} = 0,$$

where

$$\frac{d}{dt} \left( \frac{\partial U^*}{\partial \theta_k} \right) \Big|_{\Omega} = \sum_{j=1}^N \frac{\partial^2 U^*}{\partial \theta_j \partial \theta_k} \omega_0 = \omega_0 (H^*)_k \mathbf{1} = 0.$$

Thus, points in  $\Lambda$  satisfy

$$\langle ie^{i\theta_k}, P_k \mathbf{c} \rangle = 0. \quad (6.6)$$

Equation (6.6) holds only if  $P\mathbf{c} = 0$ , which implies  $\mathbf{c} = \bar{c}\mathbf{1}$  for some  $\bar{c} \in \mathbb{C}$ . Since  $\mathbf{c} = \bar{c}\mathbf{1}$  in  $\Lambda$ , then using (6.5), we observe that points  $(\mathbf{r}, \boldsymbol{\theta})$  in  $\Lambda$  also satisfy

$$\frac{\partial U^*}{\partial \theta_k} = 0. \quad (6.7)$$

Equation (6.7) holds only if  $\boldsymbol{\theta}$  is a critical point of  $U^*(\boldsymbol{\theta})$ . By the invariance principle [131, Theorem 4.4 and Corollary 4.2], every solution of the closed-loop particle model approaches  $\Lambda$  as  $t \rightarrow \infty$ . Using Lemma A.2 with  $V_1(\mathbf{x})$  replaced by  $\omega_0^2 K_0 S(\mathbf{r}, \boldsymbol{\theta})$  and  $V_2(\mathbf{x})$  replaced by  $U^*(\boldsymbol{\theta})$  completes the proof.  $\square$

Lemma 6.1 provides the framework with which we stabilize symmetric circular formations. In order to use this framework, we must identify phase potentials that are minimized by symmetric phase patterns. This is done using Lemma 3.5: *an arrangement  $\boldsymbol{\theta}$  of  $N$  phases is an  $(M, N)$ -pattern where  $M$  is a divisor of  $N$  if and only if, for all  $m \in \{1, \dots, M-1\}$ , the phase arrangement  $m\boldsymbol{\theta}$  is balanced and the phase arrangement  $M\boldsymbol{\theta}$  is synchronized.* In order to prove Lemma 3.5, we first generalize the notion of the phase order parameter  $p_\theta$  in the following way. Let  $p_{m\theta} \triangleq (1/m)p(m\boldsymbol{\theta})$ , where  $m \in \mathbb{N} \triangleq \{1, 2, 3, \dots\}$ , that is

$$p_{m\theta} \triangleq \frac{1}{mN} \sum_{j=1}^N e^{im\theta_k}. \quad (6.8)$$

Equation (6.8) represents the centroid of the phasors  $e^{i\theta}$  raised to the power  $m$ . For this reason, we refer to  $p_{m\theta}$  as the  $m$ th moment of the phasors  $e^{i\theta}$ , or  $m$ th phase moment for short. Note, the phase order parameter  $p_\theta = p_{1\theta}$  is the first phase moment. Using (6.8), if the phase arrangement  $m\boldsymbol{\theta}$  is synchronized then  $m|p_{m\theta}| = 1$ ; if  $m\boldsymbol{\theta}$  is balanced, then  $p_{m\theta} = 0$ . The following proof is based on [243, Theorem 6].

*Proof of Lemma 3.5.* Assume the phase arrangement  $\boldsymbol{\theta}$  is an  $(M, N)$ -pattern, where  $M$  is a divisor of  $N$ . This means that every phase  $\theta_k$ ,  $k = 1, \dots, N$ , belongs to one of  $M$  equally spaced clusters such that there are  $N/M$  phases in each cluster. Let  $\Theta_m$  denote the phase of cluster  $m \in \mathcal{M} \triangleq \{1, \dots, M\}$ , where

$$\Theta_m = \frac{2\pi}{M}(m-1). \quad (6.9)$$

We have

$$p_{m\boldsymbol{\theta}} = \frac{1}{mN} \sum_{j=1}^N e^{im\theta_j} = \frac{1}{mM} \sum_{l=1}^M e^{im\Theta_l} = \frac{1}{mM} \sum_{l=1}^M e^{i\frac{2\pi m}{M}(l-1)} = \frac{e^{-i\frac{2\pi m}{M}}}{mM} \sum_{l=1}^M e^{i\frac{2\pi m}{M}l}. \quad (6.10)$$

Evaluating (6.10) using Lemma A.3, yields  $p_{m\boldsymbol{\theta}} = 0$  for  $m = 1, \dots, M-1$ , and  $M|p_{M\boldsymbol{\theta}}| = 1$ . This means that  $\boldsymbol{\theta}, 2\boldsymbol{\theta}, \dots, (M-1)\boldsymbol{\theta}$  are balanced and  $M\boldsymbol{\theta}$  is synchronized.

Next, assume that  $\boldsymbol{\theta}, 2\boldsymbol{\theta}, \dots, (M-1)\boldsymbol{\theta}$  are balanced and  $M\boldsymbol{\theta}$  is synchronized. This implies  $p_{m\boldsymbol{\theta}} = 0$  and  $M|p_{M\boldsymbol{\theta}}| = 1$ . Let  $M\theta_k = \phi_0 \in \mathbb{T}$ . We evaluate  $\theta_k = \phi_0/M$  as follows:

$$e^{i\frac{\phi_0}{M}} = \left(e^{i\phi_0}\right)^{\frac{1}{M}} = e^{i(\phi_0 + \frac{2\pi}{M}(k-1))}, \quad k = 1, \dots, N.$$

This means that  $\theta_k = \phi_0/M + (2\pi/M)(k-1)/M$  and  $\theta_{k,j} = (2\pi/M)(k-j)/M$  for all pairs  $j$  and  $k$ . Since every pair of phases is separated by an integer multiple of  $2\pi/M$  radians, then each phase  $\theta_k$  belongs to one of  $M$  equally spaced clusters defined in (6.9). Let  $N_m$ , where  $m \in \mathcal{M}$ , denote the number of phases in cluster  $m$ . We seek to prove that  $N_m = N/M$  for all  $m \in \mathcal{M}$ . We have

$$mp_{m\boldsymbol{\theta}} = \frac{1}{N} \sum_{j=1}^M N_j e^{i\frac{2\pi m}{M}j} = 0, \quad (6.11)$$

for  $m = 1, \dots, M-1$  and

$$Mp_{M\boldsymbol{\theta}} = \frac{1}{N} \sum_{j=1}^M N_j e^{i2\pi j} = 1. \quad (6.12)$$

Equations (6.11) and (6.12) are a system of linear equations in the unknown variables  $\mathbf{x} \triangleq (N_1, \dots, N_M)^T$ . Namely, (6.11) and (6.12) can be written as  $A\mathbf{x} = \mathbf{b}$  where  $A \triangleq [a_{kj}] \in \mathbb{C}^{M \times M}$  and  $\mathbf{b} \triangleq (0, \dots, 0, N)^T \in \mathbb{R}^M$ . The entries in  $A$  are defined by  $[a]_{kj} \triangleq e^{i\frac{2\pi}{M}kj}$  for all pairs  $j$  and  $k$ , which means that  $A = A^T$ . The inverse of  $A$  is given by  $A^{-1} = (1/M)A^\dagger$ ,

where  $A^\dagger$  is the conjugate transpose of  $A$ . To see this, observe that

$$[AA^\dagger]_{kj} = \frac{1}{M} \sum_{l=1}^M e^{i\frac{2\pi(k-j)l}{M}}. \quad (6.13)$$

If  $j = k$ , then (6.13) evaluates to  $M$ . If  $j \neq k$ , then  $0 < |j - k| < M$  and equation (6.13) evaluates to zero by Lemma A.3. Therefore, the solution to the system of equations (6.11) and (6.12) is  $\mathbf{x} = (1/M)A^\dagger \mathbf{b}$ . Since the  $M$ th column of  $A^\dagger$  is  $\mathbf{1}$  and  $\mathbf{b}$  has only one non-zero entry, which is  $N$ , we find that  $\mathbf{x} = (N/M)\mathbf{1}$ , which completes the proof.  $\square$

Lemma 3.5 characterizes an  $(M, N)$ -pattern according to synchronization and balancing conditions for the first  $M$  phase moments. These conditions lead directly to the following expression for an all-to-all  $(M, N)$ -pattern potential:

$$U^{M,N}(\boldsymbol{\theta}) = \frac{N}{2} \sum_{m=1}^M K_m |p_{m\boldsymbol{\theta}}|^2, \quad (6.14)$$

$$K_m > 0, \quad m = 1, \dots, M-1, \quad K_M < 0.$$

The global minimum of  $U^{M,N}(\boldsymbol{\theta})$  occurs when  $p_{m\boldsymbol{\theta}} = 0$ ,  $m = 1, \dots, M-1$ , and  $M|p_{M\boldsymbol{\theta}}| = 1$ . We have the following result [243, Theorem 6, Theorem 7].

**Theorem 6.2. All-to-all symmetric phase pattern potential** *Let  $M$  be a divisor of  $N$ . The potential  $U^{M,N}(\boldsymbol{\theta})$  defined in (6.14) is smooth and rotationally symmetric. The phase arrangement  $\boldsymbol{\theta} \in \mathbb{T}^N$  is an  $(M, N)$ -pattern if and only if it is a global minimum of  $U^{M,N}(\boldsymbol{\theta})$ , which is isolated in the phase shape space.*

*Proof.* The potential  $U^{M,N}(\boldsymbol{\theta})$  is smooth since each phase moment  $p_{m\boldsymbol{\theta}}$  is a smooth function of  $\boldsymbol{\theta}$ . The potential  $U^{M,N}(\boldsymbol{\theta})$  is rotationally symmetric if  $U^{M,N}(\boldsymbol{\theta} + \theta_0 \mathbf{1}) = U^{M,N}(\boldsymbol{\theta})$ , where  $\theta_0 \in \mathbb{T}$ . In fact, we have

$$U^{M,N}(\boldsymbol{\theta} + \theta_0 \mathbf{1}) = \frac{1}{2} \sum_{m=1}^M \frac{K_m}{m^2} \left| \sum_{j=1}^N e^{im(\theta_j + \theta_0)} \right|^2 = \frac{1}{2} \sum_{m=1}^M \frac{K_m}{m^2} \underbrace{|e^{im\theta_0}|^2}_1 \left| \sum_{j=1}^N e^{im\theta_j} \right|^2 = U^{M,N}(\boldsymbol{\theta}).$$

That phase arrangement  $\boldsymbol{\theta} \in \mathbb{T}^N$  is an  $(M, N)$ -pattern if and only if it is a global minimum of  $U^{M,N}(\boldsymbol{\theta})$  is a direct consequence of Lemma 3.5, (6.8), and (6.14). Thus we need only prove that the set of  $(M, N)$ -patterns is isolated in the reduced shape space of

relative phases. Let  $\boldsymbol{\theta}$  be an  $(M, N)$ -pattern. We prove  $\boldsymbol{\theta}$  is isolated in shape space by computing the multiplicity of zero as an eigenvalue of the Hessian  $H^{M,N}$  of  $U^{M,N}$  evaluated at  $\boldsymbol{\theta}$ . We know that zero is an eigenvalue of  $H^{M,N}(\boldsymbol{\theta})$  because  $U^{M,N}(\boldsymbol{\theta})$  is rotationally symmetric; if zero is a simple eigenvalue, then  $\boldsymbol{\theta}$  is isolated in shape space.

The Hessian  $H^{M,N}$  is equivalent to (minus) the Jacobian of the closed-loop phase model (3.6) with the gradient control

$$\mathbf{u} = -\nabla U^{M,N} \triangleq -\left(\frac{\partial U^{M,N}}{\partial \theta_1}, \dots, \frac{\partial U^{M,N}}{\partial \theta_N}\right)^T. \quad (6.15)$$

We calculate the eigenvalues of the closed-loop phase model with the control (6.15) by expressing  $\nabla U^{M,N}$  in terms of a phase coupling function for all-to-all interaction. Then we apply formulas for the eigenvalues of all-to-all phase coupling functions evaluated in symmetric phase patterns from [189]; see also [15, 38].

The  $k$ th component of the gradient of  $U^{M,N}(\boldsymbol{\theta})$  is

$$\frac{\partial U^{M,N}}{\partial \theta_k} = \sum_{m=1}^M K_m \langle i e^{im\theta_k}, p_{m\theta} \rangle = \frac{1}{N} \sum_{m=1}^M \sum_{j=1}^N \frac{K_m}{m} \sin(m\theta_{j,k}).$$

Let  $\Gamma(\theta_{k,j})$  denote the phase coupling function, defined by

$$\Gamma(\theta_{k,j}) \triangleq \sum_{m=1}^M \frac{K_m}{m} \sin(m\theta_{k,j}) \quad (6.16)$$

Using (6.16), the closed-loop phase model with the control (6.15) is equivalent to

$$\dot{\theta}_k = \frac{1}{N} \sum_{j=1}^N \Gamma(\theta_{k,j}). \quad (6.17)$$

According to [189], the linearization of (6.17) near an  $(M, N)$ -pattern has  $N$  eigenvalues that can be described as the union of two sets. The first set consists of  $N - M$  identical eigenvalues associated with intra-cluster fluctuation; we denote these eigenvalues by  $\tilde{\lambda}^{(M)}$ . The second set consists of  $M$  eigenvalues associated with inter-cluster fluctuation; we denote these eigenvalues by  $\lambda_p^{(M)}$ , where  $p = 0, \dots, M-1$ . Since the Jacobian of (6.17) is the Hessian matrix  $H^{M,N}$ , which is necessarily symmetric, then all of the eigenvalues are real.

We calculate both sets of eigenvalues by taking the Fourier series expansion of the derivative of  $\Gamma(\theta_{k,j})$  with respect to its argument  $\theta_{k,j}$ . The derivative is

$$\Gamma'(\theta_{k,j}) = \sum_{m=1}^M K_m \cos(m\theta_{k,j}), \quad (6.18)$$

which is an even function. The Fourier series expansion of (6.18) has the even coefficients  $a'_l$  given by  $a'_l \triangleq K_l$ ,  $l \in \mathcal{M}$ , and  $a'_l \triangleq 0$ ,  $l = 0$  or  $l > M$ ; the odd coefficients are zero. We use the Fourier coefficients to evaluate the eigenvalues using the following formulas [189]:

$$\tilde{\lambda}^{(M)} = \sum_{l=1}^{\infty} a'_{Ml} \quad (6.19)$$

$$\lambda_p^{(M)} = \sum_{l=1}^{\infty} \left( a'_{Ml} - \frac{a'_{M(l-1)+p} + a'_{Ml-p}}{2} \right). \quad (6.20)$$

We have

$$\tilde{\lambda}^{(M)} = a'_M = K_M < 0$$

and

$$\lambda_p^{(M)} = \begin{cases} K_M - \frac{K_p + K_{M-p}}{2} < 0, & p = 1, \dots, M-1 \\ 0, & p = 0. \end{cases}$$

Consequently, the zero eigenvalue  $\lambda_0^{(M)}$  is simple, which completes the proof.  $\square$

The following result is an immediate consequence of Lemma 6.1 and Theorem 6.2 [243, Theorem 7]. Consider the shape control

$$u_k = \omega_0(1 + K_0 \langle e^{i\theta_k}, P_k \mathbf{e} \rangle) - \frac{\partial U^{M,N}}{\partial \theta_k}, \quad K_0 > 0. \quad (6.21)$$

**Corollary 6.3. All-to-all symmetric circular formation control** *Let  $M$  be a divisor of  $N$ . The results of Lemma 6.1 hold when control (6.3) is replaced by (6.21), where the all-to-all symmetric phase potential  $U^{M,N}(\boldsymbol{\theta})$  is defined in (6.14). The limiting set of circular formations has a phase arrangement in the critical set of  $U^{M,N}(\boldsymbol{\theta})$ . All of the circular formations where the phase arrangement is an  $(M, N)$ -pattern are asymptotically stable. All of the circular formations where  $U^{M,N}(\boldsymbol{\theta})$  does not reach a minimum and  $\boldsymbol{\theta}$  is isolated in shape space are unstable.*

*Proof.* Application of Lemma 6.1 and Theorem 6.2 yields the desired result.  $\square$

For  $M = 1$ , we have  $U^{M,N}(\boldsymbol{\theta}) = K_1 U(\boldsymbol{\theta})$ , where  $K_1 < 0$ . In this case, the symmetric circular formation control (6.21) stabilizes the set of synchronized circular formations and is equivalent to control (5.8) with  $K = K_1$ . This implies that Corollary 6.3 with  $M = 1$  is equivalent to Corollary 5.2 with  $K < 0$ . Both corollaries state that all of the synchronized circular formations are asymptotically stable. However, Corollary 5.2 is a stronger result than Corollary 6.3, since Corollary 5.2 states that all circular formations that are not synchronized are unstable whereas Corollary 6.3 proves instability only for the set of circular formations for which the phase arrangement is a critical point of  $U^{M,N}(\boldsymbol{\theta})$  that is isolated in shape space but not a minimum. This difference is a consequence of the fact that we have a characterization of the critical points of  $U(\boldsymbol{\theta})$  (see Lemma 4.1) but we don't have such a characterization for  $U^{M,N}(\boldsymbol{\theta})$ .

Simulations of the closed-loop particle model with the control (6.21) confirm that the set of  $(M, N)$ -patterns (for any  $M$ ) has a large but not global region of attraction. We illustrate such simulation results in Figure 6.1 for  $N = 12$  and  $M = 1, 2, 3, 4, 6$ , and 12. All of the simulations converge to the corresponding  $(M, N)$ -pattern, except for the simulation with  $M = 2$ , which is shown in Figure 6.1(b). In this simulation, the position traces a small circle, which means that the limiting phase arrangement is unbalanced and not a  $(2, N)$ -pattern. We have discovered that one can avoid convergence to unbalanced phase patterns using a heuristic, such as increasing the magnitude of gain  $K_1$ . Nonetheless, Figure 6.1(b) vividly demonstrates the limitations of Corollary 6.3.

We explore the limitations of Corollary 6.3 by seeking critical points of  $U^{M,N}(\boldsymbol{\theta})$  that are local minima, not isolated in shape space, or both. We conjecture that a reasonable starting point for this search is the set of symmetric patterns that are not  $(M, N)$ -patterns. That is, let  $\tilde{M}$  be a divisor of  $N$ . The conjecture is that if  $\tilde{\boldsymbol{\theta}}$  is a  $(\tilde{M}, N)$ -pattern, then  $\tilde{\boldsymbol{\theta}}$  may also be a local minimum of  $U^{M,N}(\boldsymbol{\theta})$  and/or a critical point of  $U^{M,N}(\boldsymbol{\theta})$  that is not isolated in shape space. If the conjecture holds, then we may find evidence for it in the

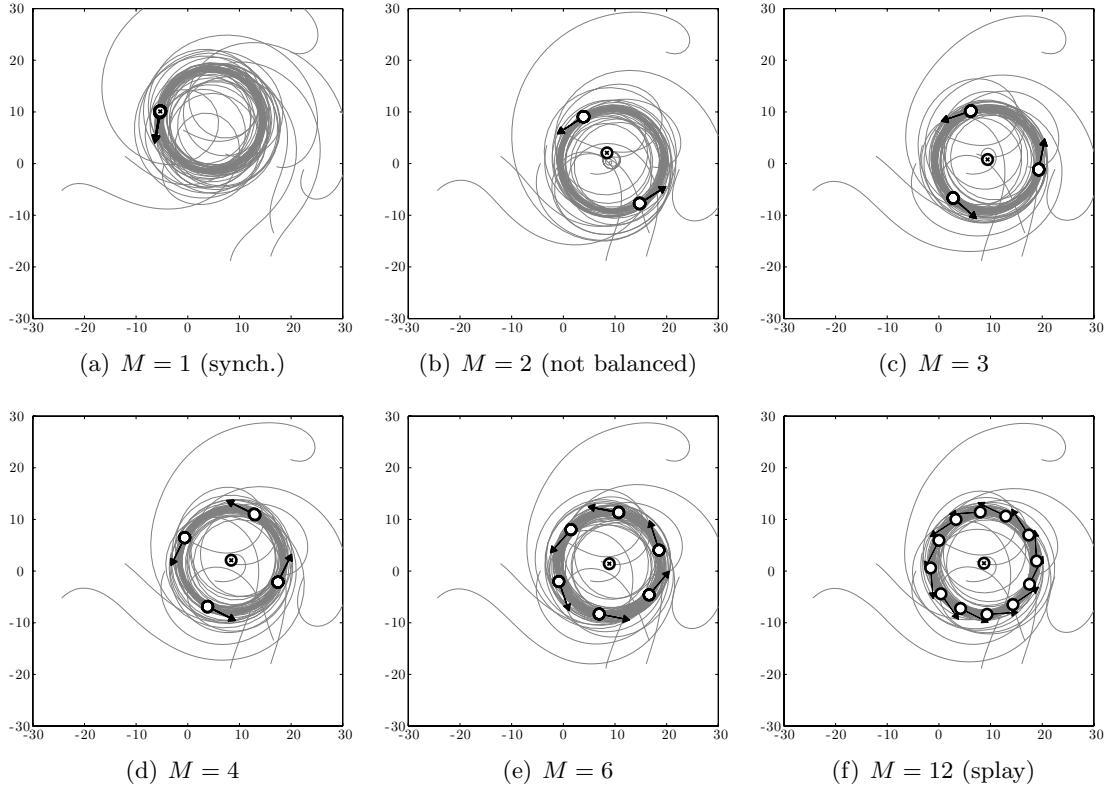


Figure 6.1: All-to-all symmetric circular formation control. Simulations of the closed-loop particle model with the all-to-all symmetric circular formation control (6.21) for  $N = 12$ ,  $\omega_0 = K_0 = 0.1$ , and  $|K_m| = 0.1$  for all  $m \in \mathcal{M}$ . We denote the position centroid  $p_r$  by a circle marked with an  $x$ ; the velocity of  $p_r$  equals the order parameter  $p_\theta$ . Each subfigure shows convergence to the set of circular formations with number of particle clusters equal to  $M$ . In subfigure (b), the position centroid traces a small circle, which means that the simulation has converged to an unbalanced phase arrangement. In every other subfigure, the limiting position centroid is fixed, which means that the phase arrangement is balanced.

eigenvalues of the Hessian  $H^{M,N}(\tilde{\theta})$ . The Hessian is defined by its components:

$$(h^{M,N})_{kj} \triangleq \begin{cases} \sum_{m=1}^M \frac{K_m}{mN} \langle e^{im\theta_k}, e^{im\theta_j} \rangle, & j \neq k \\ \sum_{m=1}^M \frac{K_m}{mN} (1 - mN \langle e^{im\theta_k}, p_{m\theta} \rangle), & j = k. \end{cases} \quad (6.22)$$

We evaluate the eigenstructure of  $H^{M,N}(\tilde{\theta})$  using specific choices of  $N$ ,  $M$ , and  $\tilde{M}$  that facilitate the analysis; a general result has not been developed. Let  $N = M = 4$  and  $\tilde{M} = 2$ . This means that  $U^{M,N}(\theta) = U^{4,4}(\theta)$  is minimized by the splay pattern shown in Figure 6.2(a). The phase arrangement  $\tilde{\theta}$  is a (2,4)-pattern, which has two synchronized clusters on opposite sides of the unit circle as shown in Figure 6.2(b). Observe that  $\tilde{\theta}$  and

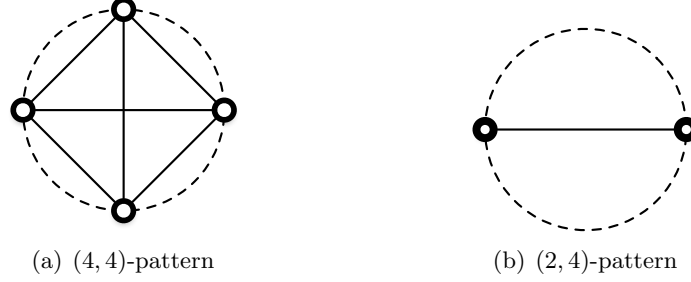


Figure 6.2: Symmetric phase patterns with all-to-all interaction. Two symmetric phase patterns for  $N = 4$  depicted on the unit circle (dashed line). (a) The splay pattern has four uniformly spaced clusters with one phase in each; (b) The (2,4)-pattern has two opposing clusters with two phases in each.

$3\tilde{\theta}$  are balanced and  $2\tilde{\theta}$  and  $4\tilde{\theta}$  are synchronized, which implies  $p_\theta = p_{3\theta} = 0$ ,  $p_{2\theta} = 1/2$ , and  $p_{4\theta} = 1/4$ . Using (6.22), we find

$$H^{M,N}(\tilde{\theta}) = C_1 \begin{bmatrix} 1 & 1 & -1 & -1 \\ 1 & 1 & -1 & -1 \\ -1 & -1 & 1 & 1 \\ -1 & -1 & 1 & 1 \end{bmatrix} + C_2 \begin{bmatrix} -3 & 1 & 1 & 1 \\ 1 & -3 & 1 & 1 \\ 1 & 1 & -3 & 1 \\ 1 & 1 & 1 & -3 \end{bmatrix}, \quad (6.23)$$

where  $C_1 \triangleq (1/N)(K_1 + K_3/3)$  is positive and  $C_2 \triangleq (1/N)(K_2/2 + K_4/4)$  can be either positive or negative.

Using (6.23), we show, for certain choices of the gains  $K_m$ , that  $\tilde{\theta}$  can be either degenerate or a local minimum. Recall that zero is an eigenvalue of  $H^{M,N}$  because  $U^{M,N}(\theta)$  is rotationally symmetric. If zero as an eigenvalue of  $H^{M,N}(\tilde{\theta})$  has multiplicity greater than one, then  $\tilde{\theta}$  is not isolated in shape space. If zero has multiplicity one and every other eigenvalue is positive, then  $\tilde{\theta}$  is a local minimum of  $U^{M,N}(\theta)$  that is isolated in shape space.

If we take  $C_2 = C_1 > 0$ , then (6.23) becomes

$$H^{M,N}(\theta) = 2C_1 \begin{bmatrix} -2 & 2 & 0 & 0 \\ 2 & -2 & 0 & 0 \\ 0 & 0 & -2 & 2 \\ 0 & 0 & 2 & -2 \end{bmatrix}.$$

In this case,  $H^{M,N}(\tilde{\theta})$  has eigenvalues zero and  $8C_1$ , which each have multiplicity two. This means that, for this choice of gains,  $\tilde{\theta}$  is not isolated in shape space. The set of gains with

$C_1 = C_2$  satisfy

$$K_1 + \frac{K_3}{3} = \frac{K_2}{2} + \frac{K_4}{4} > 0, \quad (6.24)$$

In this set, the gain  $K_4$ , which is the only negative gain, has absolute value less than  $2K_2$ .

Alternatively, if we take  $C_2 < 0$  and  $|C_2| \gg C_1$ , then (6.23) becomes

$$H^{M,N}(\boldsymbol{\theta}) \approx -C_2 \begin{bmatrix} 3 & -1 & -1 & -1 \\ -1 & 3 & -1 & -1 \\ -1 & -1 & 3 & -1 \\ -1 & -1 & -1 & 3 \end{bmatrix}.$$

In this case,  $H^{M,N}(\tilde{\boldsymbol{\theta}})$  has the following eigenvalues: zero, which has multiplicity one, and  $4|C_2|$ , which has multiplicity three. This means that, for this choice of gains,  $\tilde{\boldsymbol{\theta}}$  is isolated in shape space and a local minimum of  $U^{M,N}(\boldsymbol{\theta})$ . The set of gains with  $|C_2| \ll C_1$  satisfy

$$|K_4| \gg -4K_1 - \frac{4}{3}K_3 + 2K_2, \quad (6.25)$$

which holds, for example, if  $|K_4|$  is much larger than the other three gains.

This analysis shows that it is possible for the control (6.21) to stabilize circular formations where the phase arrangement is a symmetric phase pattern other than the desired  $(M, N)$ -pattern. The occurrence of such an event depends on the choice of the gains  $K_m$  in the  $(M, N)$ -pattern potential. Although we have not yet found a quantitative rule, we have insight from (6.24) and (6.25). The first equation implies that we should avoid choosing  $|K_M|$  less than the other  $M - 1$  gains and the second equation implies that we should avoid choosing  $|K_M|$  significantly larger than the other gains. That is, we should make  $|K_M|$  relatively large, which will also increase the rate of convergence of the highest phase moment to synchronization. However, we should avoid the temptation to make  $|K_M|$  very large, else we may converge to an undesired phase arrangement.

## 6.2 Time-invariant and Undirected Interaction

The design of a symmetric circular formation algorithm with fixed, limited interaction parallels the design of the corresponding all-to-all algorithm. The first result in this section,

which is analogous to Lemma 6.1, reduces the design problem to the design of an appropriate phase potential.

Let  $L$  be the Laplacian of a time-invariant and undirected graph  $G = (\mathcal{N}, E)$ . The following calculations are nearly identical to those in the previous section with the projector  $P$  replaced by the graph Laplacian  $L$  and  $U^*(\boldsymbol{\theta})$  replaced by a rotationally symmetric Laplacian phase potential  $W_L^*(\boldsymbol{\theta})$ . We use the term Laplacian phase potential here to imply that the  $k$ th component of the gradient of  $W_L(\boldsymbol{\theta})$  depends only on the neighboring phases  $\theta_j$ , where  $j \in \mathcal{N}_k$ . Rotational symmetry of  $W_L(\boldsymbol{\theta})$  implies  $W_L^*(\boldsymbol{\theta} + \theta_0 \mathbf{1}) = W_L^*(\boldsymbol{\theta})$ . Expanding  $W_L^*(\boldsymbol{\theta} + \theta_0 \mathbf{1})$  about the point  $\boldsymbol{\theta}$  yields

$$W_L^*(\boldsymbol{\theta} + \theta_0 \mathbf{1}) - W_L(\boldsymbol{\theta}) = \theta_0 \mathbf{1}^T \nabla W_L^*(\boldsymbol{\theta}) + \theta_0^2 \mathbf{1}^T W_L^*(\boldsymbol{\theta}) \mathbf{1} + \dots, \quad (6.26)$$

where  $\nabla W_L^*$  and  $H_L^*$  are the gradient and Hessian of  $W_L^*(\boldsymbol{\theta})$ , respectively. Rotational symmetry requires that every term on the right-hand side of (6.26) is identically equal to zero. This implies that the constant vector  $\mathbf{1}$  is orthogonal to the gradient  $\nabla W_L^*$  and  $\mathbf{1}$  is in the kernel of the Hessian  $W_L^*$ .

Consider the composite potential

$$V_L^*(\mathbf{r}, \boldsymbol{\theta}) \triangleq \omega_0^2 K_0 S_L(\mathbf{r}, \boldsymbol{\theta}) - W_L^*(\boldsymbol{\theta}), \quad K_0 > 0, \quad (6.27)$$

where the circular formation potential  $S_L(\mathbf{r}, \boldsymbol{\theta})$  is defined in (5.13). The time derivative of  $V_L^*(\mathbf{r}, \boldsymbol{\theta})$  along solutions of the closed-loop particle model (3.5) is

$$\begin{aligned} \dot{V}_L^* &= \omega_0 K_0 \sum_{j=1}^N (\omega_0 - u_j) \langle e^{i\theta_k}, L_j \mathbf{c} \rangle - \sum_{j=1}^N \frac{\partial W_L^*}{\partial \theta_j} u_j \\ &= \sum_{j=1}^N \left( \omega_0 K_0 \langle e^{i\theta_j}, L_j \mathbf{c} \rangle + \frac{\partial W_L^*}{\partial \theta_j} \right) (\omega_0 - u_j), \end{aligned}$$

where we used the fact that  $\sum_{j=1}^N \frac{\partial W_L^*}{\partial \theta_j} = \mathbf{1}^T \nabla W_L^* = 0$ . Choosing the composite shape control

$$u_k = \omega_0 (1 + K_0 \langle e^{i\theta_k}, L_k \mathbf{c} \rangle) + \frac{\partial W_L^*}{\partial \theta_k}, \quad K_0 > 0, \quad (6.28)$$

yields

$$\dot{V}_L^* = - \sum_{j=1}^N \left( \omega_0 K_0 \langle e^{i\theta_j}, L_j \mathbf{c} \rangle + \frac{\partial W_L^*}{\partial \theta_k} \right)^2 \leq 0, \quad (6.29)$$

which leads to the following result.

**Lemma 6.4. Laplacian composite phase and circular formation control** *Let  $L$  be the Laplacian of an undirected and connected graph  $G = (\mathcal{N}, E)$  and  $W_L^*(\boldsymbol{\theta})$  be a smooth and rotationally symmetric Laplacian phase potential. For the shape control (6.28), all of the solutions of the closed-loop particle model (3.5) converge to the set of circular formations with radius  $|\omega_0|^{-1}$  and direction of rotation determined by the sign of  $\omega_0 \neq 0$ . All of the circular formations in the limiting set have phase arrangements in the critical set of the phase potential  $W_L^*(\boldsymbol{\theta})$ . Every isolated local minimum of  $W_L^*(\boldsymbol{\theta})$  defines an asymptotically stable set of circular formations; every circular formation where  $W_L^*(\boldsymbol{\theta})$  does not reach a minimum and  $\boldsymbol{\theta}$  is isolated in shape space is unstable.*

*Proof.* This proof follows the proof of Lemma 6.1 with  $V^*(\mathbf{r}, \boldsymbol{\theta})$  replaced by  $V_L^*(\mathbf{r}, \boldsymbol{\theta})$ .  $\square$

To stabilize symmetric circular formations using the control (6.28), we first consider the choice  $W_L^*(\boldsymbol{\theta}) = KW_L(\boldsymbol{\theta})$ . Using this choice, Lemma 6.4 is equivalent to Theorem 5.3. Recall that Theorem 5.3 describes stabilization of synchronized and balanced circular formations with limited interaction. In order to prove asymptotic stability of certain balanced circular formations, we need the additional assumption that the graph  $G$  is circulant. It turns out that the circulant assumption also allows us to prove asymptotic stability of certain symmetric circular formations. We use the following result [241, Lemma 2], which is a consequence of Proposition 3.13 and Lemma 4.6.

**Lemma 6.5. Symmetric critical points of the Laplacian phase potential** *Let  $L$  be the Laplacian of an undirected and connected circulant graph  $G = (\mathcal{N}, E)$ . Also let  $M$  be a divisor of  $N$ . If  $\boldsymbol{\theta}$  is an  $(M, N)$ -pattern, then, for all  $m \in \mathcal{M}$ ,  $e^{im\boldsymbol{\theta}}$  is an eigenvector of  $L$  and  $m\boldsymbol{\theta}$  is a critical point of the Laplacian phase potential  $W_L(\boldsymbol{\theta})$  defined in (4.13).*

*Proof.* Assume  $\boldsymbol{\theta} \in \mathbb{T}$  is an  $(M, N)$ -pattern, which means that each phase  $\theta_k$  belongs to one of  $M$  equally spaced clusters such that there are  $N/M$  phases in each cluster. Let  $\Theta_m \triangleq (2\pi/M)(m-1)$  denote the phase of cluster  $m \in \mathcal{M}$ . Without loss of generality, assume phase  $\theta_k$  is contained in cluster  $m = 1 + (k-1) \bmod M$ , that is,

$$\theta_k = \Theta_{1+(k-1) \bmod M} = \frac{2\pi}{M}(k-1) \bmod M = \frac{2\pi}{M}(k-1), \quad (6.30)$$

where the last equality holds because we identify  $\theta_k$  and  $\theta_k + 2\pi$  on the torus  $\mathbb{T}$ . Let  $\phi_k \triangleq (2\pi/N)(k-1)$ , which implies  $m\boldsymbol{\theta} = (mN/M)\boldsymbol{\phi}$ . Using Proposition 3.13, we find

$$e^{im\boldsymbol{\theta}} = e^{i\frac{mN}{M}\boldsymbol{\phi}} = e^{i(l-1)\boldsymbol{\phi}}$$

is the  $l$ th eigenvector of  $L$ . It is of interest to find  $l$  in terms of  $m$ ,  $M$ , and  $N$ . On the torus, we have

$$(l-1)\phi_k = \frac{mN}{M}\phi_k = \frac{mN}{M}\frac{2\pi}{N}(k-1) = \frac{mN}{M}\frac{2\pi}{N}(k-1) \bmod N = \frac{mN}{M}\phi_k \bmod N,$$

which implies  $l = 1 + (mN/M) \bmod N$ .

If  $e^{im\boldsymbol{\theta}}$  is an eigenvector of  $L$ , then, using Lemma 4.6, this implies  $m\boldsymbol{\theta}$  is a critical point of  $W_L(\boldsymbol{\theta})$ , which completes the proof.  $\square$

Lemma 6.5 motivates us to investigate  $W_L(\boldsymbol{\theta})$ , where  $L$  is circulant, as a candidate symmetric phase pattern potential. In order to apply Lemma 6.4 to stabilize a symmetric circular formation, we need to find a set of  $(M, N)$ -patterns that locally extremizes  $W_L(\boldsymbol{\theta})$  and is isolated in the phase shape space. We characterize such a set in the following result, which also characterizes a set of  $(M, N)$ -patterns that are not isolated in shape space.

**Theorem 6.6. Laplacian phase potential, revisited** *Let  $L$  denote the Laplacian of an undirected and connected circulant graph  $G = (\mathcal{N}, E)$ . Also let  $M$  be a divisor of  $N$ . Let  $\boldsymbol{\psi} \in \mathbb{T}^{|E|}$  denote the vector of all of the relative phases  $\theta_{k,j}$  for all pairs  $j$  and  $k$  such that  $(k, j) \in E$ . Let  $\mathcal{E} \triangleq \{1, \dots, |E|\}$ . The Laplacian phase potential  $W_L(\boldsymbol{\theta})$  is defined in (4.13).*

*Let  $\Psi_1$  denote the set of  $(M, N)$ -patterns in which either  $\cos \psi_f > 0$  for all  $f \in \mathcal{E}$  or  $\cos \psi_f < 0$  for all  $f$ . Every phase arrangement  $\boldsymbol{\theta}$  in  $\Psi_1$  is a local extremum of  $W_L(\boldsymbol{\theta})$  that is isolated in the phase shape space. If  $\cos \psi_f > 0$  for all  $f \in \mathcal{E}$ , then  $\boldsymbol{\theta}$  is a local minimum; if  $\cos \psi_f < 0$  for all  $f \in \mathcal{E}$ , then  $\boldsymbol{\theta}$  is a local maximum.*

*Let  $\Psi_2$  denote the set of  $(M, N)$ -patterns in which  $\boldsymbol{\psi} \bmod \pi = (\pi/2)\mathbf{1}$ . The set  $\Psi_2$  contains no phase arrangements that are isolated in the phase shape space.*

*Proof.* Assume  $\boldsymbol{\theta}$  is an  $(M, N)$ -pattern, which implies it is a critical point of  $W_L(\boldsymbol{\theta})$ , by Lemma 6.5. To prove Theorem 6.6, we compute the eigenvalues of the Hessian  $H_L$  of

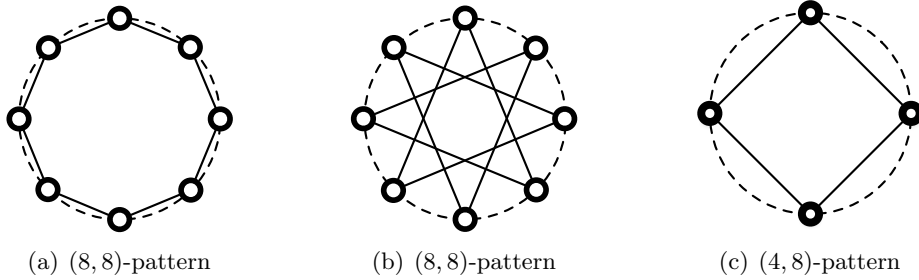


Figure 6.3: Symmetric phase patterns with ring interaction. Three symmetric phase patterns for  $N = 8$  depicted on the unit circle (dashed line). (a,b) The splay patterns have eight uniformly spaced clusters with one phase in each; (c) The (4,8)-pattern has four uniformly spaced clusters with two phases in each.

$W_L(\boldsymbol{\theta})$  evaluated at  $\boldsymbol{\theta}$ . The multiplicity of zero as an eigenvalue of  $H_L(\boldsymbol{\theta})$  determines if  $\boldsymbol{\theta}$  is isolated in shape space. Furthermore, if zero is a simple eigenvalue of  $H_L(\boldsymbol{\theta})$ , then the sign of the remaining eigenvalues determines if  $\boldsymbol{\theta}$  is a local extremum of  $W_L(\boldsymbol{\theta})$ .

Recall that the incidence matrix  $B$  of graph  $G$  satisfies  $L = BB^T$ . For every edge  $(j, k) \in E$  there is an integer  $f \in \mathcal{E} \triangleq \{1, \dots, |E|\}$  such that  $\psi_f = (B^T)_f \boldsymbol{\theta} = \theta_{k,j}$  is the phase  $\theta_k$  relative to  $\theta_j$ . Observe that

$$\sum_{j \in \mathcal{N}_k} \theta_{k,j} = L_k \boldsymbol{\theta} = B_k B^T \boldsymbol{\theta} = B_k \boldsymbol{\psi}. \quad (6.31)$$

Let  $\sin \boldsymbol{\psi} \triangleq (\sin \psi_1, \dots, \sin \psi_{|E|})$  and  $\cos \boldsymbol{\psi} \triangleq (\cos \psi_1, \dots, \cos \psi_{|E|})$ . Using (4.14) and (6.31), the  $k$ th term of the gradient of  $W_L(\boldsymbol{\theta})$  is

$$\frac{\partial W_L}{\partial \theta_k} = \sum_{j \in \mathcal{N}_k} \sin \theta_{k,j} = B_k \sin \boldsymbol{\psi},$$

which means  $\nabla W_L = B \sin \boldsymbol{\psi}$ . The Hessian  $H_L$  of  $W_L(\boldsymbol{\theta})$  has components

$$(h_L)_{kj} \triangleq \begin{cases} -\cos \theta_{k,j}, & j \in \mathcal{N}_k, \\ \sum_{l \in \mathcal{N}_k} \cos \theta_{k,l}, & j = k, \\ 0, & \text{otherwise} \end{cases} = \sum_{f=1}^{|E|} B_{kf} \cos \psi_f (B^T)_{fj}. \quad (6.32)$$

This means  $H_L = B \Phi_L B^T$ , where  $\Phi_L \triangleq \text{diag}\{\cos \boldsymbol{\psi}\}$ , is a weighted Laplacian [93, p. 286].

The remainder of the proof is a consequence of Proposition A.4.  $\square$

To illustrate Theorem 6.6, we consider the specific case of a ring interaction network, which is described by a cyclic graph. (A complete characterization of the critical points of the Laplacian phase potential  $W_L(\boldsymbol{\theta})$ , where  $L$  is the Laplacian of a cyclic graph, is presented in [123, Theorems 1 and 2].) Let  $N = 8$ . According to Theorem 6.6, the two splay patterns shown in Figures 6.3(a) and 6.3(b) are local extrema of  $W_L(\boldsymbol{\theta})$ . Pattern 6.3(b) is a local minimum because the absolute relative phase between every neighbor pair is  $\pi/4 < \pi/2$ . Pattern 6.3(a) is a local maximum because the absolute relative phase between every neighbor pair is  $3\pi/8 > \pi/2$ . The (4, 8)-pattern shown in Figure 6.3(c) is not isolated in the phase shape space, because the absolute relative phase between every neighbor pair is  $\pi/2$ .

Together, Lemma 6.4 and Theorem 6.6 yield a simple yet limited algorithm that locally stabilizes certain symmetric circular formations and destabilizes others. The algorithm is to use control (6.28) with  $W_L^*(\boldsymbol{\theta}) = KW_L(\boldsymbol{\theta})$ . If  $K < 0$ , all of the circular formations where the phase arrangement is a local minimum (respectively, maximum) of  $W_L(\boldsymbol{\theta})$  are asymptotically stable (respectively, unstable); if  $K > 0$ , all of the circular formations where the phase arrangement is a local maximum (respectively, minimum) of  $W_L(\boldsymbol{\theta})$  are asymptotically stable (respectively, unstable). Simulations of this algorithm suggest that the basin of attraction of certain  $(M, N)$ -patterns is relatively large (presumably the global extrema of  $W_L(\boldsymbol{\theta})$ ) and the basin of attraction of other  $(M, N)$ -patterns is rather small (presumably local extrema). Since  $M$  is not a parameter of  $W_L(\boldsymbol{\theta})$ , there is no way to configure the algorithm to converge to a specified set of  $(M, N)$ -patterns. In addition, convergence to certain  $(M, N)$ -patterns is not guaranteed by Theorem 6.6, such as the (4, 8)-pattern shown in Figure 6.3(c).

Limitations in this symmetric circular formation algorithm are due to limitations in the phase potential  $W_L^*(\boldsymbol{\theta}) = KW_L(\boldsymbol{\theta})$  (which was not designed for this purpose). We improve the effectiveness of the algorithm by replacing  $W_L(\boldsymbol{\theta})$  with a symmetric phase pattern potential  $W_L^{M,N}(\boldsymbol{\theta})$  that is motivated by the all-to-all potential  $U^{M,N}(\boldsymbol{\theta})$ . The Laplacian

$(M, N)$ -pattern potential is

$$W_L^{M,N}(\boldsymbol{\theta}) \triangleq -\sum_{m=1}^M \frac{K_m}{m^2} W_L(m\boldsymbol{\theta}) = -\frac{1}{2} \sum_{m=1}^M \frac{K_m}{m^2} \langle e^{im\boldsymbol{\theta}}, L e^{im\boldsymbol{\theta}} \rangle, \quad (6.33)$$

$$K_m > 0, \quad m = 1, \dots, M-1, \quad K_M < -\sum_{m=1}^{M-1} K_m.$$

We illustrate the relationship between  $W_L^{M,N}(\boldsymbol{\theta})$  and  $U^{M,N}(\boldsymbol{\theta})$  by evaluating (6.33) with  $L = NP$ , where  $P \triangleq \text{diag}\{\mathbf{1}\} - (1/N)\mathbf{1}\mathbf{1}^T$  is the projection matrix. This yields

$$\begin{aligned} W_{NP}^{M,N}(\boldsymbol{\theta}) &= -\frac{N}{2} \sum_{m=1}^M \frac{K_m}{m^2} \sum_{j=1}^N \langle e^{im\theta_j}, P_j e^{im\boldsymbol{\theta}} \rangle = -\frac{N}{2} \sum_{m=1}^M \frac{K_m}{m^2} \sum_{j=1}^N \langle e^{im\theta_j}, e^{im\theta_j} - mp_{m\theta} \rangle \\ &= -\frac{N}{2} \sum_{m=1}^M \frac{K_m}{m^2} (N - m^2 N |p_{m\theta}|^2) = -\frac{N^2}{2} \sum_{m=1}^M \frac{K_m}{m^2} + NU^{M,N}(\boldsymbol{\theta}). \end{aligned}$$

Consequently, in the case of all-to-all interaction, the two potentials  $W_L^{M,N}(\boldsymbol{\theta})$  and  $U^{M,N}(\boldsymbol{\theta})$  share the same critical points. In the case of limited interaction, we have the following result [241, Theorem 7].

**Theorem 6.7. Laplacian symmetric phase pattern potential** *Let  $L$  denote the Laplacian of an undirected and connected circulant graph  $G = (\mathcal{N}, E)$ . Also let  $M$  be a divisor of  $N$ . The potential  $W_L^{M,N}(\boldsymbol{\theta})$  is smooth and rotationally symmetric. If phase arrangement  $\boldsymbol{\theta} \in \mathbb{T}^N$  is an  $(M, N)$ -pattern, then  $\boldsymbol{\theta}$  is a local minimum of  $W_L^{M,N}(\boldsymbol{\theta})$  that is isolated in the phase shape space.*

*Proof.* The potential  $W_L^{M,N}(\boldsymbol{\theta})$  is smooth and rotationally symmetric since  $W_L(\boldsymbol{\theta})$  is smooth and rotationally symmetric. The  $k$ th term in the gradient of  $W_L^{M,N}(\boldsymbol{\theta})$  is

$$\frac{\partial W_L^{M,N}}{\partial \theta_k} = -\sum_{m=1}^M \frac{K_m}{m} \langle i e^{im\theta_k}, L_k e^{im\boldsymbol{\theta}} \rangle. \quad (6.34)$$

Assume  $\boldsymbol{\theta}$  is an  $(M, N)$ -pattern, which implies, by Lemma 6.5, that  $\boldsymbol{\theta}$  is a critical point of  $W_L^{M,N}(\boldsymbol{\theta})$ . For every edge  $(j, k) \in E$  there is an integer  $f \in \mathcal{E} \triangleq \{1, \dots, |E|\}$  such that  $\psi_f = (B^T)_f \boldsymbol{\theta} = \theta_{k,j}$  is the relative phase of  $k$  and  $j$ , where  $B$  is the incidence matrix of graph  $G$ . Using (6.34), we find that the Hessian  $H_L^{M,N}$  of  $W_L^{M,N}(\boldsymbol{\theta})$  has components

$$(h_L)_{kj} \triangleq \begin{cases} \sum_{m=1}^M K_m \cos(m\theta_{k,j}), & j \in \mathcal{N}_k, \\ -\sum_{m=1}^M K_m \sum_{l \in \mathcal{N}_k} \cos(m\theta_{k,l}), & j = k, \\ 0, & \text{otherwise} \end{cases} = -\sum_{m=1}^M K_m \sum_{f=1}^{|E|} B_{kf} \cos(m\psi_f) (B^T)_{fj}. \quad (6.35)$$

Let  $\sin(m\boldsymbol{\psi}) \triangleq (\sin(m\psi_1), \dots, \sin(m\psi_{|E|}))$ ,  $\cos(m\boldsymbol{\psi}) \triangleq (\cos(m\psi_1), \dots, \cos(m\psi_{|E|}))$ , and

$$\Phi_L^{M,N} \triangleq \sum_{m=1}^M K_m \text{diag}\{\cos(m\boldsymbol{\psi})\}. \quad (6.36)$$

Using (6.35) and (6.36), we find

$$H_L^{M,N} = B\Phi_L^{M,N}B^T,$$

which is a weighted Laplacian [93, p. 286]. Evaluating (6.36) at  $\boldsymbol{\theta}$  yields

$$\Phi_L^{M,N}(\boldsymbol{\theta}) = \sum_{m=1}^{M-1} K_m \text{diag}\{\cos(m\boldsymbol{\psi})\} + K_M \text{diag}\{\cos(M\boldsymbol{\psi})\}. \quad (6.37)$$

Since  $\cos(m\psi_f) \leq 1$ , for  $m = 1, \dots, M-1$ , and  $\cos(M\psi_f) = 1$  for all  $f \in \mathcal{E}$ , equation (6.37) means that the upper bound on  $K_M$  defined in (6.33) ensures that every diagonal element of  $\Phi_L^{M,N}(\boldsymbol{\theta})$  is negative. The remainder of the proof is a consequence of Proposition A.4.  $\square$

The following result is an immediate consequence of Lemma 6.4 and Theorem 6.7 [241, Theorem 7]. Consider the shape control

$$u_k = \omega_0(1 + K_0 \langle e^{i\theta_k}, L_k \mathbf{c} \rangle) - \frac{\partial W_L^{M,N}}{\partial \theta_k}, \quad K_0 > 0. \quad (6.38)$$

**Corollary 6.8. Laplacian symmetric circular formation control** *Let  $L$  denote the Laplacian of an undirected and connected circulant graph  $G = (\mathcal{N}, E)$ . Also let  $M$  be a divisor of  $N$ . The results of Lemma 6.4 apply when control (6.28) is replaced by (6.38), where the Laplacian symmetric phase potential  $W_L^{M,N}(\boldsymbol{\theta})$  is defined in (6.33). All of the circular formations in the limiting set have a phase arrangement in the critical set of  $W_L^{M,N}(\boldsymbol{\theta})$ . All of the circular formations where the phase arrangement is an  $(M, N)$ -pattern are asymptotically stable. All of the circular formations where  $W_L^{M,N}(\boldsymbol{\theta})$  does not reach a minimum and  $\boldsymbol{\theta}$  is isolated in shape space are unstable.*

*Proof.* Application of Lemma 6.4 and Theorem 6.7 yields the desired result.  $\square$

Corollary 6.8 does not exclude convergence to other local minima of  $W_L^{M,N}(\boldsymbol{\theta})$ . Simulations of the closed-loop particle model with the control (6.38), where  $L$  is the Laplacian of

a time-invariant and connected circulant graph  $G$  other than the complete graph, indicate that the basin of attraction of certain  $(M, N)$ -patterns is quite small. With all-to-all interaction, the basin of attraction of the same  $(M, N)$ -patterns is much larger. The closed-loop particle model with all-to-all interaction makes use of the averaged quantities  $p_r$  and  $p_{m\theta}$ . For general interaction, which we describe in the next section, these quantities are replaced by consensus variables.

### 6.3 General Interaction

The symmetric circular formation algorithms described in Sections 6.1 and 6.2 are not applicable to particle collectives with time-varying and/or directed interaction networks. In this section, we extend the dynamic circular formation control algorithm to stabilize the set of circular formations where the phase arrangement is an  $(M, N)$ -pattern.

The dynamic symmetric circular formation control is a composite (dynamic) phase and formation control motivated by the dynamic circular formation control (5.29) that stabilizes synchronized and balanced phase arrangements. Once again, the dynamic algorithm adopts the form of the all-to-all algorithm, which, in this case, is the all-to-all symmetric circular formation control (6.21). We reproduce (6.21) here, in such a way as to expose its dependence on the position centroid  $p_r$  and phase moments  $p_{m\theta}$ :

$$\begin{aligned} u_k &= \omega_0(1 + K_0\langle e^{i\theta_k}, r_k - p_r \rangle) + K_0\langle ie^{i\theta_k}, p_\theta \rangle + \sum_{m=1}^M K_m\langle ie^{im\theta_k}, p_{m\theta} \rangle, \\ &K_0 > 0, K_m > 0, m = 1, \dots, M-1, K_M < 0. \end{aligned} \quad (6.39)$$

In order to replicate the control (6.39) with limited interaction, we augment (5.29) with  $M-1$  additional consensus variables. Each additional consensus variable  $z_k^{(m)} \triangleq w_k^{(m)} e^{i(\theta_k - \omega_0 t)}$  represents the phase moment  $p_{m\theta}$ . The augmented algorithm broadens the class of interaction networks for which we can stabilize symmetric circular formations at the cost of increased algorithm complexity.

Recall  $H(\cdot)$  denotes the Heaviside function defined in (4.25). The dynamic symmetric

circular formation algorithm is described by the following shape control:

$$\begin{aligned}
u_k &= \omega_0(1 - K_0 \langle v_k, 1 \rangle) + K_0 \langle w_k, i \rangle - \sum_{m=1}^M \frac{K_m}{m} \langle w_k^{(m)}, i \rangle, \\
K_0 &> 0, K_m > 0, m = 1, \dots, M-1, K_M < 0, \\
\dot{w}_k &= -u_k i w_k - \sum_{j=1}^N l_{kj}(t) w_j e^{i\theta_{j,k}}, w_k(0) = 1, \\
\dot{v}_k &= -1 - u_k i v_k - \sum_{j=1}^N l_{kj}(t) (v_j e^{i\theta_{j,k}} - r_j e^{-i\theta_k}), v_k(0) = 0, \\
\dot{w}_k^{(m)} &= m(u_k - \omega_0) i (\mathbb{H}(K_m) - w_k^{(m)}) - \sum_{j=1}^N l_{kj}(t) w_j^{(m)} e^{im\theta_{j,k}}, w_k^{(m)}(0) = 1.
\end{aligned} \tag{6.40}$$

Computing (6.40) requires the transmission to node  $k$  of the consensus variables  $w_j$ ,  $v_j$ , and  $w_j^{(m)}$ , for all  $m \in \mathcal{M}$ , from each node  $j \in \mathcal{N}_k(t)$  for all  $t$ . It also requires the solution of  $M+2$  simultaneous first-order differential equations at each node.

**Theorem 6.9. Dynamic symmetric circular formation control** *Let  $L(t)$  be the Laplacian matrix of a graph  $G(t)$  that is uniformly connected to a single node. Also let  $M$  be a divisor of  $N$ . The shape control (6.40) enforces exponential convergence of  $z_k \triangleq w_k e^{i\theta_k}$  to  $\bar{z} \in \mathbb{C}$ ,  $y_k \triangleq v_k e^{i\theta_k} + r_k$  to  $\bar{y} \in \mathbb{C}$ , and  $z_k^{(m)} \triangleq (1/m) w_k^{(m)} e^{im(\theta_k - \omega_0 t)}$  to  $\bar{z}^{(m)} \in \mathbb{C}$  for all  $k \in \mathcal{N}$  and  $m \in \mathcal{M}$ . For the shape control (6.40), all of the solutions of the closed-loop particle model (3.5) converge to the set of circular formations with radius  $|\omega_0|^{-1}$ , direction of rotation determined by the sign of  $\omega_0 \neq 0$ , center  $\bar{c} \triangleq \bar{y} + \omega_0^{-1} i \bar{z}$ , and phase arrangement in the set of critical points of  $U^{M,N}(\boldsymbol{\theta})$  defined in (6.14).*

*If  $G(t)$  is balanced, then the following holds: (i) all of the circular formations where the phase arrangement is an  $(M, N)$ -pattern are asymptotically stable; (ii) all of the circular formations where  $U^{M,N}(\boldsymbol{\theta})$  does not reach a minimum and  $\boldsymbol{\theta}$  is isolated in shape space are unstable; and (iii) the consensus limits are  $\bar{z} = p_\theta(0)$ ,  $\bar{y} = p_r(0)$ ,  $\bar{c} = p_c(0)$ ,  $\bar{z}^{(m)} = \lim_{t \rightarrow \infty} p_{m\theta}(t) = 0$ , for  $m = 1, \dots, M-1$ , and  $\bar{z}^{(M)} = p_{M\theta}(0)$ .*

*Proof.* As in the proof of Theorem 5.4, the consensus variables  $\mathbf{z}$  and  $\mathbf{y}$  obey the consensus dynamics (4.24). This means that  $\lim_{t \rightarrow \infty} z_k(t) = \bar{z}$  and  $\lim_{t \rightarrow \infty} y_k(t) = \bar{y}$ . Each consensus variable  $z_k^{(M)}$  has the dynamics

$$\begin{aligned}
\dot{z}_k^{(M)} &= \frac{1}{M} \dot{w}_k e^{iM(\theta_k - \omega_0 t)} + (u_k - \omega_0) w_k i e^{iM(\theta_k - \omega_0 t)} \\
&= -\frac{1}{M} \sum_{j=1}^N l_{kj}(t) w_j e^{iM(\theta_j - \omega_0 t)} = -L_k(t) \mathbf{z}^{(M)},
\end{aligned}$$

where  $\mathbf{z}^{(M)} \triangleq (z_1^{(M)}, \dots, z_N^{(M)})^T$ . This implies that  $\mathbf{z}^{(M)}$  also obeys the consensus dynamics (4.24) and that  $\lim_{t \rightarrow \infty} z_k^{(M)}(t) = \bar{z}^{(M)}$ . If  $G(t)$  is balanced, then

$$\bar{z}^{(M)} = \frac{1}{MN} \sum_{j=1}^N w_k^{(M)}(0) e^{iM\theta_k(0)} = p_{M\theta}(0)$$

is a constant of motion.

The control (6.40) converges to

$$\begin{aligned} \bar{u}_k &\triangleq \omega_0(1 + K_0 \langle e^{i\theta_k}, r_k - \bar{c} \rangle) - \sum_{m=1}^{M-1} K_m \langle i e^{im(\theta_k - \omega_0 t)}, z_k^{(m)} \rangle \\ &\quad - K_M \langle i e^{iM(\theta_k - \omega_0 t)}, \bar{z}^{(M)} \rangle \\ \dot{z}_k^{(m)} &= (\bar{u}_k - \omega_0) i e^{im(\theta_k - \omega_0 t)} - L_k(t) \mathbf{z}^{(m)}, \quad m = 1, \dots, M-1. \end{aligned} \quad (6.41)$$

Note  $\mathbf{z}^{(m)}$  obeys the consensus dynamics (4.24) with an additive perturbation. Along solutions of the closed-loop particle model with the control (6.41), the perturbation is

$$(\bar{u}_k - \omega_0) i e^{im(\theta_k - \omega_0 t)} = \frac{d}{dt} \left( \frac{1}{m} e^{im(\theta_k - \omega_0 t)} \right). \quad (6.42)$$

To prove that the perturbation (6.42) vanishes, consider the quadratic form

$$\begin{aligned} V(\mathbf{r}, \boldsymbol{\theta}, \mathbf{z}^{(1)}, \dots, \mathbf{z}^{(M-1)}) &\triangleq \omega_0^2 \frac{K_0}{2} \|\mathbf{c} - \bar{c}\mathbf{1}\|^2 + \frac{K_m}{2} \sum_{m=1}^{M-1} \|\mathbf{z}^{(m)}\|^2 \\ &\quad - \frac{K_M}{2} \left\| \frac{1}{M} e^{iM(\boldsymbol{\theta} - \omega_0 t)\mathbf{1}} - \bar{z}^{(M)}\mathbf{1} \right\|^2. \end{aligned}$$

Along solutions of the closed-loop particle model with control (6.41),  $V(\mathbf{r}, \boldsymbol{\theta}, \mathbf{z}^{(1)}, \dots, \mathbf{z}^{(M-1)})$  has the time-derivative

$$\dot{V} = \sum_{j=1}^N \left( (\omega_0 - \bar{u}_j)^2 - \sum_{m=1} K_m \langle z_j^{(m)}, L_j(t) \mathbf{z}^{(m)} \rangle \right) = -\|\bar{\mathbf{u}} - \omega_0 \mathbf{1}\|^2 - \sum_{m=1}^{M-1} Q_{L(t)}(\mathbf{z}^{(m)}) \leq 0.$$

This means that  $\|\mathbf{c} - \bar{c}\mathbf{1}\|^2$ ,  $\|\mathbf{z}^{(m)}\|^2$ , and  $\|\bar{z}^{(M)}\mathbf{1}\|^2$  are all bounded on the interval  $t \in [0, \infty)$ .

By two successive applications of Lemma A.1 with  $\phi_1(t) \triangleq \sum_{m=1}^{M-1} Q_{L(t)}(\mathbf{z}^{(m)}(t))$  and  $\phi_2(t) \triangleq \|\bar{\mathbf{u}} - \omega_0 \mathbf{1}\|^2$ , one can show the following: (i)  $\|\bar{\mathbf{u}}(t) - \omega_0 \mathbf{1}\| : [0, \infty) \rightarrow \mathbb{R}$  is bounded and (ii)  $\bar{u}_k(t) \rightarrow \omega_0$  as  $t \rightarrow \infty$ . Since  $|\bar{u}_k - \omega_0|$  is the magnitude of the perturbation of the consensus dynamics  $\dot{z}_k^{(m)}$ , this implies that the perturbation in (6.41) vanishes.

Assume  $G(t)$  is balanced. The computation of the consensus limit  $\bar{z}^{(m)}$  also follows the proof of Theorem 4.10. Since  $G(t)$  is balanced, then  $\mathbf{1}^T L(t) = 0$ . Consequently, left-

multiplying  $\dot{\mathbf{z}}^{(m)}$  defined in (6.41) by  $\mathbf{1}^T$  yields

$$\mathbf{1}^T \dot{\mathbf{z}}^{(m)} = \sum_{j=1}^N \frac{d}{dt} \left( \frac{1}{m} e^{im(\theta_j - \omega_0 t)} \right) = \frac{d}{dt} (N p_{m\theta} e^{-i\omega_0 t}),$$

which integrates to  $\mathbf{1}^T \bar{\mathbf{z}}^{(m)}(t) = N p_{m\theta}(t) e^{-i\omega_0 t}$ . In the limit  $t \rightarrow \infty$ , we have  $\mathbf{1}^T \bar{\mathbf{z}}^{(m)} = N \bar{z}^{(m)} = N p_{m\theta}(t) e^{-i\omega_0 t}$ , that is,  $\bar{z}^{(m)} e^{i\omega_0 t} = p_{m\theta}(t)$ .

The closed-loop particle model with the control (5.33) asymptotically converges to the time-invariant dynamics

$$\begin{aligned} \dot{r}_k &= e^{i\theta_k} \\ \dot{\theta}_k &= \omega_0 (1 + K_0 \langle e^{i\theta_k}, c_k - \bar{c} \rangle) - \sum_{m=1}^M K_m \langle i e^{im\theta_k}, p_{m\theta} \rangle. \end{aligned} \quad (6.43)$$

Since  $\dot{\theta}_k = \bar{u}_k$  asymptotically converges to  $\omega_0$ , the solutions of (6.43) asymptotically converge to the set  $\Lambda$  of relative equilibria with

$$\omega_0 K_0 \langle e^{i\theta_k}, c_k - \bar{c} \rangle - \sum_{m=1}^M K_m \langle i e^{im\theta_k}, p_{m\theta} \rangle = 0. \quad (6.44)$$

In  $\Lambda$ ,  $\dot{\boldsymbol{\theta}} = \omega_0 \mathbf{1}$  and  $\mathbf{c}$  is constant. Taking the time-derivative of (6.44) in  $\Lambda$  yields

$$\omega_0^2 K_0 \langle i e^{i\theta_k}, c_k - \bar{c} \rangle + \underbrace{\langle e^{i\theta_k}, \dot{c}_k \rangle}_0 + \sum_{m=1}^M K_m \underbrace{\left( m \langle e^{im\theta_k}, p_{m\theta} \rangle \omega_0 - m \langle i e^{im\theta_k}, i p_{m\theta} \rangle \omega_0 \right)}_0 = 0,$$

where we used  $\dot{p}_{m\theta} = \omega_0 m i p_{m\theta}$ . Thus, points in  $\Lambda$  satisfy  $\langle i e^{i\theta_k}, c_k - \bar{c} \rangle = 0$ , which holds only if  $\mathbf{c} = \bar{c} \mathbf{1}$ , and  $\sum_{m=1}^M K_m \langle i e^{im\theta_k}, p_{m\theta} \rangle = \frac{\partial U^{M,N}}{\partial \theta_k} = 0$ . That is, every point in  $\Lambda$  is a circular formation with a phase arrangement in the critical set of  $U^{M,N}(\boldsymbol{\theta})$ . Using Lemma A.2 with  $V_1(\mathbf{x})$  replaced by  $\omega_0^2 (K_0/2) \|\mathbf{c} - \bar{c} \mathbf{1}\|^2$  and  $V_2(\mathbf{x})$  replaced by  $U^{M,N}(\boldsymbol{\theta})$ , we obtain the stability of critical points of  $U^{M,N}(\boldsymbol{\theta})$  in  $\Lambda$  from Theorem 6.2.  $\square$

To demonstrate Theorem 6.9 we include simulation results for the closed-loop particle model with control (6.40) and a proximity-based (zonal) interaction network. Let  $L(t)$  denote the Laplacian of the graph  $G(t)$  that describes the interaction network. In the simulation, interaction between two particles occurs if and only if their relative distance is less than or equal to  $\rho_0 = |\omega_0|^{-1}$ , which is the radius of the circular formation. We seek to stabilize the splay circular formation with  $N = 12$  particles, which means  $M =$

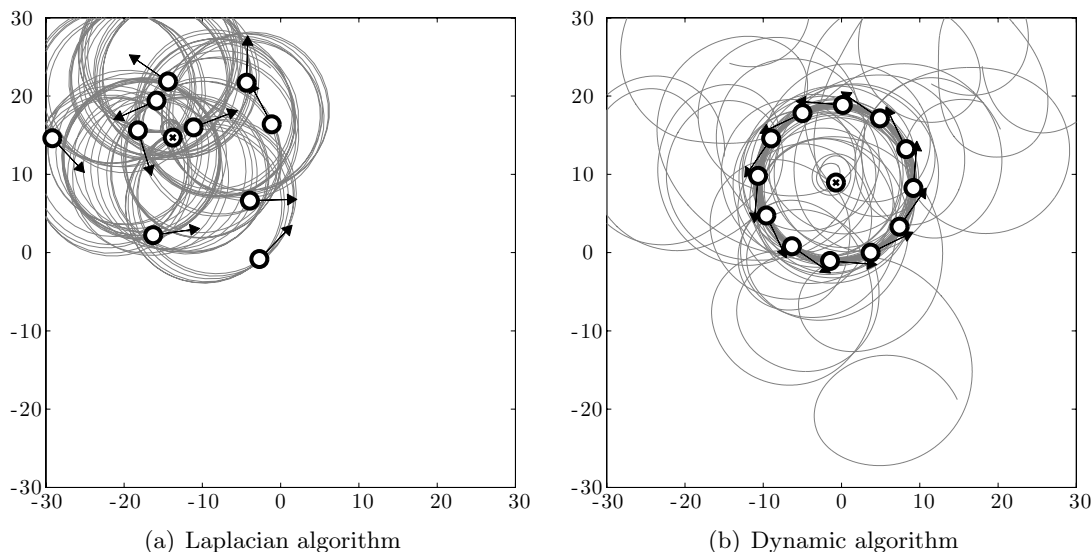


Figure 6.4: Dynamic symmetric circular formation control. Stabilization of the splay circular formation with a zonal interaction network. The perceptual zone of each particle is a circle centered at the particle with radius  $\rho_0 = |\omega_0|^{-1} = 10$ . The remaining parameter values are  $N = M = 12$ ,  $K_0 = 0.1$ , and  $|K_m| = 0.1$  for all  $m \in \mathcal{M}$ . (a) Trajectories generated by the Laplacian algorithm (6.38) with the (normalized) Laplacian  $(1/N)L(t)$ ; (b) trajectories generated by the dynamic algorithm (6.40).

12. Figure 6.4(b) illustrates the trajectories generated by the dynamic algorithm (6.40) starting from random initial conditions over a time period equivalent to six revolutions of the formation. For comparison, Figure 6.4(a) illustrates the trajectories generated by the Laplacian algorithm (6.38) with a time-varying (normalized) Laplacian  $(1/N)L(t)$  starting from the same initial conditions over a time period equivalent to six hundred revolutions (only the final six revolutions are shown). Note, for all-to-all interaction, normalizing the Laplacian by  $N$  renders the Laplacian algorithm equivalent to the limiting dynamics of the dynamic algorithm, which is the all-to-all control (6.21). Figure 6.4 demonstrates that the deficiency of the Laplacian algorithm in supporting time-varying interaction is ameliorated by the dynamic algorithm.

## Chapter 7

# Applied Control Design

In this chapter we describe extensions to the cooperative control framework motivated by applications in mobile sensor networks. In Section 7.1 we introduce a *virtual* particle to serve as a phase reference. A virtual particle can also serve as a beacon about which to center a circular formation. In Section 7.2 we describe the design of multiple, nested interaction networks to stabilize symmetric patterns on multiple circular formations. In Section 7.3 we describe control laws that stabilize symmetric formations on convex loops more suitable for oceanographic sampling.

### 7.1 Continuous Symmetry Breaking Using a Virtual Particle

In the previous chapter we describe an approach to stabilize solutions of the particle model corresponding to symmetric circular formations. This approach, like all of the steering algorithms presented thus far, relies only on shape variables to define the control law. Controls that depend only on shape variables are invariant to rigid rotation and rigid translation of all of the particles (see Section 3.2). For phase synchronization algorithms, rotation invariance means that the steady-state collective direction of motion is arbitrary; it depends only on initial conditions. Likewise, for circular formation algorithms, translation invariance means that the steady-state formation center depends arbitrarily on initial conditions.

In this section we describe an approach to break the continuous symmetries of rotation

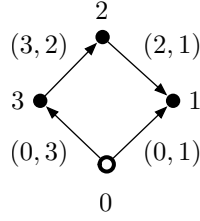


Figure 7.1: Augmented interaction network. Virtual particle 0 augments graph  $G(t) = (\{1, 2, 3\}, \{(2, 1), (3, 2)\})$  with edges  $(0, 1)$  and  $(0, 3)$ . The augmented graph is  $\tilde{G}(t) = (\{0, 1, 2, 3\}, \{(2, 1), (3, 2), (0, 1), (0, 3)\})$ .

and translation in the closed-loop particle model. We start by introducing a virtual particle with index 0 into the set of actual particles. The position  $r_0$  and phase  $\theta_0$  of particle 0 have the dynamics

$$\begin{aligned} \dot{r}_0 &= e^{i\theta_0} \\ \dot{\theta}_0 &= \omega_0, \end{aligned} \quad (7.1)$$

where  $\omega_0 \in \mathbb{R}$  is constant. Note, the dynamics of particle 0 do not depend on the dynamics of particles  $1, \dots, N$ , whereas the dynamics of particles  $1, \dots, N$  may depend on the dynamics of particle 0. This observation has implications for the overall interaction network.

Let  $G(t) = (\mathcal{N}, E(t))$  describe the interaction network of the actual particles. The overall interaction is described by the *augmented graph*  $\tilde{G}(t) \triangleq (\tilde{\mathcal{N}}, \tilde{E}(t))$ , which has node indices  $\tilde{\mathcal{N}} \triangleq \{0, \dots, N\}$  and edge set  $\tilde{E}(t) \subset \tilde{\mathcal{N}} \times \tilde{\mathcal{N}}$ . In particular,  $\tilde{E}(t)$  is the union of set  $E(t)$  with a set of edges of the form  $(0, k)$ , where  $k \in \mathcal{N}$ . There are no edges in  $\tilde{E}(t)$  directed towards node 0, as illustrated in Figure 7.1. The augmented Laplacian matrix  $\tilde{L}(t) \triangleq [\tilde{l}_{kj}]$  of  $\tilde{G}(t)$  is

$$\tilde{L}(t) = \left[ \begin{array}{c|ccc} 0 & 0 & \dots & 0 \\ \hline \tilde{l}_{10}(t) & & & \\ \vdots & L(t) - \text{diag}\{(\tilde{l}_{10}(t), \dots, \tilde{l}_{N0}(t))^T\} & & \\ \tilde{l}_{N0}(t) & & & \end{array} \right], \quad (7.2)$$

where  $\tilde{l}_{k0}(t) = -1$  if and only if  $(0, k) \in \tilde{E}(t)$  and  $\tilde{l}_{k0} = 0$  otherwise. There are no entries on the first row of the augmented Laplacian matrix, because there are no inputs to particle 0.

Because the dynamics of particle 0 are decoupled from the collective, its role is to serve

as an absolute reference in the inertial frame. When a particles is informed of the inertial reference it (temporarily) leads the remaining particles. In the case when  $\omega_0 = 0$ , then  $\theta_0(t) = \theta_0(0)$  and synchronization of phases  $0, \dots, N$  necessarily results in all phases aligned with the reference phase  $\theta_0(0)$ . Likewise, in the case  $\omega_0 \neq 0$ , then particle 0 travels in a circular orbit about the fixed center  $c_0 \triangleq r_0 + \omega_0 i e^{i\theta_0}$ . We show below augmented forms of the Laplacian and dynamic circular formation algorithms that stabilize the set of circular formations around the reference center  $c_0(0)$ . In this section, the all-to-all interaction algorithms are subsumed in the discussion of time-invariant and undirected interaction.

### 7.1.1 Time-invariant and Undirected Interaction

In this section we consider the case when  $G(t) = G(0)$  is time-invariant and undirected and the augmented graph  $\tilde{G}(t) = \tilde{G}(0)$  is time-invariant and directed (since node 0 has only outgoing edges). We provide corollaries to Theorems 4.7 and 5.3 that prove convergence to parallel and circular formations, respectively, in the presence of virtual particle 0.

Consider the *augmented Laplacian phase potential*

$$\tilde{W}_L(\boldsymbol{\theta}) \triangleq W_L(\boldsymbol{\theta}) - \frac{1}{2} \sum_{j=1}^N \tilde{l}_{j0} |e^{i\theta_j} - e^{i\theta_0}|^2, \quad (7.3)$$

where  $W_L(\boldsymbol{\theta})$  is defined by (4.13). The potential  $\tilde{W}_L(\boldsymbol{\theta})$  is positive-semidefinite and, if  $G$  is connected, then, by Lemma 4.6,  $\tilde{W}_L(\boldsymbol{\theta}) = 0$  if and only if  $\theta_k = \theta_0$  for all  $k \in \mathcal{N}$ . Using  $\dot{\theta}_0 = \omega_0$ , the time-derivative of  $\tilde{W}_L(\boldsymbol{\theta})$  along solutions of the phase model (3.6) is

$$\begin{aligned} \dot{\tilde{W}}_L &= \sum_{j=1}^N \langle i e^{i\theta_j}, L_j e^{i\boldsymbol{\theta}} \rangle u_j - l_{j0} \langle e^{i\theta_j} - e^{i\theta_0}, i e^{i\theta_j} u_j - i e^{i\theta_0} \omega_0 \rangle \\ &= - \sum_{j=1}^N \langle i e^{i\theta_j}, L_j e^{i\boldsymbol{\theta}} + \tilde{l}_{j0} e^{i\theta_0} \rangle (\omega_0 - u_j), \end{aligned}$$

where we used  $\sum_{j=1}^N \langle i e^{i\theta_j}, L_j e^{i\boldsymbol{\theta}} \rangle = \langle i B^T e^{i\boldsymbol{\theta}}, B^T e^{i\boldsymbol{\theta}} \rangle = 0$ . Choosing the control

$$u_k = \omega_0 + K \langle i e^{i\theta_k}, L_k e^{i\boldsymbol{\theta}} + \tilde{l}_{k0} e^{i\theta_0} \rangle, \quad K < 0, \quad (7.4)$$

yields

$$\dot{\tilde{W}}_L = K \sum_{j=1}^N \langle i e^{i\theta_j}, L_j e^{i\boldsymbol{\theta}} + \tilde{l}_{j0} e^{i\theta_0} \rangle^2 \leq 0,$$

which leads to the following result [241, Section VI.A].

**Corollary 7.1. Augmented Laplacian phase synchronization** *Let  $L$  be the Laplacian of an undirected and connected graph  $G = (\mathcal{N}, E)$ . Let  $\tilde{L}$  be the Laplacian of the augmented graph  $\tilde{G} \neq G$ . For the augmented control (7.4), all of the synchronized phase arrangements where  $\theta_k(t) = \theta_0(0) + \omega_0 t$  for all  $k \in \mathcal{N}$  are asymptotically stable solutions of the closed-loop phase model (3.6) with  $\dot{\theta}_0 = \omega_0$ .*

*Proof.* Using the invariance principle [131, Theorem 4.4], all of the solutions of the phase model converge to the largest invariant set  $\Omega$  where

$$\langle ie^{i\theta_k}, L_k e^{i\theta} + \tilde{l}_{k0} e^{i\theta_0} \rangle = 0. \quad (7.5)$$

In  $\Omega$ ,  $\dot{\theta} = \omega_0 \mathbf{1}$ . A sufficient condition for  $\theta \in \Omega$  is for  $\theta$  to be in the set  $\Lambda \subset \Omega$  of synchronized phase arrangements where  $\theta_k = \theta_0$  for all  $k \in \mathcal{N}$ . The set  $\Lambda$  is the global minimum of  $\tilde{W}_L(\theta)$  defined in (7.3), which shows that all of the solutions in  $\Lambda$  are asymptotically stable.  $\square$

In the case  $\omega_0 \neq 0$ , then Corollary 7.1 describes a scenario in which all of the particles orbit (different) circles such that their phases track the reference  $\theta_0(0) + \omega_0 t$ . This scenario is effectively depicted by Figure 4.1(a), although the reference phase is not shown. In the case  $\omega_0 = 0$ , then Corollary 7.1 suggests an algorithm to stabilize a parallel formation that tracks a reference trajectory [243, Section VIII.B]. The trajectory tracking algorithm, which combines (7.4) with an open-loop impulsive control, assumes that the reference phase  $\theta_0(t)$  is piecewise-constant. Let  $t_n, n = 1, 2, \dots$ , denote the times at which the reference changes. Each time the reference changes, the impulse control

$$\Delta\theta_k(t_n) = \theta_0(t_n) - \theta_k(t_n) \quad (7.6)$$

orients the velocity  $e^{i\theta_k}$  in the direction of the reference. Then the continuous control (7.4) asymptotically stabilizes a parallel formation moving in this direction. In the absence of the impulse control, the continuous control tracks the reference with a visible transient. Such a scenario is illustrated in Figure 7.2 for a complete graph  $G$ . In this simulation, particle 1 is informed by the reference phase  $\theta_0$ .

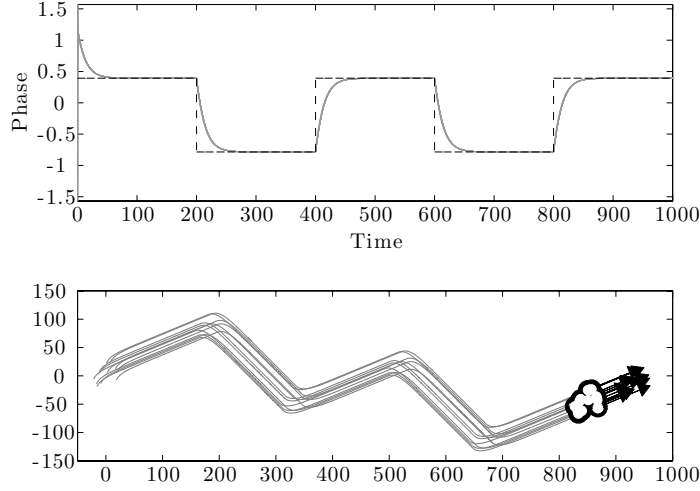


Figure 7.2: Augmented Laplacian phase control. A group of 12 particles with all-to-all interaction tracks a piecewise-constant reference phase  $\theta_0(0) \in \{\frac{\pi}{8}, \frac{\pi}{4}\}$  using the control (7.4) with  $K = 1$ ,  $\tilde{l}_{10} = -1$ , and  $\tilde{l}_{k0} = 0$  otherwise. (top) phases  $\boldsymbol{\theta}$  (solid gray lines) track reference phase  $\theta_0$  (dashed line); (bottom) corresponding particle trajectories in the plane.

Corollary 7.1 provides a local description of the effect of the reference phase  $\theta_0$  on the set of synchronized phase arrangements. It does not characterize other phase arrangements in  $\Omega$ , that is, phase arrangements that satisfy the invariance condition (7.5). We present such a characterization here. Since a general result has not been developed, we consider the case when there is exactly one edge from node 0 to a node  $k \in \mathcal{N}$  and, without loss of generality, assume  $k = 1$ . In this case, (7.5) becomes

$$\langle ie^{i\theta_1}, L_1 e^{i\boldsymbol{\theta}} - e^{i\theta_0} \rangle = 0 \quad (7.7)$$

and

$$\langle ie^{i\theta_k}, L_k e^{i\boldsymbol{\theta}} \rangle = \frac{\partial W_L}{\partial \theta_k} = 0, \quad k = 2, \dots, N. \quad (7.8)$$

If  $\boldsymbol{\theta}$  is a critical point of  $W_L(\boldsymbol{\theta})$ , then  $\boldsymbol{\theta}$  satisfies (7.8) and (7.7) becomes  $\langle ie^{i\theta_1}, e^{i\theta_0} \rangle = 0$ . This shows that  $\Omega$  contains the set of critical points of  $W_L(\boldsymbol{\theta})$  where  $\theta_1 = \theta_0 \bmod \pi$ . In fact,  $\Omega$  is equal to the set of critical points of  $W_L(\boldsymbol{\theta})$  where  $\theta_1 = \theta_0 \bmod \pi$ , which we prove by contradiction. Assume  $\boldsymbol{\theta}$  is not a critical point of  $W_L(\boldsymbol{\theta})$ . Summing (7.7) and (7.8) for all  $k = 2, \dots, N$  yields  $\langle ie^{i\theta_1}, e^{i\theta_0} \rangle = 0$  since  $\sum_{j=1}^N \langle ie^{i\theta_j}, L_j e^{i\boldsymbol{\theta}} \rangle = \langle iB^T e^{i\boldsymbol{\theta}}, B e^{i\boldsymbol{\theta}} \rangle = 0$ . This implies that (7.7) and (7.8) are equivalent to  $\langle ie^{i\theta_k}, L_k e^{i\boldsymbol{\theta}} \rangle = \frac{\partial W_L}{\partial \theta_k} = 0$  for all  $k \in \mathcal{N}$ , which

is a contradiction.

We do not have such a characterization of  $\Omega$  when there are two or more outgoing edges from node 0. For example, suppose there is an edge from node 0 to node 1 and from node 0 to node 2. One can show that, if  $\boldsymbol{\theta}$  is a critical point of  $W_L(\boldsymbol{\theta})$  with  $\theta_1 + \theta_2 = \theta_0 \bmod \pi$  or both  $\theta_1 = \theta_0 \bmod \pi$  and  $\theta_2 = \theta_0 \bmod \pi$ , then  $\boldsymbol{\theta} \in \Omega$ . However,  $\Omega$  may contain other phase arrangements that are not in the critical set of  $W_L(\boldsymbol{\theta})$ . Consider, for example, phase arrangement  $\boldsymbol{\theta}$  where  $\langle ie^{i\theta_k}, L_k e^{i\boldsymbol{\theta}} \rangle = \langle ie^{i\theta_k}, e^{i\theta_0} \rangle \neq 0$  for  $k = 1, 2$  and  $\langle ie^{i\theta_k}, L_k e^{i\boldsymbol{\theta}} \rangle = 0$  for  $k = 3, \dots, N$ . Using (7.5), we observe that  $\boldsymbol{\theta} \in \Omega$  though  $\boldsymbol{\theta}$  is not a critical point of  $W_L(\boldsymbol{\theta})$ .

Next we describe the corresponding analysis of the effect of a virtual particle on the circular formation algorithm. For the purposes of stabilizing a circular formation at a reference center  $c_0 \triangleq r_0 + \omega_0^{-1}ie^{i\theta_0}$ ,  $\omega_0 \neq 0$ , consider the augmented Laplacian circular formation potential

$$\tilde{S}_L(\mathbf{r}, \boldsymbol{\theta}) \triangleq S_L(\mathbf{r}, \boldsymbol{\theta}) - \frac{1}{2} \sum_{j=1}^N \tilde{l}_{j0} |c_{j,0}|^2, \quad (7.9)$$

where  $S_L(\mathbf{r}, \boldsymbol{\theta})$  is defined in (5.13) and  $c_{j,0} \triangleq c_j - c_0$ . The potential  $\tilde{S}_L(\mathbf{r}, \boldsymbol{\theta})$  is positive-semidefinite and, if  $G$  is connected, then  $\tilde{S}_L(\mathbf{r}, \boldsymbol{\theta}) = 0$  if and only if  $c_k = c_0$  for all  $k \in \mathcal{N}$ . Using  $\dot{c}_0 = 0$ , the time-derivative of  $\tilde{S}_L(\mathbf{r}, \boldsymbol{\theta})$  along solutions of the particle model (3.5) is

$$\begin{aligned} \dot{\tilde{S}}_L &= \sum_{j=1}^N \langle e^{i\theta_j}, L_j \mathbf{c} \rangle \omega_0^{-1} (\omega_0 - u_j) - \tilde{l}_{j0} \langle c_{j,0}, e^{i\theta_j} \rangle \omega_0^{-1} (\omega_0 - u_j) \\ &= \omega_0^{-1} \sum_{j=1}^N \langle e^{i\theta_j}, L_j \mathbf{c} - \tilde{l}_{j0} c_{j,0} \rangle (\omega_0 - u_j). \end{aligned}$$

Choosing the control

$$u_k = \omega_0 (1 + K_0 \langle e^{i\theta_k}, L_k \mathbf{c} - \tilde{l}_{k0} c_{k,0} \rangle), \quad K_0 < 0, \quad (7.10)$$

yields

$$\dot{\tilde{S}}_L = K_0 \sum_{j=1}^N \langle e^{i\theta_j}, L_j \mathbf{c} - \tilde{l}_{j0} c_{j,0} \rangle^2 \leq 0,$$

which leads to the following result [241, Section VI.A].

**Corollary 7.2. Augmented Laplacian circular formation control** *Let  $L$  be the Laplacian of an undirected and connected graph  $G = (\mathcal{N}, E)$ . Let  $\tilde{L}$  be the Laplacian of the augmented graph  $\tilde{G} \neq G$ . For the augmented control (7.10), all of the solutions of the closed-loop*

phase model (3.6) with  $\dot{\theta}_0 = \omega_0 \neq 0$  converge to the set of circular formations with radius  $|\omega_0|^{-1}$ , direction of rotation determined by the sign of  $\omega_0$ , and center  $c_0 \triangleq r_0 + \omega_0^{-1}ie^{i\theta_0}$ .

*Proof.* Let  $\tilde{\mathcal{N}}_k \triangleq \{0, \mathcal{N}_k\}$  if  $(0, k) \in \tilde{E}$  and  $\tilde{\mathcal{N}}_k \triangleq \mathcal{N}_k$  otherwise. Using the invariance principle [131, Theorem 4.4 and Corollary 4.2], all of the solutions of the phase model converge to the largest invariant set  $\Omega$  where

$$\langle e^{i\theta_k}, L_k \mathbf{c} - \tilde{l}_{k0} c_{k,0} \rangle = \langle e^{i\theta_k}, \sum_{j \in \tilde{\mathcal{N}}_k} c_{k,j} \rangle = 0. \quad (7.11)$$

In  $\Omega$ ,  $\dot{\boldsymbol{\theta}} = \omega_0 \mathbf{1}$  and  $\mathbf{c}$  is constant, which implies (7.11) holds only if  $c_k = c_0$  for all  $k \in \mathcal{N}$ .  $\square$

Corollary 7.2 is relevant to applications with an unknown, bounded drift vector field  $f(t, r_k) \in \mathbb{C}$  on the positions  $r_k$ . Assume  $|f(t, r_k)| < 1$ . We model the effect of  $f(t, r_k)$  on the particle model simply by adding it to the inertial velocity  $\dot{r}_k$ , that is,  $\dot{r}_k = e^{i\theta_k} + f(t, r_k)$ . For example, consider a constant, uniform vector field  $f(t, r_k) = f$ . Using the velocity  $\dot{r}_k - f = e^{i\theta_k}$ , which is relative to the vector field, one can show that the circular formation algorithms from Chapter 5 stabilize circular formations that rigidly translate at constant velocity  $f$  relative to the inertial frame. On the other hand, the augmented circular formation algorithm (7.10), which breaks the translational symmetry, seeks to stabilize circular formations that are fixed in the inertial frame. We illustrate the effectiveness of the augmented algorithm in the presence of a drift vector field.

Since a general result has not been developed, consider the case in which all of the particles are informed by the virtual particle. Using  $\dot{c}_k = \omega_0^{-1}(\omega_0 - u_k) + f$ , the time-derivative of  $\tilde{S}_L(\mathbf{r}, \boldsymbol{\theta})$  defined in (7.9) along solutions of the closed-loop particle model with the control (7.10) is

$$\begin{aligned} \dot{\tilde{S}}_L &= \sum_{j=1}^N \omega_0^{-1} \langle e^{i\theta_j}, L_j \mathbf{c} - \tilde{l}_{j0} c_{j,0} \rangle (\omega_0 - u_j) + \langle f, L_j \mathbf{c} - \tilde{l}_{j0} c_{j,0} \rangle \\ &= \sum_{j=1}^N K_0 \underbrace{\langle e^{i\theta_j}, L_j \mathbf{c} + c_{j,0} \rangle^2}_{\leq |L_j \mathbf{c} + c_{j,0}|^2} + \underbrace{\langle f, L_j \mathbf{c} + c_{j,0} \rangle}_{\leq |f| |L_j \mathbf{c} + c_{j,0}|}. \end{aligned}$$

The second term on the right-hand side is indefinite, which implies that  $\tilde{S}_L(\boldsymbol{\theta})$  is not guaranteed to decrease if  $|K_0| |L_k \mathbf{c} + c_{k,0}| \leq |f|$ . In the case  $c_k = c_j$  for all pairs  $k \neq 0$  and  $j \neq 0$ ,

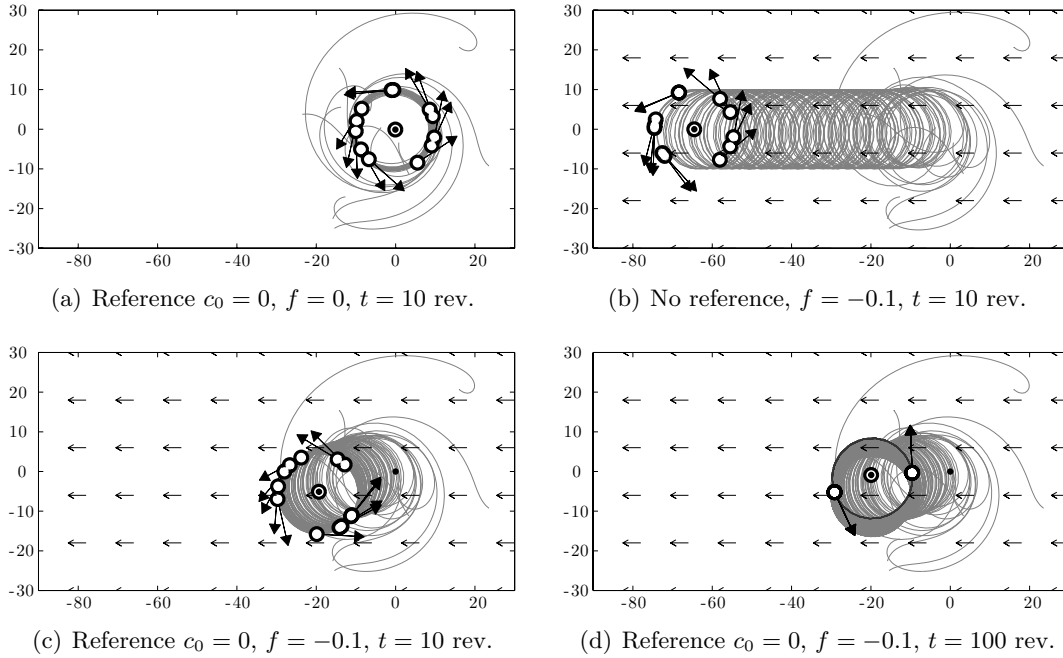


Figure 7.3: Augmented Laplacian circular formation control. Simulations with  $N = 12$ ,  $\omega_0 = 0.1$ ,  $K_0 = 0.01$ ,  $f \in \{0, -0.1\}$  (vector field not to scale), and all-to-all interaction. The simulation duration is  $t \in \{10, 100\}$  revolutions. The reference center  $c_0 = 0$  is depicted by a black dot; the centroid of circle centers is depicted by a circle marked with a  $\bullet$ . (a,c,d) Augmented control (7.10) stabilizes circular formation fixed in inertial frame; (b) original control (5.14) stabilizes circular formation fixed in frame moving at speed  $f$ .

we cannot conclude from this Lyapunov function that  $|c_{k,0}|$  decreases below  $|f/K_0|$ . This analysis suggests that the formation center is bounded away from the reference center by an error proportional to the magnitude of the flow.

We test for the existence of a lower error bound in simulation. Figure 7.3 compares the results of simulations of the augmented control (7.10) with the original control (5.14) in the presence of a drift vector field  $f = -0.1$ . The simulations show that the augmented control stabilizes a circular formation fixed in the inertial frame, whereas the original control stabilizes a circular formation fixed in a frame moving at  $f$ . In the case  $f = 0$ , the steady-state error  $c_{k,0} = 0$  for all  $k \in \mathcal{N}$ . In the case  $f = -0.1$ , we observe an error of  $2|f/K_0|$ , consistent with the predicted lower bound to within a factor of two.

For long simulation times, particles using control (7.10) in the presence of uniform

flow converge to two, nearly opposite clusters on the circle, even though no symmetric pattern is imposed by the control law. This phenomenon—reminiscent of the beads-on-a-wire example in Section 2.3.2—appears driven by the phase-dependent rotation rate about the circle center. That is, when a particle phasor  $e^{i\theta_k}$  is parallel to  $f$ , then its rotation rate about the center is faster than when  $e^{i\theta_k}$  is antiparallel to  $f$ . For a constant rate of turning  $\dot{\theta}_k = \omega_0$ , this apparently leads to particle clustering.

Note that the control (7.10) does not require knowledge of the flow  $f$ , although we use  $f$  to integrate the particle trajectories. In order to drive the formation center to the desired location, one might consider endowing the reference center  $c_0$  with dynamics that drive  $|c_{k,0}|$  to zero. Otherwise, each particle could estimate the flow field and use this estimate in its control algorithm.

### 7.1.2 General Interaction

In this section we augment the dynamic phase synchronization and circular formation algorithms to break continuous symmetries. Once again, we assume particle 0 is virtual and has the dynamics given in (7.1). Let  $G(t) = (\mathcal{N}, E(t))$  represent a time-varying and/or directed interaction network. Graph  $\tilde{G}(t) = (\tilde{\mathcal{N}}, \tilde{E}(t))$  is the augmentation of  $G(t)$ , where  $\tilde{E}(t)$  is the union of  $E(t)$  and a set of edges of the form  $(0, k)$ ,  $k \in \mathcal{N}$ . We assume that  $\tilde{G}(t)$  is uniformly connected, which implies  $\tilde{G}(t)$  is uniformly connected to node 0. Let  $\tilde{L}(t) \triangleq [\tilde{l}_{kj}(t)]$  be the Laplacian matrix of  $\tilde{G}(t)$  given by (7.2).

For the purposes of synchronization with the reference phase  $\theta_0$ , particle 0 is assigned the consensus variable  $z_0 \triangleq w_0 e^{i(\theta_0 - \omega_0 t)}$  such that  $\dot{z}_0 = \dot{w}_0 = 0$ . Using (4.30), the augmented dynamic phase synchronization algorithm is

$$\begin{aligned} \dot{u}_k &= \omega_0 - K \langle w_k, i \rangle, \quad K < 0 \\ \dot{w}_k &= -(u_k - \omega_0) i w_k - \sum_{j=0}^N \tilde{l}_{kj}(t) w_j e^{i\theta_{j,k}}, \quad w_k(0) = 1, \quad k \in \mathcal{N}. \end{aligned} \tag{7.12}$$

If  $(0, k) \in \tilde{E}(t)$ , this algorithm requires the transmission to node  $k$  of the variable  $w_0$  from node 0. If  $\omega_0$  is zero, then  $w_0(t) = w_0(0) = 1$  for all  $t$ . We have the following result [241, Section VI.A].

**Corollary 7.3. Augmented dynamic phase synchronization** *Let  $\tilde{L}(t)$  be the Laplacian of an augmented graph  $\tilde{G}(t) = (\tilde{\mathcal{N}}, \tilde{E}(t))$ . Consider the closed-loop phase model (3.6) with the augmented control (7.12). If  $\tilde{G}(t)$  is uniformly connected, then all of the solutions of (3.6) converge to the set where  $\theta_k = \theta_0 \bmod \pi$  for all  $k \in \mathcal{N}$ . All of the synchronized phase arrangements where  $\theta_k(t) = \theta_0(0) + \omega_0 t$  are asymptotically stable and all of the remaining equilibria are unstable.*

*Proof.* For all  $k \in \tilde{\mathcal{N}}$ , the time-derivative of  $z_k \triangleq w_k e^{i(\theta_k - \omega_0)t}$  along solutions of the closed-loop phase model (3.6) with control (7.12) is

$$\dot{z}_k = \dot{w}_k e^{i(\theta_k - \omega_0)t} + (u_k - \omega_0) i w_k e^{i(\theta_k - \omega_0)t} = - \sum_{j=0}^N \tilde{l}_{kj}(t) z_j.$$

This shows that  $z_k$  obeys the consensus dynamics (4.24) with respect to the augmented Laplacian  $\tilde{L}(t)$ . Since  $\dot{z}_0 = 0$ , then  $z_0(t) = z_0(0)$ , which implies  $z_k \rightarrow z_0(0)$  for all  $k \in \mathcal{N}$  as  $t \rightarrow \infty$ . The limiting dynamics are

$$\dot{\theta}_k - \omega_0 = -K \langle i e^{i(\theta_k - \omega_0 t)}, z_0(0) \rangle = -K \sin(\theta_0 - \theta_k), \quad k \in \mathcal{N}.$$

The remainder of the proof follows the proof of Theorem 4.10 with  $K < 0$  and  $\arg\{\bar{z}\}$  replaced by  $\theta_0$ .  $\square$

Corollary 7.3 shows that all of the phases tend to synchronize with the reference phase  $\theta_0$ . For  $\omega_0 = 0$ , this means that the particles join a parallel formation that moves in the direction  $\theta_0(0)$ . This result, which is independent of  $N$ , implies that a collective can exhibit parallel motion in a reference direction when as few as one particle (a leader) is informed of the reference, and that one particle has access to the reference only periodically.<sup>1</sup> And, as  $N$  increases, the percentage of informed individuals required to stabilize parallel motion in the reference direction decreases. This phenomenon was originally described in [54], and has been further explored in [179]. Leadership in this context is also studied in [284]. Note, if individuals in the collective are informed by more than one reference phase, that

---

<sup>1</sup>Time dependence of these interactions enters the proof through the assumption of uniform connectivity.

is, if there is more than one virtual particle, then  $\tilde{G}(t)$  can not be uniformly connected and Corollary 7.3 will not hold.

We turn now to the dynamic stabilization of a circular formation with reference center  $c_0 \triangleq r_0 + i\omega_0^{-1}e^{i\theta_0}$ , where  $\omega_0 \neq 0$ . In this setting, we use the consensus variables  $z_k \triangleq w_k e^{i\theta_k}$  and  $y_k \triangleq v_k e^{i\theta_k} + r_k$  for all  $k \in \tilde{\mathcal{N}}$ . The augmented dynamic circular formation algorithm is

$$\begin{aligned} u_0 &= \omega_0 \\ \dot{w}_0 &= -\omega_0 i w_0, w_0(0) = 1 \\ \dot{v}_0 &= -1 - \omega_0 i v_0, v_0(0) = 0, \end{aligned} \tag{7.13}$$

and

$$\begin{aligned} u_k &= \omega_0(1 - K_0 \langle v_k, 1 \rangle) + K_0 \langle w_k, i \rangle, K_0 > 0 \\ \dot{w}_k &= -u_k i w_k - \sum_{j=0}^N \tilde{l}_{kj}(t) w_j e^{i\theta_{j,k}}, w_k(0) = 1 \\ \dot{v}_k &= -1 - u_k i v_k - \sum_{j=0}^N \tilde{l}_{kj}(t) (v_j e^{i\theta_{j,k}} - r_j e^{-i\theta_k}), v_k(0) = 0, k \in \mathcal{N}. \end{aligned} \tag{7.14}$$

We have the following result [241, Section VI.A].

**Corollary 7.4. Augmented dynamic circular formation control** *Let  $\tilde{L}(t)$  be the Laplacian of an augmented graph  $\tilde{G}(t) = (\tilde{\mathcal{N}}, \tilde{E}(t))$  that is uniformly connected. For the control (7.14), all of the solutions of the closed-loop particle model (3.5) converge to the set of circular formations with radius  $|\omega_0|^{-1}$ , with direction of rotation determined by the sign of  $\omega_0 \neq 0$ , and center  $c_0(0) = r_0(0) + i\omega_0 e^{i\theta_0(0)}$ .*

*Proof.* For all  $k \in \tilde{\mathcal{N}}$ , the time-derivatives of  $z_k$  and  $y_k$  along solutions of the closed-loop particle model (3.5) with control (7.14) are

$$\dot{z}_k = \dot{w}_k e^{i\theta_k} + u_k w_k i e^{i\theta_k} = - \sum_{j=0}^N l_{kj}(t) z_j$$

and

$$\dot{y}_k = \dot{v}_k e^{i\theta_k} + u_k v_k i e^{i\theta_k} + e^{i\theta_k} = - \sum_{j=1}^N l_{kj}(t) y_j,$$

which means that  $z_k$  and  $y_k$  obey the consensus dynamics (4.24) with respect to the augmented Laplacian  $\tilde{L}(t)$ . Since  $\dot{z}_0 = 0$ , then  $z_0(t) = z_0(0)$ , which implies  $z_k \rightarrow z_0(0)$  for all

$k \in \mathcal{N}$  as  $t \rightarrow \infty$ . Similarly,  $\dot{y}_0 = 0$  and  $y_0(t) = y_0(0)$ , which implies  $y_k \rightarrow y_0(0)$  for all  $k \in \mathcal{N}$ . In the limit  $t \rightarrow \infty$ , the control (7.14) converges to

$$\begin{aligned} u_k &= \omega_0(1 + K_0 \langle e^{i\theta_k}, r_k - y_0(0) \rangle + K_0 \langle i e^{i\theta_k}, z_0(0) \rangle) \\ &= \omega_0(1 + K_0 \langle e^{i\theta_k}, r_k - \underbrace{(y_0(0) + \omega_0^{-1} i z_0(0))}_{c(0)} \rangle). \end{aligned}$$

The remainder of the proof follows the proof of Theorem 5.4 with  $\bar{c}$  replaced by  $c_0(0)$ .  $\square$

## 7.2 Discrete Symmetry Breaking Using Network Design

In the previous section, we introduce the notion of a virtual particle in order to break the continuous symmetries of the closed-loop particle model. Another symmetry of the particle model is invariance to *permutations* of the particle indices. For example, under all-to-all interaction, swapping the index of any particle with the index of any other particle has no effect on the solution trajectories. In addition, for time-invariant and undirected interaction, if particles  $j$  and  $k$  are neighbors and  $\mathcal{N}_k - j = \mathcal{N}_j - k$ , then swapping  $j$  and  $k$  has no effect on the solution trajectories. Since the group of permutations is finite, permutation invariance is a discrete symmetry. Although general interaction networks possess discrete symmetries too, we consider only time-invariant and undirected interaction networks here.

We are motivated to break the permutation symmetry of the particle model by the desire to stabilize a *multi-level symmetric configuration*, which is composed of multiple, symmetric (circular) formations whose collective phase arrangement is also symmetric. The circular formations in a multi-level symmetric configuration can be fixed in the plane by the presence of a reference center. Although a multi-level symmetric configuration involves a high-level of symmetry in the steady-state phase configuration, it is not invariant to all permutations. For example, consider Figure 7.4(a), which depicts a configuration involving three pairs of particles. Each pair of particles orbits a different circle that is fixed in the plane by a reference center. The phases of particles on the same circular orbit are balanced, whereas the phases of particles on different circular orbits are either synchronized or balanced.

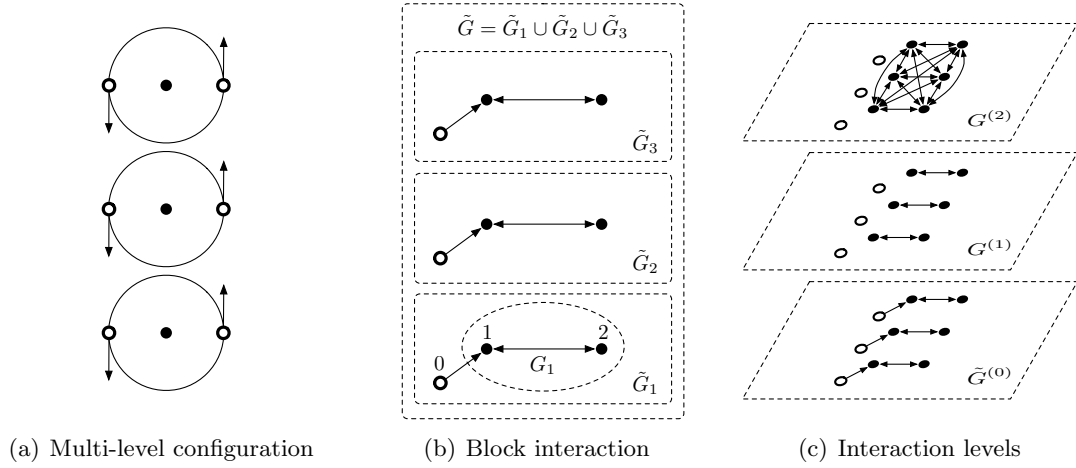


Figure 7.4: Multi-level symmetric configuration and supporting interaction network. (a) A multi-level symmetric configuration with three pairs of particles that collectively form a  $(2, 6)$ -pattern where each pair of particles forms a  $(2, 2)$ -pattern circular formation with a reference center; (b) block interaction with three blocks augmented by a virtual particle; (c) three, hierarchical levels of interaction that support the multi-level symmetric configuration shown in (a).

The configuration shown in Figure 7.4(a) contains three  $(2, 2)$ -pattern circular formations that collectively form a  $(2, 6)$ -pattern. In such a configuration, swapping indices of particles on the same circle does not change the control laws, whereas swapping indices between particles on different circles would require a change of control laws (namely each individual in the swap would need to change their circle reference).

As a first step towards an algorithm to stabilize multi-level configurations with time-invariant and undirected interaction, we introduce the notion of *block interaction*, which is so named because of the block-diagonal structure of the corresponding graph Laplacian. A block is a subset of particles that interact with one another; there is no interaction between blocks. Let  $\mathcal{B}$  denote the number of blocks. For  $b = 1, \dots, \mathcal{B}$ , graph  $G_b$  describes the interaction between all of the particles in block  $b$ . Collectively, the set of all interaction is described by the graph  $G \triangleq \bigcup_{b=1}^{\mathcal{B}} G_b$ . The Laplacian matrix  $L$  corresponding to graph  $G$  is block-diagonal and each block is the Laplacian of the graph  $G_b$ . If there is a virtual particle associated to each block, then the augmented interaction in that block is described by graph  $\tilde{G}_b$  and the collective set of block interactions is described by the graph  $\tilde{G} = \bigcup_{b=1}^{\mathcal{B}} \tilde{G}_b$ . In this

case, the virtual particles may be assigned nonzero indices so that the augmented Laplacian  $\tilde{L} \triangleq [\tilde{l}_{kj}]$ , which has dimensions  $(N + B) \times (N + B)$ , is block-diagonal. For example, the block interaction depicted in Figure 7.4(b) has three blocks, each with one virtual particle; the augmented Laplacian is

$$\tilde{L} = \text{diag}\{(1, 1, 1)^T\} \otimes \left[ \begin{array}{c|cc} 0 & 0 & 0 \\ \hline -1 & 2 & -1 \\ \hline 0 & 1 & -1 \end{array} \right] = \left[ \begin{array}{ccc|ccc|ccc} 0 & 0 & 0 & 0 & 0 & 0 & 0 & 0 & 0 \\ -1 & 2 & -1 & 0 & 0 & 0 & 0 & 0 & 0 \\ 0 & 1 & -1 & 0 & 0 & 0 & 0 & 0 & 0 \\ \hline 0 & 0 & 0 & 0 & 0 & 0 & 0 & 0 & 0 \\ 0 & 0 & 0 & -1 & 2 & -1 & 0 & 0 & 0 \\ 0 & 0 & 0 & 0 & 1 & -1 & 0 & 0 & 0 \\ \hline 0 & 0 & 0 & 0 & 0 & 0 & 0 & 0 & 0 \\ 0 & 0 & 0 & 0 & 0 & 0 & -1 & 2 & -1 \\ 0 & 0 & 0 & 0 & 0 & 0 & 0 & 1 & -1 \end{array} \right],$$

where  $\otimes$  is the Kronecker product.

For  $\tilde{L}$  the Laplacian of an augmented graph  $\tilde{G}$  with block interaction, consider the control

$$u_k = \omega_0(1 - K_0 \langle e^{i\theta_k}, \sum_{j=0}^{N+B-1} \tilde{l}_{kj} c_{k,j} \rangle), \quad K_0 < 0. \quad (7.15)$$

Since there is no interaction between blocks, (7.15) is equivalent to the augmented control (7.10) within each block. Consequently, Corollary 7.2 shows that each block of particles converges to a circular formation with reference center determined by the corresponding virtual particle.

The second step towards a multi-level symmetric configuration algorithm is the notion of *interaction levels*. The basic idea of an interaction level is to use multiple interaction networks in a single control algorithm. Each interaction network occupies one level. Define  $\mathcal{L}$  so there are  $\mathcal{L} + 1$  levels in total. Consider, for instance, Lemma 6.4 and the composite control (6.28), which contains two terms:  $\omega_0(1 + K_0 \langle e^{i\theta_k}, L_k \mathbf{c} \rangle)$ , which drives the particles to a circular formation, and  $\frac{\partial W_L^*}{\partial \theta_k}$ , which drives the phases to a critical point of a Laplacian phase potential  $W_L^*(\boldsymbol{\theta})$ . Lemma 6.4 assumes the same interaction network is used to generate both terms. In the following adaptation of Lemma 6.4, we remove this assumption in order to use multiple interaction networks in the composite control. In particular, we assign level 0 to the circular formation term and levels  $1, \dots, \mathcal{L}$  to the phase gradient term.

**Lemma 7.5. Multi-level Laplacian composite phase and formation control** Let  $\tilde{L}^{(0)}$  be the Laplacian of an undirected and connected graph  $\tilde{G}^{(0)}$ . Let  $L^{(n)}$  be the Laplacian of graph  $G^{(n)} = (\mathcal{N}, E^{(n)})$  on level  $n \in \{1, \dots, \mathcal{L}\}$  and let  $W_{L^{(n)}}^*(\boldsymbol{\theta})$  be a smooth and rotationally symmetric Laplacian phase potential. For the shape control

$$u_k = \omega_0(1 + K_0 \langle e^{i\theta_k}, L_k^{(0)} \mathbf{c} \rangle) + \sum_{n=1}^{\mathcal{L}} \frac{\partial W_{L^{(n)}}^*}{\partial \theta_k}, \quad K_0 > 0, \quad (7.16)$$

all of the solutions of the closed-loop particle model (3.5) converge to the set of circular formations with radius  $|\omega_0|^{-1}$  and direction of rotation determined by the sign of  $\omega_0 \neq 0$ . All of the circular formations in the limiting set have phase arrangements in the critical set of the phase potential  $W_L^{**}(\boldsymbol{\theta}) \triangleq \sum_{n=1}^{\mathcal{L}} W_{L^{(n)}}^*(\boldsymbol{\theta})$ . Every isolated local minimum of  $W_L^{**}(\boldsymbol{\theta})$  defines an asymptotically stable set of circular formations; every circular formation where  $W_L^{**}(\boldsymbol{\theta})$  does not reach a minimum and  $\boldsymbol{\theta}$  is isolated in shape space is unstable.

*Proof.* Since the control (7.16) is a shape control, then the closed-loop particle model evolves on the reduced shape space. Furthermore, the potential

$$V_L^{**}(\mathbf{r}, \boldsymbol{\theta}) \triangleq \omega_0^2 K_0 S_{L^{(0)}}(\mathbf{r}, \boldsymbol{\theta}) - W_L^{**}(\boldsymbol{\theta}), \quad K_0 > 0,$$

is positive definite and proper in the reduced shape space and  $\dot{V}_L^{**}(\mathbf{r}, \boldsymbol{\theta}) \leq 0$ . Let  $\Omega$  be the set of all of the points in the reduced shape space where  $\dot{V}_L^{**} = 0$ . In this set,

$$\omega_0 K_0 \langle e^{i\theta_k}, L_k^{(0)} \mathbf{c} \rangle + \frac{\partial W_L^{**}}{\partial \theta_k} = 0, \quad (7.17)$$

which implies  $\dot{\boldsymbol{\theta}} = \omega_0 \mathbf{1}$  and  $\mathbf{c}$  is constant. Let  $\Lambda$  denote the largest invariant set in  $\Omega$ . Also let  $\mathcal{N}_k^{(n)}$  denote the neighbor set of node  $k$  in graph  $G^{(n)}$ . Taking the time-derivative of (7.17) in  $\Omega$  yields

$$\langle i e^{i\theta_k}, L_k^{(0)} \mathbf{c} \rangle \omega_0^2 + \langle e^{i\theta_k}, \underbrace{\sum_{j \in \mathcal{N}_k^{(0)}} \dot{c}_{k,j}}_0 \rangle \omega_0 + \frac{d}{dt} \left( \frac{\partial W_L^{**}}{\partial \theta_k} \right) \Big|_{\Omega} = 0,$$

where, using the rotational symmetry of  $W_{L^{(n)}}^*$  for all  $n = 1, \dots, \mathcal{L}$ , we have

$$\frac{d}{dt} \left( \frac{\partial W_L^{**}}{\partial \theta_k} \right) \Big|_{\Omega} = \sum_{n=1}^{\mathcal{L}} \sum_{j=1}^N \frac{\partial^2 W_{L^{(n)}}^*}{\partial \theta_j \partial \theta_k} \omega_0 = 0.$$

Thus, points in  $\Lambda$  satisfy

$$\langle ie^{i\theta_k}, L_k^{(0)} \mathbf{c} \rangle = 0.$$

The remainder of the proof follows the proof of Lemma 6.1 with  $L_k$  replaced by  $L_k^{(0)}$  and  $U^*(\mathbf{r}, \boldsymbol{\theta})$  replaced by  $W_L^{**}(\mathbf{r}, \boldsymbol{\theta})$ .  $\square$

We use multiple interaction levels to generate multi-level symmetric configurations in the following way. Level 0 is associated to the augmented block interaction that supports stabilization of circular formations with prescribed reference centers. Each level  $n \in \{1, \dots, \mathcal{L}\}$ , for which there is also a dedicated interaction network, supports the generation of a particular phase pattern. For example, there is pairwise interaction on level 1 shown in Figure 7.4(c); this level supports the generation of three (2,2)-patterns. In the same figure, there is all-to-all interaction on level 2, which supports the generation of a (2,6)-pattern. Collectively, levels  $0, \dots, 2$  support the generation of the multi-level symmetric configuration shown in Figure 7.4(a). Note that, since level 0 contains virtual particles, then levels 1 and 2 must also contain virtual particles (even though they have no outgoing edges) in order for the particle indices to be consistent across all levels. The control law that generates this configuration is

$$u_k = \omega_0(1 - K_0 \langle e^{i\theta_k}, \sum_{j=0}^8 \tilde{l}_{kj} c_{k,j} \rangle) + \frac{\partial W_{L^{(1)}}^{2,2}}{\partial \theta_k} + \frac{\partial W_{L^{(2)}}^{2,6}}{\partial \theta_k}, \quad K_0 > 0, \quad k \in \{0, \dots, N+B-1\}. \quad (7.18)$$

Figure 7.5 illustrates the cumulative effect of this multi-level interaction network.

In order to formalize the phase component of this algorithm, let  $\mathbf{M} \triangleq (M_1, \dots, M_{\mathcal{L}})^T$  and  $\mathbf{N} \triangleq (N_1, \dots, N_{\mathcal{L}})^T$  such that  $M_n$  is a divisor of  $N_n$  for all  $n = 1, \dots, \mathcal{L}$ . Let  $W_{L^{(n)}}^{M_n, N_n}(\boldsymbol{\theta})$  be a  $(M_n, N_n)$ -pattern Laplacian phase potential. The potential  $W_L^{M, \mathbf{N}}(\boldsymbol{\theta}) \triangleq \sum_{n=1}^{\mathcal{L}} W_{L^{(n)}}^{M_n, N_n}(\boldsymbol{\theta})$  is a multi-level Laplacian symmetric phase pattern potential. Each level in  $W_L^{M, \mathbf{N}}(\boldsymbol{\theta})$  further refines the set of phase arrangements that minimize  $W_L^{M, \mathbf{N}}(\boldsymbol{\theta})$ . In fact,  $W_L^{M, \mathbf{N}}(\boldsymbol{\theta})$  is designed to isolate phase arrangements that minimize  $W_{L^{(n)}}^{M_n, N_n}(\boldsymbol{\theta})$  for all  $n = 1, \dots, \mathcal{L}$ . The following proposition summarizes the multi-level symmetric configuration algorithm.

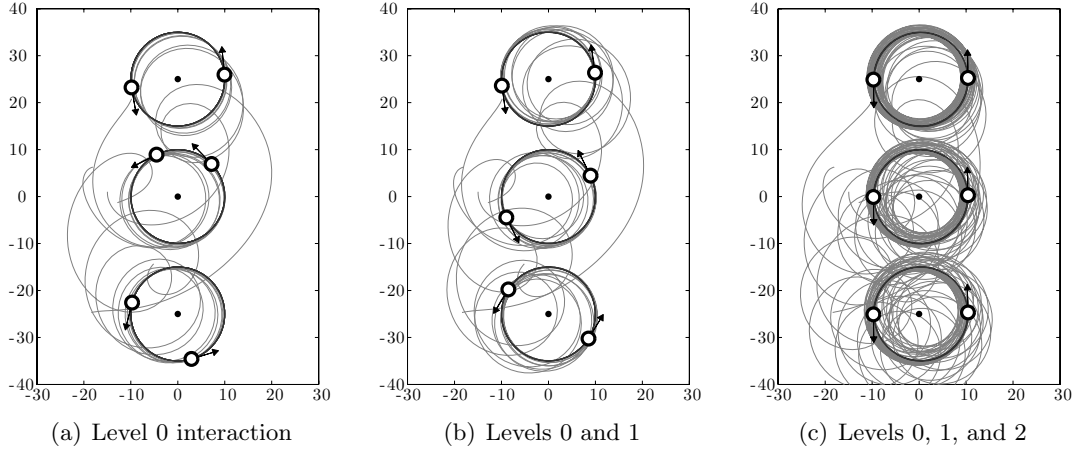


Figure 7.5: Multi-level Laplacian symmetric circular formation control. Simulations of the closed-loop particle model with the control (7.18) with  $N = 6$ ,  $K_0 = 0.1$ ,  $\omega_0 = 0.1$ , and  $|K_m| = K_0/N$ . (a) Level 0, which has an augmented block interaction, drives the particles to three circular formations with referenced centers; (b) level 0 and level 1, which has pairwise interaction, drive the particles within each circular formation to a (2,2)-pattern; (c) levels 1, 2, and level 3, which has all-to-all interaction, drives all of the particles to a (2,6)-pattern.

**Proposition 7.6. Multi-level, augmented Laplacian symmetric circular configuration control** Let  $\tilde{L}^{(0)}$  be the Laplacian of graph  $\tilde{G}^{(0)} = \bigcup_{b=1}^{\mathcal{B}} \tilde{G}_b^{(0)}$  that describes an augmented block interaction network with  $\mathcal{B}$  blocks. Let  $L^{(n)}$  be the Laplacian of graph  $G^{(n)} = (\mathcal{N}, E^{(n)})$ , where  $n \in \{1, \dots, \mathcal{L}\}$  is the interaction level. Let  $\mathbf{M} \triangleq (M_1, \dots, M_{\mathcal{L}})^T$  and  $\mathbf{N} \triangleq (N_1, \dots, N_{\mathcal{L}})^T$  such that  $M_n$  is a divisor of  $N_n$  for all  $n = 1, \dots, \mathcal{L}$ . Let  $W_{L^{(n)}}^{M_n, N_n}(\boldsymbol{\theta})$  be a  $(M_n, N_n)$ -pattern Laplacian phase potential. For the control

$$u_k = \omega_0(1 + K_0 \langle e^{i\theta_k}, \sum_{j=0}^{N+\mathcal{B}-1} \tilde{l}_{kj}^{(0)} c_{k,j} \rangle) + \sum_{n=1}^{\mathcal{L}} \frac{\partial W_{L^{(n)}}^{M_n, N_n}}{\partial \theta_k}, \quad K_0 > 0,$$

all of the trajectories of the closed-loop particle model (3.5) converge to circular orbits with radius  $|\omega_0|^{-1}$  and direction of rotation determined by the sign of  $\omega_0 \neq 0$ . All of the particles in block  $b \in \{1, \dots, \mathcal{B}\}$  converge to a circular formation with reference center determined by the corresponding virtual particle. Collectively, the circular formations in the limiting set have phase arrangements in the critical set of the phase potential  $W_L^{M, N}(\boldsymbol{\theta}) \triangleq \sum_{n=1}^{\mathcal{L}} W_{L^{(n)}}^{M_n, N_n}(\boldsymbol{\theta})$ . Every isolated local minimum of  $W_L^{M, N}(\boldsymbol{\theta})$  defines an asymptotically stable set of circular formations; every circular formation where  $W_L^{M, N}(\boldsymbol{\theta})$  does not reach

a minimum and  $\theta$  is isolated in the reduced space of relative phases is unstable.

### 7.3 Symmetric Formations on Convex Loops

All of the results presented thus far stabilize either parallel or circular formations, which are relative equilibria of the particle model. In this section, we describe algorithms using *curvature* as feedback to stabilize formations on closed loops that are not necessarily circular. These algorithms apply to a set of smooth, convex loops around which the curvature is either positive or negative but never zero.<sup>2</sup> In the absence of any virtual particles, formations on closed loops are invariant to rigid translation in the plane and, consequently, possess a translational symmetry. However, formations on closed loops are not invariant to rigid rotation in the plane because the orientation of the loop breaks the rotational symmetry. Nonetheless, the results in this section are based on, and, in many cases, mirror the results for circular formations. A coupled-phase oscillator model is central to the development.

Consider a simple, smooth, closed curve  $C$  with non-zero curvature. If particle  $k$  orbits  $C$ , then the velocity  $\dot{r}_k$  is necessarily tangent to  $C$ . Let  $c_k$ —called the center of  $C$ —denote a point in the interior of  $C$ . Let  $\mathcal{C}_k \triangleq (c_k, 1, i)$  denote a reference frame with origin  $c_k$  and unit vectors  $1$  and  $i$ . We parameterize  $C$  in  $\mathcal{C}_k$  by  $\rho : [0, 2\pi) \rightarrow \mathbb{C}$ ,  $\phi \mapsto \rho(\phi)$ , where  $\phi : \mathbb{T} \rightarrow [0, 2\pi)$ ,  $\theta_k \mapsto \phi(\theta_k)$ , is a smooth map. In this notation, the tangent vector to  $C$  is  $\frac{d\rho}{d\phi}$ , which implies

$$e^{i\theta_k} = \left| \frac{d\rho}{d\phi} \right|^{-1} \frac{d\rho}{d\phi}. \quad (7.19)$$

Equation (7.19) is a constraint on the velocity  $\dot{r}_k$ . Let  $\sigma$  denote the arc length measured along  $C$ , given by,

$$\sigma(\phi) \triangleq \int_0^\phi \left| \frac{d\rho}{d\bar{\phi}} \right| d\bar{\phi}. \quad (7.20)$$

Using  $\Sigma \triangleq \sigma(2\pi) > 0$  to denote the loop perimeter, we obtain the angular displacement of a point measured along  $C$  [301]

$$\psi(\phi) \triangleq \frac{2\pi}{\Sigma} \sigma(\phi), \quad (7.21)$$

---

<sup>2</sup>This limitation is not present in [301].

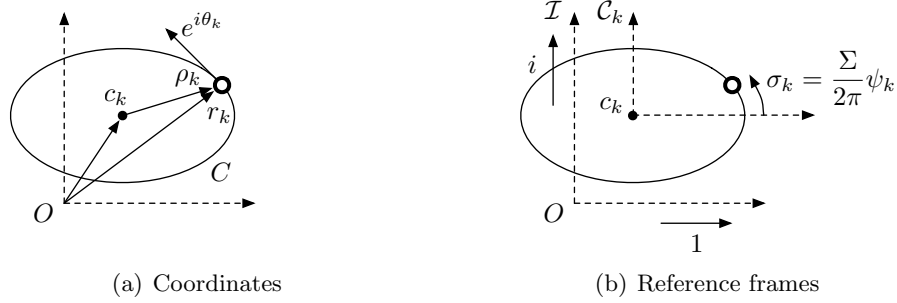


Figure 7.6: Particle orbiting closed loop  $C$ . (a) Velocity  $e^{i\theta_k}$  is tangent to  $C$ , which has center  $c_k$  and perimeter  $\Sigma$ ; (b) arc length  $\sigma_k$  is measured along loop from positive real axis of frame  $\mathcal{C}_k$  and is proportional to curve-phase  $\psi_k$ .

which we call the *curve-phase*. Figure 7.6 illustrates the center and curve-phase of an ellipse.

Under the constraint (7.19), the curvature  $\kappa$  of  $C$  is a smooth function of  $\phi$  given by

$$\kappa(\phi) \triangleq \pm \frac{d\theta_k}{d\sigma}, \quad (7.22)$$

where the positive (resp. negative) sign corresponds to counterclockwise (resp. clockwise) rotation. By assumption, the curvature of  $C$  is bounded and definite, that is  $0 < |\kappa(\phi)| < \infty$ , which means it is invertible. For example, if  $C$  is a circle with radius  $|\omega_0|^{-1}$  then  $\kappa$  is constant and is equal to  $\omega_0$ . Using the definition of arc length  $\sigma$  given by (7.20), we have

$$\kappa^{-1}(\phi) \triangleq \frac{1}{\kappa(\phi)} = \pm \frac{d\sigma}{d\theta_k} = \pm \frac{d\sigma}{d\phi} \frac{d\phi}{d\theta_k} = \pm \left| \frac{d\rho}{d\phi} \right| \frac{d\phi}{d\theta_k}. \quad (7.23)$$

Differentiating (7.21) with respect to time using (7.23), we obtain

$$\frac{d\psi}{dt} = \frac{2\pi}{\Sigma} \frac{d\sigma}{d\theta_k} \frac{d\theta_k}{dt} = \frac{2\pi}{\Sigma} |\kappa|^{-1}(\phi) \dot{\theta}_k.$$

Let  $\kappa_k \triangleq \kappa(\phi(\theta_k))$  and  $\psi_k \triangleq \psi(\phi(\theta_k))$  for  $k \in \{1, \dots, N\}$ , so that  $\psi \triangleq (\psi_1, \dots, \psi_N)^T \in \mathbb{T}^N$ . This leads to the following definition [197].

**Definition 7.7. Curve-phase model** Let  $C$  represent a convex loop with curvature  $\kappa(\phi) \neq 0$  and perimeter  $\Sigma$ . Let  $\psi_k \in \mathbb{T}$  and  $u_k \in \mathbb{R}$  denote the curve-phase and steering control for particle  $k \in \mathcal{N}$ , respectively. The curve-phase model is

$$\dot{\psi}_k = \frac{2\pi}{\Sigma} |\kappa_k|^{-1} u_k, \quad (7.24)$$

where  $u_k$  is a function of  $\psi$  only.

The curve-phase model (7.24), which is a system of coupled-phase oscillators, is analogous to the phase model (3.6). This analogy enables us to extend the results for formations on circles to formations on closed loops. Using  $\rho_k \triangleq \rho(\phi(\theta_k))$ , we define the center  $c_k$  of  $C$

$$c_k \triangleq r_k \mp \rho_k, \quad (7.25)$$

where the negative (resp. positive) sign corresponds to counterclockwise (resp. clockwise) rotation. Note, if  $C$  is a circle with radius  $|\omega_0|^{-1}$ , then  $\rho_k = -\omega_0^{-1}ie^{i\theta_k}$  and  $c_k = r_k + \omega_0^{-1}ie^{i\theta_k}$  as before. Using (7.19) and (7.23), we observe that

$$\mp \frac{d\rho}{d\theta_k} = \mp \frac{d\rho}{d\phi} \frac{d\phi}{d\theta_k} = -e^{i\theta_k} \kappa^{-1}(\phi). \quad (7.26)$$

Consequently, the time-derivative of  $c_k$  along solutions of (3.5) is

$$\dot{c}_k = e^{i\theta_k} (1 - \kappa_k^{-1} u_k). \quad (7.27)$$

Equation (7.27) shows that, if the control  $u_k = \kappa_k$ , then  $\dot{c}_k = 0$  and particle  $k$  travels around  $C$ . If  $C$  is a circle with radius  $|\omega_0|^{-1}$ , then  $u_k = \kappa_k = \omega_0$  as expected.

As a more general example of the type of loop to which this framework applies, we consider a class of loops that includes circles, ellipses, and rounded parallelograms, known as *superellipses*. Our parameterization of a superellipse is

$$\rho(\phi) = a(\cos \phi)^{\frac{1}{p}} + (i + \mu)b(\sin \phi)^{\frac{1}{p}}, \quad (7.28)$$

where  $\mu \in \mathbb{R}$  determines the skew angle. The semi-major axis length  $a$  and semi-minor axis length  $b$  satisfy  $a \geq b > 0$ . The parameter  $p = 1, 3, 5, \dots$  determines the corner sharpness. For  $\mu = 0$  and  $a > b$  (resp.  $a = b$ ), setting  $p = 1$  yields an ellipse (resp. circle) and setting  $p \geq 3$  yields a rounded rectangle (resp. rounded square). Setting  $\mu \neq 0$  and  $p > 1$  yields a rounded parallelogram. We solve for  $\kappa_k$  in (B.1) and  $\rho_k$  in (B.2) (see Appendix B). For example, setting  $\mu = 0$  and  $p = 1$  yields the ellipse curvature

$$\kappa_k = \pm \frac{1}{a^2 b^2} (a^2 \sin^2 \theta_k + b^2 \cos^2 \theta_k)^{\frac{3}{2}}. \quad (7.29)$$

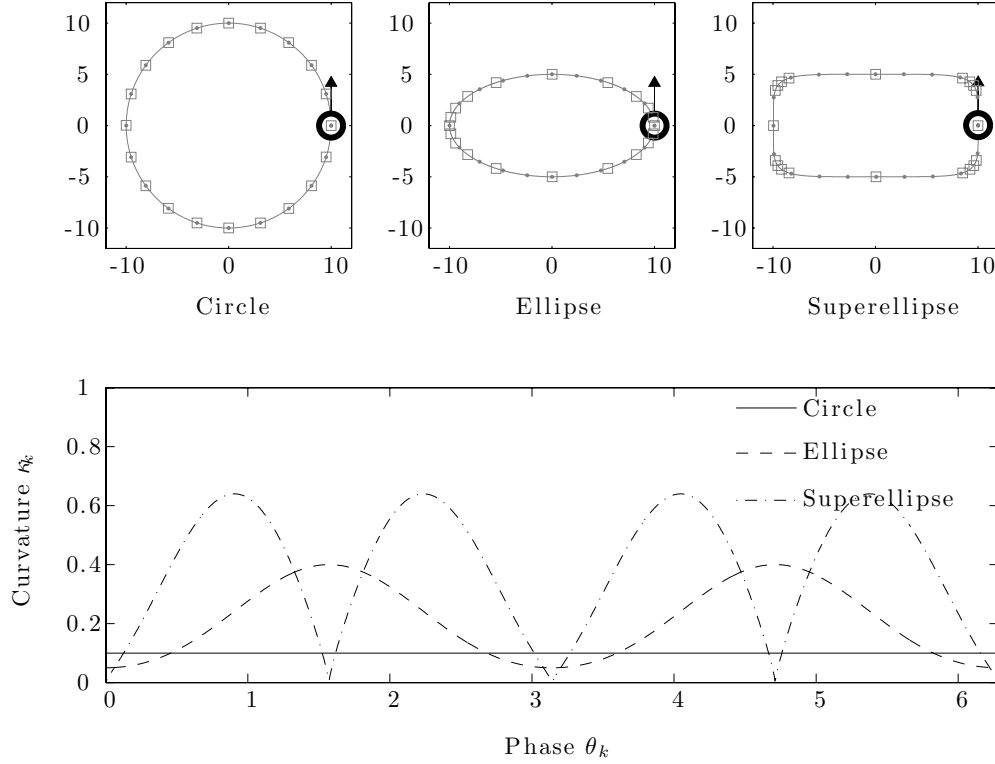


Figure 7.7: Curvature as feedback. (top) Setting  $u_k = \kappa_k$  drives particle  $k$  around the corresponding loop  $C$ . Points of equally-spaced phase  $\theta_k$  are indicated with dots; points of equally-spaced curve-phase  $\psi_k$  are indicated with squares. Circle radius  $a = 10$ ; ellipse parameters  $a = 10$ ,  $b = 5$ , and  $p = 1$ ; superellipse parameters  $a = 10$ ,  $b = 5$ ,  $p = 3$ . (bottom) Curvature  $\kappa_k$  versus phase  $\theta_k$  for the three trajectories plotted on top.

Setting  $b = a$  in (7.29) yields the constant curvature of a circle with radius  $a$ ,  $\kappa_k = \pm 1/a$ . The loops and curvatures for  $p = 1$  and 3 are illustrated in Figure 7.7 for  $\mu = 0$  and counterclockwise rotation. Note for  $p \geq 3$ , the curvature  $\kappa_k$  is zero for  $\{\theta_k \mid \theta_k = (\pi/2)j, j = 0, 1, 2, 3\}$ . Although  $\kappa_k^{-1}$  is singular at these points, they represent a set of measure zero. Simulations suggest that the results below apply to superellipses with  $p \geq 3$ , provided care is taken to avoid singularities when computing the control law.

Using curvature as feedback control does not require interaction between particles, whereas stabilizing all of the particles to orbit loop  $C$  with the same center does require interaction. We describe here such an algorithm for time-invariant and undirected interaction. This algorithm, and the extension to general communication, follows the same methodology

as circular formation algorithm. Let  $L$  be the Laplacian of a time-invariant and undirected graph  $G = (\mathcal{N}, E)$ . Let  $\mathbf{c} \triangleq (c_1, \dots, c_N)^T \in \mathbb{C}^N$ , where  $c_k$  is given by (7.25). In order to drive the particles to loop  $C$  with a common center, we choose a stabilizing control that minimizes the Laplacian quadratic form

$$S_L(\mathbf{r}, \boldsymbol{\theta}) \triangleq Q(\mathbf{c}) = \frac{1}{2} \langle \mathbf{c}, L\mathbf{c} \rangle, \quad (7.30)$$

which, if  $C$  is a circle of radius  $|\omega_0|^{-1}$ , is identical to (5.13). The potential  $S_L(\mathbf{r}, \boldsymbol{\theta})$ , which is positive-semidefinite, is zero if and only if  $c_k = c_j$  for all pairs  $k$  and  $j$ . The time-derivative of  $S_L(\mathbf{r}, \boldsymbol{\theta})$  along the solutions of (3.5) is

$$\dot{S}_L(\mathbf{r}, \boldsymbol{\theta}) = \sum_{k=1}^N \langle e^{i\theta_k}, L_k \mathbf{c} \rangle (1 - \kappa_k^{-1} u_k),$$

Choosing the Laplacian loop formation control

$$u_k = \kappa_k (1 + K_0 \langle e^{i\theta_k}, L_k \mathbf{c} \rangle), \quad K_0 > 0 \quad (7.31)$$

yields

$$\dot{S}(\mathbf{r}, \boldsymbol{\theta}) = -K_0 \sum_{k=1}^N \langle e^{i\theta_k}, L_k \mathbf{c} \rangle^2 \leq 0.$$

The closed-loop particle model with control (7.31) depends only on the particle (absolute) phases and the relative position of the loop centers of neighboring particles. Therefore, the closed-loop system is invariant to rigid translation of all loop centers. Lyapunov analysis provides the following result [197, Theorem 1], illustrated by simulation in Figure 7.8(a).

**Theorem 7.8. Laplacian loop formation control** *Let  $L$  be the Laplacian of an undirected and connected graph  $G$ . Let  $C$  be a convex loop with curvature  $\kappa \neq 0$ . All solutions of the closed-loop particle model (3.5) with the control (7.31) converge to the set of formations on  $C$  with direction of rotation determined by the sign of  $\kappa$ .*

*Proof.* The function  $S_L(\mathbf{r}, \boldsymbol{\theta})$  is positive definite and proper in the co-dimension 2 reduced space of the  $N$  particle phases  $\theta_k$  and the  $N - 1$  relative positions of the loop centers  $c_k$ . Since  $S_L(\mathbf{r}, \boldsymbol{\theta})$  is nonincreasing, by the invariance principle [131, Theorem 4.4 and Corollary

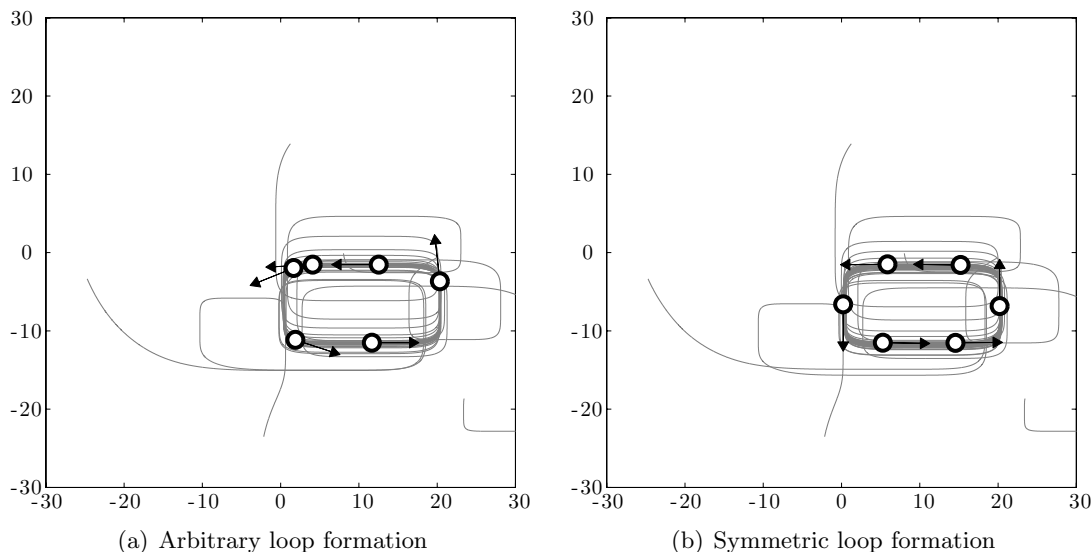


Figure 7.8: Laplacian loop formation control. Parameters  $N = 6$ ,  $K_0 = 0.1$ ,  $a = 10$ ,  $b = 5$ , and  $p = 3$ . (a) Loop formation control (7.31) stabilizes particles to loop  $C$ ; (b) symmetric loop formation control (7.39) with  $M = N$  stabilizes particles to splay pattern on loop  $C$ .

4.2], solutions in the reduced space converge to the largest invariant set  $\Omega$  where

$$\langle e^{i\theta_k}, L_k \mathbf{c} \rangle = 0.$$

In  $\Omega$ ,  $\dot{\theta}_k = \kappa_k$  and  $c_k$  is constant, which implies the invariance condition holds only if  $L\mathbf{c} = 0$ , that is, if  $c_k = c_j$  for all pairs  $k$  and  $j$ .  $\square$

Note, Theorem 7.8 does not specify the steady-state location of the formation center, which is arbitrarily determined by initial conditions. Likewise, the steady-state distribution of particles on loop  $C$  is also arbitrary. Because of the similarity between the curve-phase model (7.24) and the phase model (3.6), control of the curve-phase of particle  $k$  relative to particle  $j$  for all pairs  $k$  and  $j$  is achieved using the gradient of the Laplacian curve-phase potential

$$W_L(\boldsymbol{\psi}) \triangleq \frac{1}{2} Q_L(e^{i\boldsymbol{\psi}}) = \frac{1}{2} \langle e^{i\boldsymbol{\psi}}, L e^{i\boldsymbol{\psi}} \rangle, \quad (7.32)$$

where  $L$  is the Laplacian of an undirected and connected graph. Potential  $W_L(\boldsymbol{\psi})$  is identical to  $W_L(\boldsymbol{\theta})$  defined in (4.13) with  $\boldsymbol{\theta}$  replaced by  $\boldsymbol{\psi}$ , which means  $W_L(\boldsymbol{\psi})$  possess many of the same properties as  $W_L(\boldsymbol{\theta})$ , including rotational symmetry. Rotational symmetry of  $W_L(\boldsymbol{\psi})$

means that the vector  $\mathbf{1}$  is orthogonal to the gradient  $\nabla W_L \triangleq \left( \frac{\partial W_L}{\partial \psi_1}, \dots, \frac{\partial W_L}{\partial \psi_N} \right)^T$  and in the kernel of the Hessian  $H_L$ . The time-derivative of  $W_L(\boldsymbol{\psi})$  along solutions of (7.24) is

$$\dot{W}_L = \sum_{j=1}^N \frac{\partial W_L}{\partial \psi_j} \dot{\psi}_j = \frac{2\pi}{\Sigma} \sum_{j=1}^N \langle i e^{i\psi_j}, L_j e^{i\psi} \rangle |\kappa_k|^{-1} u_k,$$

which evaluates to zero if  $u_k = \kappa_k$ .

Let  $W_L^*(\boldsymbol{\psi})$  denote an arbitrary Laplacian curve-phase potential or linear combination of potentials. Consider the composite potential

$$V_L^*(\mathbf{r}, \boldsymbol{\theta}) \triangleq K_0 S_L(\mathbf{r}, \boldsymbol{\theta}) - \frac{\Sigma}{2\pi} W_L^*(\boldsymbol{\psi}), \quad K_0 > 0, \quad (7.33)$$

where the formation potential  $S_L(\mathbf{r}, \boldsymbol{\theta})$  is defined in (7.30). The time derivative of  $V_L^*(\mathbf{r}, \boldsymbol{\theta})$  along solutions of the closed-loop particle model (3.5) is

$$\begin{aligned} \dot{V}_L^* &= K_0 \sum_{j=1}^N (1 - \kappa_k^{-1} u_j) \langle e^{i\theta_k}, L_j \mathbf{c} \rangle - \sum_{j=1}^N \frac{\partial W_L^*}{\partial \psi_j} |\kappa_k|^{-1} u_j \\ &= \sum_{j=1}^N \left( K_0 \langle e^{i\theta_j}, L_j \mathbf{c} \rangle + \text{sgn}(\kappa_k) \frac{\partial W_L^*}{\partial \psi_j} \right) (1 - \kappa_k^{-1} u_j), \end{aligned}$$

where we used the fact that  $\sum_{j=1}^N \frac{\partial W_L^*}{\partial \psi_j} = \mathbf{1}^T \nabla W_L^* = 0$ . Choosing the composite control

$$u_k = \kappa_k (1 + K_0 \langle e^{i\theta_k}, L_k \mathbf{c} \rangle) + |\kappa_k| \frac{\partial W_L^*}{\partial \psi_k}, \quad K_0 > 0, \quad (7.34)$$

yields

$$\dot{V}_L^* = - \sum_{j=1}^N \left( K_0 \langle e^{i\theta_j}, L_j \mathbf{c} \rangle + \text{sgn}(\kappa_k) \frac{\partial W_L^*}{\partial \psi_k} \right)^2 \leq 0,$$

which leads to the following result.

**Lemma 7.9. Laplacian composite phase and loop formation control** *Let  $L$  be the Laplacian of an undirected and connected graph  $G = (\mathcal{N}, E)$ ,  $C$  be a convex loop with curvature  $\kappa \neq 0$ , and  $W_L^*(\boldsymbol{\psi})$  be a smooth and rotationally symmetric Laplacian curve-phase potential. For the control (7.34), all of the solutions of the closed-loop particle model (3.5) converge to the set of formations on loop  $C$  with direction of rotation determined by the sign of  $\kappa$ ; all of the formations in the limiting set have phase arrangements in the critical set of the phase potential  $W_L^*(\boldsymbol{\psi})$ . Every isolated local minimum of  $W_L^*(\boldsymbol{\psi})$  defines an asymptotically stable set of formations; every formation where  $W_L^*(\boldsymbol{\psi})$  does not reach a minimum and  $\boldsymbol{\psi}$  is isolated in the reduced space of relative curve-phases is unstable.*

*Proof.* For the control (7.34), the closed-loop particle model evolves on the co-dimension 2 reduced space of the  $N$  particle phases  $\theta_k$  and the  $N - 1$  relative positions of the loop centers  $c_k$ . Let  $\Omega$  be the set of all of the points in the reduced shape space where  $\dot{V}_L^* = 0$ . In this set,

$$K_0 \langle e^{i\theta_k}, L_k \mathbf{c} \rangle + \operatorname{sgn}(\kappa_k) \frac{\partial W_L^*}{\partial \psi_k} = 0, \quad (7.35)$$

which implies  $\dot{\theta}_k = \kappa_k$ ,  $\dot{\psi}_k = 0$ , and  $\dot{c}_k = 0$  for all  $k \in \mathcal{N}$ . Let  $\Lambda$  denote the largest invariant set in  $\Omega$ . Taking the time-derivative of (7.35) in  $\Omega$  yields

$$K_0 \langle i e^{i\theta_k}, L_k \mathbf{c} \rangle \kappa_k + \langle e^{i\theta_k}, \underbrace{\sum_{j=1}^N \dot{c}_{k,j}}_0 \rangle \omega_0 + \operatorname{sgn}(\kappa_k) \left. \frac{d}{dt} \left( \frac{\partial W_L^*}{\partial \psi_k} \right) \right|_{\Omega} = 0,$$

where

$$\left. \frac{d}{dt} \left( \frac{\partial W_L^*}{\partial \psi_k} \right) \right|_{\Omega} = \sum_{j=1}^N \frac{\partial^2 W_L^*}{\partial \psi_j \partial \psi_k} \dot{\psi}_j = 0.$$

Thus, points in  $\Lambda$  satisfy

$$\langle i e^{i\theta_k}, L_k \mathbf{c} \rangle = 0. \quad (7.36)$$

Equation (7.36) holds only if  $L\mathbf{c} = 0$ , which implies  $c_k = c_j$  for all pairs  $k$  and  $j$ . Using (7.35), we observe that points  $(\mathbf{r}, \boldsymbol{\theta})$  in  $\Lambda$  also satisfy

$$\frac{\partial W_L^*}{\partial \psi_k} = 0. \quad (7.37)$$

Equation (7.37) holds only if  $\boldsymbol{\psi}$  is a critical point of  $W_L^*(\boldsymbol{\psi})$ . By the invariance principle [131, Theorem 4.4 and Corollary 4.2], every solution of the closed-loop particle model approaches  $\Lambda$  as  $t \rightarrow \infty$ . Using Lemma A.2 with  $V_1(\mathbf{x})$  replaced by  $K_0 S(\mathbf{r}, \boldsymbol{\theta})$  and  $V_2(\mathbf{x})$  replaced by  $-\frac{\Sigma}{2\pi} W_L^*(\boldsymbol{\psi})$  completes the proof.  $\square$

Lemma 7.9 shows that, if we can identify a suitable curve-phase potential, then we can stabilize symmetric curve-phase patterns on convex loops. For this purpose, we adopt the same terminology as for symmetric phase patterns. That is, if  $M$  is a divisor of  $N$ , then an  $(M, N)$ -pattern  $\boldsymbol{\psi}$  is a symmetric curve-phase arrangement of  $N$  curve-phases consisting of  $M$  clusters with  $N/M$  synchronized curve-phases in each cluster. Likewise, as stated in the

following corollary, the curve-phase potential

$$W_L^{M,N}(\boldsymbol{\psi}) \triangleq -\sum_{m=1}^M \frac{K_m}{m^2} W_L(m\boldsymbol{\psi}) = -\frac{1}{2} \sum_{m=1}^M \frac{K_m}{m^2} \langle e^{im\boldsymbol{\psi}}, L e^{im\boldsymbol{\psi}} \rangle, \quad (7.38)$$

$$K_m > 0, m = 1, \dots, M-1, K_M < -\sum_{m=1}^{M-1} K_m.$$

has the same properties as the symmetric pattern potential  $W_L^{M,N}(\boldsymbol{\theta})$  given in (6.33) [197, Lemma 4].

**Corollary 7.10. Laplacian symmetric curve-phase pattern potential** *Let  $L$  denote the Laplacian of an undirected and connected circulant graph  $G = (\mathcal{N}, E)$ ,  $C$  be a convex loop with curvature  $\kappa \neq 0$ , and  $M$  be a divisor of  $N$ . The potential  $W_L^{M,N}(\boldsymbol{\psi})$  is smooth and rotationally symmetric. If phase arrangement  $\boldsymbol{\psi} \in \mathbb{T}^N$  is an  $(M, N)$ -pattern, then  $\boldsymbol{\psi}$  is a local minimum of  $W_L^{M,N}(\boldsymbol{\psi})$  that is isolated in the curve-phase shape space.*

*Proof.* The proof follows the proof of Theorem 6.7 with  $\boldsymbol{\theta}$  replaced by  $\boldsymbol{\psi}$ .  $\square$

This leads to the following result [197, Theorem 5], which mirrors Corollary 6.8. Consider the control

$$u_k = \kappa_k(1 + K_0 \langle e^{i\theta_k}, L_k \mathbf{c} \rangle) - |\kappa_k| \frac{\partial W_L^{M,N}}{\partial \psi_k}, \quad K_0 > 0. \quad (7.39)$$

A simulation of the closed-loop particle model with control (7.39) is shown in Figure 7.8(b).

**Corollary 7.11. Laplacian symmetric loop formation control** *Let  $L$  denote the Laplacian of an undirected and connected circulant graph  $G = (\mathcal{N}, E)$ ,  $C$  be a convex loop with curvature  $\kappa \neq 0$ , and  $M$  be a divisor of  $N$ . The results of Lemma 7.9 apply when control (7.34) is replaced by (7.39), where the Laplacian symmetric phase potential  $W_L^{M,N}(\boldsymbol{\psi})$  is defined in (7.38). All of the formations in the limiting set have a phase arrangement in the critical set of  $W_L^{M,N}(\boldsymbol{\psi})$ . All of the formations where the phase arrangement is an  $(M, N)$ -pattern are asymptotically stable. All of the formations where  $W_L^{M,N}(\boldsymbol{\psi})$  does not reach a minimum and  $\boldsymbol{\psi}$  is isolated in the reduced space of relative curve-phases are unstable.*

*Proof.* Application of Lemma 7.9 and Theorem 7.10 yields the desired result.  $\square$

Corollary 7.11 leads naturally to the following extension of Proposition 7.6 to control symmetric formations on multiple loops.

**Proposition 7.12. Multi-level, augmented Laplacian symmetric loop configuration control** *Let  $\tilde{L}^{(0)}$  be the Laplacian of graph  $\tilde{G}^{(0)} = \bigcup_{b=1}^{\mathcal{B}} \tilde{G}_b^{(0)}$  that describes an augmented block interaction network with  $\mathcal{B}$  blocks. Let  $L^{(n)}$  be the Laplacian of graph  $G^{(n)} = (\mathcal{N}, E^{(n)})$ , where  $n \in \{1, \dots, \mathcal{L}\}$  is the interaction level. Let  $\mathbf{M} \triangleq (M_1, \dots, M_{\mathcal{L}})^T$  and  $\mathbf{N} \triangleq (N_1, \dots, N_{\mathcal{L}})^T$  such that  $M_n$  is a divisor of  $N_n$  for all  $n = 1, \dots, \mathcal{L}$ . Let  $W_{L^{(n)}}^{M_n, N_n}(\boldsymbol{\psi})$  be a  $(M_n, N_n)$ -pattern Laplacian curve-phase potential and  $C$  be a convex loop with curvature  $\kappa \neq 0$ . For the control*

$$u_k = \kappa_k \left( 1 + K_0 \left\langle e^{i\theta_k}, \sum_{j=0}^{N+\mathcal{B}-1} \tilde{l}_{kj}^{(0)} c_{k,j} \right\rangle \right) + \sum_{n=1}^{\mathcal{L}} \frac{\partial W_{L^{(n)}}^{M_n, N_n}}{\partial \psi_k}, \quad K_0 > 0,$$

*all of the trajectories of the closed-loop particle model (3.5) converge to the set of formations on loop  $C$  with direction of rotation determined by the sign of  $\kappa_k$ . All of the particles in block  $b \in \{1, \dots, \mathcal{B}\}$  converge to a formation on loop  $C$  with reference center determined by the corresponding virtual particle. Collectively, the formations in the limiting set have phase arrangements in the critical set of the phase potential  $W_L^{\mathbf{M}, \mathbf{N}}(\boldsymbol{\psi}) \triangleq \sum_{n=1}^{\mathcal{L}} W_{L^{(n)}}^{M_n, N_n}(\boldsymbol{\psi})$ . Every isolated local minimum of  $W_L^{\mathbf{M}, \mathbf{N}}(\boldsymbol{\psi})$  defines an asymptotically stable set of formations; every formation where  $W_L^{\mathbf{M}, \mathbf{N}}(\boldsymbol{\theta})$  does not reach a minimum and  $\boldsymbol{\psi}$  is isolated in the reduced space of relative curve-phases is unstable.*

Proposition 7.12 provides a decentralized control algorithm to steer self-propelled particles on symmetric patterns suitable for applications in sensing networks. In the next chapter, we describe the software infrastructure generated to implement this and other control algorithms on a fleet of underwater gliders.



## Chapter 8

# Glider Control Synthesis

The feedback control algorithms in the previous chapter are applied to coordinate a fleet of underwater gliders using an automatic control system called the *Glider Coordinated Control System* (GCCS). The GCCS, which we describe in this chapter, is designed to perform automatic feedback control at the level of the fleet. The modular design of the GCCS enables a glider control algorithm to “plug and play”. The GCCS uses both a detailed glider model and a simple particle model to plan glider trajectories. Development of the GCCS was assisted by previous experience with performing fleet-level feedback control of underwater gliders [83].

The GCCS—currently 16,000 lines of source code—is a modular, cross-platform software suite written in MATLAB®. The GCCS planning module runs on a single computer onshore and communicates to gliders at sea via satellites. The GCCS also serves as a simulation testbed for development of coordinated control algorithms. Simulated (virtual) gliders operate in realistic ocean fields that are provided as input. Accordingly, it is possible to use the GCCS to explore and test solutions to many of the challenges that come with controlling a network of gliders in the ocean.

The three main GCCS modules are shown in Figure 8.1: (i) the GCCS *planner*, which is the real-time controller, (ii) the GCCS *simulator*, which can serve as control testbed or to predict glider motion in real time, and (iii) the GCCS *remote input/output* (IO) module,

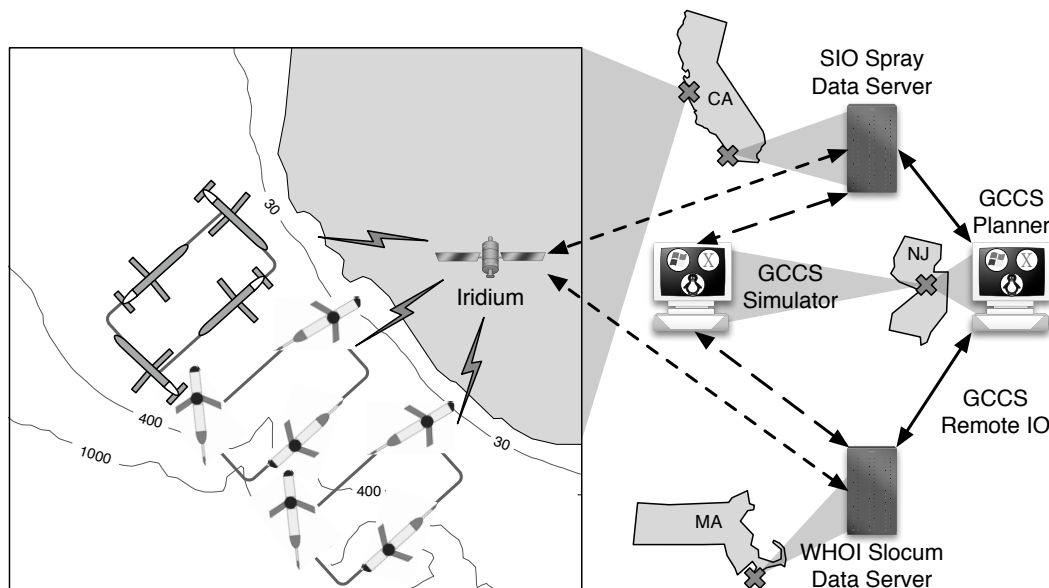


Figure 8.1: The Glider Coordinated Control System. The GCCS running on a computer in Princeton, New Jersey. The three major components are the glider planner, the glider simulator, and the remote input/output (IO). The glider data servers, which are located in Woods Hole, Massachusetts and La Jolla, California, connect via Iridium satellite communication to the gliders as they periodically come to the surface (shown near Monterey Bay, California). Figure after [201].

which interfaces to gliders indirectly through the glider data servers. The input to the planner is a set of glider coordinated trajectories (GCT), described in the next section. To plan trajectories for the gliders, which surface asynchronously, the GCCS uses two different models: a simple glider model—such as the particle model described in Chapter 3—that is integrated to compute desired trajectories (with or without coordinated control), and a detailed glider model—described in Section 8.2.2—that is integrated to estimate three-dimensional glider motions in the presence of flow. We refer to the software that integrates these two models as the glider integrator and particle integrator, respectively.

## 8.1 Specifying Glider Trajectories

The input to the GCCS planner module is a description of the desired set of *glider coordinated trajectories* (GCT). The GCCS is designed to facilitate incorporation of alternate

feedback control algorithms. As a result, the specification of the GCT, described below, is fairly general and not control-specific. Consequently, GCTs can be constructed that are not feasibly stabilized by the algorithms in Chapter 7. Likewise, the GCT specification is not yet adequate to generate all of the permutations of the control algorithms described in Chapter 7.

A GCT has three main components, which are all contained in a self-describing XML<sup>1</sup> file: (i) a description of the *operating domain*; (ii) a list of the closed loops—called *tracks*—and their properties; and (iii) a structured glider list—called the *glider tree*—that specifies the gliders and their properties, including track assignments. The glider tree determines the interaction network to be used in the control design as well as the desired steady-state configuration of the gliders.

To explain the contents of a GCT, we describe an example that is illustrated in Figure 8.2. This example contains six gliders deployed near Point Año Nuevo, California. It corresponds to a multi-level, augmented symmetric formation such as the one shown in Figure 7.4(a). In the illustration, the operating domain is a black rectangle that circumscribes three superelliptic tracks depicted by dashed gray lines. Each of three glider pairs—*we05/we08*, *we07/we09*, and *we10/we12*—is assigned to travel clockwise around a single track. Levels 1 and 2 of the interaction network in Figure 7.4(c), superimposed on the illustration in Figure 8.2, are designed to support balancing of the curve-phases of the pair of gliders on each track and synchronizing or balancing of the curve-phases of any two gliders on different tracks.

The first component of the GCT, the operating domain, specifies the shape, location, size, and orientation of the region inside of which the gliders operate. The rectangular operating domain used in the example is described in Table 8.1. The domain location is specified by the coordinates  $x$  and  $y$  of the center of the rectangle. The size of the domain is specified by its width  $2a$  and height  $2b$ , and the orientation is specified by an angle  $ori$ . The choice of units in which to specify the values of the domain properties is flexible since

---

<sup>1</sup>The XML format provides compatibility with an optimization tool—not described here—that generates GCTs for maximum mapping performance [146].

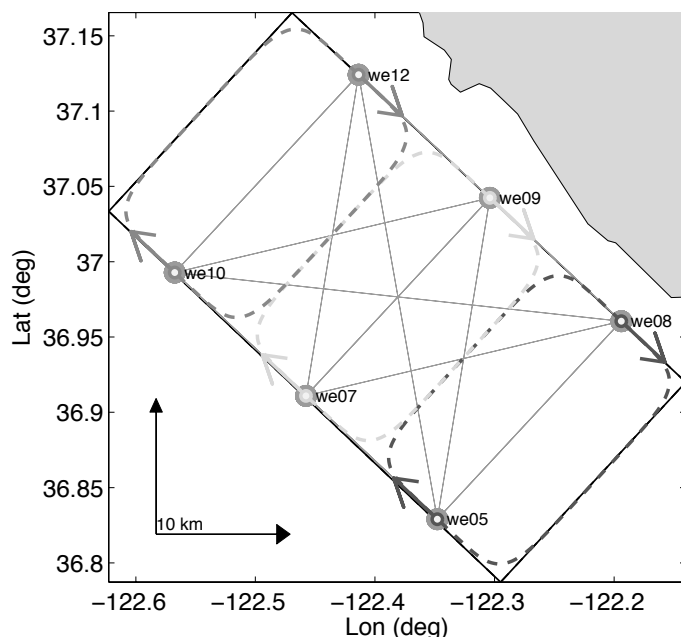


Figure 8.2: Illustration of a GCT near Point Año Nuevo, California. Gray region in north-east corner of plot is land; Point Año Nuevo is located at  $122.35^\circ$  W longitude and  $37.12^\circ$  N latitude. Six gliders travel clockwise around three separate tracks such that the curve-phase of gliders on each track are balanced and the curve-phase of any two gliders on different tracks are synchronized or balanced.

a description of the units is embedded in the GCT file along with the property value.

The second component of a GCT, the track list, specifies the name, shape, location, size, orientation, and other properties of the closed loops around which the gliders should travel. In the example, the specification of the southernmost track—called `track1`—is given in Table 8.2. The track location is determined by the coordinates  $x$  and  $y$  of the center of the superellipse. The size of the superellipse is specified by the lengths of its semi-major  $a$  and semi-minor  $b$  axes; the orientation is specified by an angle `ori`. The parametrization (7.28) of a superellipse also requires a value for the parameter  $p$ , which determines the corner sharpness (see Section 7.3).

The third component of a GCT, the glider tree, specifies the glider properties including track assignment, the (particle) interaction network, and the desired steady-state pattern of the gliders on their tracks. The glider properties, as shown in Table 8.3, are manufacturer

```

<domain>
  <rectangle>
    <x> <units> deg </units> <value> -122.3817 </value> </x>
    <y> <units> deg </units> <value> 36.9765 </value> </y>
    <a> <units> met </units> <value> 20000 </value> </a>
    <b> <units> met </units> <value> 10000 </value> </b>
    <ori> <units> deg </units> <value> 137 </value> </ori>
  </rectangle>
</domain>

```

Table 8.1: Specification of a GCT operating domain. The domain is a 10 km  $\times$  20 km rectangle centered at 122.3817° W longitude and 36.9765° N latitude. The fifth line `<ori>` specifies the rectangles' orientation.

```

<tracks>
  <superellipse>
    <name> track1 </name>
    <x> <units> deg </units> <value> -122.2713 </value> </x>
    <y> <units> deg </units> <value> 36.8950 </value> </y>
    <a> <units> met </units> <value> 10000 </value> </a>
    <b> <units> met </units> <value> 6667 </value> </b>
    <ori> <units> deg </units> <value> 47 </value> </ori>
    <p> <value> 3 </value> </p>
  </superellipse>
  <superellipse> ... </superellipse>
  :
</tracks>

```

Table 8.2: Specification of a GCT track list. The first track, called `track1`, is a 6.7 km  $\times$  10 km supellipse centered at 122.2713° W longitude and 36.8950° N latitude.

`mnf`, serial number `sn`, model, track assignment, `direction` of rotation on the track, curve-phase `phase` (see Section 7.3), and control. The symbols `group` and `group phase` also appear in Table 8.3 and are explained below.

Figure 8.3 illustrates the example GCT glider tree. This glider tree corresponds to levels 1 and 2 of the multi-level interaction network shown in Figure 7.4(c). The nodes in the glider tree are depicted by circles: a white circle represents a glider, whereas a gray circle represents a group of gliders. A (directed) edge from a group to a glider or from a group to another group—a subgroup—means the group contains the glider or the subgroup. The group that contains all of the groups and gliders is called the *root*. If a group contains

```

<group>
  <group>
    <phase> <value> 0 </value> <units> pct </units> </phase>
    <glider>
      <mnf> w </mnf>
      <sn> 7 </sn>
      <model> e </model>
      <track> track1 </track>
      <direction> 1 </direction>
      <phase> <value> 0 </value> <units> pct </units> </phase>
      <control> sellipse_control </control>
    </glider>
    <glider> ... </glider>
    :
  </group>
  :
</group>

```

Table 8.3: Specification of a GCT structured glider list. Each glider’s name is a concatenation of the manufacturer `mnf`, `model`, and serial number `sn` property values. The first glider in the list, `we07`, is assigned to travel clockwise around `track1` using the `sellipse_control`, which is the multi-level, augmented Laplacian symmetric loop configuration control described in Proposition 7.12.

a glider, then the particle representation of that glider interacts via a time-invariant and undirected graph with all of the other gliders in the group. Likewise, each glider in a subgroup interacts with all of the other gliders in other subgroups. In the glider tree shown in Figure 8.3, the set of all subgroups and gliders represents interaction level 1 described by graph  $G^{(1)}$  in Figure 7.4(c). The set of all groups and gliders represents interaction level 2 described by graph  $G^{(2)}$ .

The glider tree also specifies the desired relative curve-phases of all of the interacting gliders. Each node in the tree graph other than the root, whether it is a glider or a group, is assigned a curve-phase `phase`. The curve-phase of each glider is the sum of the curve-phases of the nodes reached by a directed path from the root of the tree to the glider node. The value of the curve-phase of a glider relative to the curve-phase of another glider determines the desired relative curve-phase between the gliders in steady-state motion. If there is a path between two gliders in the interaction network generated by the glider tree, then their

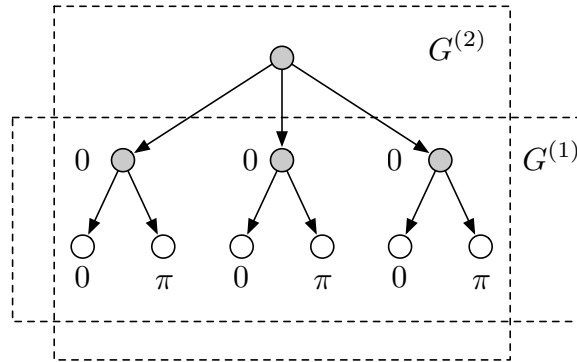


Figure 8.3: A GCT glider tree corresponding to levels 1 and 2 of the multi-level interaction network example shown in Figure 7.4(c). Each gray node represents a group of gliders and each white node represents a glider. In this example, all of the nodes other than the root are assigned a curve-phase value of 0 or  $\pi$ .

relative curve-phase is feedback stabilized. In the glider tree shown in Figure 8.3, which corresponds to the multi-level pattern in Figure 7.4(a), each subgroup has phase zero and contains a pair of gliders whose relative curve phase is  $\pi$ . This means the control law should seek to balance the curve-phases of the gliders in each pair and synchronize or balance the curve-phases of gliders in different subgroups. From the set of glider curve-phases and their interaction network, the GCCS planner determines the parameters used by the control law to stabilize the desired pattern.

## 8.2 Modeling Glider Motion

In Section 8.2.1, we describe the simple model of glider motion used by the GCCS to plan future trajectories. In Section 8.2.2, we describe the detailed model of glider motion used by the GCCS to predict glider motion underwater.

### 8.2.1 Simple Glider Model

The GCCS planner integrates a simple glider model to generate the glider planned trajectories. In order to support ongoing control design efforts, there are currently several particle models that can be used by the GCCS planner. In all of the models, gliders are represented

by point masses (particles) traveling at constant speed  $s_0 > 0$  in a horizontal plane. The position of particle  $k$  is  $r_k \in \mathbb{C}$  and the orientation of its velocity is  $\theta_k$  (see Section 3.1). The particle speed is the effective horizontal speed of the glider, that is, the glider's horizontal speed relative to the flow, scaled by the fraction of time spent underwater.

The default particle model in the GCCS is

$$\begin{aligned}\dot{r}_k &= s_0 e^{i\theta_k}, \\ \dot{\theta}_k &= u_k,\end{aligned}\tag{8.1}$$

where  $k = 1, \dots, N$  is the glider index. The default model (8.1) is identical to the particle model (3.5), except that instead of traveling at unit speed each particle travels at the glider effective speed  $s_0$  (see Table D.1 in Appendix D). When  $s_0 \neq 1$ , feedback control algorithms designed for use with the unit speed particle model (3.5) can be adapted for use with (8.1).

A limitation of (8.1) as a simple model of glider motion is that it assumes the control input is continuous. A particle model with a discrete-control input at frequency  $1/T$  is

$$\begin{aligned}\dot{r}_k &= s_0 e^{i\theta_k}, \\ \dot{\theta}_k &= u_k(t^*), \quad k = 1, \dots, N,\end{aligned}\tag{8.2}$$

where  $t^* = \lfloor t/T \rfloor T$  is the time of the most recent control computation.

Because the control is constant over intervals of length  $T$ , model (8.2) generates piecewise-circular trajectories. A discrete-control particle model that generates piecewise-linear trajectories is

$$\begin{aligned}\dot{r}_k &= s_0 e^{i\theta_k(t^*)}, \\ \theta_k(t^*) &= \theta_k(t^* - T) + u_k(t^*)T, \quad k = 1, \dots, N.\end{aligned}\tag{8.3}$$

In (8.3), the control

$$u_k(t^*) = \frac{\theta_k(t^*) - \theta_k(t^* - T)}{T}$$

is the forward-Euler approximation of a continuous control. Euler-method error estimates are proportional to the square of the step size  $T$  [33, pp. 424-427]. Therefore, feedback control algorithms designed for (8.1) will work with (8.3) if  $T$  is sufficiently small.

The particle models (8.1)–(8.3) are all second-order models in which the control  $u_k$  determines the (rate of) change of the phase  $\theta_k$ . In a first-order, or *kinematic*, particle

model such as

$$\begin{aligned}\dot{r}_k &= s_0 e^{i\theta_k}, \\ \theta_k &= u_k, \quad k = 1, \dots, N,\end{aligned}\tag{8.4}$$

the control  $u_k$  determines  $\theta_k$  itself.

It may be advantageous to consider a variation of the kinematic model (8.4) in the presence of (an unknown) flow  $f_k \in \mathbb{C}$ . For example, in the model

$$\begin{aligned}\dot{r}_k &= f_k + s_0 e^{i\theta_k}, \\ \theta_k &= u_k, \quad k = 1, \dots, N,\end{aligned}\tag{8.5}$$

the flow  $f_k$  is a drift vector field on the particle position. The model (8.5) does not, however, account for the effect of the glider onboard control system. If the flow  $f_k$  satisfies  $|f_k| < s_0$ , one might assume that the glider onboard control will effectively cancel the component  $f'_k$  of the flow orthogonal to the desired direction of motion. This assumption leads to the following kinematic model

$$\begin{aligned}\dot{r}_k &= (|f_k - f'_k| + s'_0) e^{i\theta_k}, \\ \theta_k &= u_k, \quad k = 1, \dots, N,\end{aligned}\tag{8.6}$$

where  $s'_0 < s_0$  is the new glider effective speed, which is reduced by fighting the flow and increased by “tailwinds”.

Another assumption implicit in the model (8.6) is that the glider onboard control system has a perfect estimate of the flow. One might consider replacing  $f'_k$  with a decentralized estimate of the cross-track flow. However, adding further complexity to the particle model increases the difficulty of obtaining theoretical results for the closed-loop model. Nonetheless, a detailed model of glider motion is essential to practical implementation of the GCCS. We describe such a model next.

### 8.2.2 Detailed Glider Model

The (detailed) *glider model* is a discrete-time, three-dimensional, kinematic model of glider motion subject to the glider onboard pitch, heading and buoyancy control [201].<sup>2</sup> The

<sup>2</sup>An even more detailed glider model is described in [97, pp. 147-180].

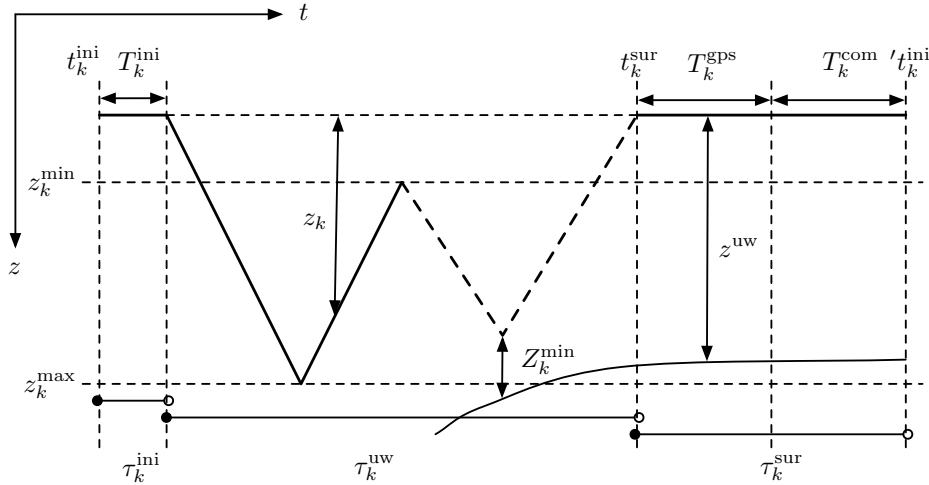


Figure 8.4: Coordinates for the glider model. Axes are time  $t$  and depth  $z$  during a single dive that progresses from left to right:  $t_k^{\text{ini}}$  is the dive initialization time,  $t_k^{\text{sur}}$  is the surface time, and  $t_k^{\text{ini}'}$  is the time at which the next dive initializes. The curved solid line in the lower right corner represents the ocean bottom. Figure after [201].

second-order transient effects of the onboard control are not modeled. Instead we assume a fixed vertical speed and glide angle (pitch angle plus angle of attack) for both ascent and descent. Gliders move at constant speed in the direction of their desired headings and are advected by a three-dimensional flow field. We describe separately the equations of motion for three phases of a single dive: on the surface before the dive (dive initialization); underwater during the dive; and on the surface after the dive.

Figure 8.4 illustrates the coordinates used in the glider model. The gliders are labeled by the integers  $k \in \{1, \dots, N\}$ , where  $N$  is the number of gliders. Let  $t \geq 0$  represent absolute time in the glider integrator. We denote the time step and discrete-time step index by  $\Delta t \in \mathbb{R}^+$  and  $n \in \mathbb{Z}$ , respectively. The superscript  $\text{sur}$  (resp.  $\text{uw}$ ) stands for *surface* (resp. *underwater*). For glider  $k$ , let  $z_k$  denote depth,  $z_k^{\text{min}}$  denote minimum inflection depth (the shallowest depth at which the glider switches from ascending to descending),  $z_k^{\text{max}}$  denote maximum inflection depth,  $Z_k^{\text{min}}$  denote minimum altitude, and  $z^{\text{uw}}$  denote bathymetry (water depth). Also for glider  $k$ , let  $t_k^{\text{ini}}$  denote dive initialization time,  $t_k^{\text{sur}}$  denote dive surface time,  $T_k^{\text{ini}}$  denote pre-dive surface duration,  $T_k^{\text{gps}}$  denote the duration of a GPS-position fix, and  $T_k^{\text{com}}$  denote the duration of shore communication. Lastly, let

$\tau_k^{\text{ini}} \triangleq [t_k^{\text{ini}}, t_k^{\text{ini}} + T_k^{\text{ini}})$  denote the time interval before glider  $k$  dives,  $\tau_k^{\text{uw}} \triangleq [t_k^{\text{ini}} + T_k^{\text{ini}}, t_k^{\text{sur}})$  denote during the dive, and  $\tau_k^{\text{sur}} \triangleq [t_k^{\text{sur}}, t_k^{\text{sur}} + T_k^{\text{gps}} + T_k^{\text{com}})$  denote after the dive. For convenience, we denote the end of interval  $\tau$  by  $\bar{\tau}$ . Parameter values used during a glider experiment are provided in Table D.1 (see Appendix D).

We use the ellipsoid  $E$  to model the earth shape. The glider integrator uses geodetic coordinates  $R_k \triangleq (\lambda_k, \phi_k) \in E$  for the position of the  $k$ th glider, where  $\lambda_k$  and  $\phi_k$  are latitude and longitude, respectively. Let  $\Gamma : E \times E \rightarrow \mathbb{R}^+$  and  $\eta : E \times E \rightarrow S^1$  be functions for computing distance and azimuth on the earth given in (C.1) and (C.2), respectively, in Appendix C. Appendix C also describes a transformation between local (complex) coordinates and geodetic coordinates.

**Glider Position** The  $k$ th glider position  $R_k$  at time  $t \geq t_k^{\text{ini}}$  is the solution to the following discrete-time model, which depends on the position  $R_k$ , depth  $z_k$ , and waypoint index  $p_k \in \mathbb{N}$ . We denote the  $p_k$ th waypoint by  $\omega_k^{p_k} \in E$ . Let  $f_k \in \mathbb{R}^2$  be the horizontal component of the  $k$ th glider velocity with respect to an earth-fixed frame.

1. Before the dive,  $t \in \tau_k^{\text{ini}} = [t_k^{\text{ini}}, t_k^{\text{ini}} + T_k^{\text{ini}})$ , and

$$R_k(n+1) = R_k(n) + f_k^{\text{sur}}(R_k(n))\Delta t, \quad n = 1, \dots, \left\lfloor \frac{t - t_k^{\text{ini}}}{\Delta t} \right\rfloor,$$

where  $R_k(1)$  is the position of the glider at  $t^{\text{ini}}$  and  $f^{\text{sur}}$  is its velocity when passively drifting on the surface.

2. During the dive,  $t \in \tau_k^{\text{uw}} = [t_k^{\text{ini}} + T_k^{\text{ini}}, t_k^{\text{sur}})$ , and

$$R_k(n+1) = R_k(n) + f_k^{\text{uw}}(R_k(n), z_k(n), p_k(n))\Delta t, \quad n = \left\lfloor \frac{\bar{\tau}_k^{\text{ini}}}{\Delta t} \right\rfloor, \dots, \left\lfloor \frac{t - t_k^{\text{ini}}}{\Delta t} \right\rfloor,$$

where  $f^{\text{uw}}$  is the total velocity underwater.

3. After the dive,  $t \in \tau_k^{\text{sur}} = [t_k^{\text{sur}}, t_k^{\text{sur}} + T_k^{\text{gps}} + T_k^{\text{com}})$ , and

$$R_k(n+1) = R_k(n) + f_k^{\text{sur}}(R_k(n))\Delta t, \quad n = \left\lfloor \frac{\bar{\tau}_k^{\text{uw}}}{\Delta t} \right\rfloor, \dots, \left\lfloor \frac{t - t_k^{\text{ini}}}{\Delta t} \right\rfloor.$$

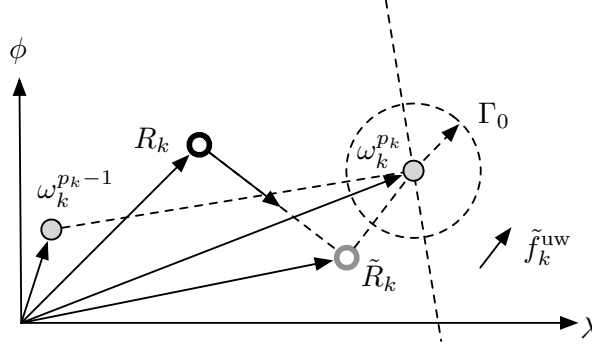


Figure 8.5: Waypoint geometry and completion conditions. The glider position  $R_k$ , previous waypoint  $\omega_k^{p_k-1}$ , and current waypoint  $\omega_k^{p_k}$  in geodetic coordinates, where  $\lambda$  and  $\phi$  represent longitude and latitude, respectively. The glider, which reaches  $\omega_k^{p_k}$  in the presence of the flow  $\tilde{f}_k^{\text{uw}}$  by steering towards  $\tilde{R}_k$ , satisfies the radius waypoint condition by entering the dashed circle of radius  $\Gamma_0$  centered at the current waypoint  $\omega_k^{p_k}$ . The finish line condition is satisfied when the glider crosses the dashed line through  $\omega_k^{p_k}$ . Figure after [201].

Since the gliders have no propulsion on the surface, the glider surface velocity  $f^{\text{sur}}$  is equal to the flow velocity. Flow velocity on the surface is estimated by displacement of the glider between sequential GPS fixes. Let  $s_k$  denote glider horizontal speed relative to the flow and  $\eta_k$  denote its absolute direction of motion. The horizontal component  $f^{\text{uw}}$  of the glider's total velocity underwater, which is the sum of the horizontal glider velocity  $s_k e^{i\eta_k}$  relative to the flow and the estimated horizontal flow velocity  $\tilde{f}_k^{\text{uw}}$ , depends on the ocean currents and the glider's onboard control system. We compute  $s_k$  from the desired vertical speed and glide angle. We assume that  $\eta_k$ , which is the orientation of the horizontal glider velocity, equals the desired heading of the glider, determined by the onboard control system depending on the glider estimate of the flow.

The onboard heading control algorithms are proprietary and not described here. Instead, we summarize a sample algorithm to compute the desired heading  $\eta_k$  given that the glider seeks to travel along a direct path from  $R_k$  to  $\omega_k^{p_k}$  in the presence of flow. Let  $\tilde{R}_k$  denote the hypothetical location of the glider if it travels from  $R_k$  along heading  $\eta_k \triangleq \arg\{\tilde{R}_k - R_k\}$  for time  $T_k$  in the absence of flow (see Figure 8.5). Heading  $\eta_k$  is correct if the glider reaches  $\omega_k^{p_k}$  after time  $T_k$  in the presence of flow  $\tilde{f}_k^{\text{uw}}$ . Note,  $s_k T_k = |\tilde{R}_k - R_k|$  is the distance relative

to the flow traveled by the glider over  $T_k$ . We have

$$\omega_k^{p_k} - \tilde{R}_k = T_k \tilde{f}_k^{\text{uw}} = \frac{|\tilde{R}_k - R_k|}{s_k} \tilde{f}_k^{\text{uw}}$$

and, using the geometry illustrated in Figure 8.5,

$$\eta_k \triangleq \arg\{\tilde{R}_k - R_k\} = \arg\left\{\omega_k^{p_k} - R_k - \frac{|\tilde{R}_k - R_k|}{s_k} \tilde{f}_k^{\text{uw}}\right\}. \quad (8.7)$$

Equation (8.7), which is a transcendental equation in the unknown  $\tilde{R}_k$ , can be solved under certain conditions on  $\tilde{f}_k^{\text{uw}}$ . A conservative condition sufficient to solve (8.7) is  $|\tilde{f}_k^{\text{uw}}| < s_k$ .

To determine the glider waypoint number  $p_k(n)$ , we integrate from the starting waypoint number  $p_k(n)$  using

$$p_k(n+1) = \begin{cases} p_k(n) + 1 & \text{if } \Psi(R_k(n), p_k(n)) \\ p_k(n) & \text{otherwise,} \end{cases}$$

where  $\Psi(R_k(n), p_k(n))$  is a boolean waypoint completion condition. For example, the *radius waypoint condition* illustrated in Figure 8.5 is  $\Psi^{\text{cir}}(R_k(n), p_k(n)) \triangleq \Gamma(R_k(n), \omega_k^{p_k(n)}) < \Gamma_0$ , where  $\Gamma_0 \in \mathbb{R}^+$  is the radius of a vertical cylinder centered at the waypoint. In the presence of strong flow, the radius waypoint condition—combined with a heading algorithm that steers the glider directly toward the waypoint—can result in the glider turning into the flow. Traveling into the flow can severely impede the forward progress of a glider. An alternate waypoint completion condition—called the *finish line condition*—is satisfied if the glider crosses the line that passes through the current waypoint and is perpendicular to the line connecting the previous and current waypoints. This algorithm is used by some gliders in the presence of strong flow [64].

**Glider Depth** While underwater, a glider makes either a single descent and ascent or continuously descends and ascends until the maximum dive duration  $T_k^{\text{max}}$  elapses. In shallow water, the roller-coaster motion minimizes time spent on the surface where the glider is vulnerable to surface currents and boats. Let  $g^{\text{uw}}$  be the vertical component of the glider total velocity. We denote the dive direction by  $\zeta_k \in \{-1, +1\}$ , where  $+1$  represents

descent and  $-1$  represents ascent (depth is positive down). The  $k$ th glider depth at time  $t$  is the solution to the following discrete-time model, which depends on the position  $R_k$ , depth  $z_k$ , and dive direction  $\zeta_k$ .

1. Before the dive,  $t \in \tau_k^{\text{ini}}$ , and

$$z_k(n) = 0, \quad n = 1, \dots, \left\lfloor \frac{t - t_k^{\text{ini}}}{\Delta t} \right\rfloor.$$

2. During the dive,  $t \in \tau_k^{\text{uw}}$ , and

$$z_k(n+1) = z_k(n) + g_k^{\text{uw}}(R_k(n), z_k(n), \zeta_k(n))\Delta t, \quad n = \left\lfloor \frac{\bar{\tau}_k^{\text{ini}}}{\Delta t} \right\rfloor, \dots, \left\lfloor \frac{t - t_k^{\text{ini}}}{\Delta t} \right\rfloor,$$

where  $g^{\text{uw}}$  is the vertical component of the glider velocity.

3. After the dive,  $t \in \tau_k^{\text{sur}}$ , and

$$z_k(n) = 0, \quad n = \left\lfloor \frac{\bar{\tau}_k^{\text{uw}}}{\Delta t} \right\rfloor, \dots, \left\lfloor \frac{t - t_k^{\text{ini}}}{\Delta t} \right\rfloor.$$

The vertical component  $g^{\text{uw}}$  of the glider velocity is the sum of the glider vertical velocity relative to the flow and the estimated vertical flow velocity (if available). We compute the dive direction  $\zeta_k \in \{-1, 1\}$  by integrating from the initial condition  $\zeta_k(1) = 1$  using

$$\zeta_k(n+1) = \begin{cases} -1 & \text{if } (z_k(n) > z_k^{\text{max}}) \cup (t > T_k^{\text{max}}) \cup (z_k(n) > z^{\text{uw}}(R_k(n)) - Z_k^{\text{min}}) \\ 1 & \text{if } (z_k(n) < -\zeta_k(n)z_k^{\text{min}}) \cup (t < T_k^{\text{max}}) \\ \zeta_k(n) & \text{otherwise.} \end{cases}$$

In words, the glider ascends if it exceeds its maximum inflection depth, it exceeds the maximum dive duration, or its altitude is less than the minimum allowable altitude. If the glider is ascending before the end of the maximum dive duration, the dive direction reverses when the glider is shallower than the minimum inflection depth.

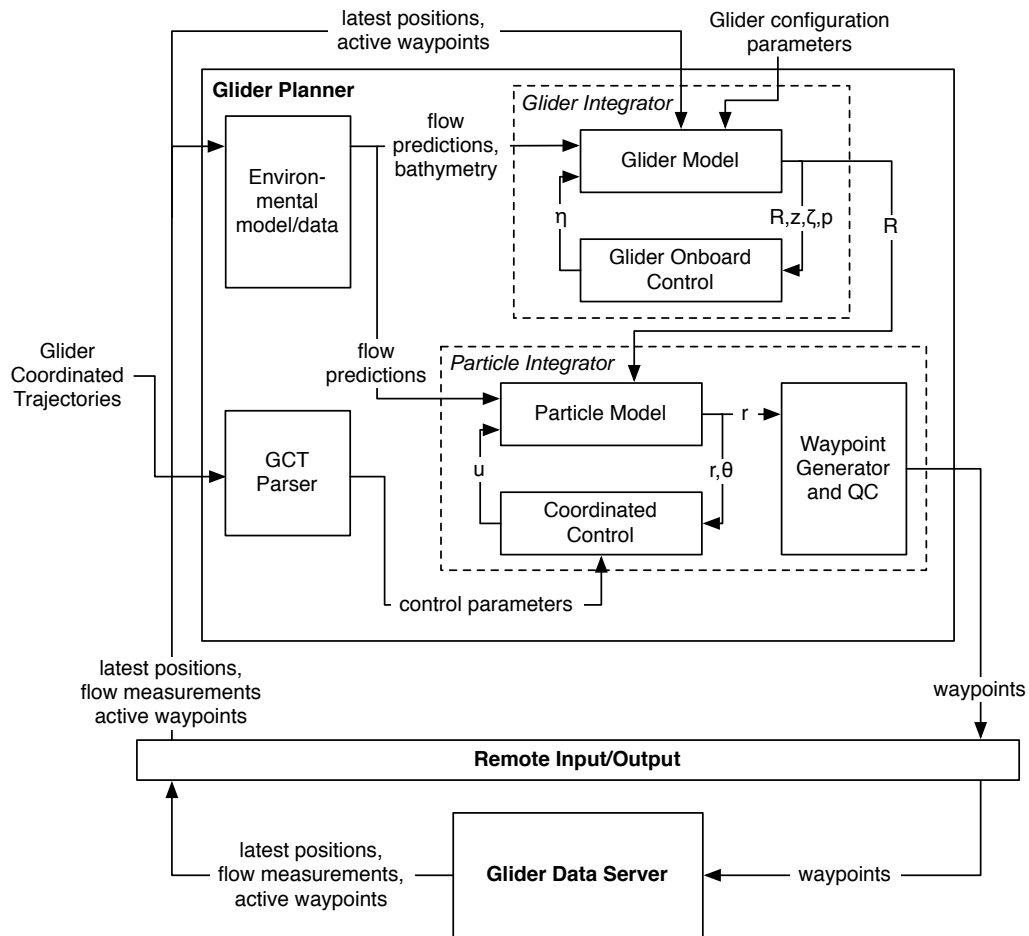


Figure 8.6: Glider planner block diagram. The planner creates waypoints to steer the fleet to a GCT by integrating the glider model for prediction and the particle model for planning. The glider planner interfaces to the glider data server via the remote IO. Figure after [201].

## 8.3 The Glider Coordinated Control System: Architecture and Operation

### 8.3.1 Glider Planner

The glider planner encapsulates the multi-vehicle control algorithm shown in Figure 8.6. The interplay between the glider model and the particle model is fundamental to the design of the planner. The planner uses the glider model to predict glider motion underwater and the particle model to plan future glider trajectories. The planned trajectories originate from

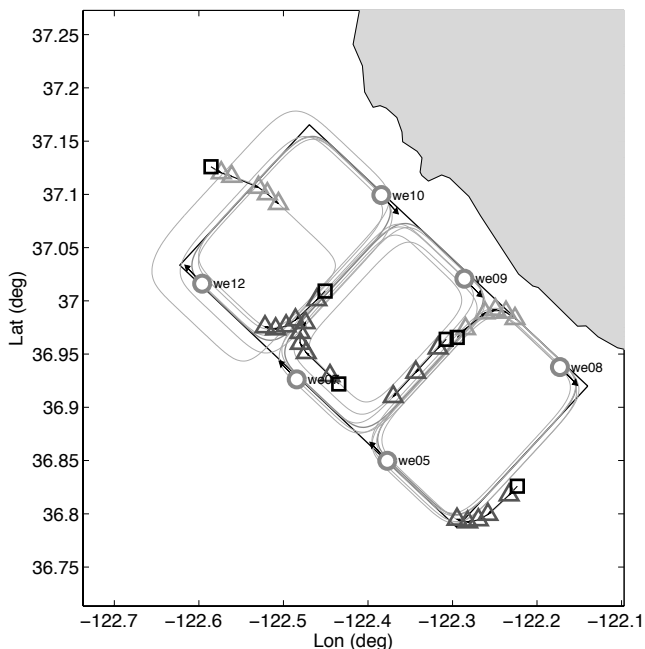


Figure 8.7: Output of a GCCS planning cycle. Each glider’s planned trajectory (thin gray line) originates at the last surface position (black square) and terminates at the planned position (gray circle). Waypoints (gray triangles) are shown for the first twelve hours of the planned trajectories. Note that the planned trajectories converge to the desired GCT shown in Figure 8.2.

the position and time of the next expected surfacing of each glider as shown in Figure 8.7.

Planning new trajectories for all gliders occurs simultaneously; we call the sequence of steps that produces new glider trajectories a *planning cycle*. A planning cycle starts whenever a glider surfaces and ends when the planner generates new waypoints for all gliders. Due to operational concerns like reduced effective speed and hazardous boat traffic, the gliders do not wait on the surface for their new waypoints. Instead, gliders use the most recent set of waypoints that were computed before they surfaced. The planning cycle executes immediately after a glider surfaces, since new waypoints for all gliders are computed whenever a single glider surfaces. The planning-cycle frequency depends on the number of gliders in the water and the surfacing frequency of each glider.

The planner uses the detailed glider model to predict each glider’s underwater trajectory and next surfacing location and time. This prediction uses the surface and underwater flow OA forecast obtained from all recent glider flow measurements. For each glider that has surfaced since the last planning cycle, the planner calculates inaccuracies in the predictions of effective speed, expected surface position, and expected surface time. Prediction errors are useful for gauging glider and planner performance. The main step in the planning cycle, described in more detail below, is to integrate the particle model to generate planned trajectories. The planner converts the planned trajectory of each glider to a list of waypoints. Waypoints must pass a quality control filter (QC) before transmission to the glider data server. Surfacing when expected is one requirement to pass QC and failure to do so serves as an indication of potential problems with the glider or the glider data server.

**Particle Integrator** At the core of the glider planner is the *particle integrator*, which generates the glider planned trajectories using closed-loop (coordinated) control of the particle model. The particle-integration algorithm is complicated by the fact that gliders surface asynchronously and do not wait on the surface for new waypoints. When the particle integration initializes, one or more gliders has recently surfaced and all gliders are underway.

During each planning cycle, the particle integrator coordinates particles that represent gliders on the surface with particles that represent gliders underwater. The particle integrator takes as input the trajectory predicted for each glider by the glider integrator as well as the desired tracks and coordination specified in the GCT. The output of the particle integrator is a new set of waypoints for each glider. The particle integrator uses a MATLAB® ODE solver to integrate trajectories from the time  $t_0$  of the most recent glider surfacing to the planning horizon  $t_0 + T$ . The initial position of each particle is the position of the glider at the next expected surfacing location and time  $t_k^{\text{sur}}$ . One can choose the initial phase to maximize the convergence rate of the control. For example, during the GCCS experiments described in Chapter 9, the GCCS initialized the particle phases to maximize convergence rate to the desired track.

For each glider  $k$  that is predicted to have not yet surfaced by time  $t$ , we set the

<b>Goal:</b>	Integrate feedback control algorithm using asynchronous initial conditions.
<b>Inputs:</b>	Predicted trajectories up to next expected surfacing, desired tracks and coordination (GCT)
<b>Outputs:</b>	New waypoints for all gliders

---

*During every planning cycle, the particle integrator performs:*

- 1: Set the integration start time  $t_0$  to most recent glider actual surface time,  $t_0 = \max_{k=1, \dots, N} t_k^{\text{sur}}$
- 2: **for** each particle  $k = 1, \dots, N$ , Set initial positions  $r_k(t_0)$  to glider (surface) position at time  $t_k^{\text{sur}}$ , **end for**
- 3: **for** each particle  $k = 1, \dots, N$ , Set initial headings  $\theta_k(t_0)$  according to control-specific algorithm, **end for**
- 4: Call ODE solver with initial conditions  $\mathbf{r}(t_0)$  and  $\boldsymbol{\theta}(t_0)$  and time span  $t \in [t_0, t_0 + T]$

*During every iteration, the ODE solver performs:*

- i: **for** each particle  $k = 1, \dots, N$ ,  
  - if**  $t < t_k^{\text{sur}}$ , Set position  $r_k(t)$  and heading  $\theta_k(t)$  to glider predicted underwater position and heading, **end if****end for**
- ii: Compute steering control  $\dot{\boldsymbol{\theta}}(t) = \mathbf{u}(t)$  and particle velocity  $\dot{\mathbf{r}}(t)$  using  $\mathbf{r}(t)$  and  $\boldsymbol{\theta}(t)$
- iii: **for** each particle  $k = 1, \dots, N$ ,  
  - if**  $t < t_k^{\text{sur}}$ , Set steering control  $\dot{\theta}_k(t)$  and particle velocity  $\dot{r}_k(t)$  to zero, **end if****end for**
- iv: **for** each particle, Overwrite start of planned trajectory with predicted trajectory up to expected surface time, **end for**
- v: **for** each particle, Generate waypoints for  $r_k(t)$ ,  $t > t_k^{\text{sur}}$ , and run quality control, **end for**

Table 8.4: Particle integrator algorithm. This algorithm is executed by the GCCS planner to plan glider trajectories that converge to the configuration specified in the GCT.

corresponding particle position  $r_k(t)$  and heading  $\theta_k(t)$  to the predicted underwater position and heading. Then, the coordinated control algorithm computes the steering controls  $\mathbf{u}(t)$  and velocities  $\dot{\mathbf{r}}(t)$  for all particles using  $\mathbf{r}(t)$  and  $\boldsymbol{\theta}(t)$ . For each glider  $k$  that is predicted to have not yet surfaced by  $t$ , we set the steering control  $u_k(t)$  and velocity  $\dot{r}_k(t)$  to zero. After the ODE solver computes the planned trajectories, we replace the portion of each trajectory that occurs before the next expected surface time with the predicted underwater trajectory. A pseudo-code description of this algorithm is provided in Table 8.4.

**Waypoint Generation and Quality Control Filter** We convert the glider planned trajectories to waypoints and verify the waypoints using QC. There are two alternate waypoint generation methods. In the first method, the waypoints are spaced uniformly in time (assuming constant glider effective speed). In the second method, we convert portions of the planned trajectory with lower (resp. higher) curvature to fewer (resp. more) waypoints subject to a maximum (resp. minimum) spacing constraint. The latter method clusters waypoints near tight turns and spreads out waypoints along straight portions of the planned glider trajectories. To provide robustness to delays and errors incurred in satellite communication between the glider data server and the glider, each waypoint file that passes QC has a unique message number and an expiration date.

Waypoint quality control is required for safe, automated operation of gliders. To pass QC, the following criteria must be met: (1) the last glider position update must not be too old; (2) all waypoints other than those at the start of the list must be inside a prescribed bounding box; (3) waypoints must not be shallower than the glider minimum operating depth; and (4) waypoints must be spaced by no more (resp. less) than the maximum (resp. minimum) allowable spacing. We remove waypoints that are too shallow. Failure to meet any requirement other than (3) results in rejection of the entire waypoint list.

### 8.3.2 Glider Simulator

In addition to providing a real-time controller, the GCCS serves as a simulation testbed for glider coordinated control algorithms. One can also use the glider simulator during a glider deployment to predict glider motion in ocean flow forecasts. A central advantage is the ability to test strategies in the presence of strong flow and communication and feedback constraints and uncertainties, challenges that are not yet fully addressed by theoretical methods. The glider simulator uses the glider model to predict glider motion. To predict the motion of a coordinated fleet of gliders, we run the glider simulator in tandem with the glider planner. The software interface between the glider planner and simulator is identical to the interface between the glider planner and the real gliders; the simulated gliders produce

the same data files as the real gliders. This feature enables use of the GCCS, in conjunction with a virtual ocean model, to conduct virtual experiments.

**Glider Integrator** A central component of both the glider planner and simulator is the glider integrator, which integrates the detailed glider model to predict glider trajectories in the ocean. Predicting glider trajectories is critical to glider planning since new trajectories are generated while gliders are underwater. We model the motion of each glider and its onboard control system under the influence of the bathymetry (water depth) and currents (water velocity). The bathymetry is important because gliders maintain a minimum altitude above the bottom. Ocean currents are important because they advect gliders and also because gliders respond to their onboard current estimates.

The glider onboard control system integrates its position, which is called the “dead-reckoned position”, from estimates of its horizontal speed and heading. The GCCS predicts both glider position and glider dead-reckoned position. These predictions differ if, for example, the planner uses a more accurate flow estimate than the glider.

### 8.3.3 Remote Input/Output

Robust networking enables the GCCS to run automatically. The remote IO module supports communication over the Internet between the glider planner and glider simulator as well as between the glider planner and the glider data servers. In addition, the remote IO module publishes real-time glider planner status for monitoring and supervision of the GCCS as shown in Figure 8.7. To support timely operator intervention, the remote IO module sends email notification of software or operational errors.

## Chapter 9

# GCCS Experimental Results

The Glider Coordinated Control System (GCCS) is the software infrastructure described in the previous chapter that implements our cooperative control framework on a fleet of underwater gliders. In this chapter we describe a field experiment during which the GCCS controlled six gliders in Monterey Bay in August 2006. In preparation for this field experiment, we tested the GCCS during two glider deployments not described here: a sea-trial with two gliders in Buzzard’s Bay, Massachusetts in March 2006 [299] and a three glider whale-tracking excursion in the Great South Channel off of Cape Cod, Massachusetts in May 2006.<sup>1</sup> During the Monterey Bay experiment, the GCCS operated continuously for nearly 24 days with minimal human intervention. In addition to experiments with real gliders, we have conducted multiple virtual experiments in which the GCCS has served as both glider planner and glider simulator.

In this chapter, we focus on GCCS experimental results from the *Adaptive Sampling and Prediction* (ASAP) research initiative. We describe ASAP in Section 9.1. In Section 9.2 we summarize results from an ASAP virtual pilot experiment. In Section 9.3, we present results from the ASAP 2006 field experiment in Monterey Bay.

---

<sup>1</sup>For a description of a previous whale-tracking excursion in the Great South Channel, see [182].

## 9.1 Adaptive Sampling and Prediction Research Initiative

ASAP is a five year Multidisciplinary University Research Initiative (MURI) funded in 2004 by the Office of Naval Research on the topic of “Coupled Observation, Adaptive Sampling, and Forecast in the Real Environment” [144]. ASAP involves collaboration between physical oceanographers, ocean modelers, and control engineers from many universities, including Princeton, the Scripps Institution of Oceanography (SIO), the Woods Hole Oceanographic Institution (WHOI), Harvard, the California Institute of Technology, the Naval Postgraduate School, and the Massachusetts Institute of Technology. A central focus of ASAP is to design and demonstrate optimal ocean sampling strategies for multiple, mobile sensor platforms—particularly gliders and propellor-driven AUVs. These strategies may have broader applicability. According to the research topic announcement, ASAP has the potential to make contributions to Department of Defense needs in “battlefield awareness, mine countermeasures, and combating terrorism including methods for monitoring weapons of mass destruction and tools for chem/bio defense, decision making, adaptive command and control of groups of autonomous vehicles, and more capable networked, interoperable, mobile, dynamic systems” [265].

The ASAP ocean-science objective is to study the three-dimensional dynamics of the coastal upwelling center that appears annually in Monterey Bay. To achieve this objective, MURI participants seek to integrate advanced ocean models with novel, adaptive sampling strategies. The ASAP proposal identifies three adaptive sampling tasks [144]. The first adaptive sampling task is to minimize mapping error (see Section 2.2) in a mapping domain containing an upwelling center. This task motivated the adaptive sampling strategy in Section 2.3.3. The second task is to identify and track localized dynamic features within the mapping domain. For strategies motivated by the second task, see, for example [84]. The third task is to minimize uncertainty in the dynamic model predictions of the ocean processes in the mapping domain. Strategies developed to address this objective are based on advanced ocean modeling techniques; see, for example, [150, 147, 27, 159, 247].

The dynamics of ocean processes influence the design and adaptation of sampling tra-

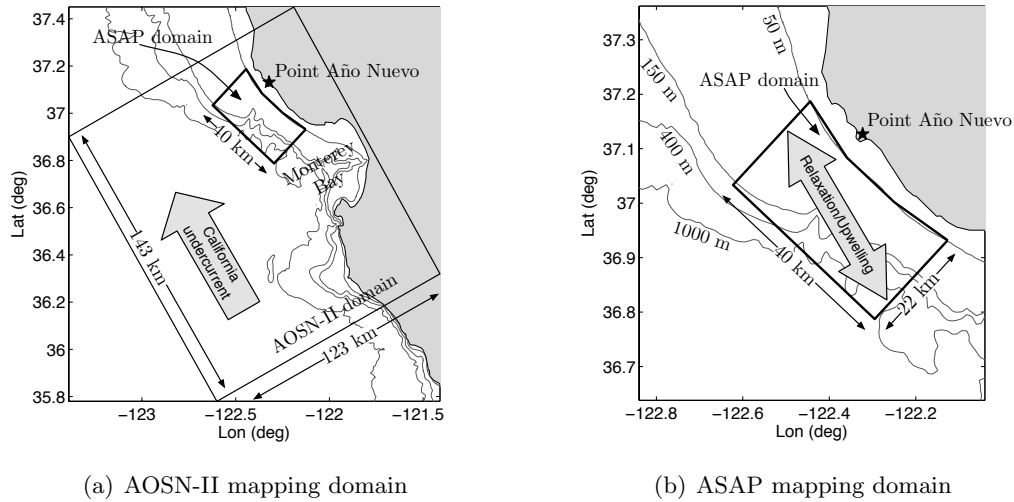


Figure 9.1: AOSN-II and ASAP mapping domains and ocean circulation. (a) The AOSN-II mapping domain from a 2003 field experiment contains Monterey Bay and is bounded by a 123 km by 143 km box in which the prevailing flow year-round is the deep, poleward California undercurrent; (b) for the 2006 field experiment, the ASAP domain, whose shallow side is bounded by the 50 m depth contour just off of Point Año Nuevo, is designed to densely sample the annual upwelling of cold, deep seawater that travels offshore or equatorward across the mouth of the bay. Upwelling activity is intermittently replaced with warm, poleward flow during relaxation.

jectories. As such, adaptive sampling strategies in Monterey Bay should be informed by the ocean science of the upwelling processes. We summarize below some basic oceanography on upwelling events in Monterey Bay and discuss the adaptive sampling plan in this context, following [248, 218, 217]. For a general reference on ocean circulation in Monterey Bay, see, for example, [35].

### 9.1.1 Upwelling in Monterey Bay

During an upwelling event in Monterey Bay, cold water from deep below the ocean surface rises and mixes with the warm water on the ocean surface. The cold water often emerges just north of the bay, near Point Año Nuevo (see Figure 9.1). Partly due to the Coriolis force from the earth's rotation and partly due to equatorward winds, upwelled water near Point Año Nuevo tends to flow offshore or south across the mouth of the bay [227]. During periods

of active upwelling, the water temperature inside the bay can be elevated, a phenomenon known as “shadowing” [96].

Although upwelling occurs in the summer, it is supported by several year-round components of the California Current System (CCS) [217]. One component of the CCS—the California undercurrent—is a deep, poleward flow (that is, it flows toward the North pole) [218]. Because deep water is nutrient-rich, upwelling can spur plankton activity in the bay [194, 264]. This activity, combined with the ocean circulation, results in complex dynamics of carbon production and advection [208].

The summertime ocean circulation in Monterey Bay oscillates between upwelling and *relaxation*. During relaxation, poleward flow crosses the mouth of the bay past Point Año Nuevo, as shown in Figure 9.1(b). Relaxation-favorable wind conditions are weak winds from any direction or strong winds from the south. Transitions from upwelling to relaxation or from relaxation to upwelling can produce a scenario in which both poleward and equatorward flow are observed simultaneously. In this scenario, onshore flow bifurcates (divides into two branches) near Point Año Nuevo. Water to the north flows poleward and water to the south flows equatorward.

The three-dimensional dynamics of upwelling in the vicinity of Point Año Nuevo was a focus of one ASAP pilot study and the major ASAP field experiment. The pilot study, carried out in 2006 in advance of the August 2006 field experiment, consisted of a series of “virtual” pilot experiments conducted in simulation. During the ASAP 2006 virtual pilot study and field experiment, the mapping domain was contained in a 22 km by 40 km box (see Figure 9.1(b)). The shallow side of the mapping domain is the 50 m depth contour.<sup>2</sup> For the purposes of evaluating glider mapping performance, we refer to the offshore, northern and southern edges as the *boundary* of the mapping domain. *In situ* data collected along the boundary of the mapping domain can be combined with remote sensing of the surface of the mapping domain to estimate the flux of mass, heat, and salt [228].<sup>3</sup>

---

<sup>2</sup>Gliders stayed outside the 50 m depth contour in order to avoid getting tangled in the kelp that grows along the California coastline.

<sup>3</sup>Zero-flux boundary conditions are assumed on the shallow side and bottom of the mapping domain. However, water can “leak” into the southwest corner, which exceeds the gliders’ maximum dive depth.

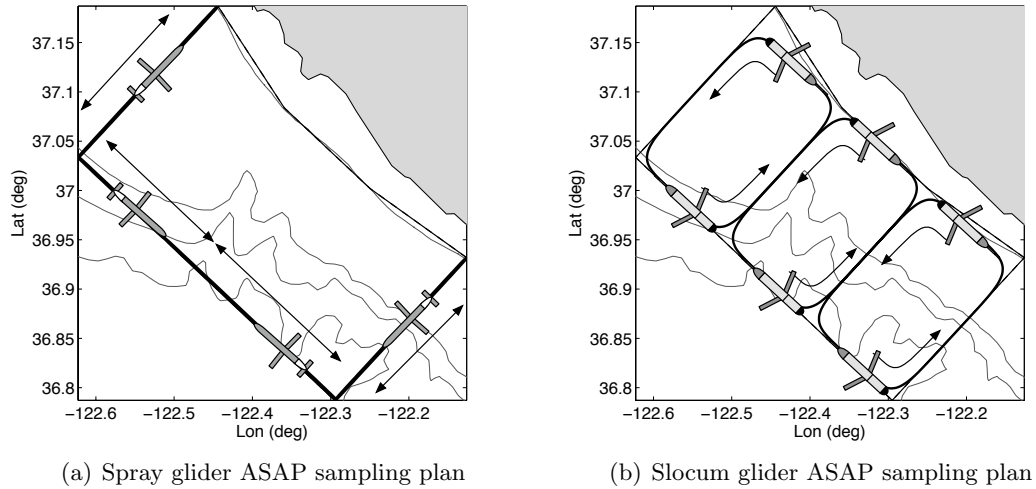


Figure 9.2: Default ASAP glider sampling plans. (a) Four Spray gliders patrol four linear tracks along the offshore boundaries of the ASAP mapping domain; (b) three pairs of Slocum gliders orbit in unison three superelliptical tracks contained in the mapping domain.

### 9.1.2 ASAP Glider Experimental Methods

In order to better understand the dynamics of upwelling and relaxation events, a combination of autonomous and manned sensor platforms, both stationary and mobile, was deployed to sample with high resolution both the interior and the boundary of the ASAP mapping domain. A group of four Spray gliders, equipped with upward-looking acoustic sensors to measure water velocity, were initially dedicated to patrolling the boundary of the mapping domain on three to four linear tracks shown in Figure 9.2(a). A group of six Slocum gliders, which were not equipped with velocity sensors, were assigned to sample both the interior and boundary of the domain on three 13.3 km by 20 km superelliptical tracks, as shown in Figure 9.2(b). The counterclockwise direction of rotation of the Slocum gliders around each track was initially chosen in expectation of the equatorward upwelled flow to be weaker near shore. When this assumption holds, then the fastest circuit around the tracks is obtained by traveling counterclockwise. The long sides of the default Slocum tracks are touching so that gliders on these tracks would repeatedly sample two interior, cross-shelf lines.

The number of Slocum gliders on each default track can be justified using our analysis of mapping error in space and time in Section 2.2.2. Each default track shown in Figure 9.2(b) has a perimeter of 61.2 km. The Slocum glider effective speed used in the GCCS for planning is  $s_0 = 0.32$  m/s or  $s_0 = 27.8$  km/day (see Table D.1). Using decorrelation lengths estimated from the AOSN-II experiment ( $\sigma = 22$  km and  $\tau = 2.2$  days, respectively [229]) we can compute the glider non-dimensionalized speed  $\mathfrak{s}_0 \triangleq (s_0\tau)/\sigma = 2.8$ . When the non-dimensionalized speed is greater than one, a Slocum glider is temporally-constrained (see Section 2.2.2). Temporally-constrained sensor platforms have an along-track swath width of  $s_0\tau$ . To cover a one-dimensional periodic track of length  $|\mathcal{B}|$ , we need  $\lceil |\mathcal{B}|/(s_0\tau) \rceil$  gliders. In this case, we need exactly one glider per track, since  $|\mathcal{B}| = s_0\tau = 61.2$  km. Assigning two gliders to each track provides insurance for glider failure or reduction in glider effective speed. It also allows gliders to effectively sample processes at shorter temporal scales.

During the ASAP experiments, gliders were steered by a combination of automatic and assisted-manual control. During the pilot experiments, the GCCS controlled (and simulated) all of the Spray and Slocum gliders. During the ASAP field experiment, operators at SIO designed and monitored the Spray glider trajectories. The GCCS—running on a computer at Princeton—controlled the Slocum gliders. The desired glider tracks were designed and adapted by the ASAP team. Operational conditions leading to adaptation of glider tracks included glider deployment/recovery and changing ocean currents. Glider tracks were also adapted based on observations of new features such as an eddy moving offshore, and insights gleaned from interpretation of data and real-time ocean models.

The GCCS steered gliders during the ASAP experiments using the multi-level, augmented Laplacian symmetric loop configuration control described in Proposition 7.12 (see Section 7.3). This control law steers a group of gliders to a set of GCTs, described in Section 8.1. The ASAP GCT tracks were superelliptical with parameter  $p = 3$  (see Section 7.3). For this parameter value, the glider tracks have nearly straight edges and smooth, rounded corners. Other parameters used for the GCCS control law and the GCCS glider model are provided in Table D.1 (see Appendix D).

The GCCS used an uncoordinated control law to steer gliders from their initial deployment locations to the vicinity of their desired track. The uncoordinated control law, based on [301], steers a glider orthogonal to the level curves of an energy function minimized by points along the desired track. The GCCS used the uncoordinated control law to steer a glider whenever it was outside a rectangular box containing the desired track. The box dimensions were 50% larger than the dimensions of the track.

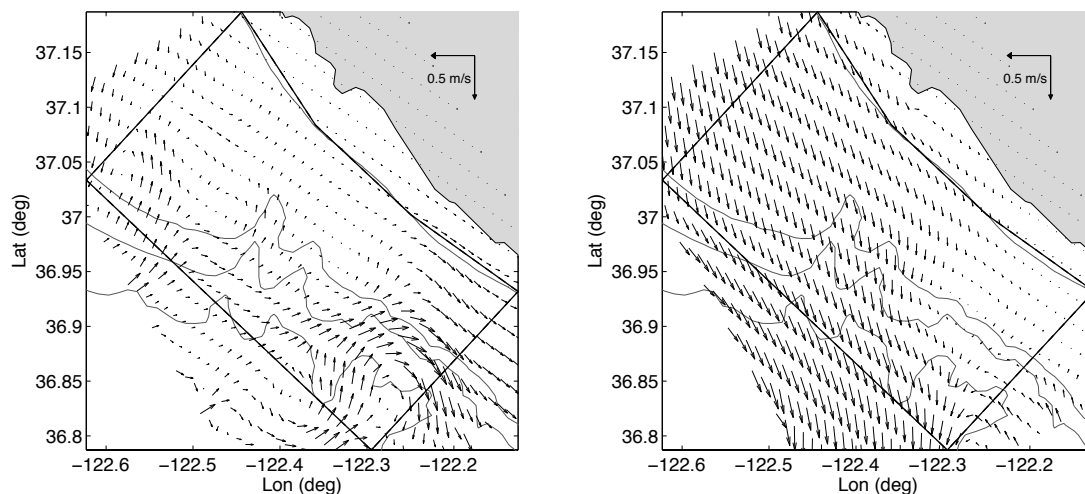
Next we describe results and preliminary analysis for ASAP gliders under GCCS automatic control. A more thorough analysis of the joint operation of gliders under automatic control with gliders under semi-autonomous and assisted-manual control is in preparation.

## 9.2 Summary of an ASAP Virtual Pilot Experiment

In preparation for the ASAP field experiment in Monterey Bay in August 2006, a series of a dozen virtual pilot experiments (VPEs) were conducted during the period from January 2006 to July 2006. The whole ASAP team participated in five official VPEs, during which the GCCS generated glider measurement data that were assimilated into one or more ocean models. We conducted seven unofficial VPEs to further refine the glider experimental plan and to test the GCCS planner. The VPEs and subsequent analysis were instrumental in selecting the default glider experimental plan shown in Figure 9.2.

We summarize here a portion of one official VPE conducted with the entire ASAP team in March 2006. This was the second VPE overall and the first VPE in which we demonstrated adaptation of the glider sampling plan [201]. During this experiment, the GCCS planner controlled a glider fleet of four Sprays and six Slocums generated by the GCCS simulator. The GCCS remote input/output module transferred simulated glider data and waypoints between the GCCS planner and GCCS simulator via the WHOI and SIO glider data servers. Ocean modelers assimilated the virtual glider data in real-time.

During the March 2006 VPE, the gliders sampled and were advected by a model ocean generated by the Harvard Ocean Prediction System. The model ocean is based on data collected during the AOSN-II field experiment in August 2003 [3]. It contains temperature,



(a) VPE model ocean at 15:00 GMT on August 13 (b) VPE model ocean at 15:00 GMT on August 18

Figure 9.3: Snapshots of model-ocean flow conditions during ASAP VPE. The March 2006 experiment used a model ocean based on data collected during the AOSN-II field experiment in August 2003. The flow vector fields were computed from glider depth-averaged flow estimates using OA with  $\sigma = 22$  km and  $\tau = 2.2$  days and noise variance equal to 10% of the process variance  $\sigma_0$ . The flow is assumed to have zero mean and unit variance. (a) Circulating flow, depth-averaged over top 200 m, indicative of transition from relaxation to upwelling; (b) strong equatorward flow indicative of upwelling activity.

salinity, and three-dimensional flow velocity at 500 meter horizontal resolution with 22 vertical levels over a 35 day period starting August 6, 2003. The virtual gliders sampled the model ocean for a two week period starting at 15:00 GMT on August 11, 2003.

The model ocean exhibited flow circulation representative of an upwelling event. We used the glider depth-averaged flow measurements to make an OA map of the flow conditions at 15:00 GMT on August 13. This snapshot shows circulating flow indicative of a transition from relaxation to upwelling (see Figure 9.3(a)). We made another OA map of depth-averaged flow velocity at 15:00 GMT on August 18. Equatorward flow in this snapshot indicates upwelling activity (see Figure 9.3(b)). The magnitude of equatorward flow in this snapshot exceeds the glider effective speed. Another model ocean with even greater flow speeds was used in subsequent VPEs.

All of the gliders, both Spray and Slocum alike, were controlled during this VPE by

the GCCS. However, since a Spray glider travels at a different speed than a Slocum glider, the Spray gliders were coordinated separately from the Slocum gliders. The algorithmic framework has not yet been implemented within the GCCS to automatically coordinate gliders traveling at different speeds. We evaluate coordination performance by the degree to which glider trajectories converge to the desired GCT, as measured qualitatively by distance from the assigned track and relative spacing along the track. Quantitative analysis of glider performance, other than mapping performance, is deferred to the discussion of the ASAP field experiment in Section 9.3.

At the start of the deployment, four virtual Spray gliders—SIO13, SIO14, SIO15, and SIO16—were assigned to travel clockwise with uniform spacing around a 10 km by 20 km superellipse track encompassing the northern boundary of the ASAP domain as shown in Figure 9.4(a). The thin gray lines connecting all four of the gliders in Figure 9.4(a) reflect the glider interaction network specified in the GCT (see Section 8.1). Although the gliders appear in numerical order around the track in Figure 9.4(a), the actual sequence of gliders around the track is not specified by the GCT.<sup>4</sup> The Spray gliders were configured to dive to a maximum dive depth of 400 m or to within 5 m of the bottom. (In the GCCS detailed glider model, a Spray glider descends and ascends only once per dive, so there is no minimum dive depth or maximum dive time.) All of the gliders were deployed in the vicinity of their assigned tracks and with approximately the desired spacing. Subsequent VPEs used more realistic initial conditions.

The Spray glider initial communication strategy degraded their coordination performance. For the first three days of the deployment, the virtual Spray gliders performed simulated Iridium communication after every dive, spending a total of seven minutes on the surface between dives. In shallow water with surface currents of 0.15 m/s to 0.35 m/s, the Spray gliders surfaced frequently and made poor progress around the track. Their median effective speed dipped to 0.2 m/s. Note glider effective speed is measured by the ratio of the distance between sequential profile positions to the interval between the profile times.

---

<sup>4</sup>Because the ASAP glider experimental plan was finalized subsequent to this VPE, the Spray gliders were assigned to be coordinated on a loop inside the mapping domain and did not simply patrol the boundary.

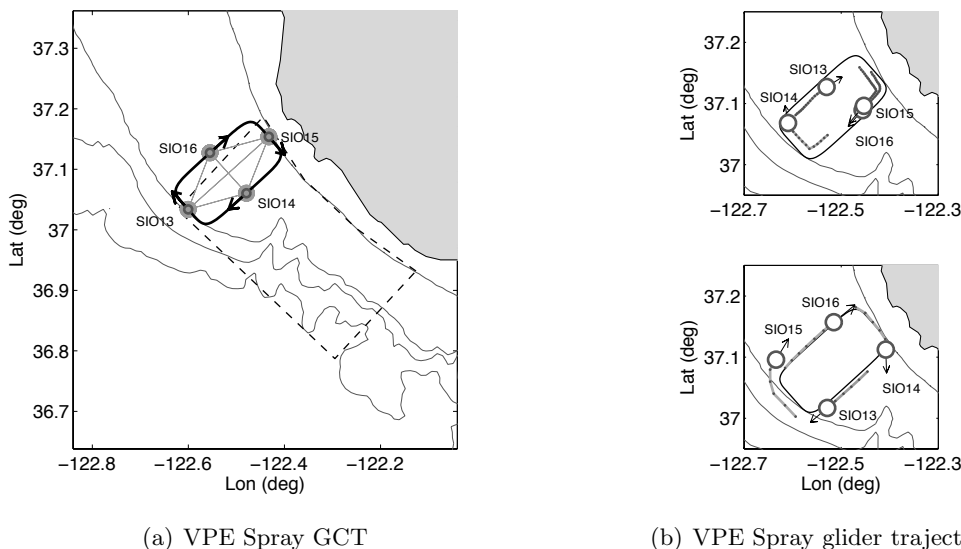


Figure 9.4: Spray GCT and snapshots of glider trajectories during an ASAP VPE. (a) Four virtual Spray gliders—SIO13, SIO14, SIO15, SIO16—were assigned to travel clockwise with uniform spacing around a 10 km by 20 km superelliptical track encompassing the northern boundary of the ASAP domain; (b, top) frequent and lengthy surfacings combined with strong surface currents degraded coordination performance over the twelve hours preceding 9:00 GMT on August 15; (b, bottom) reducing the frequency with which gliders surfaced to communicate improved coordination performance, as evidenced by their trajectories from 3:00 to 15:00 GMT on August 18.

The glider positions after four days in the water are shown in the top panel of Figure 9.4(b). On the fourth day of the deployment, we reconfigured the Spray gliders to communicate on surfacing only if two or more hours had elapsed since the last communication. In this configuration, the glider effective speed recovered by 25% to 0.25 m/s. The coordination performance also recovered, as shown in the bottom panel of Figure 9.4(b).

Figure 9.4(b) also illustrates how the GCCS automatically regulates glider progress around the track to achieve the desired along-track spacing between the gliders. To “slow down” a glider as it moves around a track, the control algorithm used during the ASAP experiments steers a glider to an outside “lane”. To “speed up” a glider, the algorithm steers it to an inner lane. In the bottom panel of Figure 9.4(b), SIO15 travels along an outside lane so as to increase separation from SIO16, which is traveling around the track

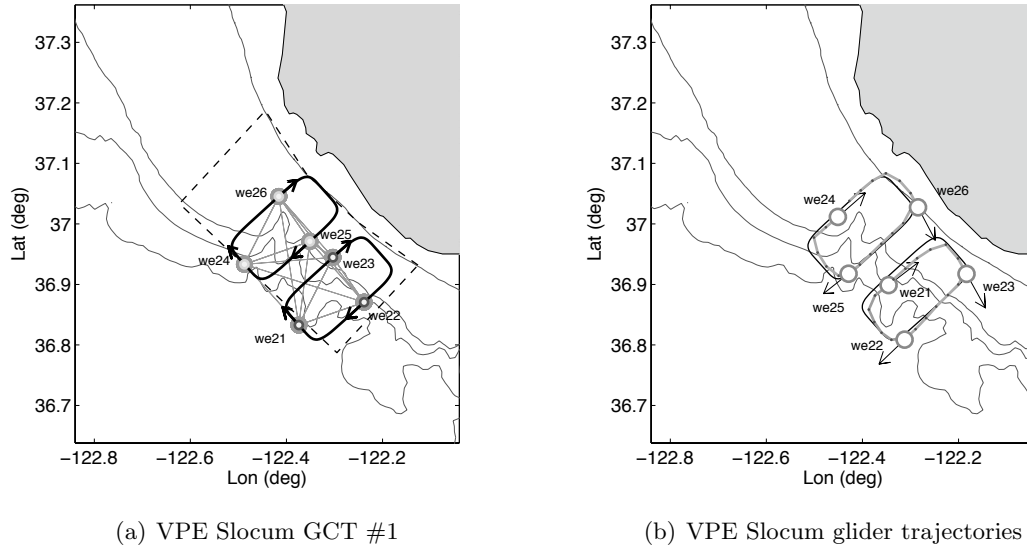


Figure 9.5: Slocum GCT and snapshots of glider trajectories during an ASAP VPE. (a) Six virtual Slocum gliders are assigned to form two synchronized subgroups of three gliders each on two 10 km by 20 km superelliptical tracks; (b) Slocum glider coordination performance is very good at 9:00 on August 15, as evidenced by twelve hours of glider trajectories.

ahead of SIO15.

At the start of the deployment, the group of six virtual Slocum gliders—*we21*, *we22*, *we23*, *we24*, *we25*, and *we26*—formed two equal and synchronized subgroups on two 10 km by 20 km superelliptical tracks. The three gliders in each subgroup were equally spaced around their assigned track, as shown in Figure 9.5(a). Each Slocum glider was configured to dive to 200 m or to within 5 m of the bottom. Gliders inflected at a minimum dive depth of 5 m. Recall that the glider begins its final ascent after  $T^{\max}$  has elapsed since its initial descent (see Section 8.2.2). The maximum dive time  $T^{\max}$  for Slocum gliders during this VPE was two hours.

The maximum dive time is determined by trading-off different priorities. Increasing the maximum dive time decreases the amount of time a glider spends on the surface. When a glider is on the surface, it drifts passively and is at risk of getting damaged by surface traffic. Short dives also reduce effective speed, which reduces mapping performance. However, longer dives decrease the frequency of GCCS feedback, which decreases coordination

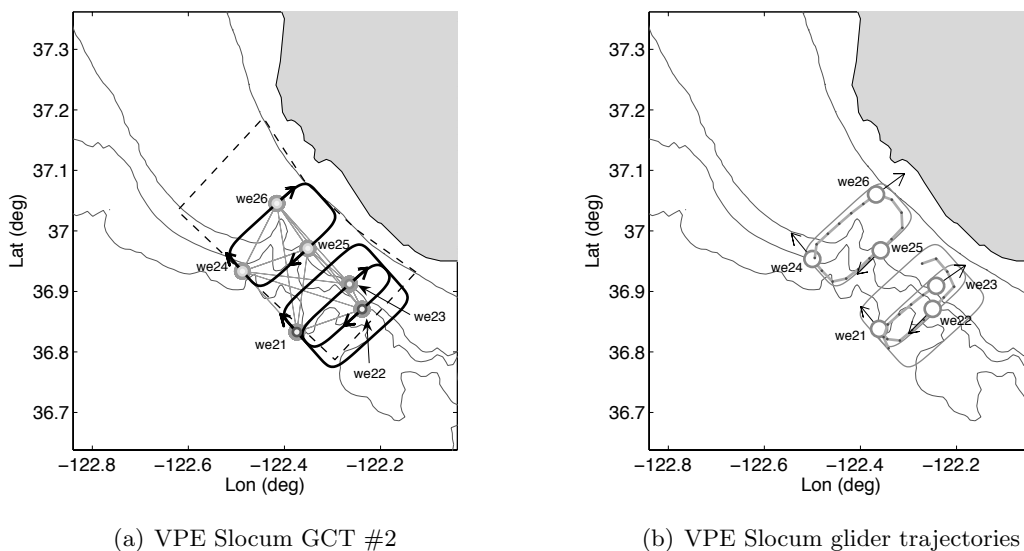


Figure 9.6: Slocum GCT and snapshots of glider trajectories after adaptation of sampling plan during ASAP VPE. (a) Adaptation of VPE GCT shown in Figure 9.5(a) entailed the creation of a new track extending outside ASAP mapping domain; a scout glider, we23, was assigned to the new track with the original inter-glider coordination. (b) Slocum glider coordination performance on the adapted GCT is very good as evidenced by twelve hours of glider trajectories preceding 9:00 GMT on August 18.

performance. Simulations show that setting  $T^{\max}$  as large as three hours does not appear to impair coordination performance in the ASAP domain. However, this value might not produce acceptable track-following accuracy on smaller tracks.

During the first four days of the VPE the GCCS achieved good spacing of the Slocum subgroups around each track and good synchronization of the two subgroups (see Figure 9.5(b)). At 9:00 GMT on August 15, we created an additional, 10 km by 20 km superelliptical track that extends 5 km outside the ASAP mapping domain to the south and overlaps the original southern-most track. A so-called “scout” Slocum glider was assigned to orbit the new track while remaining coordinated with the other Slocums as shown in Figure 9.6(a). Three days after the adaptation of the GCT, the Slocum glider collective coordination performance was very good (see Figure 9.6(b)). That is, if one superimposes the original southern track on top of the new southern track, the three Slocums assigned to these two tracks are uniformly spaced. Similarly, if one superimposes all three tracks, all

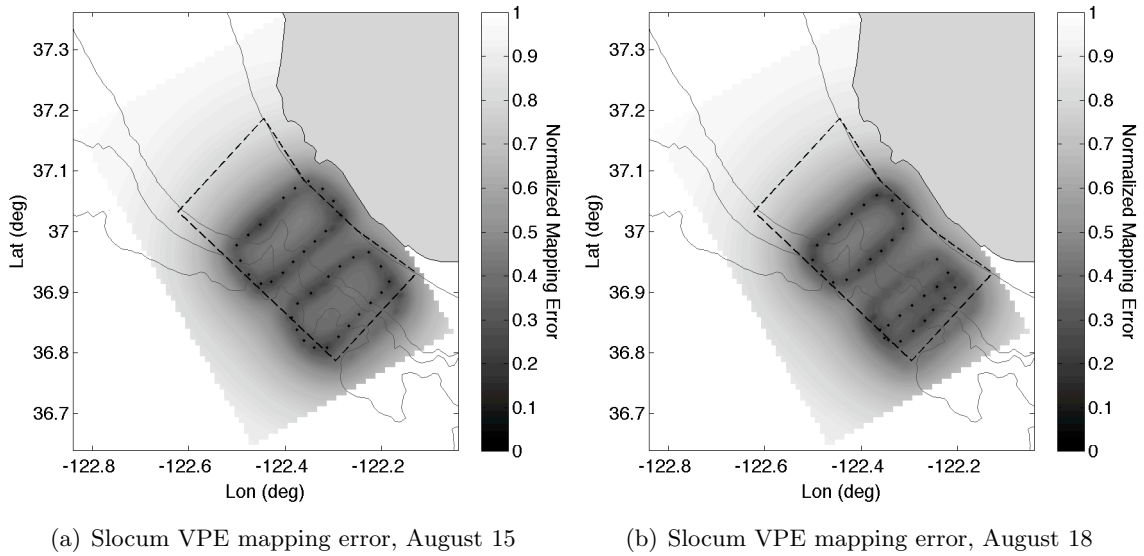


Figure 9.7: Slocum glider normalized mapping error during ASAP VPE. The mapping error was computed using decorrelation lengths  $\sigma = 22$  km and  $\tau = 2.2$  days and noise covariance equal to 10% of  $\sigma_0$ . (a) Snapshot from 9:00 GMT on August 15 shows that mapping error is suppressed along Slocum tracks and elevated between and inside tracks; (b) snapshot from 9:00 GMT on August 18 (after adaptation of GCT), shows that mapping error is more uniformly suppressed in the region covered by the overlapping tracks.

six Slocums form two nearly-synchronized subgroups.

The scout-glider adaptation demonstrates how a glider can be used to sample outside the mapping domain without compromising mapping performance either inside or on the boundary of the mapping domain [201]. We computed mapping error of the Slocum glider profiles, with decorrelation lengths  $\sigma = 22$  km and  $\tau = 2.2$  days and noise covariance equal to 10% of  $\sigma_0$ . The flow is assumed to have zero mean and unit variance. The mapping error at 9:00 GMT on August 15 is shown in Figure 9.7(a) and again, three days later, in Figure 9.7(b). A time series of the mapping performance is plotted in Figure 9.8. The time series shows no degradation of performance after the GCT was adapted.

The scout-glider adaptation also reveals an interesting feature of the mapping error generated by gliders assigned to overlapping tracks. Before adaptation, the mapping error was suppressed along both Slocum tracks and elevated between and inside the tracks as shown in Figure 9.7(a). After the adaptation, the mapping error was suppressed along all

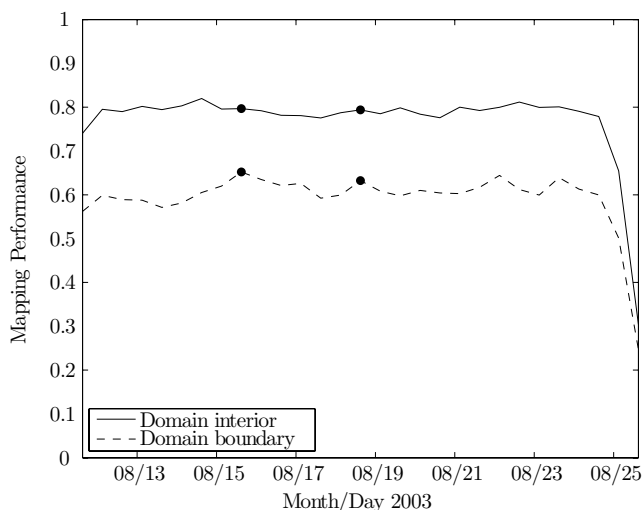


Figure 9.8: Slocum mapping performance  $\mathcal{I}(t)$  during ASAP VPE. The black dots correspond to the snapshots of the mapping error illustrated in Figures 9.7(a) and 9.7(b). Mapping performance is elevated with low variation throughout the VPE, suggesting good coordination performance. Adaptation of the GCT, which occurred at 9:00 GMT on August 15, had no observable effect on the mapping performance either inside the domain or on its boundary.

three tracks in proportion to the number of gliders on the track and partially suppressed inside the two overlapping tracks, shown in Figure 9.7(b). This phenomenon suggests overlapping tracks as a track-placement strategy that more uniformly suppresses mapping error throughout the domain. This strategy requires neither faster gliders nor more of them.

VPEs conducted in light and moderate flow yielded glider trajectories close to the desired tracks. The results from subsequent VPEs conducted in more severe flow conditions, imply that the main challenge to coordination performance of suitably configured gliders is from ocean currents. This observation is supported by the results from the ASAP 2006 field experiment, described next.

### 9.3 ASAP 2006 Field Experiment

The ASAP 2006 field experiment (FE), conducted during the month of August, incorporated a heterogeneous group of autonomous and manned sensor platforms, including gliders,

AUVs, aircraft, ships, satellites, and moorings. During the FE a fleet of four Sprays—SIO05, SIO11, SIO12, and SIO13—were operated under semi-autonomous control with manual assistance by R. Davis at SIO for 44 days from July 21 to September 2. The Spray gliders, deployed from Moss Landing inside Monterey Bay, mostly adhered to tracks along the boundary of the mapping domain in accordance with the default sampling plan shown in Figure 9.2(a).<sup>5</sup>

A fleet of six Slocum gliders—*we05*, *we07*, *we08*, *we09*, *we11*, and *we12*—operated under GCCS automatic control for nearly 24 days from July 27 to August 23. On three occasions during this time period, a Slocum glider was removed from the water due to operational problems. At the end of the time period, only four Slocums gliders remained in the water. The Slocum gliders, deployed from Santa Cruz just outside the eastern corner of the ASAP mapping domain, were steered by the GCCS to a series of fourteen GCTs based on the default Slocum glider plan shown in Figure 9.2(b). Selected GCCS glider and control parameters are provided in Appendix D. The GCCS simulator was also used to predict glider motion in real-time ocean forecasts, although these results are not described here.

When in the water, both Spray and Slocum gliders collected profiles as described in Section 2.1, except for intermittent lapses. The profile times for all gliders are plotted in Figure 9.9. Profiles contained in the gray box were collected by gliders under GCCS automatic control. The collection of profiles by glider *we08* stopped for several days during the first week of August. This lapse was caused when the glider detected a water leak and was pulled out of the water. Slocum glider *we12* stopped collecting profiles when it was recovered on August 12 after a rudder-fin failure. A water leak was detected by glider *we07* on August 19 and, due to concerns that all of the Slocum gliders were susceptible to leaks, all of the active Slocum gliders were recovered.

Although no Spray glider sustained a reduction of profile collection during the experiment, on occasion a Spray glider had trouble steering in shallow water with high flow speeds. On several occasions, a Spray glider deviated substantially from its desired track,

---

<sup>5</sup>For a description of the Spray steering algorithm, see [66].

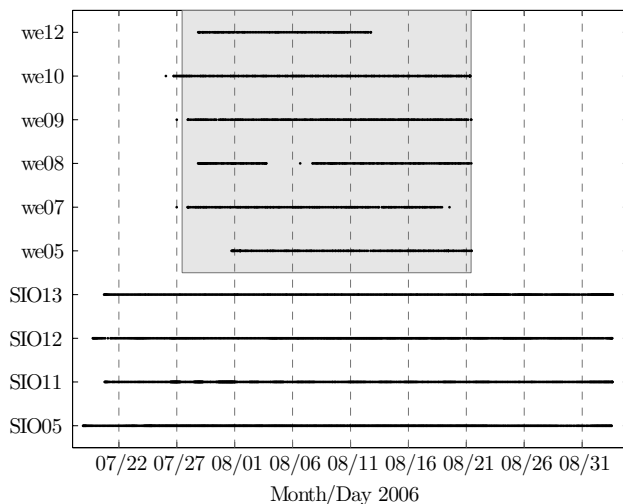
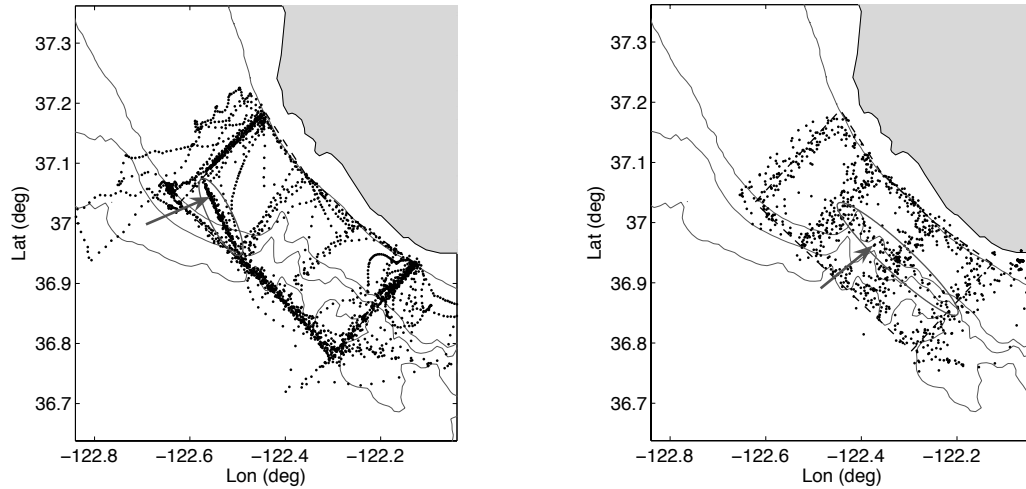


Figure 9.9: Times of glider profiles collected during ASAP 2006 FE. Profiles contained in gray box were collected by a glider under automatic control of the GCCS. Glider *we08* temporarily stopped collecting profiles for a several days starting August 2 due a water leak; *we12* stopped collecting profiles and was recovered on August 12 due to a rudder-fin failure. All of the active Slocum gliders were recovered on August 21. Spray gliders suffered no reduction of profile collection during nearly six weeks in the water.

or was not able to make progress along its track, in moderate to strong flow conditions. The profile locations for both Spray and Slocum gliders are shown in Figure 9.10. Spray gliders travelled primarily on the boundary of the mapping domain. Profiles collected outside of the mapping domain are evidence of large deviations from the desired track (some profiles south of the domain were collected during deployment and recovery).

The number of Spray glider profiles shown in Figure 9.10(a) exceeds the number of Slocum glider profiles in Figure 9.10(b) for two reasons: (i) the Spray gliders were in the water longer overall; and (ii) a Spray glider makes only one inflection per dive, whereas a Slocum glider makes multiple inflections per dive. Only one profile per dive was uploaded to a glider data server during the experiment by a glider of either type.

Two major adaptations of the default glider sampling plan are visible in Figure 9.10. First, a line of Spray profiles cuts diagonally across the northwestern corner of the mapping domain (see Figure 9.10(a)). Starting early in August, this line was patrolled by Spray gliders in lieu of the original boundary. The second major adaptation is a line of Slocum



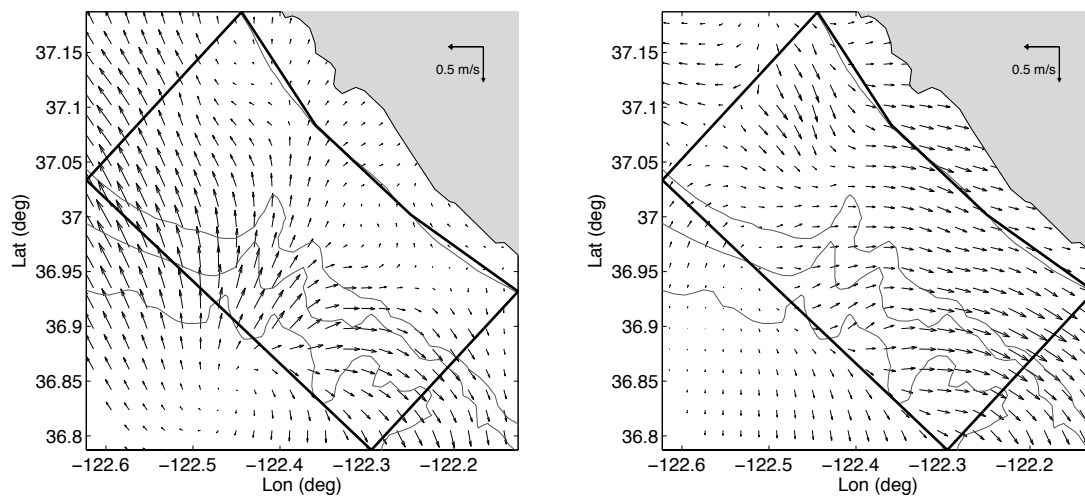
(a) ASAP FE Spray glider profile locations

(b) ASAP FE Slocum glider profile locations

Figure 9.10: Locations of glider profiles collected during ASAP 2006 FE. (a) Spray gliders collected profiles primarily on the boundary of the ASAP box. Profiles north or west of the mapping domain were collected during large, current-induced deviations from the desired track. Profiles collected along the modified domain boundary are contained in a gray ellipse marked with an arrow. (b) Slocum gliders collected profiles inside the mapping domain and on its boundary. Slocum gliders reported fewer profiles during the experiment than Spray gliders. Profiles collected over the canyon head are contained in a gray ellipse marked with an arrow.

profiles bisecting the original two, southern tracks (see Figure 9.10(b)). Profiles on this line were collected by Slocum gliders on four smaller tracks, each half as large as an original track. The tracks were created so gliders might be able to detect cold water upwelling over the top of the canyon head in the south-central portion of the mapping domain. Slocum gliders were assigned to the four new tracks during the period August 11–16.

The ocean circulation during the FE consisted of the following two transitions: from upwelling to relaxation and, then, from relaxation to upwelling [216]. A snapshot of the depth-averaged flow in the mapping domain during the relaxation-to-upwelling transition is shown in Figure 9.11(a). A snapshot of upwelling flow is shown in Figure 9.11(b). Both snapshots were generated from Spray and Slocum depth-averaged flow estimates using OA with decorrelation lengths  $\sigma = 22$  km and  $\tau = 2.2$  days and noise variance equal to 10% of the process variance  $\sigma_0$ . The flow is assumed to have zero mean and unit variance. During



(a) ASAP FE OA flow, 17:00 GMT August 8

(b) ASAP FE OA flow, 00:00 GMT August 11

Figure 9.11: Two snapshots of the ocean circulation during the ASAP FE. The flow vector field was computed from glider depth-averaged flow estimates using OA with  $\sigma = 22$  km and  $\tau = 2.2$  days and noise variance equal to 10% of the process variance  $\sigma_0$ . The flow is assumed to have zero mean and unit variance. (a) Flow transition from relaxation to upwelling advected gliders out of the mapping domain; (c) equatorward flow indicative of an upwelling.

the bifurcating flow condition shown in Figure 9.11(a), it was particularly challenging to keep gliders in the domain. Gliders in the northern-half of the domain were advected north and west and gliders in the southern-half of the domain were advected south and east. The flow snapshot in Figure 9.11(b) shows equatorward flow indicative of upwelling activity.

Strong and highly variable flow conditions such as the ones shown in Figure 9.11 presented a major challenge to steering the gliders along their assigned tracks with the desired spacing. We plot in the top two panels of Figure 9.12(a) the frequency distribution of flow speed and direction, respectively, measured by the Slocum gliders during the period of GCCS activity from July 27 to August 23. Approximately 80% of the measured flow speeds were less than 0.27 m/s. However, 10% of the measured flow speeds exceeded 0.32 m/s, which is the Slocum glider effective speed predicted by the GCCS. Note that the frequency distribution of flow direction is bimodal: the most common flow direction was poleward (along the shore) and the second-most common flow direction was onshore. This suggests

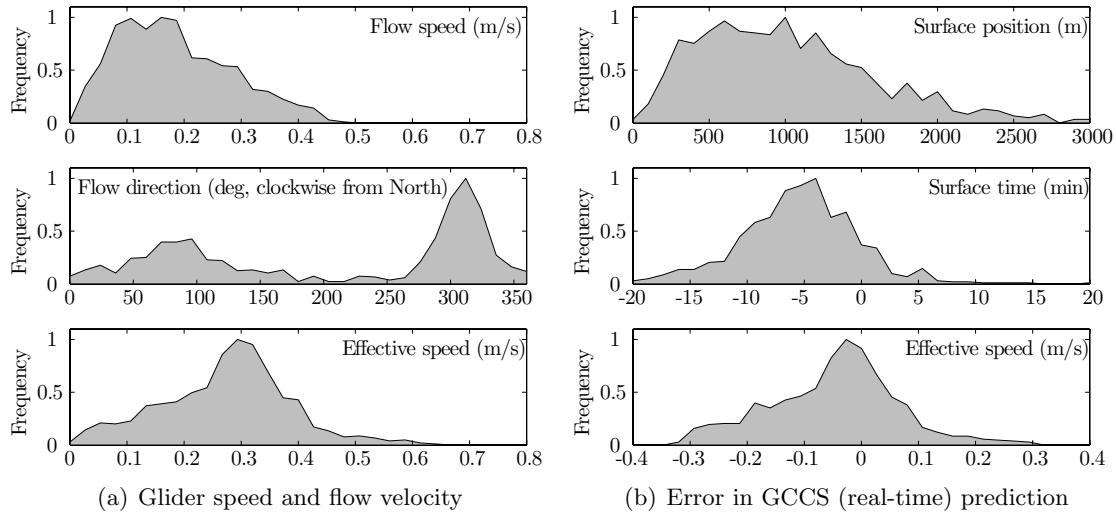


Figure 9.12: ASAP FE flow velocity and GCCS prediction accuracy. Each frequency distribution is scaled by its mode frequency. (a, top) Depth-averaged flow speed estimated by Slocum gliders during period of GCCS activity; (a, middle) distribution of depth-averaged flow directions is bimodal: flow was predominantly poleward with less frequent onshore component; (a, bottom) Slocum glider effective speed ranged from zero to more than 0.6 m/s. (b, top) GCCS errors in predicting Slocum glider surface position; (b, middle) Distribution of GCCS errors in predicting Slocum glider surface time shows a negative bias of 5 minutes; (b, bottom) Distribution of errors between Slocum glider effective speed and GCCS prediction (0.32 m/s).

that upwelling activity—characterized by equatorward flow—was relatively weak.

The frequency distribution of Slocum glider effective speed during the ASAP FE is shown in the bottom panel of Figure 9.12(a). The mode of this distribution is 0.3 m/s. Effective speeds less than 0.3 m/s occurred more frequently than effective speeds greater than 0.3 m/s. This implies that Slocum gliders spent more time traveling against the flow than they spent traveling with it. Effective speed decreases when a glider travels in the opposite direction of the prevailing ocean currents; it increases when a glider travels in the same direction as the current.

Strong and highly variable flow generates large errors in the GCCS prediction of where and when a glider will surface. We plot in the top two panels of Figure 9.12(b) the frequency distributions of errors in the GCCS prediction of glider surface position and time. Approximately 80% of the surface position errors were less than 1.6 km. However, 10% of

the surface position error exceeded 2 km. The frequency distribution of errors in surface time shows a negative bias of 5 minutes. That is, the most frequent error in the GCCS prediction of when a glider would surface was 5 minutes later than the actual surface time. Despite this bias, 80% of the surface time errors were less than 10.7 minutes. In the bottom panel of Figure 9.12(b), we show the frequency distribution of errors in predicting effective speed, which is the difference between glider effective speed and the GCCS prediction of 0.32 m/s (see Table D.1).

We examine the impact of strong flow and GCCS prediction errors on the coordination performance of the Slocum gliders in the next section. Coordination performance measures the degree to which the gliders achieved the configuration specified in the GCT. Since the GCTs were designed to collect measurements with sufficient spatial and temporal separation, good coordination performance results in good mapping performance. And, conversely, poor coordination performance leads to poor mapping performance. We discuss ASAP FE glider mapping performance and its relation to glider coordination performance in Section 9.3.2.

### 9.3.1 Evaluation of Coordination Performance

During the ASAP 2006 FE, the GCCS controlled up to six Slocum gliders continuously for nearly 24 days using fourteen GCTs. A timeline of the GCTs used during the ASAP FE is shown in Figure 9.13. Some GCTs lasted less than a day; the longest GCT lasted 4.1 days (GCT #11). During each GCT, the GCCS automatically coordinated three to six Slocum gliders to converge to their assigned tracks with the desired spacing. In this section, we focus on evaluating the performance of the GCCS during three GCTs: #6, #9, and #11. We also summarize selected GCT adaptations before or after each of these three GCTs.

Operational reasons often motivated GCT adaptation to improve mapping performance, such as when a glider was deployed, recovered, or not functioning properly. GCTs #1–3 were used to transition the Slocum gliders from their initial deployment location into the default Slocum sampling pattern shown in Figure 9.2(b). During this time, we08 detected

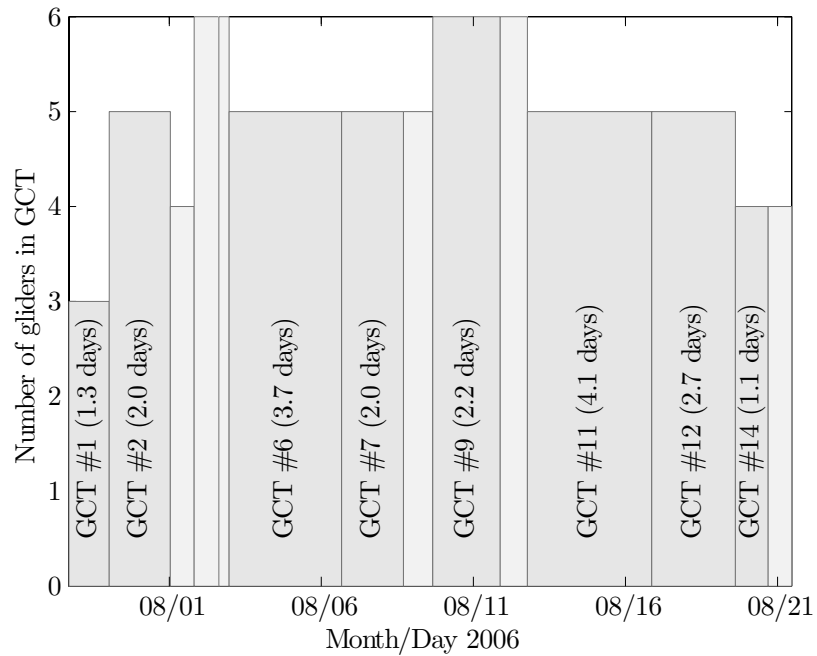


Figure 9.13: Timeline of GCTs used by the GCCS to control Slocum gliders during ASAP 2006 FE. The GCT was adapted to improve mapping performance in response to changes in the ocean features, such as the onset of upwelling, and for operational reasons, such as when a glider was deployed, recovered, or not functioning properly. GCTs lasting less than one day are shaded light gray and not labeled.

a water leak and went under manual control, which is why GCT #3 shows a reduction in number of gliders from five to four. All six Slocum gliders were under GCCS control GCTs #4 and #5, although we08 was subsequently recovered to repair the water leak. Glider we08 returned to the water starting with GCT #9. At the start of GCT #11, we12 was placed under manual control due to a rudder-fin failure; it was immediately recovered and taken out of the water for the rest of the experiment. Glider we07 was placed under manual control during GCT #14 and #15 due to leak indications.

Each GCT can be viewed as a mini-experiment, during which the GCCS steered the gliders around a set of tracks with prescribed spacing measured along the tracks. We can quantitatively evaluate the coordination performance of the GCCS during each GCT using the following metrics, illustrated in Figure 9.14.

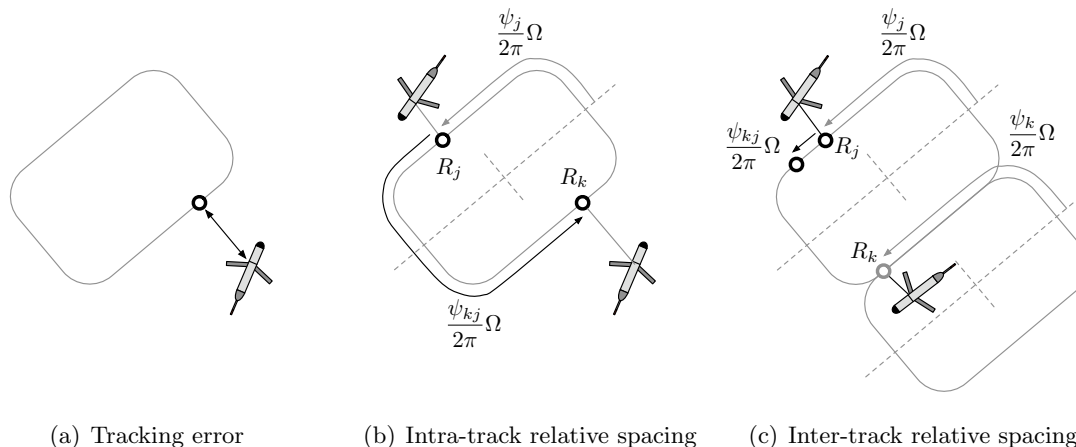


Figure 9.14: Metrics of coordination performance. (a) The tracking error is the shortest distance between a glider and its assigned track. (b) The spacing error between two gliders on the same track is proportional to the difference between the desired and actual curve-phase measured between the gliders along the track (in this case the desired relative curve-phase is  $\pi$ ). Spacing error is illustrated here by the relative spacing  $(\psi_{kj}/2\pi)\Omega$  of points  $R_k$  and  $R_j$ , where  $\Omega$  is the track perimeter. (c) The spacing error between two gliders on different tracks is proportional to the difference between the desired and actual curve-phase of point  $R_k$  relative to  $R_j$  (in this case the desired relative curve-phase is 0).

**Definition 9.1. Tracking error** *The tracking error of a glider at time  $t$  is the shortest distance between the glider and its assigned track at time  $t$ .*

The tracking error of a glider, which has units of distance, is a measure of its track-following accuracy only if the closest point on the track is where the glider is trying to go. For example, the tracking error may not be a good metric for a glider in the interior of a very skinny track, when the closest point on the track is actually on the opposite side of where it is trying to go. Such a situation did not occur during the ASAP FE.

**Definition 9.2. Spacing error** *Consider two gliders labeled  $k$  and  $j$ . Suppose the gliders are assigned to tracks 1 and 2, respectively, with a desired relative curve-phase  $\bar{\psi}_{kj}$  (see Sections 7.3 and 8.1); tracks 1 and 2 must have the same perimeter, but they may have different shapes, locations, or orientations. Let  $R_k$  denote the point on track 1 closest to glider  $k$  at time  $t$  and  $R_j$  denote the point on track 2 closest to glider  $j$  at time  $t$ . The*

spacing error between gliders  $k$  and  $j$  at time  $t$  is

$$|(\psi_{kj} - \bar{\psi}_{kj} + \pi) \bmod (2\pi) - \pi|/\pi,$$

where  $\psi_{kj} \triangleq \psi_k - \psi_j$  is the curve-phase  $\psi_k$  of  $R_k$  relative to the curve-phase  $\psi_j$  of  $R_j$ .

Although Definitions 9.1 and 9.2 are, by design, independent of the control algorithm used during the ASAP FE, they do depend on some of the notations and assumptions introduced in Section 7.3. For example, Definition 9.2 is subject to the assumption that each track is a smooth, closed loop. To evaluate the spacing error, which is a number in the interval  $[0, 1]$ , each point on  $C$  is mapped from local  $r_k$  to geodetic  $R_k$  coordinates using the transformations in Appendix C. The curve-phase  $\psi_k$  of  $R_k$  equals the curve-phase of  $r_k$ .

We start our analysis of coordination performance with GCT #6, which was active for 3.7 days from 23:15 GMT August 2 to 16:05 GMT August 6. During this time, the GCCS steered five gliders around three tracks as shown in Figure 9.15(a). Gliders **we10** and **we12** were assigned to travel clockwise around the northern track with relative curve-phase  $\pi$ , **we07** and **we09** were assigned to travel clockwise around the middle track with relative curve-phase  $\pi$ , and **we05** was assigned to travel clockwise around the southern track. In addition, the curve-phase of each glider on the northern track relative to the curve-phase of either glider on the middle track was specified to be zero. A snapshot of the glider trajectories and depth-averaged flow measurements for the 24 hours preceding 6:00 GMT August 4 is shown in Figure 9.15(b). Gliders **we07** and **we09** have good spacing. The spacing error between **we10** and **we12** increased when **we12** was pushed by a poleward current across the deep end of the northern track in just two dives and, simultaneously, the progress of **we10** across the shallow end of the track was impeded by poleward flow near the shore.

The poleward flow in the mapping domain became increasingly strong during GCT #6. This process, indicative of relaxation, ultimately led to adaptation of the GCT. Each glider's effective speed is shown in Figure 9.16, along with its depth-averaged flow measurements. The glider effective speed fluctuates around its predicted value of 0.32 m/s, ranging from over 0.5 m/s when traveling with the flow, to nearly zero when traveling against the flow. We

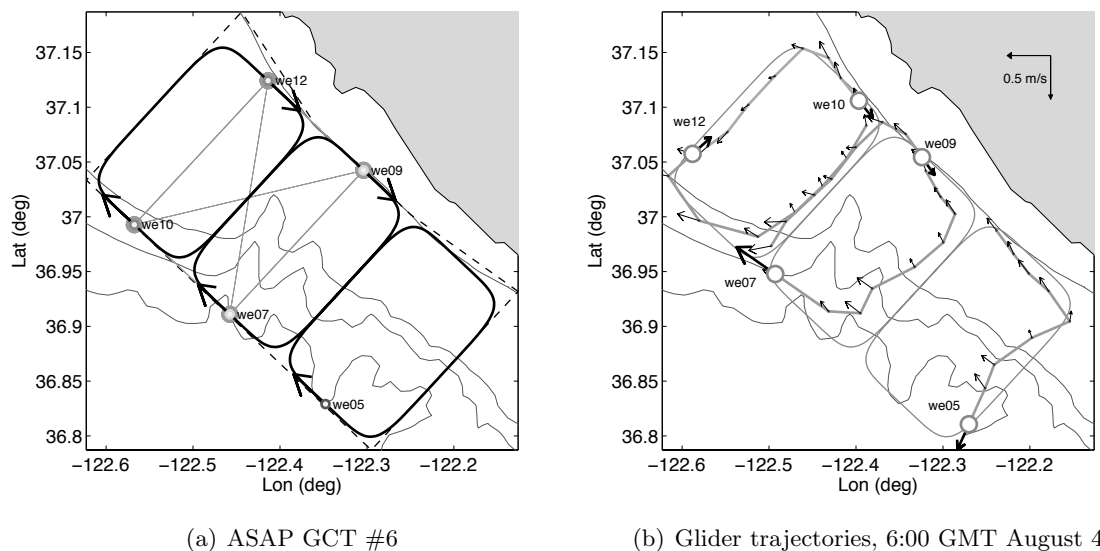


Figure 9.15: Slocum glider trajectories and depth-averaged flow measurements during ASAP 2006 FE GCT #6. (a) All of the gliders were steered clockwise around three different tracks; the relative curve-phase of gliders we07, we09, we10, we12 was also controlled by the GCCS to achieve the desired pattern. (b) Trajectories (gray lines) and flow measurements (thin black arrows) shown for 24 hour period prior to 6:00 GMT August 4; each glider's effective speed is indicated by a thick black arrow. Glider coordination performance, while initially good, was eventually degraded by strong poleward flow.

observe that the effective speed is nearly zero for four out of five gliders at the conclusion of GCT #6 (identified in Figure 9.16 by a vertical line on day 3.7). All of the gliders got stuck on the shallow end of their tracks when they tried to head equatorward against the flow. We reversed the direction of rotation of all of the gliders from clockwise to counterclockwise in GCT #7. The idea was to take advantage of the strong poleward flow near shore and have the gliders combat the poleward flow in deep water, where it appeared weaker.

When glider forward progress was impeded by the flow, coordination performance deteriorated. We plot for GCT #6 the tracking error in Figure 9.17(a) and the spacing error in Figure 9.17(b). For the first three days of GCT #6, tracking error for all of the gliders was less than two kilometers, except for short periods. Likewise, during this time, the intra-track spacing error of glider pairs we10/we12 and we07/we09, shown in the top of Figure 9.17(b), remained under 40%, and, on three occasions, dropped nearly to zero. Other than one

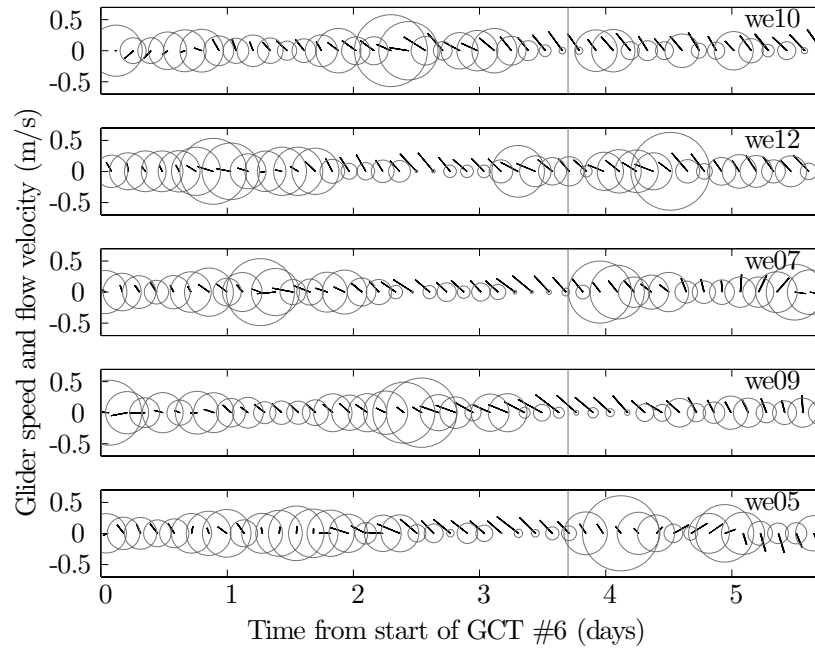


Figure 9.16: Slocum glider speed and depth-averaged flow velocity during GCT #6. Glider effective speed at time  $t$  is denoted by the radius of the circle centered at time  $t$  and speed 0. The depth-averaged flow velocity at time  $t$  is depicted by a black line with one end at time  $t$  and speed 0; the length of the line is the speed and its orientation corresponds to the orientation of the flow velocity (that is, up is north and right is east). By day 3, the forward progress of all of the gliders had been substantially impeded by strong poleward flow, which prompted adaptation of the GCT at time  $t = 3.7$  days (vertical black line). In GCT #7, gliders reversed direction and experienced an initial burst of speed when they were advected by the flow.

brief spike on day 1, the inter-track spacing error of glider pairs we10/we09 and we07/we12 during the first three days also remained under 40%. Large tracking and spacing errors on the third day prompted us to switch the GCT.

When the gliders reversed direction of rotation under GCT #7 (see Figure D.1(b)), coordination performance partially recovered. We see in Figure 9.17(a) that, after day 3.7, the tracking error of we07 remains low and the tracking error of we09 shrinks. After day 5, the spacing error of this glider pair also recovers. However, the tracking and spacing errors for the gliders we10 and we12 did not recover under GCT #7, prompting the switch to GCT #8. Under GCT #8 (see Figure D.1(c)) gliders we10 and we12 were briefly sent in opposite directions around the northern track to quickly recover proper separation.

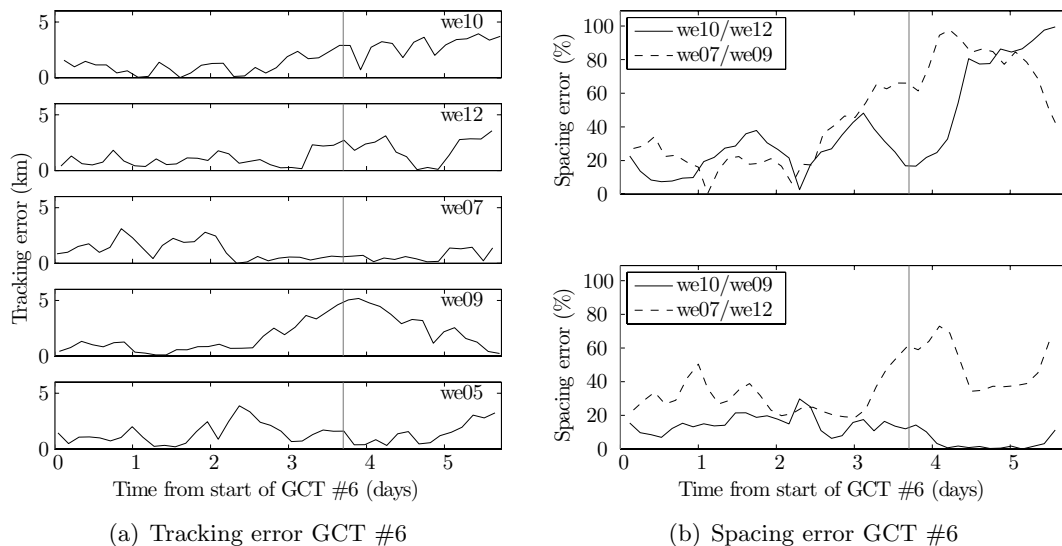
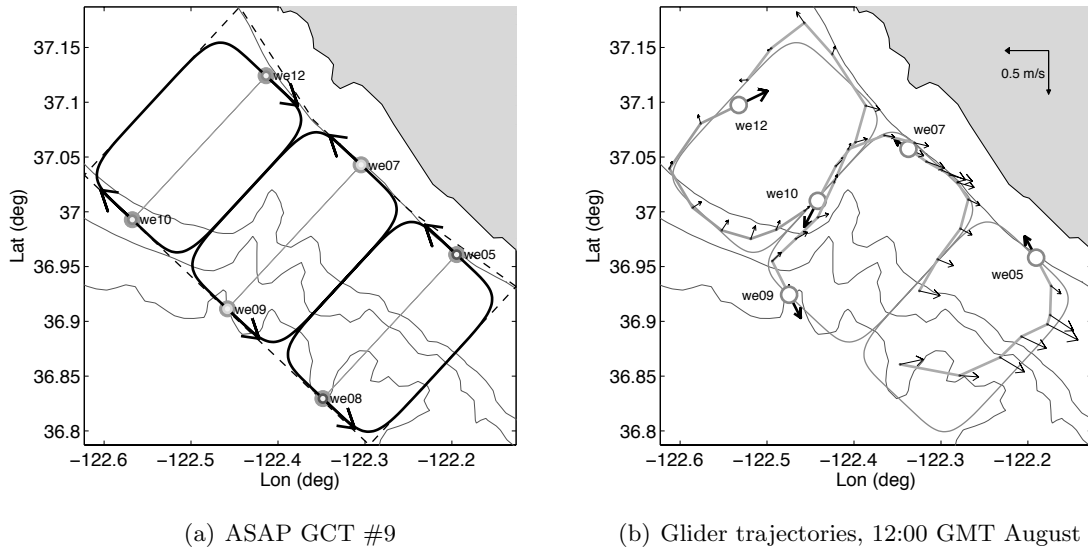


Figure 9.17: Coordination performance of Slocum gliders during GCT #6. The start of GCT #7 is shown by a dotted vertical line at  $t = 3.7$  days. (a) Until  $t = 3$  days, tracking error of all gliders remained less than two kilometers, except for short periods; (b, top) until  $t = 3$  days, intra-track spacing error remained under 40%; (b, bottom) except for one spike on day 1, inter-track spacing error from  $t = 0$  days to  $t = 3$  days also remained under 40%. Gliders reversed direction under GCT #7, which started at  $t = 3.7$  days; we07 and we09 recovered good coordination performance, but we10 and we12 did not.

The GCCS achieved good glider coordination performance during GCT #9, which ran for 2.2 days from 16:00 GMT August 9 to 21:09 GMT August 11. GCT #9 marked the return of glider we08 to GCCS control, its leak repaired. Under GCT #9, the GCCS steered all six Slocum gliders to three tracks as shown in Figure 9.18(a). The GCT specified three glider pairs—we10/we12, we07/we09, and we05/we08—to have relative curve-phase of  $\pi$ . Each glider pair was assigned to a different track and there was no inter-track coordination.

During GCT #9, there was moderate onshore and weak poleward flow in the western and north portions of the mapping domain, respectively. Strong equatorward flow in the southeastern corner was indicative of a transition to upwelling. The glider trajectories and depth-averaged flow measurements for the 24 hour period prior to 12:00 GMT August 11 are shown in Figure 9.18(b). Glider we08, initially located near the southern corner of the mapping domain, is not visible in this figure, having been advected by the flow to a location southeast of the mapping domain. We observe in Figure 9.19 that the effective



(a) ASAP GCT #9

(b) Glider trajectories, 12:00 GMT August 11

Figure 9.18: Slocum glider trajectories and depth-averaged flow measurements during ASAP 2006 FE GCT #9. (a) Three glider pairs were assigned to have intra-track relative curve-phase of  $\pi$  with no inter-track coordination; (b) other than for we08, which was advected by strong equatorward flow out of view to the southeast, tracking error is low and spacing error on the middle and northern tracks is low.

speed of we08 was reduced to nearly zero for over 12 hours. When we08 slowed down, we05 actually cut across the southern corner of the southern track and “passed” we08, meaning the curve-phase of we05 relative to we08 changed sign. No glider other than we08 experienced prolonged interruptions of forward progress during GCT #9.

Coordination performance, depicted in Figure 9.20, recovered during GCT #8 and remained good during GCT #9, except for gliders we05 and we08. Tracking error for the four gliders on the middle and northern tracks was less than two kilometers. We observe in Figure 9.20(b) that spacing error was below 10% for we10 and we12, orbiting the northern track in the weakest flow, whereas spacing error was between 10% and 40% for we07 and we09, orbiting the middle track in moderate, bifurcating flow. Spacing error was the worst for we05 and we08, situated on the southern track in the strongest flow. Spacing error for these two gliders did recover by the end of GCT #9, after we05 passed we08 and we08 returned to the track.

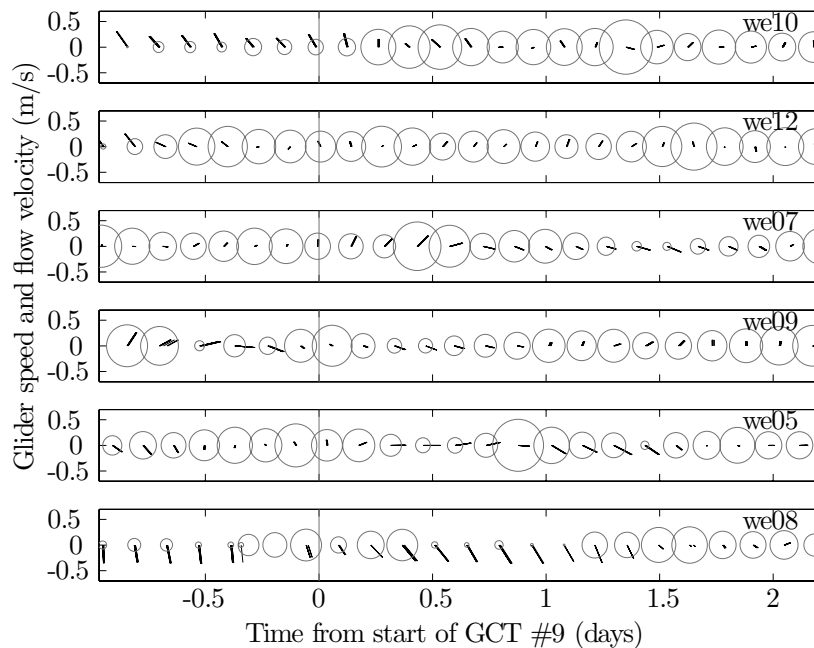


Figure 9.19: Slocum glider speed and depth-averaged flow velocity during GCT #9. This period of the FE was characterized by strong equatorward flow in the southern portion of the mapping domain, which reduced nearly to zero the effective speed of we08. Moderate onshore and weak poleward flow in the middle and northern portions of the domain did not substantially impair the forward progress of gliders deployed there.

The adaptation from GCT #9 to GCT #10, shown in Figure D.2(a), was initiated by an ocean science objective and affected only the two gliders on the middle track. The ASAP team proposed to split the middle track into two smaller tracks, so that gliders would sample the along-shore line bisecting the original middle track. This bisecting line follows the canyon head, the region where cold water was presumed to be emerging. The hypothesis that this is where cold water was emerging would be tested by gliders we07 and we09 collecting profiles along each of the new tracks. Later, during GCT #12, the southern track would be similarly split into two more new tracks orbited by we05 and we08 (see Figure D.2(b)).

GCT #10, which ran for less than a day, was adapted to GCT #11 shown in Figure 9.21(a), when we12 sustained a terminal failure of its rudder-fin. During GCT #11, which ran for 4.1 days from 18:26 GMT August 12 to 20:47 GMT August 16, we10 orbits

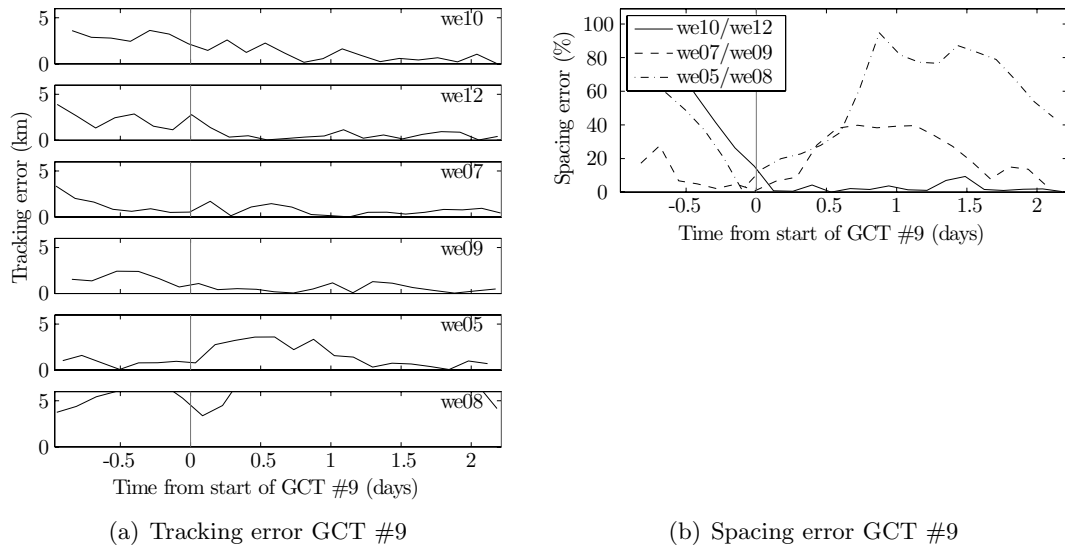


Figure 9.20: Coordination performance of Slocum gliders during GCT #9. The start of GCT #9 is depicted by the vertical line at  $t = 0$  days. (a) The tracking error of the four gliders on the middle and northern tracks declined during GCT #8 to less than two kilometers during GCT #9, whereas the tracking error of we05 and we08 exceeded five kilometers; (b) intra-track spacing error between glider pairs was best on the northern track, where there was weak flow, and worst on the southern track, where the flow was strong. There was no inter-track coordination during GCTs #8 or #9.

the northern track alone. All of the other track assignments and coordination are the same in GCT #11 as in GCT #10: we07 and we09 were assigned to orbit with relative curve-phase 0 the two small tracks circumscribed by the original middle track; we05 and we08 were assigned to orbit the large, southern track with relative curve-phase  $\pi$ .

The GCCS achieved high coordination performance during GCTs #10 and #11 in the presence of moderate, onshore flow. Figure 9.22, which shows glider effective speed and depth-averaged flow measurements, indicates only one moment of halted progress, sustained by we05 in onshore flow on the first day. Other gliders experienced only mild fluctuations of effective speed. Glider we05 halted, not because of flow conditions, but because of an interruption in satellite communication.<sup>6</sup> Nonetheless, tracking error for all gliders, shown

<sup>6</sup>When we05 recovered communication, it downloaded GCCS waypoints based on we05's last reported surface position. Since we05's last reported surface position was several dives old, these waypoints caused we05 to backtrack for one dive. This sequence of events led to the following addition to the GCCS waypoint quality control (QC): waypoints fail QC if the last known surface position of the glider is outdated.

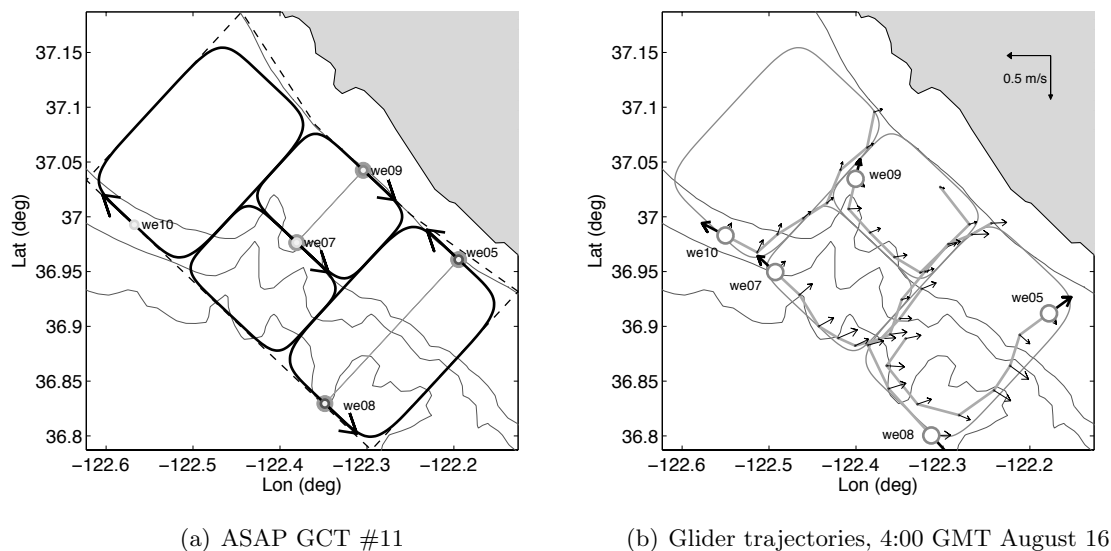


Figure 9.21: Slocum glider trajectories and depth-averaged flow measurements during ASAP 2006 FE GCT #11. (a) Gliders we07 and we09 are assigned to orbit with synchronized curve-phases two new tracks designed to collect profiles across the canyon head; (b) good coordination performance in the presence of moderate, onshore flow.

in Figure 9.23(a), was consistently less than two kilometers. The intra-track spacing error of we05 and we08, plotted in the top of Figure 9.23(b), experienced a temporary surge when the forward progress of we05 was impaired; it subsequently recovered to less than 30%. The inter-track spacing error of we07 and we09, shown in the bottom of Figure 9.23(b), decreases sharply during GCT #8 and remains below 40% during GCT #11. This figure nicely illustrates the GCCS “step” response to adaptation of the GCT from #9 to #10.

Subsequent GCT adaptation after GCT #11 occurred with the intent to first split and then widen the southern track. GCT #12, shown in Figure D.2(b), split the southern track into two, smaller tracks, that, like the smaller tracks in GCT #11, were designed to allow gliders to sample along the canyon head in the along-shore direction. In this GCT, four gliders were assigned to orbit with synchronized curve-phases the four small tracks, that is, the desired inter-track curve-phase of any one of these gliders relative to any other glider was zero. Execution of GCT #12 ended after 2.7 days when we07 broadcast a leak warning and was recovered. GCT #13 was created but never used. In GCT #14, shown

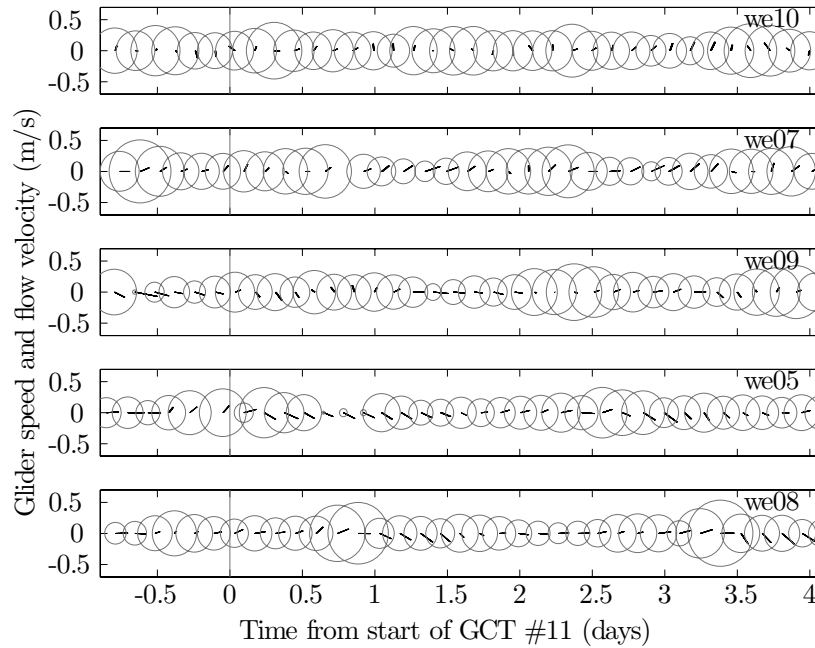


Figure 9.22: Slocum glider speed and depth-averaged flow velocity during GCT #11. Only we05 sustained an interruption of forward progress, due to communication problems, which occurred between  $t = 0.5$  day and  $t = 1$  day.

in Figure D.2(c), we09 returned to the large, middle track for just over a day. GCT #15, which lasted less than a day, was the final GCT. It addressed the ASAP team proposition to collect profiles outside the mapping domain by moving 10 km to the southwest the small, southernmost track (see Figure D.2(d)).

### 9.3.2 Evaluation of Mapping Performance

We evaluate the glider mapping domain during the ASAP FE both inside the domain and on its boundary by plotting separately the mapping performance of Slocum gliders and Spray gliders in Figures 9.24(a) and 9.24(b), respectively. The mapping performance of all of the gliders is plotted in 9.24(c). In all three figures, the period when the GCCS was active, which corresponds to the period when the Slocum gliders were in the water, is colored gray. The Slocum glider mapping performance dipped when the Slocum glider coordination was poor and it recovered when coordination performance improved.

Figure 9.24(a) shows that the Slocum gliders achieved a relatively high mapping perfor-

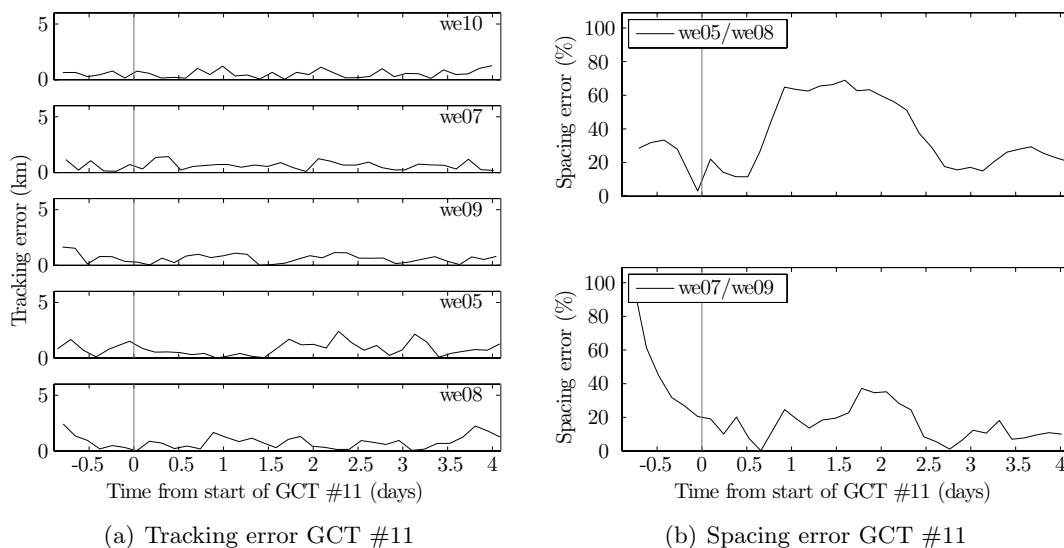
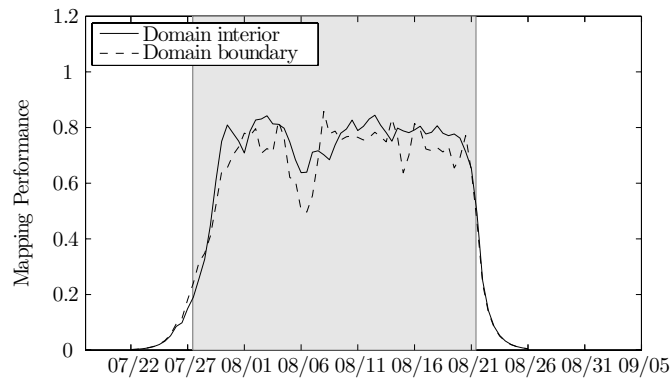


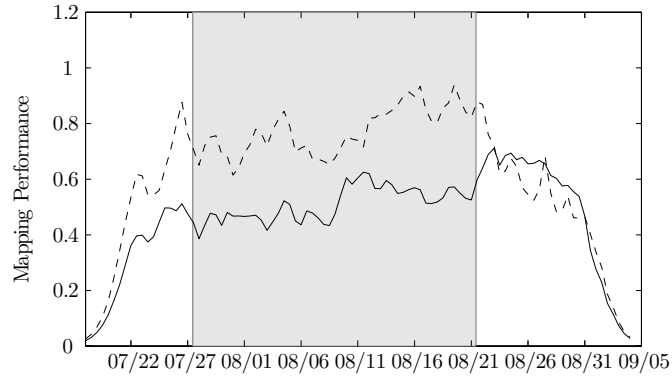
Figure 9.23: Coordination performance of Slocum gliders during GCT #11. (a) Except for short periods, tracking error was less than two kilometers for all of the gliders; (b, top) intra-track spacing error between we05 and we08 experienced a surge, then recovered, when we05 was temporarily slowed; (b, bottom) inter-track spacing error between we07 and we09 decreased rapidly and remained below 40%, illustrating the “step” response to adapting GCT #9 to GCT #10.

mance inside the mapping domain and on its boundary. In fact, the mapping performance inside and on the domain is nearly the same. As expected, the mapping performance ramps up when the gliders first enter the water at the end of July and ramps down when they were recovered around August 21. During the period of time when they were in the water, the Slocum glider mapping performance is generally level, with some fluctuations. The largest downward fluctuation occurs on August 6, during GCT #6, when coordination performance suffered due to adverse flow conditions (see discussion in previous section). The fact that mapping performance recovered subsequent to adaptation of the GCT shows how coordinated motion control can impact mapping performance. Additional connections between the Slocum glider coordination performance and Slocum glider mapping performance is the subject of ongoing analysis.

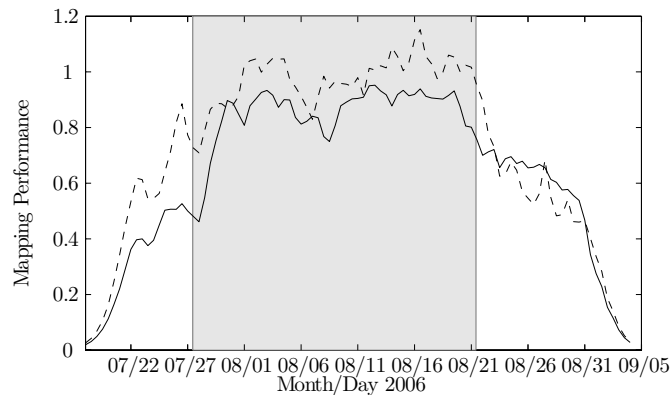
For much of the experiment, Spray glider mapping performance, plotted in Figure 9.24(b), is distinctly higher on the boundary of the mapping domain than in its interior. This result



(a) ASAP FE Slocum glider mapping performance



(b) ASAP FE Spray glider mapping performance



(c) ASAP FE combined glider mapping performance

Figure 9.24: Glider mapping performance during ASAP 2006 FE. The mapping performance ramps up when the gliders enter the water and ramps down when the gliders come out of the water. The portion of all three plots that is shaded gray corresponds to the period of time during which the GCCS was actively steering the Slocum gliders. Note mapping error is normalized to a scale from 0 to 1, but mapping performance is not (see Section 2.2).

is, of course, consistent with the Spray glider sampling plan shown in Figure 9.2(a), which dedicated the Spray gliders to patrolling tracks along the sides of the domain. The only period of time during which the mapping performance was not higher on the boundary occurred after the Slocum gliders were recovered. At this point, the Spray gliders were reassigned to tracks that sampled both the domain boundary and its interior. As a whole, the Spray glider mapping performance was much higher during the ASAP 2006 FE than during the AOSN-II experiment in 2003 (see Figure 2.12), which is due in large part to the higher profile density in 2006. There were five Spray gliders deployed during the AOSN-II experiment, versus four Spray gliders in the ASAP FE, but the AOSN-II mapping domain was nearly ten times larger than the ASAP mapping domain.

The combined mapping performance of the Spray and Slocum gliders is shown in Figure 9.24(c). During the periods of time before and after the Slocum gliders were in the water, the combined performance is equal to the Spray glider mapping performance. When both Spray gliders and Slocum gliders were in the water, the combined mapping performance is higher than the mapping performance of either the Spray gliders or Slocum gliders separately, although mapping performance does not add linearly. During this period of time, the combined mapping performance is higher on the boundary of the mapping domain than inside it. Some of the fluctuations in the Spray and Slocum mapping performance are visible in the combined mapping performance, although other fluctuations are visible too.

The degree to which the mapping performance of the Spray gliders reinforces and extends the mapping performance of the Slocum gliders depends on the positions and times of the Spray glider profiles relative to the positions and times of the Slocum glider profiles. The combined mapping performance experiences the greatest boost over the separate mapping performances when profiles in the combined set of profiles are not bunched together. The coordination of the Spray gliders, which were steered with manual intervention, and the Slocum gliders, which were steered automatically by the GCCS, is the subject of ongoing analysis. Here, we make the following simple observation: we might have been better able to match the combined mapping performance on the boundary and interior of the mapping

domain by reducing the size of the Slocum glider tracks so as to overlap less with the domain boundary. This would have tipped the balance of the Slocum mapping performance in favor of the interior so that the combined mapping performance on the boundary was better balanced with the combined mapping performance in the interior.



# Chapter 10

## Conclusion

### 10.1 Summary of Contributions

This thesis describes a cooperative control framework for stabilization of collective motion of self-propelled particles. We present and analyze a systematic and versatile design methodology to generate decentralized control algorithms that stabilize moving formations of particles with possibly limited interaction. A large family of patterns can be generated including parallel formations, circular formations, and symmetric formations on multiple, convex loops. Formation design is motivated by applications in environmental monitoring with mobile sensor platforms.

The thesis also describes a software infrastructure—the Glider Coordinated Control System (GCCS)—that uses feedback control at the level of the fleet to steer gliding underwater vehicles to a set of coordinated trajectories. We describe experimental results from an at-sea demonstration in August 2006, when the GCCS controlled six underwater vehicles continuously for nearly twenty-four days in support of an oceanographic field experiment studying coastal upwelling. This practical implementation of a theoretical methodology supports collaborative and adaptive data collection by a large fleet with minimal operator intervention. Collecting data along coordinated trajectories improves the information content of the entire data set: this information may help oceanographers develop new insights into physical

or biological processes pertinent to improving our understanding of the environment and climate change.

### 10.1.1 Control of Collective Motion

Feedback control to coordinated glider trajectories is developed using a simple model of vehicle motion, described in Chapter 3. In this model, which was studied by Justh and Krishnaprasad in the context of controlling autonomous air vehicles [126, 127], each vehicle is represented by a particle moving at a constant speed in a plane subject to steering control. A feature of the particle model emphasized in this thesis is that the orientation of a particle's velocity is described by an angle called the phase. The collection of all  $N$  phases evolves on the  $N$ -torus, a nonlinear manifold central to the study of coupled-phase oscillators. Accordingly, the particles can be viewed as having coupled-oscillator dynamics, a paradigm used throughout the thesis. Another fundamental paradigm described in Chapter 3 is the use of a graph to describe the (time-varying and directed) network of particle interactions. Each node in the graph represents a particle and each edge represents (directed) flow of information between particles. Since our cooperative control algorithms use state feedback, particles steer using information pertaining to the current state of other particles. We describe particle interaction in the theoretical framework using the matrix representation of the interaction network, called the graph Laplacian.

We use level of interaction between particles—all-to-all, undirected and time-invariant, and time-varying and directed—to classify the results for stabilization of relative equilibria of the particle model, including parallel and circular formations. In Chapter 4, we introduce and analyze control-Lyapunov algorithms for phase synchronization and balancing, which in the particle model correspond to parallel motion of all particles and motion of all particles about a fixed position centroid, respectively. The case in which each particle interacts with all other particles is addressed in Section 4.1. In this case, we show that a commonly studied model of synchronization of coupled-phase oscillators—the Kuramoto model—is a gradient system with respect to a quadratic potential, called the all-to-all phase potential. Using the

sign of the coupling gain, we can drive the phase arrangement to either the global minimum of the phase potential (phase balancing) or the global maximum (phase synchronization). The all-to-all phase potential and corresponding gradient control are extended in Section 4.2 to particles with limited, time-invariant, and undirected interaction and, in Section 4.3, to particles with time-varying and/or directed interaction. The latter section describes a dynamic algorithm to achieve synchronization and balancing on the  $N$ -torus adapted by Scardovi *et al.* from the literature on Euclidean consensus [233].

The notion of consensus on a Euclidean space applies directly to stabilization of circular formations, described in Chapter 5. In a circular formation, which is a relative equilibrium of the particle model, the particles converge to circular motion about a common point (the consensus). In Section 5.1 we describe a decentralized circular formation algorithm for all-to-all interaction. As with the phase synchronization and balancing algorithms in Chapter 4, the circular formation algorithm is extended in Section 4.2 to particles with limited, time-invariant, and undirected interaction and, in Section 4.3, to particles with time-varying and/or directed interaction. The latter section follows the development of the dynamic phase synchronization and balancing algorithm in Section 4.3, where particles incorporate into their steering control not only the relative state information of interacting particles but also shared estimates of the collective phase centroids. In the dynamic circular formation algorithm, particles compute and share estimates of the collective position centroid.

Chapter 6, which has the same structure as Chapters 4 and 5, describes cooperative control algorithms to stabilize symmetric phase patterns. Symmetric phase arrangements contain clusters of phases uniformly distributed around the unit circle. We show that, for any level of particle interaction, combining the symmetric-pattern phase control with the corresponding circular formation algorithm from Chapter 5 yields an algorithm to locally stabilize symmetric patterns of particles moving around a circle. We provide guidelines for choosing control gains that expand the basin of attraction of the desired pattern.

### 10.1.2 Sampling with Autonomous Vehicles

In order to design ocean sampling trajectories, we develop a quantitative measure of sampling performance, described in Chapter 2. This metric, based on a classical linear estimation technique called objective analysis (OA), evaluates the quantity of information concerning a multi-dimensional stochastic process contained in a set of irregularly-spaced and timed measurements. To increase the information content of a measurement set, a glider fleet should collect data at points that are distributed in space and time according to the spatial and temporal decorrelation scales of the process of interest. Basically, measurements should not be too close or too far apart. To justify this heuristic, in the introduction to Chapter 2 we describe an extended analogy between ocean sampling and lawn-mowing. In Section 2.1, we review the operational configuration of underwater gliders and provide a new comparison of the sampling capabilities of gliders and their faster-moving cousin, the propellor-driven AUV. The OA-based metric is quantitatively defined in Section 2.2, and a distinction between temporally- and spatially-constrained sensor platforms is introduced. In Section 2.3 we summarize the sampling performance of a glider fleet during a 2003 deployment, prior to the development of the GCCS. Using several numerical examples as additional motivation, we formulate a coherent strategy for adaptive sampling with a fleet of underwater gliders. This strategy prescribes automatic control of a glider fleet to coordinated motion about closed paths using a decentralized cooperative algorithm. The glider paths and coordination on those paths are selected to maximize sampling performance and can be adapted by an operator.

Algorithms yielding symmetric formations of moving particles are adapted in Chapter 7 to the application of mobile sensor networks. In Section 7.1, we introduce a virtual particle into the collective to serve as a reference. Since the dynamics of the virtual particle are unaffected by the motion of the real particles, the particle's presence breaks the rotational and translational symmetries thus far preserved by the closed-loop particle model. We show how this approach can be used to track a piecewise-linear reference trajectory, or to stabilize circular motion about a reference beacon even when particles are advected by a drift vector

field. Another symmetry of the closed-loop particle model with all-to-all interaction is invariance to permutation of particle labels. We show in Section 7.2 how the design of particle networks can be combined with multiple, virtual particles to generate algorithms that stabilize symmetric formations spanning multiple circles. The applicability of these algorithms to ocean sampling with autonomous vehicles is enhanced in Section 7.3, where we use a coupled-phase oscillator framework to describe and coordinate particle positions on convex loops other than circles. Special attention is given to a class of curves known as the superellipse, which includes circles, ellipses, and rounded rectangles.

Feedback control of a glider fleet using cooperative algorithms is synthesized by the software suite called the Glider Coordinated Control System (GCCS), described in Chapter 8. As summarized in Section 8.1, the GCCS takes as input a specification of a desired sampling pattern defined in terms of a set of glider coordinated trajectories (GCT). The glider sampling pattern is adapted when an operator changes the GCT input. To steer gliders to the GCT, the GCCS utilizes the simple model of glider motion to plan future trajectories and a detailed model to predict glider motion underwater. These models are described in Sections 8.2.1 and 8.2.2, respectively. The detailed model is a three-dimensional kinematic representation of glider motion including emulation of the glider onboard steering rules in the presence of flow. The active components of the GCCS during real-time operation are the planning and remote input/output modules. The GCCS also contains a simulation module that facilitates development and testing of glider coordinated control strategies through virtual experiments. The GCCS simulator enables software-in-the-loop and hardware-in-the-loop testing, which are both integral to the development of a control infrastructure for ocean-going systems.

Experimental results from an at-sea demonstration of the GCCS are included in Chapter 9. This demonstration was conducted in support of a multi-disciplinary research initiative called Adaptive Sampling and Prediction (ASAP). An overview of ASAP, which represents a collaborative effort of researchers from multiple universities and institutions, is presented in Section 9.1. ASAP researchers seek to develop strategies for optimal asset

distribution for environmental monitoring and prediction, such as the one formulated in Section 2.3. This strategy was tested in March 2006 during a virtual pilot experiment with the GCCS acting as both glider planner and glider simulator, as described in Section 9.2. Because this pilot experiment was conducted virtually, it helped prepare participants for the subsequent field experiment without the additional cost or complexity of running a pilot experiment in the field. During the August 2006 ASAP field experiment, the GCCS operated with minimal operator intervention and no major errors or failures. We describe this experiment in Section 9.3, focusing on quantifying the performance of the glider fleet using both the OA-based metric and novel coordination metrics. This analysis illustrates the role of GCT adaptation in responding to flow conditions and oceanographic objectives.

## 10.2 Ongoing and Proposed Work

This thesis is structured to follow a smooth arc from theory to application: principles from cooperative control are developed and put into practice in an underwater mobile sensor network. The pairing of theory and application is not, however, a perfect fit. There are a number of practical challenges to increasing the autonomy of underwater vehicles not yet addressed in our theoretical framework. Some of these challenges are described in Section 10.2.1. Although the framework is deficient in some ways, in other ways it surpasses the demands of this application. We summarize in Section 10.2.2 ongoing and proposed work on the application of our cooperative control framework to the study of interaction networks in biological collectives.

### 10.2.1 Increasing Autonomy of Underwater Gliders

Autonomy enables gliders to operate collaboratively with high sampling performance and without operator intervention. One contribution of this thesis is to increase glider autonomy by designing and demonstrating a prototype system—the GCCS—for automating fleet-level coordination (see Figure 10.1). The GCCS, which runs on a computer on shore, steers gliders to a set of operator-specified trajectories by generating waypoints, which are the

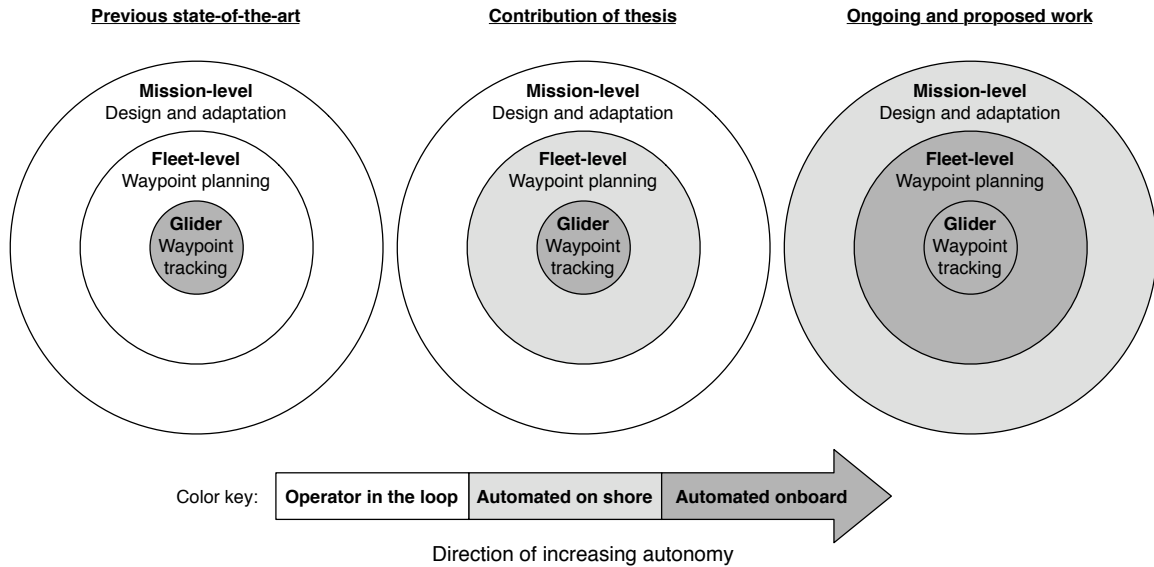


Figure 10.1: Increasing autonomy of underwater gliders. The control system onboard each glider automatically steers it along a list of waypoints, which are traditionally planned manually by an operator. As described in this thesis, automating fleet-level waypoint planning reduces the demand for operator intervention and may improve sampling performance. Glider autonomy can be further increased by migrating waypoint planning onboard, and developing automated algorithms for mission-level design and adaptation.

latitude and longitude coordinates of a destination point. We propose to further increase glider autonomy in two ways, illustrated in Figure 10.1: (i) migrate the fleet-level control algorithms onboard each glider, so that gliders plan their own waypoints; and (ii) automate the design and adaptation of the glider coordinated trajectories to better achieve mission-level objectives. Increased autonomy will enable gliders to accomplish new missions in the areas of national defense and environmental monitoring. In turn, these new missions engender a wide variety of exciting theoretical challenges.

Decentralized, onboard waypoint-planning in a collaborating glider fleet scales better with the number of gliders than centralized on-shore waypoint planning, since decentralized planning potentially eliminates a communication and computation bottleneck at the planning hub. However, increasing glider autonomy through decentralized, onboard waypoint-planning requires addressing the inter-glider communication challenge, which is required for coordinated planning. Because gliders surface asynchronously to use radio frequency or

satellite communication devices, they often have no reliable means for direct peer-to-peer communication. One might emulate peer-to-peer communication using a central hub that relays pertinent information to each glider about other gliders, but this would not eliminate the communications bottleneck. Another solution is to install onboard each glider an acoustic modem, which enables information transmission and reception underwater using sound waves [254]. Although acoustic modems are not typically present onboard gliders partly due to space or power constraints, they enable gliders to broadcast state and measurement information to other gliders within acoustic range. Gliders operate essentially silently, so they offer good platforms for acoustic wave reception.<sup>1</sup> Algorithms for amplitude, frequency, and content of data transmission could be developed to minimize power consumption while maintaining a network connectivity. Our results for dynamic algorithms on uniformly connected networks suggest that short-range glider communication may be sufficient to achieve fleet-level coordination.

Automating the design and adaption of mission-level planning would further increase glider autonomy, even if not performed onboard. Mission-level planning generates the desired (coordinated) paths for gliders to follow. For example, in our framework, the output of mission-level planning is encapsulated in a set of glider coordinated trajectories (GCT), which the GCCS uses as input to plan glider waypoints. Adaptation of the GCT currently requires operator intervention approximately once every day or two, although this frequency would likely increase with the number of gliders deployed. In some scenarios—during glider deployment or recovery, in response to severe flow conditions, or when the mission objectives change—the GCT could be changed automatically using existing techniques. To adapt the GCT, the GCCS could determine candidate GCTs using numerical optimization of a suitable metric, as described in [146, 108]. Then, by simulating glider trajectories with GCCS simulator using ocean model forecasts, the GCCS could automatically evaluate the candidates. The merits of this approach would be improved by developing cooperative control algorithms to expand the suite of glider sampling strategies.

---

<sup>1</sup>As opposed to propeller-driven AUVs, whose propeller noise can mask weak incoming transmissions.

We suspect that algorithms to generate quasi-periodic and non-periodic coordinated trajectories may be desirable, especially in dynamic flow conditions. Automated trajectory adaptation driven by decentralized estimation or classification approaches are considered in [101, 82, 186, 215, 210, 43, 211, 295, 158]. Adaptive sampling strategies driven by distributed parameter estimation are described in [137, 276] and [277, pp. 103-149].

Increased autonomy will enable underwater gliders to tackle new missions in support of national security. The number one priority mission identified in the Navy unmanned, underwater vehicle master plan is intelligence, surveillance, and reconnaissance (ISR) [85] (for an updated, extended version, see [71]). For this mission, which supports activities like harbor and port monitoring, vehicles must covertly collect data above and/or below the surface while remaining undetected. We hypothesize that gliders would make good ISR nodes for several reasons: (i) as mentioned before, they have an extremely quiet acoustic signature; (ii) like AUVs, they can carry a variety of payloads, albeit low-power ones; (iii) their high endurance would enable a persistent presence not achievable with AUVs. As with oceanographic missions, overall ISR mission performance might be boosted by feedback at the level of the fleet. For example, we envision gliders deployed to collaboratively enforce a virtual “tripwire” that dynamically reshapes to interrogate possible surface or undersea intruders. The theoretical challenges that would enable collaborative ISR missions with gliders are very rich: for example, one topic is decentralized, dynamic target allocation for mobile sensors with kinematic constraints [14].

Another mission enabled by increased glider autonomy is environmental monitoring at a planetary-scale, after the vision of Stommel [258]. In this scenario, a large fleet of gliders are deployed across an ocean basin, forming a sustained, adaptive observational system that can lead to improved understanding of global climate processes and climate change. Such a system would complement the existing Argo network, composed of nearly 3000 drifting ocean profilers [2]. Drifters are an abundant source of oceanographic data [61, 62]. A network of glider profiles could not only drift with the prevailing currents, but also steer to maintain uniform coverage or focus measurements in regions of interest. Controlling

such a network would require the development of new feedback algorithms, with particular attention to mitigating or harnessing drift vector fields generated by ocean currents. In order to model motion at the planetary-scale, gliders might be represented by self-propelled particles moving on the surface of a sphere or an ellipsoid, rather than a plane. Control of vertical motion might prove useful too, for example, to capitalize on variations of flow with ocean depth. The recent successful crossing of the Gulf Stream by a Spray underwater glider (see, for example, [181]) suggests that a glider ocean observing network may soon be feasible. Techniques developed for steering sensor platforms in an ocean observation system may be applicable to steering under-actuated platforms such as balloons to sample the atmosphere [114, 4].

### 10.2.2 Interaction Networks in Biological Collectives

Application of the theoretical framework described in this thesis to studying biological collectives is the subject of ongoing and proposed work encompassing empirical and theoretical research. Quantitatively assessing the properties of interaction networks in biological collectives using existing and new tools from a cooperative control framework may yield new insights into grouping behavior. The interaction network can be induced from organism trajectory data based on assumptions about the organisms' perceptual geometry. When represented by a time-varying and possibly directed graph, the interaction network is decoupled from species-specific sensing modes or actuation mechanics. Central objectives of this research include the following: (i) to find evidence for the coexistence of different grouping behavior within an animal group; and (ii) to seek underlying principles for collective motion across different species, sensing modalities, and grouping mechanisms. The coexistence of strategies within the group might be detected by examining local connectivity properties of the network. Principles underlying collective motion may be apparent by comparing and contrasting global connectivity properties of different biological systems.

One method to construct an interaction network from a set of organism trajectories is illustrated in Figure 10.2. This type of network, called a proximity-based interaction

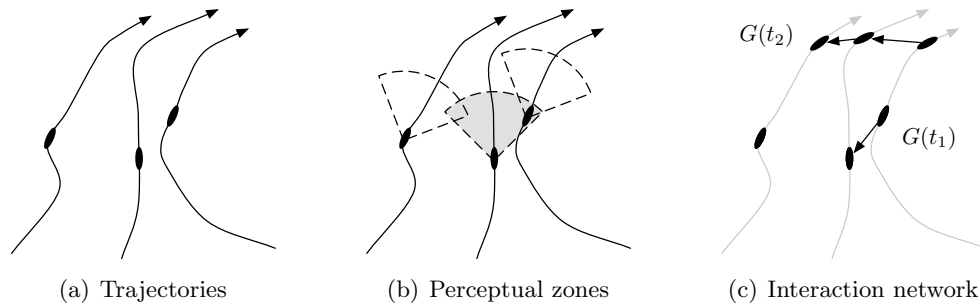


Figure 10.2: Illustration of dynamic interaction network for three organisms. The interaction network, which varies with time, is constructed from the individual trajectories shown in (a) using the geometry of the perceptual zones, depicted by dashed wedges in (b). Only the gray wedge contains a neighbor. Panel (c) shows the interaction network at time  $t_1$  and again at a later time  $t_2$ .

network, is defined in Section 3.3. Each individual in the group is represented by a node in a graph  $G(t)$ ; the number of nodes may vary if individuals join or leave the group. A perceptual zone is attached to each individual as depicted in Figure 10.2(b). For every organism contained in a perceptual zone at time  $t$ , there is a directed edge from its node to the node representing the focal individual. Note that all of the edges in the graph will be undirected if the perceptual zone is radially symmetric and centered on the sensing organism (that is, there is no “blind spot”), whereas some of the edges in the graph will be directed if the perceptual zone is asymmetric or not centered on the sensing organism. As the organisms move, the set of neighbors perceived by each individual may change, leading to time-variation of  $G(t)$ . Generating a proximity-based interaction network depends on assumptions about the size and shape of perceptual zones, whereas generating a nearest-neighbor interaction does not (see Section 3.3). Accordingly, nearest-neighbor interactions generate an interaction network independent of the organisms’ perceptual geometry.

New insights have been attained by analyzing interaction networks of biological collectives with tools from our current theoretical framework. Using a set of fish trajectories generated by Parrish and Grünbaum [104], we have begun studying synchronization of the orientation of a two-dimensional projection of fish velocity [200]. By representing velocity orientation by a phase angle, we can compute the Laplacian phase potential defined in Sec-

tion 4.2 for both proximity-based and nearest-neighbor interaction networks. A histogram of the time trace of the Laplacian phase potential reveals a bimodal distribution of fish activity in a four-fish school: the first mode represents parallel motion in the same direction; the second mode represents mixed parallel and antiparallel motion, such as when three fish move in parallel and the fourth moves in the opposite direction. This analysis may help biologists model the mechanisms that link individual fish behavior to the motion of a school. There are open questions on this topic that have important consequences in ecology and evolutionary biology [135, pp. 137-150].

More realistic modeling of animal aggregations may be attained by extending the particle framework to three-dimensions [235, 230]; see also [252, 25, 128, 176]. A three dimensional framework for cooperative control may also have applications in coordination of micro-AUVs [282, 267] and autonomous aerial vehicles [20, 165]. Our experience with ocean sampling suggests that feedback control at the level of the fleet potentially enables coordinated information gathering with autonomous vehicles in air and space.

# Appendix A

## Supplemental Theoretical Results

The first supplemental result is a consequence of Barbalat's lemma [131, Lemma 8.2] and is based on the proof of [241, Theorem 4]. It is used in the proofs of Theorem 4.10, Corollary 4.11, Corollary 5.5, and Theorem 6.9.

**Lemma A.1. Application of Barbalat's lemma** *Let  $\phi_1(t) \geq 0$  and  $\phi_2(t) \geq 0$ . If there is a function  $V(t) \geq 0$  such that  $V(0)$  is finite and  $\dot{V} = -\phi_1(t) - \phi_2(t) \leq 0$ , then  $\phi_2(t) : [0, \infty) \rightarrow \mathbb{R}$  is bounded; if  $\phi_2(t)$  has a bounded derivative, then  $\phi_2(t) \rightarrow 0$  as  $t \rightarrow \infty$ .*

*Proof.* If  $\sqrt{\int_0^t \phi_2(\tau) d\tau}$  has a finite limit as  $t \rightarrow \infty$ , then  $\phi_2(t) : [0, \infty) \rightarrow \mathbb{R}$  is bounded. If  $\sqrt{\int_0^t \phi_2(\tau) d\tau}$  has a finite limit as  $t \rightarrow \infty$  and  $\phi_2(t)$  is uniformly continuous, then Barbalat's lemma [131, Lemma 8.2] states that  $\phi_2(t) \rightarrow 0$  as  $t \rightarrow \infty$ .

Consider the integral

$$\int_0^t \phi_2(\tau) d\tau = V(0) - \underbrace{\left( V(t) + \int_0^t \phi_1(\tau) d\tau \right)}_{\geq 0},$$

which implies  $\lim_{t \rightarrow \infty} \sqrt{\int_0^t \phi_2(\tau) d\tau}$  exists and is finite. This completes the first part of the proof. Assume  $\dot{\phi}_2(t)$  is bounded, which implies  $\phi_2(t)$  is Lipschitz continuous. Since Lipschitz continuity implies uniform continuity, this completes the second part of the proof.  $\square$

The following lemma is based on [243, Theorem 3]. It is used to prove Corollary 5.2, Theorem 5.3, Corollary 5.5, Lemma 6.1, Theorem 6.9, and Lemma 7.9.

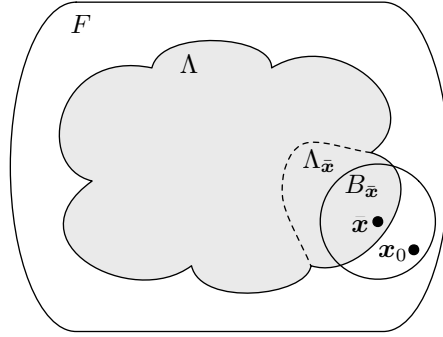


Figure A.1: Geometric representation of sets in the proof of Lemma A.2.

**Lemma A.2. Interconnected system with a nondegenerate, gradient subsystem**

Consider the interconnected system

$$\dot{\mathbf{x}} = \mathbf{f}_1(\mathbf{x}) + \mathbf{f}_2(\mathbf{x}), \quad (\text{A.1})$$

which evolves on a smooth manifold. Suppose there exists continuously differentiable functions  $V_1(\mathbf{x})$  and  $V_2(\mathbf{x})$  that satisfy the following conditions:  $V_1(\mathbf{x})$  is positive semidefinite and nonincreasing along solutions of the subsystem  $\dot{\mathbf{x}} = \mathbf{f}_1(\mathbf{x})$ ; the subsystem  $\dot{\mathbf{x}} = \mathbf{f}_2(\mathbf{x})$  is a gradient system with respect to the potential  $V_2(\mathbf{x})$  and a subset of the critical points of  $V_2(\mathbf{x})$  are nondegenerate. Assume  $V(\mathbf{x}) \triangleq V_1(\mathbf{x}) + V_2(\mathbf{x})$  is nonincreasing along solutions of (A.1). Let  $\Omega$  be the set of all points where  $\dot{V} = 0$  and let  $\Lambda$  be the largest invariant set in  $\Omega$ . If  $V_1(\mathbf{x}) = 0$  and  $\nabla V_2 = 0$  in  $\Lambda$ , then: (i) every isolated local minimum of  $V_2(\mathbf{x})$  defines an asymptotically stable set of equilibria of (A.1); and (ii) every isolated critical point of  $V_2(\mathbf{x})$  that is not a minimum is unstable.

*Proof.* Assume  $V_1(\mathbf{x}) = 0$  and  $\nabla V_2 = 0$  in  $\Lambda$ .

(i) Because  $V(\mathbf{x}) = V_2(\mathbf{x})$  in  $\Lambda$ , local minima of  $V_2(\mathbf{x})$  correspond to local minima of  $V(\mathbf{x})$ . Any connected subset of  $\Lambda$  on which  $V_2(\mathbf{x})$  reaches a strict minimum is therefore asymptotically stable.

(ii) Let  $F$  be the set of all points where  $V_1(\mathbf{x}) = 0$ , which implies  $F$  contains  $\Lambda$  (see Figure A.1). Note that because  $\Lambda$  is a set of equilibria,  $V(\mathbf{x}) = V_2(\mathbf{x})$  is constant on any connected subset of  $\Lambda$ . Consider an isolated critical point  $\bar{\mathbf{x}} \in \Lambda$  such that  $V_2(\bar{\mathbf{x}})$

is not a minimum and denote by  $\Lambda_{\bar{\mathbf{x}}}$  the connected component of  $\Lambda$  containing  $\bar{\mathbf{x}}$ . To show instability of  $\bar{\mathbf{x}}$ , consider a compact neighborhood  $B_{\bar{\mathbf{x}}} \in F$  such that  $B_{\bar{\mathbf{x}}}$  contains no other critical point of  $V_2(\mathbf{x})$ . Let  $\mathbf{x}_0 \in B_{\bar{\mathbf{x}}}/\Lambda_{\bar{\mathbf{x}}}$  such that  $V_2(\mathbf{x}_0) < V_2(\bar{\mathbf{x}})$ , which implies  $V(\mathbf{x}_0) < V(\bar{\mathbf{x}})$ . Since  $\dot{V} \leq 0$ , then a solution with initial condition  $\mathbf{x}_0$  cannot converge to  $\Lambda_{\bar{\mathbf{x}}}$  and therefore leaves  $B_{\bar{\mathbf{x}}}$  after finite time. Since  $V_2(\bar{\mathbf{x}}) = V(\bar{\mathbf{x}})$  is not a minimum, then  $\mathbf{x}_0$  can be chosen arbitrarily close to  $\bar{\mathbf{x}}$ , which proves instability of  $\bar{\mathbf{x}}$ .  $\square$

The following lemma is from [243, Lemma 1]. It is used in the proof of Lemma 3.5 (see Section 6.1).

**Lemma A.3. Summation of the roots of unity** *Let  $m, M \in \mathbb{N} \triangleq \{1, 2, 3, \dots\}$  and*

$$P_m^{(M)} \triangleq \sum_{l=1}^M e^{i\frac{2\pi m}{M}l}. \quad (\text{A.2})$$

*If  $\frac{m}{M} \in \mathbb{N}$ , then  $P_m^{(M)} = M$ , otherwise  $P_m^{(M)} = 0$ .*

*Proof.* If  $\frac{m}{M} \in \mathbb{N}$  then  $e^{i\frac{2\pi m}{M}l} = 1$  for all  $l \in \mathbb{N}$  which proves the first part of the lemma. To prove the second part, we treat (A.2) as the sum of a geometric series and evaluate it for all  $m \in \mathbb{N}$  that satisfy  $\frac{m}{M} \notin \mathbb{N}$ . Multiplying both sides of equation (A.2) by  $e^{i\frac{2\pi m}{M}}$  gives,

$$P_m^{(M)} e^{i\frac{2\pi m}{M}} = \sum_{l=1}^M e^{i\frac{2\pi m}{M}(l+1)} = P_m^{(M)} - e^{i\frac{2\pi m}{M}} + e^{i\frac{2\pi m}{M}(M+1)}.$$

Rearranging terms and solving for  $P_m^{(M)}$  yields,

$$P_m^{(M)} = e^{i\frac{2\pi m}{M}} \frac{e^{i2\pi m} - 1}{e^{i\frac{2\pi m}{M}} - 1}, \quad (\text{A.3})$$

which shows that  $P_m^{(M)} = 0$  since the numerator of (A.3) vanishes for all  $m$  and the denominator is nonzero for all  $m$  that satisfy  $\frac{m}{M} \notin \mathbb{N}$ .  $\square$

The following result is an application of [93, Lemma 13.9.1] and the Gershgorin circle theorem [116, Theorem 6.1.1] (see also [48]). It is used to prove Theorems 6.6 and 6.7.

**Proposition A.4. Weighted graph Laplacian** *Let  $L = BB^T$  be the Laplacian matrix of a time-invariant, undirected and connected graph  $G = (\mathcal{N}, E)$ , where  $B \in \mathbb{R}^{N \times |E|}$  is the*

incidence matrix. Let  $\phi_f \in \mathbb{R}$  denote the weight associated to edge  $f \in \mathcal{E} \triangleq \{1, \dots, |E|\}$  and let  $\boldsymbol{\phi} \triangleq (\phi_1, \dots, \phi_{|E|})$ . The matrix  $\tilde{L} \triangleq B\Phi B^T \in \mathbb{R}^{N \times N}$ , where  $\Phi = \text{diag}\{\boldsymbol{\phi}\} \in \mathbb{R}^{|E| \times |E|}$ , is a weighted Laplacian. If all of the edge weights are positive or all of the edge weights are negative, then zero as an eigenvalue of  $\tilde{L}$  has multiplicity one and the nonzero eigenvalues of  $\tilde{L}$  have the same sign as the edge weights.

## Appendix B

# Curvature and Parameterization of a Superellipse

This appendix supplements material in Section 7.3 describing stabilization of a formation on a superellipse. Using the parameterization (7.28), we have

$$\frac{d\rho}{d\phi} = -\frac{a}{p}(\cos \phi)^{\frac{1-p}{p}} \sin \phi + (i + \mu)\frac{b}{p}(\sin \phi)^{\frac{1-p}{p}} \cos \phi$$

and, using the velocity constraint (7.19), we find

$$\tan \theta_k = \frac{\frac{b}{p}(\sin \phi)^{\frac{1-p}{p}} \cos \phi}{-\frac{a}{p}(\cos \phi)^{\frac{1-p}{p}} \sin \phi + \mu \frac{b}{p}(\sin \phi)^{\frac{1-p}{p}} \cos \phi}.$$

From these we compute

$$\cot \theta_k = -\frac{a}{b}(\cot \phi)^{\frac{1-p}{p}} \tan \phi + \mu$$

and

$$\cot \phi = \left( \frac{b}{a}(\mu - \cot \theta_k) \right)^{\frac{p}{1-2p}}.$$

Consequently,

$$\begin{aligned} \frac{d\phi}{d\theta_k} &= \frac{1 + \cot^2 \theta_k}{\frac{a}{b} \left( \frac{2p-1}{p} \right) (\cot \phi)^{\frac{1-3p}{p}} (1 + \cot^2 \phi)} \\ &= \frac{1 + \cot^2 \theta_k}{\frac{a}{b} \left( \frac{2p-1}{p} \right) \left( \frac{b}{a}(\mu - \cot \theta_k) \right)^{\frac{1-3p}{1-2p}} \left( 1 + \left( \frac{b}{a}(\mu - \cot \theta_k) \right)^{\frac{2p}{1-2p}} \right)} \end{aligned}$$

and

$$\begin{aligned}
\frac{d\rho}{d\phi} &= -\frac{a}{p}(\cos\phi)^{\frac{1}{p}}\tan\phi + (i+\mu)\frac{b}{p}(\sin\phi)^{\frac{1}{p}}\cot\phi \\
&= \frac{\frac{a}{p}\tan\phi\left(-1+(i+\mu)\frac{b}{a}(\tan\phi)^{\frac{1-2p}{p}}\right)}{\left(1+\tan^2\phi\right)^{\frac{1}{2p}}} \\
&= \frac{\frac{a}{p}\left(\frac{b}{a}(\mu-\cot\theta_k)\right)^{\frac{p}{2p-1}}(-1+(i+\mu)(\mu-\cot\theta_k)^{-1})}{\left(1+\left(\frac{b}{a}(\mu-\cot\theta_k)\right)^{\frac{2p}{2p-1}}\right)^{\frac{1}{2p}}}.
\end{aligned}$$

Using

$$\frac{d\rho}{d\theta_k} = \frac{d\rho}{d\phi} \frac{d\phi}{d\theta_k},$$

we obtain

$$\begin{aligned}
\frac{d\rho}{d\theta_k} &= \frac{\frac{a}{p}\left(\frac{b}{a}(\mu-\cot\theta_k)\right)^{\frac{p}{2p-1}}(-1+(i+\mu)(\mu-\cot\theta_k)^{-1})}{\left(1+\left(\frac{b}{a}(\mu-\cot\theta_k)\right)^{\frac{2p}{2p-1}}\right)^{\frac{1}{2p}}} \times \\
&\quad \frac{1+\cot^2\theta_k}{\frac{a}{b}\left(\frac{2p-1}{p}\right)\left(\frac{b}{a}(\mu-\cot\theta_k)\right)^{\frac{1-3p}{1-2p}}\left(1+\left(\frac{b}{a}(\mu-\cot\theta_k)\right)^{\frac{2p}{1-2p}}\right)} \\
&= \frac{ae^{i\theta_k}}{2p-1} \left[ \sin\theta_k(\mu\sin\theta_k - \cos\theta_k)^2 \left(1 + \left(\frac{b}{a}(\mu - \cot\theta_k)\right)^{\frac{2p}{2p-1}}\right)^{\frac{1}{2p}} \times \right. \\
&\quad \left. \left(1 + \left(\frac{b}{a}(\mu - \cot\theta_k)\right)^{\frac{2p}{1-2p}}\right) \right]^{-1}.
\end{aligned}$$

Using

$$\frac{d\rho}{d\theta_k} = e^{i\theta_k} \kappa_k^{-1},$$

we obtain

$$\begin{aligned}
\kappa_k &= \pm \frac{2p-1}{a} \sin\theta_k(\mu\sin\theta_k - \cos\theta_k)^2 \left(1 + \left(\frac{b}{a}(\mu - \cot\theta_k)\right)^{\frac{2p}{2p-1}}\right)^{\frac{1}{2p}} \times \\
&\quad \left(1 + \left(\frac{b}{a}(\mu - \cot\theta_k)\right)^{\frac{2p}{1-2p}}\right). \tag{B.1}
\end{aligned}$$

We also find

$$\begin{aligned}
\rho_k &= a(\cos\phi)^{\frac{1}{p}} \left(1 + (i+\mu)\frac{b}{a}(\tan\phi)^{\frac{1}{p}}\right) \\
&= \frac{a\left(1+(i+\mu)\frac{b}{a}\left(\frac{b}{a}(\mu-\cot\theta_k)\right)^{\frac{1}{2p-1}}\right)}{\left(1+\left(\frac{b}{a}(\mu-\cot\theta_k)\right)^{\frac{2p}{2p-1}}\right)^{\frac{1}{2p}}} \\
&= \frac{a(\sin\theta)^{\frac{1}{2p-1}}+(i+\mu)b\left(\frac{b}{a}(\mu\sin\theta-\cos\theta)\right)^{\frac{1}{2p-1}}}{\left((\sin\theta)^{\frac{2p}{2p-1}}+\left(\frac{b}{a}(\mu\sin\theta-\cos\theta)\right)^{\frac{2p}{2p-1}}\right)^{\frac{1}{2p}}}. \tag{B.2}
\end{aligned}$$

## Appendix C

# Geodetic Utilities

This appendix describes geodetic utilities used by the GCCS (see Chapter 8) for calculating distance and azimuth (heading) on the earth. They are also used to compute the OA metric (see Section 2.2).

Let  $\lambda$  and  $\phi$  denote longitude and latitude, respectively. We use the following radii of curvature for approximating distance, azimuth, and velocity on the earth geoid:  $\Gamma_\phi : [-\frac{\pi}{2}, \frac{\pi}{2}] \rightarrow \mathbb{R}^+$  and  $\Gamma_\lambda : [-\frac{\pi}{2}, \frac{\pi}{2}] \rightarrow \mathbb{R}^+$  given by

$$\Gamma_\phi(\phi) = \frac{a(1 - e^2)}{(1 - e^2 \sin^2 \phi)^{\frac{3}{2}}}$$

and

$$\Gamma_\lambda(\phi) = \frac{a}{(1 - e^2 \sin^2 \phi)^{\frac{1}{2}}},$$

where  $a$  and  $e$  are the semi-major axis and eccentricity of the earth geoid, respectively, given in Table C.1.

Using  $R_k = (\lambda_k, \phi_k) \in [0, 2\pi) \times [-\frac{\pi}{2}, \frac{\pi}{2}] = S^2$ , we define the distance function  $\Gamma : S^2 \times S^2 \rightarrow \mathbb{R}^+$ , where

$$\Gamma^2(R_1, R_2) = \left[ (\lambda_1 - \lambda_2) \Gamma_\lambda \left( \frac{\phi_1 + \phi_2}{2} \right) \cos \left( \frac{\phi_1 + \phi_2}{2} \right) \right]^2 + \left[ (\phi_1 - \phi_2) \Gamma_\phi \left( \frac{\phi_1 + \phi_2}{2} \right) \right]^2. \quad (\text{C.1})$$

The onboard distance functions are glider-specific and not reproduced here.

Parameter	Value	Definition
$a$	6378137 m	Semi-major axis
$F$	1/298.257223563	Flattening
$e$	0.0818	Eccentricity: $e \triangleq \sqrt{2F - F^2}$

Table C.1: WGS84 geoid parameters. Geodetic parameters describing the earth ellipsoid based on a 1984 geographic survey [70]. WGS84 is the reference system used by GPS.

The azimuth function  $\eta : S^2 \times S^2 \rightarrow S^1$  is given by

$$\eta(R_1, R_2) = \tan^{-1} \left[ \frac{(\lambda_2 - \lambda_1) \Gamma_\lambda \left( \frac{\phi_1 + \phi_2}{2} \right) \cos \left( \frac{\phi_1 + \phi_2}{2} \right)}{(\phi_2 - \phi_1) \Gamma_\phi \left( \frac{\phi_1 + \phi_2}{2} \right)} \right], \quad (\text{C.2})$$

where we use the four quadrant inverse tangent and azimuth is measured clockwise from north. The onboard azimuth functions are glider-specific and not reproduced here.

The distance and azimuth functions provide a means to convert between local (flat) and geodetic coordinates. We convert the point  $r \in \mathbb{C}$  from local (complex) to geodetic coordinates  $R \triangleq (\lambda, \phi) \in S^2$  using the transformation  $\mu : \mathbb{C} \times S^2 \times S^1 \rightarrow S^2$  given by

$$R = \mu(r, R_0, \varphi_0) \triangleq R_0 + \left( \frac{\text{Re}(re^{i\varphi_0})}{\rho_\lambda(\phi_0) \cos \phi_0}, \frac{\text{Im}(re^{i\varphi_0})}{\rho_\phi(\phi_0)} \right), \quad (\text{C.3})$$

where  $R_0 = (\lambda_0, \phi_0)$  is the origin of the local coordinate frame, which is rotated with respect to the geodetic coordinate frame by  $\varphi_0$ . The inverse transformation  $\chi : S^2 \times S^2 \times S^1 \rightarrow \mathbb{C}$  from the geodetic coordinate  $R$  to the local coordinate  $r$  is given by

$$r = \chi(R, R_0, \varphi_0) \triangleq \rho(R_0, R) e^{i(\frac{\pi}{2} - \eta(R_0, R) - \varphi_0)} = \rho(R_0, R) i e^{-i(\eta(R_0, R) + \varphi_0)}. \quad (\text{C.4})$$

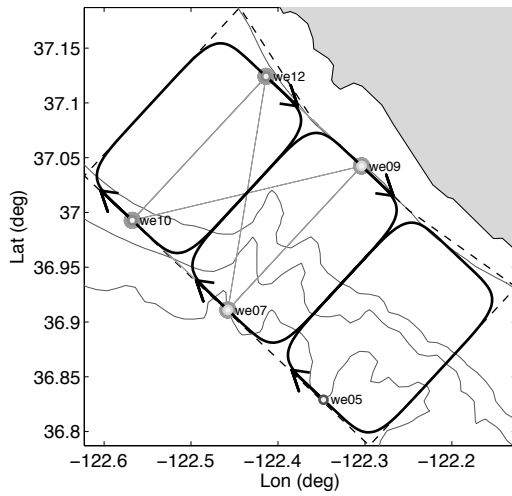
## Appendix D

# Supplemental Experimental Materials

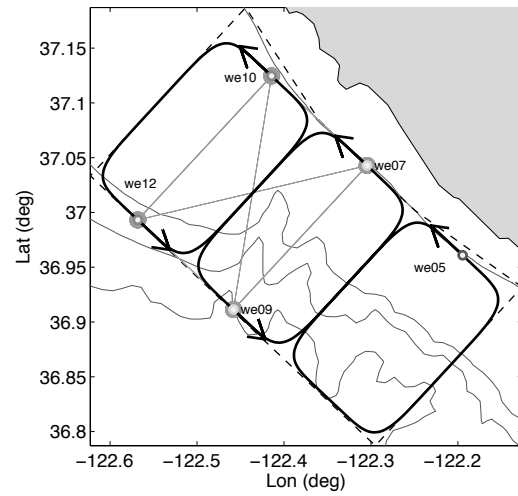
This appendix contains material related to the GCCS experimental results described in Sections 9.2 and 9.3. Table D.1 contains a list of parameter values used during the ASAP experiments. Figures D.1 and D.2 illustrate the sequence of GCTs used during the ASAP 2006 field experiment.

Parameter	Value	Definition
$K_0$	$2/(a+b)$	Track-following gain ( $2a$ is track width, $2b$ is track height)
$K_m$	0.05	Coordination gain for all $m = 1, \dots, M$
$\Delta t$	30 s	Glider-integrator time step
$\alpha$	$2.5^\circ$	Angle of attack
$\beta$	$25^\circ$	Pitch angle
$g_0$	0.18 m/s	Vertical speed
$s_k$	0.35 m/s	Through-water speed (horizontal): $s_k \triangleq g_0 / \tan(\alpha + \beta)$
$Z^{\min}$	10 m	Minimum altitude
$z^{\max}$	200 m	Deep inflection depth
$z^{\min}$	5 m	Shallow inflection depth
$\Gamma_0$	250 m	Radius waypoint condition distance
$T^{\text{gps}}$	60 s	GPS fix duration
$T^{\text{com}}$	420 s	Shore-communication duration
$T^{\text{ini}}$	210 s	Pre-dive surface duration
$T^{\text{max}}$	3 hr	Maximum dive duration
$T^{\text{sur}}$	810 s	Total surface duration per dive: $T^{\text{sur}} \triangleq T^{\text{ini}} + T^{\text{gps}} + T^{\text{com}}$
$s_0$	0.32 m/s	Effective speed (horizontal), $s_0 \triangleq (s_k T^{\text{max}}) / (T^{\text{max}} + T^{\text{sur}})$

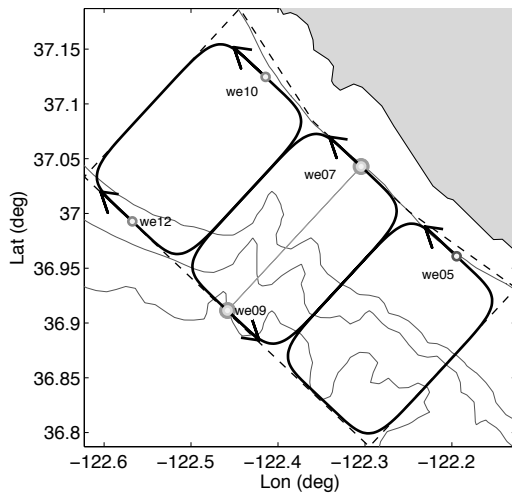
Table D.1: GCCS parameters used during ASAP August 2006 FE. The gains  $K_0$  and  $K_m$  appear in the multi-level, augmented Laplacian symmetric loop configuration control described in Proposition 7.12 (see Section 7.3). The remaining parameters are described in the detailed glider model in Section 8.2.2.



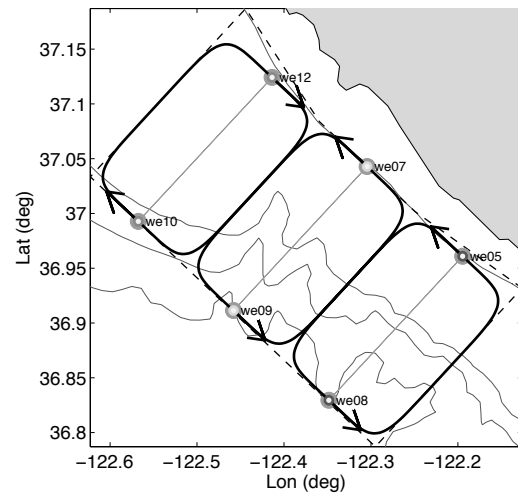
(a) ASAP GCT #6



(b) ASAP GCT #7

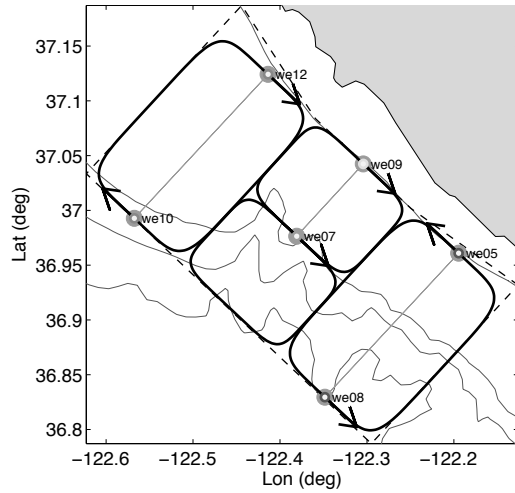


(c) ASAP GCT #8

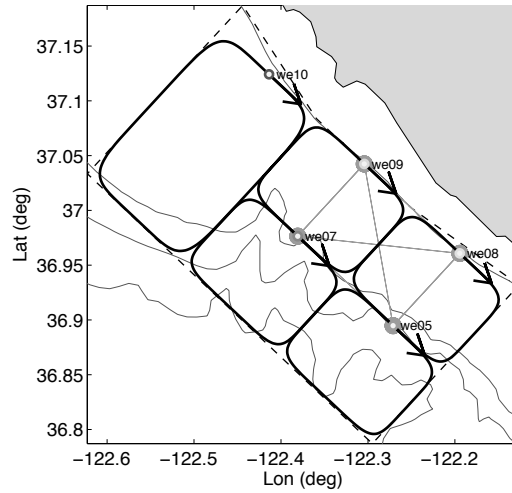


(d) ASAP GCT #9

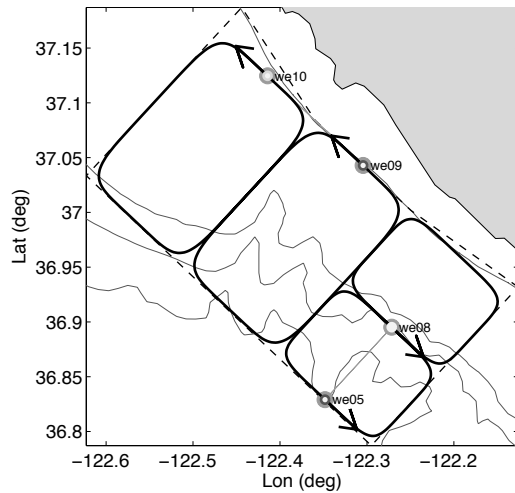
Figure D.1: GCTs used during ASAP 2006 field experiment from 23:15 GMT August 2 to 21:09 GMT August 11. A total of fourteen GCTs were used by the GCCS during the field experiment.



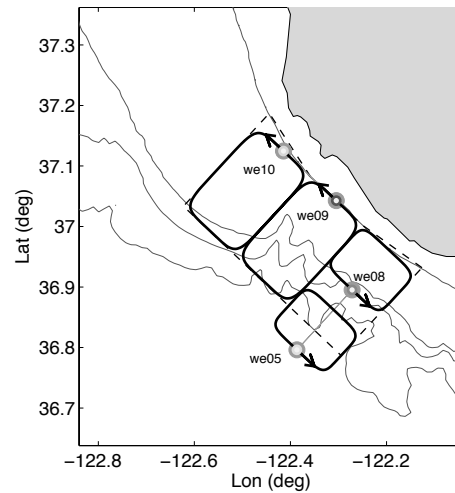
(a) ASAP GCT #10



(b) ASAP GCT #12



(c) ASAP GCT #14



(d) ASAP GCT #15

Figure D.2: GCTs used during ASAP 2006 field experiment from 21:09 GMT August 11 to 11:10 GMT August 21. A total of fourteen GCTs were used by the GCCS during the field experiment. Not shown here are GCT #11, which appears in Figure 9.21(a), and GCT #13, which was created but not used.

# References

- [1] [online]Cornell Lab of Ornithology. Available from: <http://www.birds.cornell.edu/BOW/EURSTA> [cited 18 June 2007].
- [2] [online]National Oceanic and Atmospheric Administration, Pacific Marine Environmental Laboratory Argo Profiling Float Project. Available from: <http://floats.pmel.noaa.gov> [cited 18 June 2007].
- [3] [online]ASAP – Monterey Bay 2006 – Harvard Home Page. Available from: [http://oceans.deas.harvard.edu/ASAP/index\\_ASAP.html](http://oceans.deas.harvard.edu/ASAP/index_ASAP.html) [cited 19 June 2007].
- [4] K. M. Aaron, M. K. Heun, and T. Nock. A method for balloon trajectory control. *Adv. in Space Research*, 30(5):1227–1232, 2002.
- [5] J. A. Acebrón, L. L. Bonilla, C. J. P. Vecente, F. Ritort, and R. Spigler. The Kuramoto model: A simple paradigm for synchronization phenomena. *Rev. Modern Physics*, 77(1):137–185, 2005.
- [6] D. Aeyels and J. A. Rogge. Existence of partial entrainment and stability of phase locking behavior of coupled oscillators. *Prog. Theoretical Physics*, 112(6):921–942, 2004.
- [7] E. An, M. R. Dhanak, L. K. Shay, S. Smith, and J. V. Leer. Coastal oceanography using a small AUV. *J. Atmos. Oceanic Tech.*, 18(2):215–234, 2001.

- [8] J. L. Anderson and S. L. Anderson. A Monte Carlo implementation of the nonlinear filtering problem to produce ensemble assimilations and forecasts. *Monthly Weather Review*, 127(12):2741–2758, 1999.
- [9] B. W. Andrews, K. M. Passino, and T. A. Waite. Foraging theory for autonomous vehicle decision-making system design. *J. Intelligent and Robotic Systems*, 49(1):39–65, 2007.
- [10] D. Angeli and P.-A. Bliman. Stability of leaderless multi-agent systems. Extension of a result by Moreau. *Mathematics of Control, Signals and Systems*, 18(4):293–322, 2006.
- [11] I. Aoki. An analysis of the schooling behavior of fish: Internal organization and communication process. *Bull. Ocean Research Institute, Univ. Tokyo*, 12:1–65, 1980.
- [12] I. Aoki. A simulation study on the schooling mechanism in fish. *Bull. Japanese Society Scientific Fisheries*, 48(8):1081–1088, 1982.
- [13] D. G. Aronson, M. Golubitsky, and J. Mallet-Paret. Ponies on a merry-go-round in large arrays of Josephson junctions. *Nonlinearity*, 4:903–910, 1991.
- [14] A. Arsie and E. Frazzoli. Efficient routing of multiple vehicles with no communications. *Int. J. Robust and Nonlinear Control*, to appear. Available from: <http://ares.lids.mit.edu.edu/papers/Arsie.Frazzoli.IJRNC07.DRAFT.pdf>.
- [15] P. Ashwin and J. W. Swift. The dynamics of  $n$  weakly coupled identical oscillators. *J. Nonlinear Science*, 2(1):69–108, 1992.
- [16] F. M. Atay and T. Biyikoğlu. Graph operations and synchronization of complex networks. *Phys. Rev. E*, 72(1):016217, 2005.
- [17] R. Bachmayer and N. E. Leonard. Vehicle networks for gradient descent in a sampled environment. In *Proc. 41st IEEE Conf. Decision and Control*, volume 1, pages 112–117, Las Vegas, Nevada, December 2002.

- [18] M. Banaji. Clustering in globally coupled oscillators. *Dynamics Systems*, 17(3):263–285, 2002.
- [19] N. Barth and C. Wunsch. Oceanographic experiment design by simulated annealing. *J. Physical Oceanography*, 20(9):1249–1263, 1990.
- [20] R. W. Beard, T. W. McLain, D. B. Nelson, D. Kingston, and D. Johanson. Decentralized cooperative aerial surveillance using fixed-wing miniature UAVs. *Proc. IEEE*, 94(7):1306–1324, 2006.
- [21] J. G. Bellingham. New oceanographic uses of autonomous underwater vehicles. *Marine Technology Society J.*, 31(3):34–47, 1997.
- [22] J. G. Bellingham and Y. Zhang. Observing processes that vary in time and space with heterogeneous mobile networks. In *Proc. Int. Workshop on Underwater Robotics for Sustainable Management of Marine Ecosystems and Environmental Monitoring*, pages 9–16, Genoa, Italy, November 2005.
- [23] A. A. Bennett and J. J. Leonard. A behavior-based approach to adaptive feature detection and following with autonomous underwater vehicles. *IEEE J. Oceanic Engineering*, 25(2):213–226, 2000.
- [24] A. L. Bertozzi, M. Kemp, and D. Marthaler. Determining environmental boundaries: Asynchronous communication and physical scales. In V. Kumar, N. Leonard, and A. S. Morse, editors, *Cooperative Control: A Post-Workshop Volume 2003 Block Island Workshop on Cooperative Control*, number 309 in Lecture Notes in Control and Information Sciences, pages 25–42. Springer-Verlag, 2005.
- [25] P. Bhatta and N. E. Leonard. Stabilization and coordination of underwater gliders. In *Proc. 41st IEEE Conf. Decision and Control*, volume 2, pages 2081–2086, Las Vegas, Nevada, December 2002.
- [26] N. Biggs. *Algebraic Graph Theory*. Cambridge University Press, second edition, 1993.

- [27] C. H. Bishop, B. J. Etherton, and S. J. Majumdar. Adaptive sampling with the ensemble transform Kalman filter. Part I: Theoretical aspects. *Monthly Weather Review*, 129(3):420–436, 2001.
- [28] E. Biyik and M. Arcak. Area aggregation and time scale modeling for sparse nonlinear networks. In *Proc. 45th IEEE Conf. Decision and Control*, pages 4046–4051, San Diego, California, December 2006.
- [29] A. M. Bloch, P. S. Krishnaprasad, J. E. Marsden, and T. S. Ratiu. Asymptotic stability, instability and stabilization of relative equilibria. In *Proc. 10th American Control Conference*, pages 1120–1125, Boston, Massachusetts, June 1991.
- [30] F. T. Boesch and J. F. Wang. Super line-connectivity properties of circulant graphs. *SIAM J. Alg. Disc. Meth.*, 7(1):89–98, 1986.
- [31] S. Boi, I. D. Couzin, N. D. Buono, N. R. Franks, and N. F. Britton. Coupled oscillators and activity waves in ant colonies. *Proc. Biological Sciences*, 266(1417):371–378, 1999.
- [32] W. M. Boothby. *An Introduction to Differentiable Manifolds and Riemannian Geometry*. Academic Press, 2003.
- [33] W. E. Boyce and R. C. DiPrima. *Elementary Differential Equations and Boundary Value Problems*. John Wiley & Sons, seventh edition, 2001.
- [34] S. Boyd, P. Diaconis, and L. Xiao. The fastest mixing Markov chain on a graph. *SIAM Review*, 46(4):667–689, 2004.
- [35] L. C. Breaker and W. W. Broenkow. The circulation of Monterey Bay and related processes. *Oceanography and Marine Biology: Annual Review*, 32:1–64, 1994.
- [36] F. P. Bretherton, R. E. Davis, and C. B. Fandry. A technique for objective analysis and design of oceanographic experiments applied to MODE-73. *Deep-Sea Research*, 23(7):559–582, 1976.

- [37] F. P. Bretherton and J. C. McWilliams. Estimations from irregular arrays. *Rev. Geophysics and Space Physics*, 18(4):789–812, 1980.
- [38] E. Brown, P. Holmes, and J. Moehlis. Globally coupled oscillator networks. In E. Kaplan, J. Marsden, and K. Sreenivasa, editors, *Perspectives and Problems in Nonlinear Science: A Celebratory Volume in Honor of Larry Sirovich*, pages 183–215. Springer, 2003.
- [39] E. Brown, J. Moehlis, and P. Holmes. On phase reduction and response dynamics of neural oscillator populations. *Neural Computation*, 16(4):673–715, 2004.
- [40] E. T. Brown. *Neural Oscillators and Integrators in the Dynamics of Decision Tasks*. PhD thesis, Princeton University, June 2004. Available from: [http://math.nyu.edu/~ebrown/papers/eric.brown\\_dissertation.pdf](http://math.nyu.edu/~ebrown/papers/eric.brown_dissertation.pdf).
- [41] J. Buhl, D. J. T. Sumpter, I. D. Couzin, J. J. Hale, E. Despland, E. R. Miller, and S. J. Simpson. From disorder to order in marching locusts. *Science*, 312(5778):1402–1406, 2006.
- [42] F. Bullo. *Nonlinear Control of Mechanical Systems: A Riemannian Geometry Approach*. PhD thesis, California Institute of Technology, Pasadena, California, August 1998. Available from: <http://motion.mee.ucsb.edu/pdf/phd-fb-7aug98.pdf>.
- [43] C. J. Cannell and D. J. Stilwell. A comparison of two approaches for adaptive sampling of environmental processes using autonomous underwater vehicles. In *Proc. OCEANS 2005 MTS/IEEE Conf.*, volume 2, pages 1514–1521, Washington, District of Columbia, September 2005.
- [44] M. Cao, D. A. Spielman, and A. S. Morse. A lower bound on convergence of a distributed network consensus algorithm. In *Proc. 44th IEEE Conf. Decision and Control*, pages 2356–2361, Seville, Spain, December 2005.
- [45] C. G. Cassandras and W. Li. Sensor networks and cooperative control. *Eur. J. Control*, 11(4-5):436–463, 2005.

- [46] S. Chatterjee and E. Seneta. Toward consensus: Some convergence theorems on repeated averaging. *J. Applied Probability*, 14(1):89–97, March 1977.
- [47] H. Choset. Coverage for robotics—a survey of recent results. *Annals of Mathematics and Artificial Intelligence*, 31(1-4):113–126, 2001.
- [48] F. Chung and K. Oden. Weighted graph Laplacians and isoperimetric inequalities. *Pacific J. Mathematics*, 192(2):257–274, 2000.
- [49] F. R. K. Chung. *Spectral Graph Theory*. Number 92 in Regional Conference Series in Mathematics. American Mathematical Society, 1997.
- [50] J. J. Collins and I. N. Stewart. Coupled nonlinear oscillators and the symmetries of animal gaits. *J. Nonlinear Science*, 3(1):349–392, 1993.
- [51] J. Cortés. Distributed gradient ascent of random fields by robotic sensor networks. Submitted to *46th IEEE Conf. Decision and Control*. Available from: <http://www.ams.ucsc.edu/~jcortes/research/cf32.html>.
- [52] J. Cortés, S. Martínez, T. Karatas, and F. Bullo. Coverage control for mobile sensing networks. *IEEE Trans. Robotics and Automation*, 20(2):243–255, 2004.
- [53] I. D. Couzin, R. James, D. Mawdsley, D. P. Croft, and J. Krause. Social organization and information transfer in schooling fishes. In C. Brown, K. N. Laland, and J. Krause, editors, *Fish Cognition and Behavior*, Fish and Aquatic Resource Series 11, chapter 9, pages 166–185. Blackwell Publishing, 2006.
- [54] I. D. Couzin, J. Krause, N. R. Franks, and S. A. Levin. Effective leadership and decision-making in animal groups on the move. *Nature*, 433(7025):513–516, 2005.
- [55] I. D. Couzin, J. Krause, R. James, G. D. Ruxton, and N. R. Franks. Collective memory and spatial sorting in animal groups. *J. Theor. Biol.*, 218(1):1–11, 2002.
- [56] E. Creed, J. Kerfoot, C. Mudgal, S. Glenn, O. Schofield, C. Jones, D. Webb, and T. Campbell. Automated control of a fleet of Slocum gliders within an operational

- coastal observatory. In *Proc. OCEANS 2003 MTS/IEEE Conf.*, volume 2, pages 726–730, San Diego, California, September 2003.
- [57] F. Cucker and S. Smale. Emergent behavior in flocks. *IEEE Trans. Automatic Control*, 52(5):852–862, 2007.
- [58] T. B. Curtin and J. G. Bellingham. Autonomous ocean-sampling networks. *IEEE J. Oceanic Engineering*, 26(4):421–423, 2001.
- [59] T. B. Curtin, J. G. Bellingham, J. Catipovic, and D. Webb. Autonomous oceanographic sampling networks. *Oceanography*, 6(3):86–94, 1993.
- [60] P. J. Davis. *Circulant Matrices*. John Wiley & Sons, Inc., 1979.
- [61] R. E. Davis. Drifter observations of coastal surface currents during CODE: The method and descriptive view. *J. Geophysical Research*, 90(C3):4741–4755, 1985.
- [62] R. E. Davis. Drifter observations of coastal surface currents during CODE: The statistical and dynamic views. *J. Geophysical Research*, 90(C3):4756–4772, 1985.
- [63] R. E. Davis. Objective mapping by least squares fitting. *J. Geophysical Research*, 90(C3):4773–4777, 1985.
- [64] R. E. Davis. Personal communication, 2004-2006.
- [65] R. E. Davis, C. E. Eriksen, and C. P. Jones. Autonomous buoyancy-driven underwater gliders. In G. Griffiths, editor, *The Technology and Applications of Autonomous Underwater Vehicles*, chapter 3, pages 37–58. Taylor and Francis, 2002.
- [66] R. E. Davis, N. E. Leonard, and D. M. Fratantoni. Routing strategies for underwater gliders. submitted to *Deep-Sea Research II*.
- [67] M. H. DeGroot. Reaching a consensus. *J. Amer. Stat. Ass.*, 69(345):118–121, 1974.
- [68] J. L. Deneubourg and S. Goss. Collective patterns and decision-making. *Ethology, Ecology, and Evolution*, 1(4):295–311, 1989.

- [69] K. L. Denman and M. R. Abbott. Time scales of pattern evolution from cross-spectrum analysis of advanced very high resolution radiometer and coastal zone color scanner imagery. *J. Geophysical Research*, 99(C4):7433–7442, 1994.
- [70] U. S. Department of Defense. Department of Defense World Geodetic system 1984. Technical Report NIMA TR8350.2, National Imagery and Mapping Agency, 3 January 2000. Third edition, amendment 1. Available from: <http://earth-info.nga.mil/GandG/publications/tr8350.2/wgs84fin.pdf>.
- [71] U. S. Department of the Navy. The Navy Unmanned Undersea Vehicle (UUV) Master Plan. Available online: <http://www.navy.mil/navydata/technology/uuvmp.pdf>, November 2004.
- [72] T. D. Dickey. The emergence of concurrent high-resolution physical and bio-optical measurements in the upper ocean and their applications. *Rev. Geophysics*, 29(3):383–413, 1991.
- [73] R. Diestel. *Graph Theory*. Number 173 in Graduate Texts in Mathematics. Springer, third edition, 2005.
- [74] M. R. D’Orsogna, Y. L. Chuang, A. L. Bertozzi, and L. S. Chayes. Self-propelled particles with soft-core interactions: Patterns, stability, and collapse. *Phys. Rev. Letters*, 96(10):104302–1–4, March 17, 2006.
- [75] L. E. Dubins. On curves of minimal length with a constraint on average curvature, and with prescribed initial and terminal positions and tangents. *Amer. J. Mathematics*, 79(3):497–517, 1957.
- [76] L. Edelstein-Keshet. Collective motion. In W. Alt and G. Hoffmann, editors, *Biological Motion: Proceedings of a workshop held in Königswinter, Germany, March 16-19, 1989*, number 89 in Lecture Notes in Biomathematics, pages 528–532. Springer-Verlag, 1990.

- [77] C. C. Eriksen, T. J. Osse, R. D. Light, T. Wen, T. W. Lehman, P. L. Sabin, J. W. Ballard, and A. M. Chiodi. Seaglider: A long-range autonomous underwater vehicle for oceanographic research. *IEEE J. Oceanic Engineering*, 26(4):424–436, 2001.
- [78] M. N. Evans, A. Kaplan, and M. A. Cane. Optimal sites for coral-based reconstruction of global sea surface temperature. *Paleoceanography*, 13(5):502–516, 1998.
- [79] J. A. Fax and R. M. Murray. Graph Laplacians and stabilization of vehicle formations. In *Proc. 15th IFAC World Congress*, pages 283–288, Barcelona, Spain, July 2002.
- [80] J. A. Fax and R. M. Murray. Information flow and cooperative control of vehicle formations. *IEEE Trans. Automatic Control*, 49(9):1465–1476, 2004.
- [81] H. J. S. Feder, J. J. Leonard, and C. M. Smith. Adaptive mobile robot navigation and mapping. *Int. J. Robotics Research*, 18(7):650–668, 1999.
- [82] E. Fiorelli, P. Bhatta, N. E. Leonard, and I. Schulman. Adaptive sampling using feedback control of an autonomous underwater glider fleet. In *Proc. 13th. Int. Symp. on Unmanned Untethered Submersible Technology*, August 2003.
- [83] E. Fiorelli, N. E. Leonard, P. Bhatta, D. A. Paley, R. Bachmayer, and D. M. Fratantoni. Multi-AUV control and adaptive sampling in Monterey Bay. *IEEE J. Oceanic Engineering*, 31(4):935–948, 2006.
- [84] E. A. Fiorelli. *Cooperative Vehicle Control, Feature Tracking and Ocean Sampling*. PhD thesis, Princeton University, 2005. Available from: <http://www.princeton.edu/~naomi/theses/EAFiorelli-thesis-101005.pdf>.
- [85] B. Fletcher. UUV master plan: A vision for Navy UUV development. In *Proc. OCEANS 2000 MTS/IEEE Conf.*, volume 1, pages 65–71, Providence, Rhode Island, September 2000.
- [86] G. Flierl, D. Grünbaum, S. Levin, and D. Olson. From individuals to aggregations: the interplay between behavior and physics. *J. Theor. Biol.*, 196(4):397–454, 1999.

- [87] G. F. Franklin, J. D. Powell, and A. Emani-Naeini. *Feedback Control of Dynamic Systems*. Prentice Hall, fourth edition, 2002.
- [88] D. M. Fratantoni. Personal communication, 2004-2006.
- [89] R. A. Freeman, P. Yang, and K. M. Lynch. Distributed estimation and control of swarm formation statistics. In *Proc. 2006 Amer. Control Conf. (electronic)*, Minneapolis, Minnesota, 2006. (7 pages).
- [90] R. A. Freeman, P. Yang, and K. M. Lynch. Stability and convergence properties of dynamic average consensus estimators. In *Proc. 45th IEEE Conf. Decision and Control*, pages 398–403, San Diego, California, December 2006.
- [91] L. S. Gandin. *Objective Analysis of Meteorological Fields*. Israel Program for Scientific Translations, Jerusalem, 1965.
- [92] L. Gao and D. Cheng. Comment on “Coordination of groups of mobile autonomous agents using nearest neighbor rules”. *IEEE Trans. Automatic Control*, 50(11):1913–1916, 2005.
- [93] C. Godsil and G. Royle. *Algebraic Graph Theory*. Number 207 in Graduate Texts in Mathematics. Springer-Verlag, 2001.
- [94] D. Golomb, D. Hansel, B. Shraiman, and H. Sompolinsky. Clustering in globally coupled phase oscillators. *Physical Review A*, 45(6):3516–3531, 1992.
- [95] M. Golubitsky, K. Josić, and E. Shea-Brown. Winding numbers and average frequencies in phase oscillator networks. *J. Nonlinear Science*, 16(3):201–231, 2006.
- [96] W. M. Graham and J. L. Largier. Upwelling shadows as nearshore retention sites: the example of northern Monterey Bay. *Continental Shelf Research*, 17(5):509–532, 1997.
- [97] J. G. Graver. *Underwater Gliders: Dynamics, Control and Design*. PhD thesis, Princeton University, Princeton, New Jersey, 2005. Available from: <http://www.princeton.edu/~naomi/theses/jggraver-thesis-4-11-05.pdf>.

- [98] R. M. Gray. Toeplitz and circulant matrices: A review. *Foundations and Trends in Communications and Information Theory*, 2(3):155–239, 2006.
- [99] G. Grégoire and H. Chaté. Onset of collective and cohesive motion. *Phys. Rev. Letters*, 92(2):025702, 2004.
- [100] G. Grégoire, H. Chaté, and Y. Tu. Moving and staying together without a leader. *Physica D*, 181(3-4):157–170, 2003.
- [101] B. Grocholsky. *Information-Theoretic Control of Multiple Sensor Platforms*. PhD thesis, University of Sydney, 2002. Available from: <http://www.grasp.upenn.edu/~bpg/BenGrocholskyThesis.pdf>.
- [102] D. Grünbaum. Translating stochastic density-dependent individual behavior with sensory constraints to an Eulerian model of animal swarming. *J. Math. Biol.*, 33(1):139–161, 1994.
- [103] D. Grünbaum. Schooling as a strategy for taxis in a noisy environment. *Evolutionary Ecology*, 12(5):503–522, 1998.
- [104] D. Grünbaum, S. Viscido, and J. K. Parrish. Extracting interactive control algorithms from group dynamics of schooling fish. In V. Kumar, N. Leonard, and A. S. Morse, editors, *Cooperative Control: A Post-Workshop Volume 2003 Block Island Workshop on Cooperative Control*, number 309 in Lecture Notes in Control and Information Sciences, pages 104–117. Springer-Verlag, 2005.
- [105] S. Gueron and S. A. Levin. Self-organization of front patterns in large wildebeest herds. *J. Theor. Biol.*, 165(4):541–552, 1993.
- [106] S. Gueron and S. A. Levin. The dynamics of group formation. *Mathematical Biosciences*, 128(1-2):243–264, 1995.
- [107] S. Gueron, S. A. Levin, and D. I. Rubenstein. The dynamics of herds: from individuals to aggregations. *J. Theor. Biol.*, 182(1):85–98, 1996.

- [108] D. Gurkins. Optimal patterns and control for sampling via mobile sensor networks. Master's thesis, Princeton University, Princeton, New Jersey, June 2007.
- [109] E. C. Hackert, R. N. Miller, and A. J. Busalacchi. An optimized design for a moored instrument array in the tropical Atlantic Ocean. *J. Geophysical Research*, 103(C4):7491–7509, 1998.
- [110] P. Hadley and M. R. Beasley. Dynamical states and stability of linear arrays of Josephson junctions. *Appl. Phys. Letters*, 50(10):621–623, 1987.
- [111] W. D. Hamilton. Geometry for the selfish herd. *J. Theor. Biol.*, 31(2):295–311, 1971.
- [112] W. J. Hamilton. Evidence concerning the function of nocturnal call notes of migratory birds. *The Condor*, 64(5):390–401, 1962.
- [113] Y. Hatano and M. Mesbahi. Agreement over random networks. *IEEE Trans. Automatic Control*, 50(11):1867–1872, 2005.
- [114] M. K. Heun, R. S. Schlaifer, K. Aaron, K. Nock, A. Pankine, N. E. Leonard, E. A. Belbruno, and P. Bhatta. Computer simulations of global networks of stratospheric balloons. In *6th Symp. on Integrated Observing Systems (electronic)*, Orlando, Florida, January 2001. 8 pages.
- [115] N. G. Hogg. Oceanographic data for parameter estimation. In P. Malanotte-Rizzoli, editor, *Modern Approaches to Data Assimilation in Ocean Modeling*, pages 57–76. Elsevier, 1996.
- [116] R. A. Horn and C. R. Johnson. *Matrix Analysis*. Cambridge University Press, 1985.
- [117] M. A. Hsieh, S. G. Loizou, and V. Kumar. Stabilization of multiple robots on stable orbits via local sensing. In *Proc. IEEE Int. Conf. Robotics and Automation*, pages 2312–2317, Rome, Italy, April 2007.

- [118] B. L. Hua, J. C. McWilliams, and W. B. Owens. An objective analysis of the POLY-MODE local dynamics experiment. Part II: Streamfunction and potential vorticity fields during the intensive period. *J. Phys. Oceanography*, 16(3):506–522, 1986.
- [119] C. Huepe and M. Aldana. Intermittency and clustering in a system of self-driven particles. *Phys. Rev. Letters*, 92(16):168701–1–4, 2004.
- [120] A. Huth and C. Wissel. The movement of fish schools: A simulation model. In W. Alt and G. Hoffmann, editors, *Biological Motion: Proceedings of a workshop held in Königswinter, Germany, March 16-19, 1989*, number 89 in Lecture Notes in Biomathematics, pages 577–590. Springer-Verlag, 1990.
- [121] T. Inanc, S. C. Shadden, and J. E. Marsden. Optimal trajectory generation in ocean flows. In *Proc. 2005 Amer. Control Conf.*, pages 674–679, Portland, Oregon, June 2005.
- [122] A. Jadbabaie, J. Lin, and A. S. Morse. Coordination of groups of mobile autonomous agents using nearest neighbor rules. *IEEE Trans. Automatic Control*, 48(6):988–1001, 2003.
- [123] J. Jeanne, N. E. Leonard, and D. Paley. Collective motion of ring-coupled planar particles. In *Proc. Joint 44th IEEE Conf. Decision and Control and European Control Conf.*, pages 3929–3934, Seville, Spain, December 2005.
- [124] S. A. Jenkins, D. E. Humphreys, J. Sherman, C. Jones, N. Leonard, J. Graver, and R. Bachmayer. Alternatives for enhancement of transport economy in underwater gliders. In *Proc. OCEANS 2003 MTS/IEEE Conf.*, volume 2, pages 948–950, San Diego, California, September 2003.
- [125] E. Justh and P. S. Krishnaprasad. Convergence analysis of a class of networks of nonlinear coupled oscillators. In *Proc. 34th IEEE Conf. Decision and Control*, pages 1284–1289, New Orleans, Louisiana, December 1995.

- [126] E. W. Justh and P. S. Krishnaprasad. A simple control law for UAV formation flying. Technical Report 2002-38, Institute for Systems Research, University of Maryland, 2002. Available from: [http://techreports.isr.umd.edu/reports/2002/TR\\_2002-38.pdf](http://techreports.isr.umd.edu/reports/2002/TR_2002-38.pdf).
- [127] E. W. Justh and P. S. Krishnaprasad. Equilibria and steering laws for planar formations. *Systems and Control Letters*, 52(1):25–38, 2004.
- [128] E. W. Justh and P. S. Krishnaprasad. Natural frames and interacting particles in three dimensions. In *Proc. Joint 44th IEEE Conf. Decision and Control and European Control Conf.*, pages 2841–2846, Seville, Spain, December 2005.
- [129] E. Kalnay. *Atmospheric modeling, data assimilation and predictability*. Cambridge University Press, 2003.
- [130] M. Kemp, A. L. Bertozzi, and D. Marthaler. Multi-UUV perimeter surveillance. In *Proc. 2004 IEEE/OES Autonomous Underwater Vehicles Workshop*, pages 102–107, Sebasco Estates, Maine, June 2004.
- [131] H. K. Khalil. *Nonlinear Systems*. Prentice Hall, third edition, 2002.
- [132] Y. Kim and M. Mesbahi. On maximizing the second smallest eigenvalue of a state-dependent graph Laplacian. In *Proc. 2005 Amer. Control Conf.*, pages 99–103, Portland, Oregon, June 2005.
- [133] E. Klavins and D. E. Koditschek. Phase regulation of decentralized cyclic robotic systems. *Int. J. Robotics Research*, 21(3):257–275, 2002.
- [134] N. Kopell and G. B. Ermentrout. Symmetry and phaselocking in chains of weakly coupled oscillators. *Commun. Pure Appl. Math.*, 39(5):623–660, 1986.
- [135] J. Krause and G. D. Ruxton. *Living in Groups*. Oxford Series in Ecology and Evolution. Oxford University Press, 2002.

- [136] P. S. Krishnaprasad. Relative equilibria and stability of rings of satellites. In *Proc. 39th IEEE Conf. Decision and Control*, pages 1285–1288, Sydney, Australia, December 2000.
- [137] S. Kumar and J. H. Seinfeld. Optimal location of measurements for distributed parameter estimation. *IEEE Trans. Automatic Control*, AC-23(4):690–698, 1978.
- [138] Y. Kuramoto. Self-entrainment of a population of coupled non-linear oscillators. In *Proc. Int. Symp. Mathematical Problems in Theoretical Physics*, pages 420–422, Kyoto, Japan, January 1975. Kyoto University.
- [139] Y. Kuramoto. *Chemical oscillations, waves, and turbulence*. Springer-Verlag, 1984.
- [140] G. Lafferriere, A. Williams, J. S. Caughman, and J. J. P. Veerman. Decentralized control of vehicle formations. *Systems and Control Letters*, 54(9):899–910, 2005.
- [141] L. D. Landau and E. M. Lifshitz. *Fluid Mechanics*, volume 6 of *Course of Theoretical Physics*. Butterworth-Heinemann, second edition, 1987. Translated from Russian by J. B. Sykes and W. H. Reid.
- [142] F. Lekien and N. E. Leonard. Non-uniform coverage and cartograms. Submitted to *SIAM J. Control and Optimization*, Special issue on “Control and optimization in cooperative networks”. Available from: <http://www.princeton.edu/~naomi/publications/2007/lekienleonard26Jan07.pdf>.
- [143] J. J. Leonard and H. J. S. Feder. Decoupled stochastic mapping. *IEEE J. Oceanic Engineering*, 26(4):561–571, 2001.
- [144] N. Leonard, R. Davis, D. M. Fratantoni, P. F. J. Lermusiaux, J. E. Marsden, S. R. Ramp, A. R. Robinson, H. Schmidt, and R. Bachmayer. Optimal asset distribution for environmental assessment and forecasting based on observations, adaptive sampling, and numerical prediction. Proposal for *2004 Department of Defense Multidisciplinary Research Program of the University Research Initiative* on “Coupled Observation, Adaptive Sampling, and Forecast in the Real Environment”.

- [145] N. E. Leonard and E. Fiorelli. Virtual leaders, artificial potentials and coordinated control of groups. In *Proc. 40th IEEE Conf. Decision and Control*, pages 2968–2973, Orlando, Florida, December 2001.
- [146] N. E. Leonard, D. A. Paley, F. Lekien, R. Sepulchre, D. M. Fratantoni, and R. E. Davis. Collective motion, sensor networks and ocean sampling. *Proc. IEEE*, 95(1):48–74, 2007.
- [147] P. F. J. Lermusiaux. Data assimilation via error subspace statistical estimation, Part II: Mid-Atlantic bight shelfbreak front simulations, and ESSE validation. *Monthly Weather Review*, 127(8):1408–1432, 1999.
- [148] P. F. J. Lermusiaux. On the mapping of multivariate geophysical fields: Sensitivity to size, scales and dynamics. *J. Atmos. Oceanic Tech.*, 19(10):1602–1637, 2002.
- [149] P. F. J. Lermusiaux, C.-S. Chiu, G. G. Gawarkiewicz, P. Abbot, A. R. Robinson, P. J. Haley, W. G. Leslie, S. J. Majumdar, A. Pang, and F. Lekien. Quantifying uncertainties in ocean predictions. *Oceanography*, 19(1):80–94, 2006.
- [150] P. F. J. Lermusiaux and A. R. Robinson. Data assimilation via error subspace statistical estimation, Part I: Theory and schemes. *Monthly Weather Review*, 127(8):1385–1407, 1999.
- [151] S. Levin. Conceptual and methodological issues in the modeling of biological aggregations. In J. K. Parrish and W. M. Hamner, editors, *Animal Groups in Three Dimensions*, chapter 16, pages 247–256. Cambridge University Press, 1987.
- [152] S. A. Levin. Random walk models of movement and their implications. In T. G. Hallam and S. A. Levin, editors, *Mathematical Ecology, an Introduction*, volume 17 of *Biomathematics*, pages 149–154. Springer-Verlag, 1986.
- [153] P. B. Liebelt. *An Introduction to Optimal Estimation*. Addison-Wesley, 1967.

- [154] Z. Lin, M. Broucke, and B. Francis. Local control strategies for groups of mobile autonomous agents. *IEEE Trans. Automatic Control*, 49(4):622–629, 2004.
- [155] Z. Lin, B. Francis, and M. Maggiore. Necessary and sufficient graphical conditions for formation control of unicycles. *IEEE Trans. Automatic Control*, 50(1):121–127, 2005.
- [156] Z. Liu, Y.-C. Lai, and F. C. Hoppensteadt. Phase clustering and transition to phase synchronization in a large number of coupled nonlinear oscillators. *Phys. Rev. E*, 63(5):055201, 2001.
- [157] D. R. Lynch and D. J. McGillicuddy, Jr. Objective analysis for coastal regimes. *Continental Shelf Research*, 21(11):1299–1315, 2001.
- [158] K. M. Lynch, I. B. Schwartz, P. Yang, and R. A. Freeman. Decentralized environmental modeling by mobile sensor networks. Submitted to *IEEE Trans. Robotics*. Available from: <http://lims.mech.northwestern.edu/~lynch/papers/tro2006/tro2006.pdf>.
- [159] S. J. Majumdar, C. H. Bishop, and B. J. Etherton. Adaptive sampling with the ensemble transform Kalman filter. Part II: Field program implementation. *Monthly Weather Review*, 130(5):1356–1369, 2002.
- [160] J. Manyika and H. Durrant-Whyte. *Data Fusion and Sensor Management: A Decentralized Information-Theoretic Approach*. Ellis Horwood, 1994.
- [161] J. E. Marsden and T. S. Ratiu. *Introduction to Mechanics and Symmetry*. Springer, 2nd edition, 1999.
- [162] J. A. Marshall and M. E. Broucke. On invariance of cyclic group symmetries in multiagent formations. In *Proc. 44th IEEE Conf. Decision and Control*, pages 746–751, Seville, Spain, December 2005.
- [163] J. A. Marshall, M. E. Broucke, and B. A. Francis. Formations of vehicles in cyclic pursuit. *IEEE Trans. Automatic Control*, 49(11):1963–1974, 2004.

- [164] S. Martínez and F. Bullo. Optimal sensor placement and motion coordination for target tracking. *Automatica*, 42(4):661–668, 2006.
- [165] I. A. McManus and R. A. Walker. Multidisciplinary approach to intelligent unmanned-airborne-vehicles mission planning. *J. Aircraft*, 43(2):318–335, 2006.
- [166] J. C. McWilliams, W. B. Owens, and B. L. Hua. An objective analysis of the POLY-MODE local dynamics experiment. Part I: General formalism and statistical model selection. *J. Phys. Oceanography*, 16(3):483–504, 1986.
- [167] D. Menemenlis, P. Fieguth, C. Wunsch, and A. Willsky. Adaptation of a fast optimal interpolation algorithm to the mapping of oceanographic data. *J. Geophysical Research*, 102(C5):10,573–10,584, 1997.
- [168] H. Mercier and A. C. de Verdière. Space and time scales of mesoscale motions in the eastern North Atlantic. *J. Physical Oceanography*, 15(2):171–183, 1985.
- [169] R. Merris. Laplacian matrices of graphs: A survey. *Linear Algebra and its Applications*, 197(198):143–176, 1994.
- [170] C. D. Meyer. *Matrix Analysis and Applied Linear Algebra*. Society for Industrial and Applied Mathematics, 2000.
- [171] G. Meyers, H. Phillips, N. Smith, and J. Sprintall. Space and time scales for optimal interpolation of temperature–tropical Pacific Ocean. *Prog. Oceanography*, 28(3):189–218, 1991.
- [172] K. Mischaikow, H. Smith, and H. R. Thieme. Asymptotically autonomous semiflows: Chain recurrence and Lyapunov functions. *Trans. Amer. Math. Society*, 347(5):1669–1685, 1995.
- [173] B. Mohar. The Laplacian spectrum of graphs. In Y. Alavi, G. Chartrand, O. R. Oellermann, and A. J. Schwenk, editors, *Graph Theory, Combinatorics, and Applications*, pages 871–898. Wiley, 1991.

- [174] L. Moreau. Stability of continuous-time distributed consensus algorithms. arXiv: math.OC/0409010 v1, September 2004. Available from: <http://arxiv.org/pdf/math/0409010>.
- [175] L. Moreau. Stability of multiagent systems with time-dependent communication links. *IEEE Trans. Automatic Control*, 50(2):169–182, 2005.
- [176] N. Moshtagh and A. Jadbabaie. Distributed geodesic control laws for flocking of nonholonomic agents. *IEEE Trans. Automatic Control*, 52(4):681–686, 2007.
- [177] W. G. Müller. *Collecting Spatial Data*. Physica-Verlag, 2nd edition, 2001.
- [178] S. S. Mupparapu, S. G. Chappell, R. J. Komerska, D. R. Blidberg, R. Nitzel, C. Benton, D. O. Popa, and A. C. Sanderson. Autonomous systems monitoring and control (ASMAC) – an AUV fleet controller. In *Proc. 2004 IEEE/OES Autonomous Underwater Vehicles Workshop*, pages 119–126, Sebasco Estates, Maine, June 2004.
- [179] B. Nabet, N. E. Leonard, I. Couzin, and S. Levin. Leadership in animal group motion: A bifurcation analysis. In *Proc. 17th Int. Symp. Math. Theory of Networks and Systems (electronic)*, Kyoto, Japan, July 2006. (14 pages).
- [180] S. Nair and N. E. Leonard. Stabilization of a coordinated network of rotating rigid bodies. In *Proc. 43rd IEEE Conf. Decision and Control*, pages 4690–4695, Paradise Island, Bahamas, December 2004.
- [181] A. E. Nevala. A glide across the Gulf Stream. *Oceanus*, 44(1), 2005. (2 pages). Available from: <http://www.whoi.edu/oceanus/viewArticle.do?id=3821>.
- [182] A. E. Nevala. To find whales, follow their food. *Oceanus*, 20 January 2006. Available from: <http://www.whoi.edu/oceanus/viewArticle.do?id=9213&archives=true>.
- [183] S. Nichols and K. Wiesenfeld. Non-neutral dynamics of splay states in Josephson-junction arrays. *Phys. Rev. E*, 50(1):205–212, 1994.

- [184] H. Nijmeijer and A. van der Schaft. *Nonlinear Dynamical Control Systems*. Springer-Verlag, 1990.
- [185] P. Ögren, M. Egerstedt, and X. Hu. A control Lyapunov function approach to multiagent coordination. *IEEE Trans. Robotics and Automation*, 18(5):847–851, 2002.
- [186] P. Ögren, E. Fiorelli, and N. E. Leonard. Cooperative control of mobile sensor networks: Adaptive gradient climbing in a distributed environment. *IEEE Trans. Automatic Control*, 49(8):1292–1302, 2004.
- [187] S. Oh, L. Schenato, P. Chen, and S. Sastry. Tracking and coordination of multiple agents using sensor networks: System design, algorithms and experiments. *Proc. IEEE*, 95(1):234–254, 2007.
- [188] A. Okubo. Dynamical aspects of animal grouping: Swarms, schools, flocks, and herds. *Adv. Biophys.*, 22:1–94, 1986.
- [189] K. Okuda. Variety and generality of clustering in globally coupled oscillators. *Physica D*, 63(3-4):424–436, 1993.
- [190] R. Olfati-Saber. Flocking for multi-agent dynamic systems: Algorithms and theory. *IEEE Trans. Automatic Control*, 51(3):401–420, 2006.
- [191] R. Olfati-Saber, J. A. Fax, and R. M. Murray. Consensus and cooperation in networked multi-agent systems. *Proc. IEEE*, 95(1):215–233, 2007.
- [192] R. Olfati-Saber and R. M. Murray. Consensus problems in networks of agents with switching topology and time-delays. *IEEE Trans. Automatic Control*, 49(9):1520–1533, 2004.
- [193] R. Olfati-Saber and J. S. Shamma. Consensus filters for sensor networks and distributed sensor fusion. In *Proc. IEEE 44th Conf. Decision and Control*, pages 6698–6703, Seville, Spain, December 2005.

- [194] R. A. Olivieri and F. P. Chavez. A model of plankton dynamics for the coastal upwelling system of Monterey Bay, California. *Deep-Sea Research II*, 47(5):1077–1106, 2000.
- [195] A. Olshevsky and J. N. Tsitsiklis. Convergence rates in distributed consensus and averaging. In *Proc. 45th IEEE Conf. Decision and Control*, pages 3387–3392, San Diego, California, December 2006.
- [196] D. Paley, N. E. Leonard, and R. Sepulchre. Collective motion: Bistability and trajectory tracking. In *Proc. 43rd IEEE Conf. Decision and Control*, pages 1932–1937, Paradise Island, Bahamas, December 2004.
- [197] D. A. Paley, N. E. Leonard, and R. Sepulchre. Stabilization of symmetric formations to motion around convex loops. *Systems and Control Letters*, under review. Available from: <http://www.princeton.edu/~dpaley/papers/sc106.pdf>.
- [198] D. A. Paley, N. E. Leonard, and R. Sepulchre. Oscillator models and collective motion: Splay state stabilization of self-propelled particles. In *Proc. Joint 44th IEEE Conf. Decision and Control and European Control Conf.*, pages 3935–3940, Seville, Spain, December 2005.
- [199] D. A. Paley, N. E. Leonard, and R. Sepulchre. Collective motion of self-propelled particles: Stabilizing symmetric formations on closed curves. In *Proc. 45th IEEE Conf. Decision and Control*, pages 5067–5072, San Diego, California, December 2006.
- [200] D. A. Paley, N. E. Leonard, R. Sepulchre, D. Grünbaum, and J. K. Parrish. Oscillator models and collective motion: Spatial patterns in the dynamics of engineered and biological networks. *IEEE Control Systems Magazine*, Special issue on “Complex networked control systems”, to appear August 2007.
- [201] D. A. Paley, F. Zhang, and N. E. Leonard. Cooperative control for ocean sampling: The Glider Coordinated Control System. *IEEE Trans. Control Systems Technol-*

- ogy, accepted. Available from: [http://www.princeton.edu/~naomi/publications/2006/tcst06\\_submitted.pdf](http://www.princeton.edu/~naomi/publications/2006/tcst06_submitted.pdf).
- [202] A. Papachristodoulou and A. Jadbabaie. Synchronization in oscillator networks: Switching topologies and non-homogeneous delays. In *Proc. 44th IEEE Conf. Decision and Control*, pages 5692–5697, Seville, Spain, December 2005.
- [203] J. K. Parrish, S. V. Viscido, and D. Grünbaum. Self-organized fish schools: An examination of emergent properties. *Biol. Bull.*, 202(3):296–305, 2002.
- [204] B. L. Partridge. Rigid definitions of schooling behaviour are inadequate. *Animal Behavior*, 30(1):298–299, 1982.
- [205] B. L. Partridge. The structure and function of fish schools. *Scientific American*, 246(6):114–123, 1984.
- [206] L. M. Pecora and T. L. Carroll. Master stability functions for synchronized coupled systems. *Phys. Rev. Letters*, 80(10):2109–2112, 1998.
- [207] M. J. Perry and D. L. Rudnick. Observing the ocean. *Oceanography*, 16(4):31–36, 2003.
- [208] C. H. Pilskaln, J. B. Paduan, F. P. Chavez, R. Y. Anderson, and W. M. Berelson. Carbon export and regeneration in the coastal upwelling system of Monterey Bay, central California. *J. Marine Research*, 54(6):1149–1178, 1996.
- [209] A. Pogromsky, G. Santoboni, and H. Nijmeijer. Partial synchronization: From symmetry towards stability. *Physica D*, 172(1):65–87, 2002.
- [210] D. O. Popa, A. C. Sanderson, R. J. Komerska, S. S. Mupparapu, D. R. Blidberg, and S. G. Chappell. Adaptive sampling algorithms for multiple autonomous underwater vehicles. In *Proc. 2004 IEEE/OES Autonomous Underwater Vehicles Workshop*, pages 108–118, Sebasco Estates, Maine, June 2004.

- [211] M. Porfiri, D. G. Roberson, and D. J. Stilwell. Environmental tracking and formation control of a platoon of autonomous vehicles subject to limited communication. In *Proc. 2006 IEEE Conf. Robotics and Automation*, pages 595–600, Orlando, Florida, May 2006.
- [212] P.-M. Poulain and P. P. Niiler. Statistical analysis of the surface circulations in the California Current System using satellite-tracked drifters. *J. Phys. Oceanography*, 19(10):1588–1603, 1989.
- [213] T. M. Powell, C. V. W. Lewis, E. N. Curchitser, D. B. Haidvogel, A. J. Hermann, and E. L. Dobbins. Results from a three-dimensional, nested biological-physical model of the California Current System and comparisons with statistics from satellite imagery. *J. Geophysical Research—Oceans*, 111(C7):C07018, 2006.
- [214] D. V. Radakov. *Schooling in the ecology of fish*. J. Wiley, 1973. Translated from Russian by H. Mills.
- [215] M. Rahimi, R. Pon, W. J. Kaiser, G. S. Sukhatme, D. Estrin, and M. Srivastava. Adaptive sampling for environmental robotics. In *Proc. 2004 IEEE Int. Conf. Robotics and Automation*, volume 4, pages 3537–3544, New Orleans, Louisiana, April 2004.
- [216] S. Ramp. Personal communication, 2006.
- [217] S. R. Ramp, R. E. Davis, N. E. Leonard, I. Shulman, Y. Chao, A. R. Robinson, J. Marsden, P. Lermusiaux, D. Fratantoni, J. D. Paduan, F. Chavez, X. S. Liang, W. Leslie, and Z. Li. The autonomous ocean sampling network (AOSN) predictive skill experiment in the Monterey Bay. Submitted to *Deep-Sea Research II*.
- [218] S. R. Ramp, J. D. Paduan, I. Shulman, J. Kindle, F. L. Bahr, and F. Chavez. Observations of upwelling and relaxation events in the northern Monterey Bay during August 2000. *J. Geophysical Research—Oceans*, 110(C7):C07013, 2005.

- [219] W. Ren and R. W. Beard. Consensus seeking in multiagent systems under dynamically changing interaction topologies. *IEEE Trans. Automatic Control*, 50(5):655–661, 2005.
- [220] W. Ren, R. W. Beard, and E. M. Atkins. Information consensus in multivehicle cooperative control. *IEEE Control Systems Magazine*, 27(2):71–82, 2007.
- [221] E. Rimon and D. E. Koditschek. Exact robot navigation using artificial potential functions. *IEEE Trans. Robotics and Automation*, 8(5):501–518, 1992.
- [222] A. R. Robinson and S. M. Glenn. Adaptive sampling for ocean forecasting. *Naval Research Reviews*, 51(2):28–38, 1999.
- [223] A. R. Robinson and P. F. J. Lermusiaux. Data assimilation for modeling and predicting coupled physical-biological interactions in the sea. In A. R. Robinson, J. R. McCarthy, and B. J. Rothschild, editors, *The Sea: Biological-Physical Interactions in the Ocean*, chapter 12, pages 475–536. John Wiley & Sons, 2002.
- [224] E. O. Rogers, J. G. Genderson, W. S. Smith, G. G. Denny, and P. J. Farley. Underwater acoustic glider. In *Proc. 2004 IEEE Int. Geoscience and Remote Sensing Symp.*, volume 3, pages 2241–2244, Anchorage, Alaska, September 2004.
- [225] J. Rogge and D. Aeyels. Decentralized control of vehicle platoons with interconnection possessing ring topology. In *Proc. 44th IEEE Conf. Decision and Control*, pages 1491–1496, Seville, Spain, December 2005.
- [226] J. A. Rogge and D. Aeyels. Stability of phase locking in a ring of unidirectionally coupled oscillators. *J. Phys. A: Math. Gen.*, 37(46):11135–11148, 2004.
- [227] L. K. Rosenfeld, F. B. Schwing, N. Garfield, and D. E. Tracy. Bifurcated flow from an upwelling center: A cold water source for Monterey Bay. *Continental Shelf Record*, 14(9):931–964, 1994.

- [228] D. L. Rudnick and R. E. Davis. Mass and heat budgets on the northern California continental shelf. *J. Geophysical Research*, 93(C11):14013–14024, 1988.
- [229] D. L. Rudnick, R. E. Davis, C. C. Eriksen, D. M. Fratantoni, and M. J. Perry. Underwater gliders for ocean research. *Marine Technology Society Journal*, 38(1):48–59, 2004.
- [230] A. Sarlette, R. Sepulchre, and N. E. Leonard. Autonomous rigid body attitude synchronization. Submitted to *46th IEEE Conf. Decision and Control*. Available from: [http://www.montefiore.ulg.ac.be/~sarlette/Data/ssl\\_cdc2007.pdf](http://www.montefiore.ulg.ac.be/~sarlette/Data/ssl_cdc2007.pdf).
- [231] A. V. Savkin. Coordinated collective motion of groups of autonomous mobile robots: Analysis of Vicsek’s model. *IEEE Trans. Automatic Control*, 49(6):981–989, 2004.
- [232] K. Savla, F. Bullo, and E. Frazzoli. On traveling salesperson problems for Dubins’ vehicle: Stochastic and dynamic environments. In *Proc. 44th IEEE Conf. Decision and Control*, pages 4530–4535, Seville, Spain, December 2005.
- [233] L. Scardovi, A. Sarlette, and R. Sepulchre. Synchronization and balancing on the  $N$ -torus. *Systems and Control Letters*, 56(5):335–341, 2007.
- [234] L. Scardovi and R. Sepulchre. Collective optimization over average quantities. In *Proc. 45th IEEE Conf. Decision and Control*, pages 3369–3374, San Diego, California, December 2006.
- [235] L. Scardovi, R. Sepulchre, and N. E. Leonard. Stabilization laws for collective motion in three dimensions. To appear in *Proc. European Control Conference*, Kos, Greece, July 2007. Available from: [http://www.montefiore.ulg.ac.be/~scardovi/pub/ecc\\_final.pdf](http://www.montefiore.ulg.ac.be/~scardovi/pub/ecc_final.pdf).
- [236] O. Schofield, T. Bergmann, P. Bissett, J. F. Grassle, D. B. Haidvogel, J. Kohut, M. Moline, and S. M. Glenn. The long-term ecosystem observatory: An integrated coastal observatory. *IEEE J. Oceanic Engineering*, 27(2):146–154, 2002.

- [237] B. Schulz, B. Hobson, M. Kemp, and J. Meyer. Field results of multi-UUV missions using Ranger micro-UUVs. In *Proc. OCEANS 2003 MTS/IEEE Conf.*, volume 2, pages 956–961, San Diego, California, September 2003.
- [238] R. Sepulchre, D. Paley, and N. Leonard. Stabilization of collective motion of self-propelled particles. In *Proc. 16th Int. Symp. Mathematical Theory of Networks and Systems (electronic)*, Leuven, Belgium, July 2004. (10 pages).
- [239] R. Sepulchre, D. Paley, and N. Leonard. Collective motion and oscillator synchronization. In V. Kumar, N. Leonard, and A. S. Morse, editors, *Cooperative Control: A Post-Workshop Volume 2003 Block Island Workshop on Cooperative Control*, number 309 in Lecture Notes in Control and Information Sciences, pages 189–228. Springer-Verlag, 2005.
- [240] R. Sepulchre, D. Paley, and N. E. Leonard. Graph Laplacian and Lyapunov design of collective planar motions. In *Proc. Int. Symp. Nonlinear Theory and its Applications*, pages 217–232, Bruges, Belgium, October 2005.
- [241] R. Sepulchre, D. A. Paley, and N. E. Leonard. Stabilization of planar collective motion with limited communication. *IEEE Trans. Automatic Control*, accepted. Available from: <http://www.princeton.edu/~naomi/publications/2006/TACII.pdf>.
- [242] R. Sepulchre, D. A. Paley, and N. E. Leonard. Group coordination and cooperative control of steered particles in the plane. In K. Y. Pettersen, J. T. Gravdahl, and H. Nijmeijer, editors, *Group Coordination and Cooperative Control*, number 336 in Lecture Notes in Control and Information Sciences, pages 217–232. Springer, 2006.
- [243] R. Sepulchre, D. A. Paley, and N. E. Leonard. Stabilization of planar collective motion: All-to-all communication. *IEEE Trans. Automatic Control*, 52(5):811–824, 2007.
- [244] J. Sherman, R. E. Davis, W. B. Owens, and J. Valdes. The autonomous underwater glider “Spray”. *IEEE J. Oceanic Engineering*, 26(4):437–446, 2001.

- [245] N. Shimoyama, K. Sugawara, T. Mizuguchi, Y. Hayakawa, and M. Sano. Collective motion in a system of motile elements. *Phys. Rev. Letters*, 76(20):3870–3873, May 13 1996.
- [246] I. Shulman, S. H. D. Haddock, D. J. McGillicuddy, Jr., J. D. Paduan, and W. P. Bissett. Numerical modeling of bioluminescence distributions in the coastal oceans. *J. Atmos. Oceanic Tech.*, 20(7):1060–1068, 2003.
- [247] I. Shulman, D. J. McGillicuddy, Jr., M. A. Moline, S. H. D. Haddock, J. C. Kindle, D. Nechaev, and M. W. Phelps. Bioluminescence intensity modeling and sampling strategy optimization. *J. Atmospheric and Oceanic Technology*, 22(8):1267–1281, 2005.
- [248] I. Shulman, C.-R. Wu, J. K. Lewis, J. D. Paduan, L. K. Rosenfeld, J. D. Kindle, S. R. Ramp, and C. A. Collins. High resolution modeling and data assimilation in the Monterey Bay area. *Continental Shelf Research*, 22(8):1129–1151, 2002.
- [249] M. Silber, L. Fabiny, and K. Wiesenfeld. Stability results for in-phase and splay-phase states of solid-state laser arrays. *J. Opt. Soc. Am. B*, 10(6):1121–1129, 1993.
- [250] A. Sinha and D. Ghose. Generalization of linear cyclic pursuit with application to rendezvous of multiple autonomous agents. *IEEE Trans. Automatic Control*, 51(11):1819–1824, 2006.
- [251] B. Sinopoli, C. Sharp, L. Schenato, S. Schaffert, and S. S. Sastry. Distributed control applications within sensor networks. *Proc. of the IEEE*, 91(8):1235–1246, 2003.
- [252] T. R. Smith, H. Hanssmann, and N. E. Leonard. Orientation control of multiple underwater vehicles. In *Proc. 40th IEEE Conf. Decision and Control*, volume 5, pages 4598–4603, Orlando, Florida, December 2001.
- [253] P. Souères, A. Balluchi, and A. Bicchi. Optimal feedback control for route tracking with a bounded-curvature vehicle. *Int. J. Control*, 74(10):1009–1019, 2001.

- [254] E. M. Sozer, M. Stojanovic, and J. G. Proakis. Underwater acoustic networks. *IEEE J. Oceanic Engineering*, 25(1):72–83, 2000.
- [255] D. P. Spanos, R. Olfati-Saber, and R. M. Murray. Dynamics consensus on mobile networks. In *Proc. 16th IFAC World Congress (electronic)*, Prague, Czech Republic, July 2005. (6 pages).
- [256] D. Stammer. On eddy characteristics, eddy transports, and mean flow properties. *J. Phys. Oceanography*, 28(4):727–739, 1989.
- [257] I. Stewart, M. Golubitsky, and M. Pivato. Symmetry groupoids and patterns of synchrony in coupled cell networks. *SIAM J. Applied Dynamical Systems*, 2(4):609–646, 2003.
- [258] H. Stommel. The Slocum mission. *Oceanography*, 2(1):1989, 22-25.
- [259] S. H. Strogatz. From Kuramoto to Crawford: Exploring the onset of synchronization in populations of coupled oscillators. *Physica D*, 143(1-4):1–20, 2000.
- [260] S. H. Strogatz and R. E. Mirollo. Splay states in globally coupled Josephson arrays: Analytical predictions of Floquet multipliers. *Phys. Rev. E*, 47(1):220–227, 1993.
- [261] J. Sun, S. Boyd, L. Xiao, and P. Diaconis. The fastest mixing Markov process on a graph and a connection to a maximum variance unfolding problem. *SIAM Review*, 48(4):681–699, 2006.
- [262] S. Susca, S. Martínez, and F. Bullo. Monitoring environmental boundaries with a robotic sensor network. *IEEE Trans. Control Systems Technology*, accepted. Available from: <http://motion.mee.ucsb.edu/pdf/2006f-smb.pdf>.
- [263] H. J. Sussman. A general theorem on local controllability. *SIAM J. Control and Optim.*, 25(1):158–194, 1987.

- [264] M. T. Suzuki, C. M. Preston, F. P. Chavez, and E. F. DeLong. Quantitative mapping of bacterioplankton populations in seawater: Field tests across and upwelling plume in Monterey Bay. *Aquatic Microbial Ecology*, 24(2):117–127, 2001.
- [265] T. F. Swean. Coupled observation, adaptive sampling, and forecast in the real environment. Topic #10 of the *Broad Agency Announcement for the 2004 Department of Defense Multidisciplinary Research Program of the University Research Initiative*. Available from: [http://afosr-io.afosr.af.mil/documents/ONR.BAA\\_Announcement\\_03\\_012.pdf](http://afosr-io.afosr.af.mil/documents/ONR.BAA_Announcement_03_012.pdf).
- [266] H. G. Tanner, A. Jadbabaie, and G. J. Pappas. Flocking in fixed and switching networks. *IEEE Trans. Automatic Control*, 52(5):863–868, 2005.
- [267] P. A. Tester, S. R. Kibler, B. Hobson, and R. W. Litaker. A test of an autonomous underwater vehicle as a monitoring tool in shallow water. *African J. Marine Science*, 28(2):251–255, 2006.
- [268] J. Toner and Y. Tu. Long-range order in a two-dimensional dynamical XY model: How birds fly together. *Phys. Rev. Letters*, 75(23):4326–4329, 1995.
- [269] J. Toner and Y. Tu. Flocks, herds, and schools: A quantitative theory of flocking. *Phys. Rev. E*, 58(4):4828–4858, 1998.
- [270] C. M. Topaz and A. L. Bertozzi. Swarming patterns in a two-dimensional kinematic model for biological groups. *SIAM J. Appl. Math.*, 65(1):152–174, 2004.
- [271] K. Y. Tsang, R. E. Mirollo, S. H. Strogatz, and K. Wiesenfeld. Dynamics of a globally coupled oscillator array. *Physica D*, 48(1):102–112, 1991.
- [272] L. S. Tsimring, N. R. Rulkov, M. L. Larsen, and M. Gabbay. Repulsive synchronization in an array of phase oscillators. *Phys. Rev. Letters*, 95(1):014101, 2005.

- [273] J. N. Tsitsiklis. *Problems in Decentralized Decision Making and Computation*. PhD thesis, Massachusetts Institute of Technology, 1984. Available from: <http://web.mit.edu/jnt/www/Papers/PhD-84-jnt.pdf>.
- [274] J. N. Tsitsiklis and D. P. Bertsekas. Comment on “Coordination of groups of mobile autonomous agents using nearest neighbor rules”. *IEEE Trans. Automatic Control*, 52(5):968–969, 2007.
- [275] J. N. Tsitsiklis, D. P. Bertsekas, and M. Athans. Distributed asynchronous deterministic and stochastic gradient optimization algorithms. *IEEE Trans. Automatic Control*, 31(9):803–812, September 1986.
- [276] D. Uciński. Optimal sensor location for parameter estimation of distributed processes. *Int. J. Control*, 73(13):1235–1248, 2000.
- [277] D. Uciński. *Optimal Measurement Methods for Distributed Parameter System Identification*. CRC Press, Boca Raton, Florida, 2004.
- [278] J. L. van Hemmen and W. F. Wreszinski. Lyapunov function for the Kuramoto model of nonlinearly coupled oscillators. *J. Statistical Physics*, 72(1/2):145–166, 1993.
- [279] M. Veneziani, A. Griffa, A. M. Reynolds, and A. J. Mariano. Oceanic turbulence and stochastic models from subsurface Lagrangian data for the northwest Atlantic Ocean. *J. Phys. Oceanography*, 34(8):1884–1906, 2004.
- [280] T. Vicsek, A. Czirók, E. Ben-Jacob, I. Cohen, O. Shochet, and A. Tenenbaum. Novel type of phase transition in a system of self-driven particles. *Phys. Rev. Lett.*, 75(6):1226–1229, 1995.
- [281] S. V. Viscido, J. K. Parrish, and D. Grünbaum. Individual behavior and emergent properties of fish schools: A comparison of observation and theory. *Marine Ecology Progress Series*, 273:239–249, 8 June 2004.

- [282] D. Walker. Micro autonomous underwater vehicle concept for distributed data collection. In *Proc. OCEANS 2006 MTS/IEEE Conf.*, pages 1–4, Boston, Massachusetts, September 2006.
- [283] L.-S. Wang and P. S. Krishnaprasad. Gyroscopic control and stabilization. *J. Non-linear Science*, 2(4):367–415, 1992.
- [284] W. Wang and J.-J. E. Slotine. A theoretical study of different leader roles in networks. *IEEE Trans. Automatic Control*, 51(7):1156–1161, July 2006.
- [285] S. Watanabe and S. Strogatz. Constants of motion for superconductor arrays. *Physica D*, 74(3-4):197–253, 1994.
- [286] D. C. Webb, P. J. Simonetti, and C. P. Jones. SLOCUM: An underwater glider propelled by environmental energy. *IEEE J. Oceanic Engineering*, 26(4):447–452, 2001.
- [287] K. Wiesenfeld, C. Bracicowski, G. James, and R. Roy. Observation of antiphase states in a multimode laser. *Phys. Rev. Letters*, 65(14):1749–1752, 1990.
- [288] M. Wikelski, D. Moskowitz, J. S. Adelman, J. Cochran, D. S. Wilcove, and M. L. May. Simple rules guide dragonfly migration. *Biology Letters*, 2(3):325–329, 2006.
- [289] M. Wikelski, E. M. Tarlow, A. Raim, R. H. Diehl, R. P. Larkin, and G. H. Visser. Costs of migration in free-flying songbirds. *Nature*, 423(6941):704, 2003.
- [290] J. S. Willcox. Oceanographic surveys with autonomous underwater vehicles: Performance metrics and survey design. Master’s thesis, Massachusetts Institute of Technology, 1998. Available from: <http://library.mit.edu/item/000860143>.
- [291] J. S. Willcox, J. G. Bellingham, Y. Zhang, and A. B. Baggeroer. Performance metrics for oceanographic surveys with autonomous underwater vehicles. *IEEE J. Oceanic Engineering*, 26(4):711–725, 2001.

- [292] A. T. Winfree. Biological rhythms and the behavior of populations of coupled oscillators. *J. Theor. Biol.*, 16(1):15–42, 1967.
- [293] L. Xiao and S. Boyd. Fast linear iterations for distributed averaging. *Systems and Control Letters*, 53:65–78, 2004.
- [294] P. Yang, R. A. Freeman, and K. M. Lynch. Optimal information propagation in sensor networks. In *Proc. 2006 IEEE Int. Conf. Robotics and Automation*, pages 3122–3127, Orlando, Florida, May 2006.
- [295] P. Yang, R. A. Freeman, and K. M. Lynch. Distributed cooperative active sensing using consensus filters. In *Proc. 2007 IEEE Int. Conf. Robotics and Automation*, pages 405–410, Roma, Italy, April 2007.
- [296] M. K. S. Yeung and S. H. Strogatz. Time delay in the Kuramoto model of coupled oscillators. *Physical Review Letters*, 82(3):648–651, 1999.
- [297] X. Yu, T. Dickey, J. Bellingham, D. Manov, and K. Streitlien. The application of autonomous underwater vehicles for interdisciplinary measurements in Massachusetts and Cape Cod Bays. *Continental Shelf Research*, 22(15):2225–2245, 2002.
- [298] M. Zhan, G. Hu, Y. Zhang, and D. He. Generalized splay state in coupled chaotic oscillators induced by weak mutual resonant interactions. *Phys. Rev. Letters*, 86(8):1510–1513, 2001.
- [299] F. Zhang, D. M. Fratantoni, D. A. Paley, J. M. Lund, and N. E. Leonard. Control of coordinated patterns for ocean sampling. *Int. J. Control*, Special issue on “Navigation, guidance and control of uninhabited underwater vehicles”, in press. Available from: [http://www.princeton.edu/~naomi/publications/2006/IJCPaper\\_submitted.pdf](http://www.princeton.edu/~naomi/publications/2006/IJCPaper_submitted.pdf).
- [300] F. Zhang and N. E. Leonard. A controller design method under infrequent, asynchronous sensing. In *Proc. 10th Int. Conf. Hybrid Systems: Computation and Control*, pages 790–794, Pisa, Italy, April 2007.

- [301] F. Zhang and N. E. Leonard. Coordinated patterns of unit speed particles on a closed curve. *Systems and Control Letters*, 56(6):397–407, 2007.
- [302] Y. Zhang. *Spectral Feature Classification of Oceanographic Processes Using an Autonomous Underwater Vehicle*. PhD thesis, Massachusetts Institute of Technology, 2000.
- [303] Y. Zhang, A. B. Baggeroer, and J. G. Bellingham. Spectral-feature classification of oceanographic processes using an autonomous underwater vehicle. *IEEE J. Oceanic Engineering*, 26(4):726–741, 2001.



# Index

- all-to-all circular formation control, 92
  - composite phase control, 111
  - symmetric circular formation, 116
- all-to-all circular formation potential, 92
- all-to-all interaction, 64
- all-to-all phase potential, 70
  - critical points, 70
  - symmetric phase pattern, 114
- all-to-all synchronization and balancing, 72
  - circular formation, 95
  - constant rotation, 74
- augmented interaction network, 134
- autonomous ocean sampling network (AOSN),
  - 12, 39
- balanced graph, 65
- balanced phases, 53
- block interaction, 145
- circulant graph, 65, 66, 122
- circular formation, 57
- co-array design, 32
- complete graph, 63
- connectivity of a graph, 64
- consensus, 8, 81, 83
- controllability, 61
- curvature, 151
- curve-phase, 151, 164
  - model, 151
- cyclic (ring) graph, 65, 88
- dynamic circular formation control, 101
  - augmented with virtual particle, 143
  - symmetric circular formation, 129
- dynamic consensus filter, 89
- dynamic synchronization and balancing, 85
  - augmented with virtual particle, 142
  - circular formation, 105
  - constant rotation, 88
- effective speed, of a glider
  - measured, 28, 189
  - predicted, 168
- glider coordinated trajectories (GCT), 162
- incidence matrix  $B$ , 65
- inflection, of a glider dive, 24, 170
- interaction network, 62
  - levels, 146
- Kuramoto model, 74

- Laplacian circular formation control, 98
  - augmented with virtual particle, 138
  - composite phase control, 122
  - multi-level, composite control, 147
  - multi-level, composite symmetric circular formation, 149
  - symmetric circular formation, 127
- Laplacian circular formation potential, 97
- Laplacian curve-phase pattern potential, 158
- Laplacian loop formation control, 154
  - multi-level, augmented symmetric loop formation, 159
  - composite curve-phase control, 156
  - symmetric curve-phase pattern, 158
- Laplacian matrix  $L$ , 64
- Laplacian phase potential, 76, 123
  - augmented with virtual particle, 135
  - critical points, 77, 122
  - symmetric phase pattern, 126
- Laplacian quadratic form, 75
  - properties of, 75
- Laplacian synchronization and balancing, 79
  - augmented with virtual particle, 136
  - circular formation, 98
  - constant rotation, 80
- mapping domain, 19
- multi-level symmetric configuration, 144
- objective analysis (OA), 28
  - covariance function, 29
  - decorrelation lengths, 28
  - mapping error, 31
  - mapping performance, 31, 40, 211
  - measurement-noise variance, 29
- parallel formation, 57
- particle model, 51, 167
- perceptual zone, 67, 226
- phase model, 52
- phase order parameter  $p_\theta$ , 52
- planning cycle, 176
- profile, of glider measurements, 26
- projection matrix  $P$ , 64
- proximity-based interaction network, 67
  - nearest-neighbor, 67
  - zonal, 67
- quality control (QC) of waypoints, 179
- relative equilibria, 13, 62
- relaxation, of upwelling, 184
- rooted graph, 63
- shape control, 59
- shape space, 57
- shape variables, 60
- Slocum glider, 22, 169
- spacing error, 202
- spatially-constrained sensor platform, 35
- splay pattern, 55

Spray glider, 23, 169  
superellipse, 152, 233  
symmetric phase pattern, 55, 56  
synchronized phases, 9, 53  
  
temporally-constrained sensor platform, 35,  
186  
time-invariant graph, 63  
track (desired glider path), 38, 163  
tracking error, 202  
  
undirected graph, 63  
  
virtual particle, 134  
  
waypoint, 24  
waypoint completion condition, 173